Universitat Autònoma de Barcelona

On-surface synthesis of nitrogen-doped graphene-based nanoarchitectures: 0D nanographenes, 1D nanoribbons and 2D nanoporous graphene

María Tenorio Tuñas

AUTONOMOUS UNIVERSITY OF BARCELONA

DOCTORAL THESIS

On-surface synthesis of nitrogen-doped graphene-based nanoarchitectures: 0D nanographenes, 1D nanoribbons and 2D nanoporous graphene

María Tenorio Tuñas

Tutor:
Dr. Marta González Silveira

Directors:
Dr. César Moreno
Prof. Aitor Mugarza

Atomic Manipulation and Spectroscopy Group
Catalan Institute of Nanoscience and Nanotechnology

January, 2022

Programa de Doctorat en Física

"…Until the age of 70, nothing I drew was worthy of notice. At 73 years I was somewhat able to fathom the growth of plants and trees, and the structure of birds, animals, insects and fish. Thus when I reach 80 years, I hope to have made increasing progress, and at 90 to see further into the underlying principles of things, so that at 100 years I will have achieved a divine state in my art, and at 110, every dot and every stroke will be as though alive. Those of you who live long enough, bear witness that these words of mine are not false."

K. Hokusai

Abstract

Monolayer graphene has shown to possess distinguished physical properties, which make it one of the starring nanomaterials of the present and of the future. However, some missing properties in graphene limit its applications, such as the lack of band gap, relevant for electronics and optics; the selective reactivity, crucial for sensing, or the permeability, critical for sieving. The modification of its structure has seemed to become the best and most simple strategy to make it suitable for the implementation in nanodevices. Among the structural engineering strategies, the most straightforward approaches imply both scaling down and doping, which have been achieved for years with the top-down method. Nonetheless, with the incoming demand of smaller and more efficient devices, the atomic precision of the novel materials is imperative, something not feasible with the aforementioned technique. It has been demonstrated that the bottom-up protocol is the most appropriate method to achieve the desired functionalities of the nanostructure with atomic precision.

By using bottom-up strategies, graphene nanostructures can be synthesized either in solution or on a suitable catalytic surface. Even though the synthesis in solution has bestowed a huge variability of different nanostructures, it makes challenging having monodisperse solution of large aromatic nanostructures and characterize them with the same atomic precision that they are synthesize.

The surface-assisted synthesis is an alternative to overcome this issues. Furthermore, with the development of the Scanning Tunneling Microscope, the access to the observation and manipulation of single atoms, molecules or bigger nanostructures became possible, enabling the study of their local properties. In this regard, there have been remarkable works related to the on-surface synthesis of 0D nanographenes, 1D graphene nanoribbons, and 2D nanoporous graphenes. In this thesis dissertation, we address the growth of the three of them, focusing on the introduction of dopants and

synthesis of hybrid components. In particular, we put emphasis in the synthesis of 2D nanoporous structures, which has been challenging due to the irreversibility of the reactions on the surface, impeding its extension in the long range order. Very recently, in 2018 our group created a 2D Nanoporous graphene (NPG), with long range order and monodisperse distribution of hole size of less than one nanometer, and of the same shape. It was a leap for the engineering of nanostructured graphene, paving the way for the design of filters, and for the implementation of graphene in semiconductor devices.

This landmark opened an avenue to the study of the subfield of nanoporology (coined by C. Moreno to refer to the synthesis and study of nanopores) in graphene, guessing that the strategy could be generalized for nanopore tuning. One of the first and most important approaches is being able to substitutionally dope the edges of the pores with heteroatoms, and the on-surface synthesis of doped graphene nanoribbons can be taken as a guiding example.

In this work, the on-surface synthesis of a doped 2D nanoporous graphene is systematically studied. The first part of this thesis dissertation starts by the description of the synthetic route to grow the material, facing the challenges related to the thermal instability of the precursors and intermediate steps. 1D N-doped graphene nanoribbons are synthesized, and their structural and electronic properties are studied. Then, we describe a method to grow doped graphene nanopores from coupled graphene nanoribbons, although we do not achieve the already mentioned long range order.

In the second part of the thesis the aforementioned challenges are overcome by proposing a novel strategy that we presume to be extendable to different kinds of hybrid nanoarchitectures. In particular, our N-doped nanoporous graphene, made by the intercalation of two types of graphene nanoribbons, can also be recognized as a nanometer scale superlattice of type-II heterojunctions. Notably, the interface, made by the lateral intercoupling of alternating undoped and N-doped graphene nanoribbons, shows atomically sharp band discontinuities, and the accumulation of charges at both sides of the junctions promotes the generation of interface quantum dipoles. This ultimate confinement of the heterojunction electronic reconstruction enables the realization of 1 nm scale superlattices with well-defined and substantial band offsets.

In the third part of this thesis dissertation we study a kinetically driven route to grow N-doped nanographene chains, which feature zig-zag edges. We also test the concept of going beyond the synthesis of GNRs, by inducing further interribbon transformations to create new complex structures. We demonstrate this with two examples, AGNRs with topologically-induced superlattice bands, and AGNRs with fused nanopores, in particular annulene groups.

Overall, the results of this thesis provide a deep insight and systematic analysis into the on-surface synthesis of graphene nanoarchitectures, in particular 0D nannographenes, 1D graphene nanoribbons, and 2D nanoporous graphene, which have been intrinsically doped with nitrogen heteroatoms. We proved the different reaction pathways originated from the same or very similar molecular precusor depending on the growth conditions. Specially, we provide a very important landmark in the synthesis of 2D lateral superlattice heterostructures that feature sharp discontinuities down to the single carbon-carbon bond limit, and which can be extended to other nanoarchitectures.

Contents

List of Abbreviations

AFM	**A**tomic **F**orce **M**icroscopy
AGNR	**A**rmchair **G**raphene **N**anoribbon
AM	**A**mplitude **M**odulation
ARPES	**A**ngle **R**esolved **P**hotoemission **S**pectroscopy
BE	**B**inding **E**nergy
CBM	**C**onduction **B**and **M**inimum
CDH	**C**yclo **D**e **H**ydrogenation
CH/CC	**C**onstant **H**eight **C**onstant **C**urrent
DFT	**D**ensity **F**unctional **T**heory
FCC	**F**ace **C**entered **C**ubic
FM	**F**requency **M**odulation
HCP	**H**exagonal **C**lose **P**acked
IPS	**I**mage **P**otential **S**tate
LDOS	**L**ocal **D**ensity **O**f **S**tates
LT	**L**ow **T**emperature
NPG	**N**ano **P**orous **G**raphene
PDOS	**P**rojected **D**ensity **O**f **S**tates
QP	**Q**uadrupole **P**robe
RT	**R**oom **T**emperature
SPT	**S**ymmetry **P**rotected **T**opology
SS	**S**urface **S**tate
STM	**S**canning **T**unnelling **M**icroscopy
STS	**S**canning **T**unnelling **S**pectroscopy
VBM	**V**alence **B**and **M**aximum
UC	**U**nit **C**ell

Chapter 1

Introduction

In this first section, the procedure towards the synthesis of graphene nanoarchitectures, grown with atomic precision and on catalytic substrates is introduced. Then, three different types of graphene-based nanoarchitectures are considered: 0D nanographenes, 1D graphene nanoribbons, and 2D nanoporous graphene. A wider description is devoted to the requirements for the proper growth of graphene nanoribbons with the expected electronic properties. The last part of this section focuses on the chirality on the surfaces.

1.1 From pristine graphene to graphene nanostructures

Nanostructuring graphene has bestowed a plethora of new properties to this versatile 2D honeycomb carbon monolayer [1]. Even though monolayer graphene possesses outstanding mechanical, optical, thermal and electronic properties [2–5], its lack of band gap, as well as impermeability and inertness, complicates its implementation in microelectronics, sieving and sensing applications. Consequently, the engineering of graphene-based 0D dots, 1D chains or 2D porous nanostructures (Figure 1.1) is a strategy that allows to combine the advantages of the pristine monolayer with new desired properties.

The lateral quantum confinement of electrons provides an effective way to induce and engineer band gaps [6]. By doing so, the semimetallic graphene becomes semiconducting, thus feasible to be implemented in logic systems [7–9]. Besides, the electron confinement in 0D quantum dots can make molecular graphene [10] a single photon emitter [11, 12], a spin filter [11], a laser [13] or the photoluminescence can be tuned depending on their

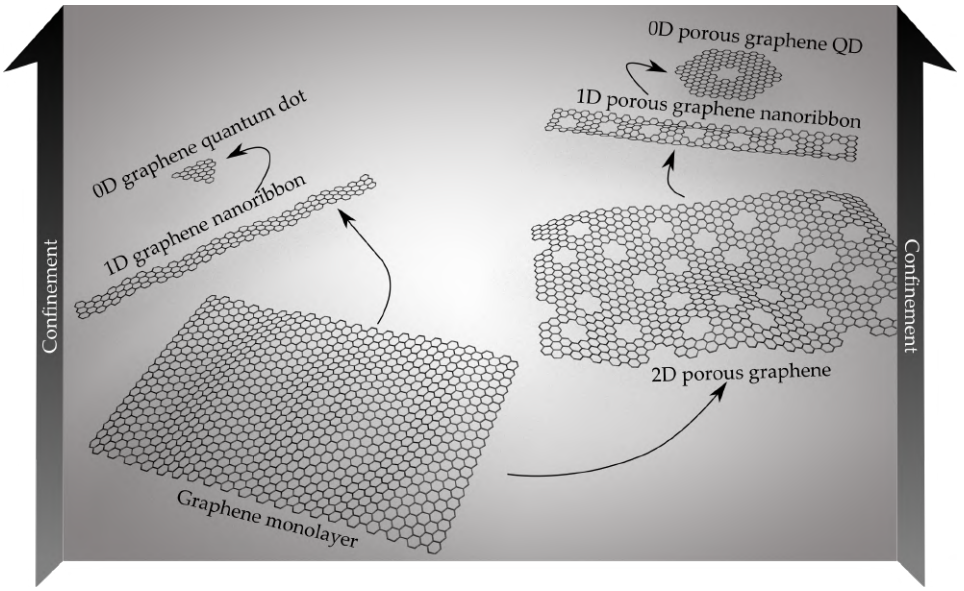

FIGURE 1.1: The nanostructuring strategies of graphene followed in this work.

structure [14–16]. Furthermore, the increase of 1D-edge versus 2D-bulk ratio upon nanostructuring exposes active sites to allocate functional groups that endow graphene with catalytic [17, 18], biosensing [19], optical [16, 20] and exotic electronic properties [21]. In addition, doting graphene with nanopores transforms this mechanically robust and flexible membrane into a semiconducting and permeable system, thus becoming very interesting as a protein and DNA sequencer [22], gas sensor [23], atomic and molecular filter [24] or for electrochemical storage [25].

Since the isolation and characterization of monolayer graphene [1], the strategies to build both 1D chains and 2D porous networks generally carry many disadvantages, as they followed a 'top-down' protocol: starting from the bulk material (graphene) it is miniaturized towards the desired nanostructure [26]. This generally triggers an uncontrolled number of defects, with reconstructed edges, dangling bonds, and sp^3-like carbon atoms, which perturbs in an uncontrollable way the high carrier mobility of graphene. The reconstructed edges generated by this method are generally advantageous in the sense that they facilitate the doping and functionalization of the monolayer, but do not offer control on the local doping distribution and selectivity on a specific functional group [27], acquiring a very poor

specificity on the sensed target or sieved species. Besides, the ribbons made by top-down approach (carbon nanotube unzipping, graphene lithography) are not narrow enough to generate a significant opening of the band gap [28], thus not suitable for their application in microelectronics.

As an alternative, 0D graphene quantum dots and 1D graphene nanoribbons have been synthesized in solution by bottom-up approaches. Developed during the 20th century, it was boosted by the works of K. Müllen, pioneer in the synthesis of a huge family of polycyclic aromatic hydrocarbons (PAHs) [29–33]. However, this method presents several disadvantages: the solubility is generally limited to organic solvents and the presence of aggregates in solution is unavoidable unless passivating groups are added to the most reactive sites of the molecule, or bulky ligands are added for steric hindrance. Even though the method offers an unlimited capability for structural engineering with the so desired atomic precision, the solution synthesis of these compounds is generally accompanied by contamination and low purity.

1.2 On-surface synthesis: from nanostructures to nanoarchitectures

The surface-assisted chemistry has come up as an interesting alternative to overcome the aforementioned drawbacks, enabling the synthesis of new 0D PAHs and even much larger 1D and 2D nanostructures with the same atomic precision as the conventional solution synthesis, but avoiding their aggregation in 3D.

These advantages enabled the design of more complex nanostructures with *a la carte* properties. Moreover, the confinement of the nanostructures on an atomically flat metallic surface enables the study of their properties by surface sensitive techniques and/or local probes and even their local modification via atomic manipulation. The capability of this technique to build complex structures levels up the definition of the grown system from 'nanostructures' to 'nanoarchitectures', a term coined by Ariga and Aono in 2015 [34], aiming to conceptualize the development of the nanomaterials in the recent years.

Among all different synthesized structures, 0D, 1D and 2D carbon-based aromatic systems (sp^2 bond configuration) have attracted most of the attention due to their versatility [35]. In particular, graphene-based nanomaterials have been of major interest [11, 33, 36–38] as they exhibit very interesting and tunable chemical and physical properties.

1.2.1 Surface-assisted synthesis of 0D nanographenes

The solution synthesis of nanographenes was propelled more than 70 years ago and it has been incessantly increasing until nowadays (Figure 1.2). Thanks to the development of the STM it was possible to observe these systems at the nanoscale and study the local properties. Soon, it was realized that, beyond depositing the intact nanographenes on the surface for their study [39], new routes to induce their formation out of the solution synthesis could be reached [40], hence increasing the variability of different chemical routes [41].

Surface-assisted synthesis of 0D nanographenes may follow two different routes: (i) by undergoing **intra**- molecular reactions (Figure 1.2 b-c) [46] and/or (ii) by undergoing **inter**- molecular reactions with (quasi) identical precursors (Figure 1.2 d-e). The first scenario generally refers to new generation of intra- molecular bonds due to an external stimuli, such as tip manipulation (Figure 1.2 b) [42] of thermally assisted (Figure 1.2 c) [43, 47, 48].

The route that involves the synthesis via **inter**- molecular reactions strongly depends on the number and distribution of activation sites in order to obtain either a finite or an infinite system. Figures 1.2 d)-e) show the two possibilities to grow 0D nanographenes implying inter- molecular reactions (as well as intra-). If there is only one activation site (Figure 1.2 d), the route will trigger the formation of 0D nanographene covalent dimers [44, 49]. On the other hand, if the precursor is two-fold substituted by activation sites, it will depend on their distribution that the system becomes a finite 0D nanographene or, an infinite 1D graphene nanoribbons (which will be described in the next section). If the substitution is *meta*- distributed (1.2 e), generally these systems may close in circle, creating quantum dots with inner cavities [45, 50]. If the precursor has been *para*- two-fold substituted, the coupling can be infinite and consequently grow 1D graphene nanoribbons

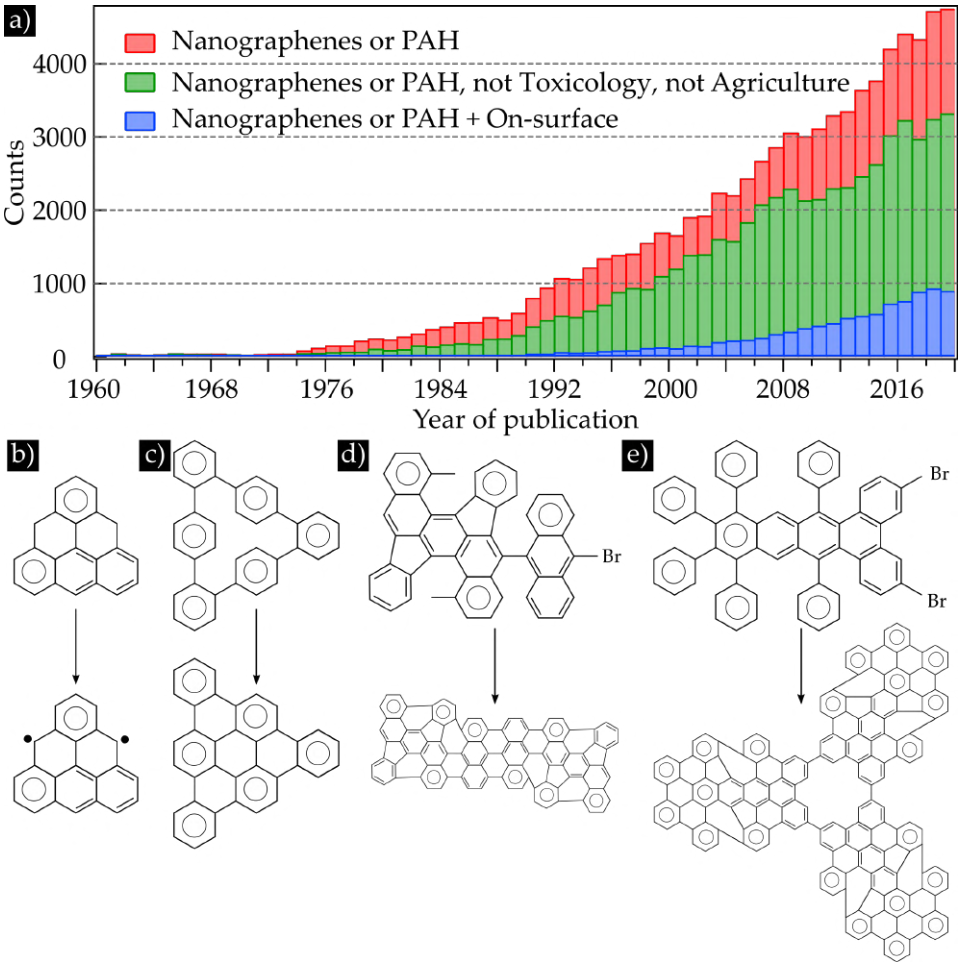

FIGURE 1.2: On-surface synthesis of nanographenes. a) Literature about nanographenes, taken from the database of Web of Science. The labels indicate the filtering terms used in each case. Examples of nanographene precursors and the respective products grown via b) AFM tip manipulation [42], c) intra- molecular cyclodehydrogenation [43], d)-e) inter- molecular coupling with either single halogenated [44] d) or two-fold halogenated precursor in *meta*- position e) [45].

[51]. Likewise, if the precursor is many-fold substituted with activation sites, generally a 2D covalent organic framework or porous graphene nanoribbons will be formed [52, 53].

In the last three years, there has been an increased effort in the synthesis and local study of nanographenes with an open shell character [11, 42, 54–65], as they may show coherent spins, with big inelastic excitation energies, becoming interesting for spintronics and quantum technologies. The combination of solution with on-surface synthesis at ultra high vacuum conditions has allowed to synthesize specific molecules with high reactivity due to their unpaired spins. Beyond the solely demonstration of synthesis of nanographenes hosting unpaired spins, there is groundbreaking attempt on synthesizing coupled nanographenes via the growth of 1D chains in order to induce collective magnetism [58, 59]. Most of literature is related with triangulene derivatives, with very few studies on the synthesis of periacene-based chains. In this thesis the rational on-surface synthesis of periacene-derivative 1D chains is studied, including doping and chirality.

1.2.2 From 0D nanographenes to 1D graphene nanoribbons

The coupling of few precursors to create finite 0D nanographenes can be extrapolated to an infinite 1D polymeric chain. In 2010, inspired by the strategy of the surface version of the Ullmann coupling reaction ignited by Grill [66] the synthesis of graphene nanoribbons was demonstrated for the first time [51]. The method comprised two steps, the Ullmann polymerization of bianthracene precursors into 1D chains, followed by a planarization triggered by the cyclodehydrogenation. The recipe was originally demonstrated with two different kinds of molecular precursors, which gave either armchair or chevron graphene nanoribbons (GNRs). This landmark evidenced that the method could be generalized to other nanostructures, opening the field of the on-surface synthesis (OSS) of atomically precise graphene nanoribbons.

The on-surface reaction pathway towards the pioneer 7 armchair graphene nanoribbon [51] (7-AGNR, where '7' stands for the number of carbon atoms in the orthogonal direction of the ribbon backbone) on a Au(111) surface is depicted in detail in Figure 1.3 [51, 67]. The molecular precursor is a 10,10'-dibromo-9,9'-bisanthracene (DBBA) molecule. This molecule displays a non-planar conformation as in gas phase: the two bisanthracene subunits are tilted in a scissor-like conformation due to the steric hindrance between confronted hydrogen atoms (Figure 1.3, a). Activated by the catalytic surface under an applied temperature, the carbon-halogen bond (in

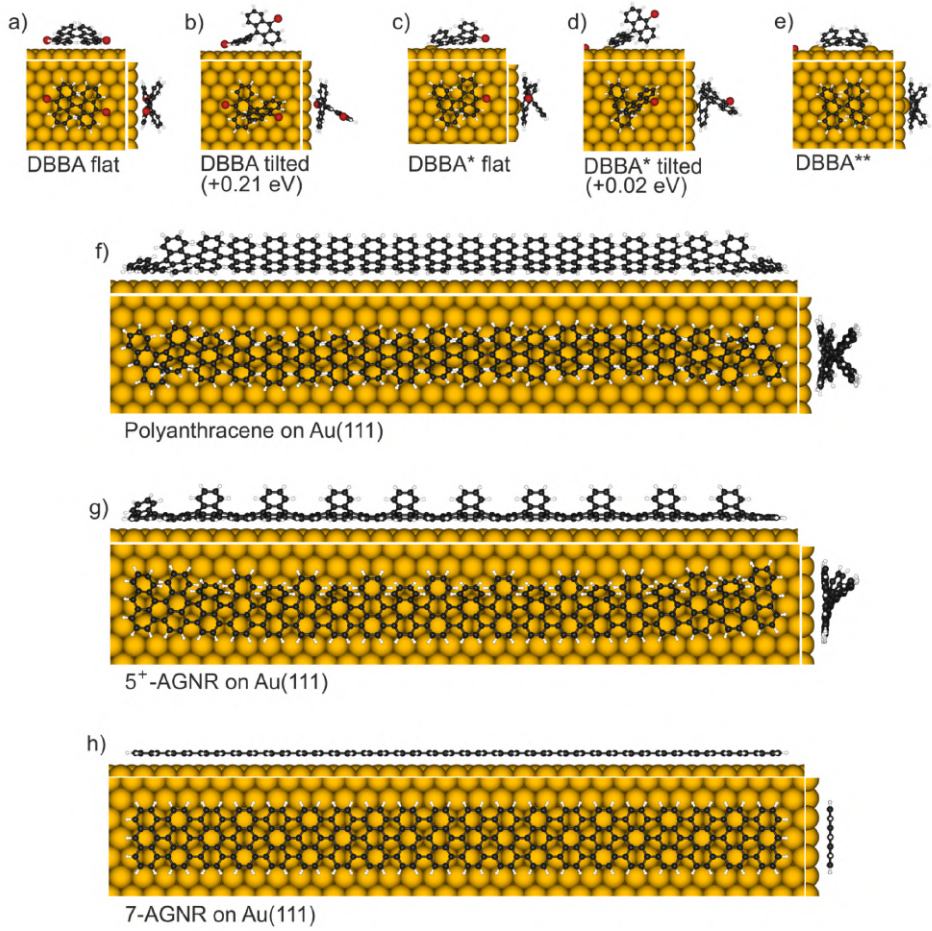

FIGURE 1.3: Schematic representation of the reaction pathway for the on-surface synthesis of 7-AGNR on the catalytic Au(111) surface using 10,10′-dibromo-9,9′-bianthryl (DBBA) as molecular precursor, with the respective intermediate states. The scheme is taken from Ref. [67].

this particular case, bromine) cleaves out of the core molecule and a radical is created, which will bond to an uplifted gold atoms from the surface (Figure 1.3, c-e). The radical will diffuse until it finds another molecule in the same conditions, undergoing the Ullmann coupling reaction that will create a DBBA-dimer. If this is repeated consecutively, a DBBA oligomer or polyanthracene chain is grown (Figure 1.3, f). At higher temperature, the Au(111) activates the C-H bonds of nearby anthracene and they undergo the dehydrogenative aryl-aryl coupling reaction with a domino-like tendency

by only one side (Figure 1.3, g). Eventually, the whole system planarizes and the GNR is formed (Figure 1.3, h).

Some years after the demonstration of on-surface Ullmann polymerization, Grill's group introduced another ingredient to further control the direction of the covalent networks: by combining different aryl halides at specific positions they could selectively clave each halide due to their different activation energy, leading to a hierarchical control of the growth from 1D chains to 2D structures [68] (Figure 1.4).

One year later, C. Bronner and co-workers proved the on-surface synthesized graphene nanoribbons can be intrinsically doped with heteroatoms [69] (Figure 1.4), demonstrating that the shift of the electronic band gaps of the semiconducting graphene nanostructures, in particular graphene nanoribbons, was directly proportional to the number of dopants. The same year, as-grown GNRs were taken out of their Ultra-high vacuum (UHV) growth conditions to be proven as FET devices for the first time [70].

These landmarks (Figure 1.4) were decisive to grow graphene-based heterojunctions [71–73]. The combination of different graphene nanoribbon components through their carbon backbone demonstrated that heterojunctions could be built from the coupling of GNRs with different electronic properties, creating staggered electronic bands [71] or confining the electronic wavefunctions within a graphene-based quantum dot [72]. However, this type of systems are very difficult to be implemented in a device since they are randomly distributed on the surface and the size of each component cannot be controlled. In this thesis dissertation we demonstrate the realization of ordered, nanometer size 1D superlattice of heterojunctions within 2D nanoporous graphene structures.

It was soon realized that heterojunctions could be created from a single molecular precursor that embedded the two components [74]. The ability to control the periodicity of these structures allowed the synthesis of superlattices containing topologically-induced bands. This was firstly modelled in 2017 [74] and then experimentally demonstrated in 2018 [75, 76], a trending subtopic in the on-surface synthesis field nowadays [77–80].

If there is something present in all these works related to the on-surface

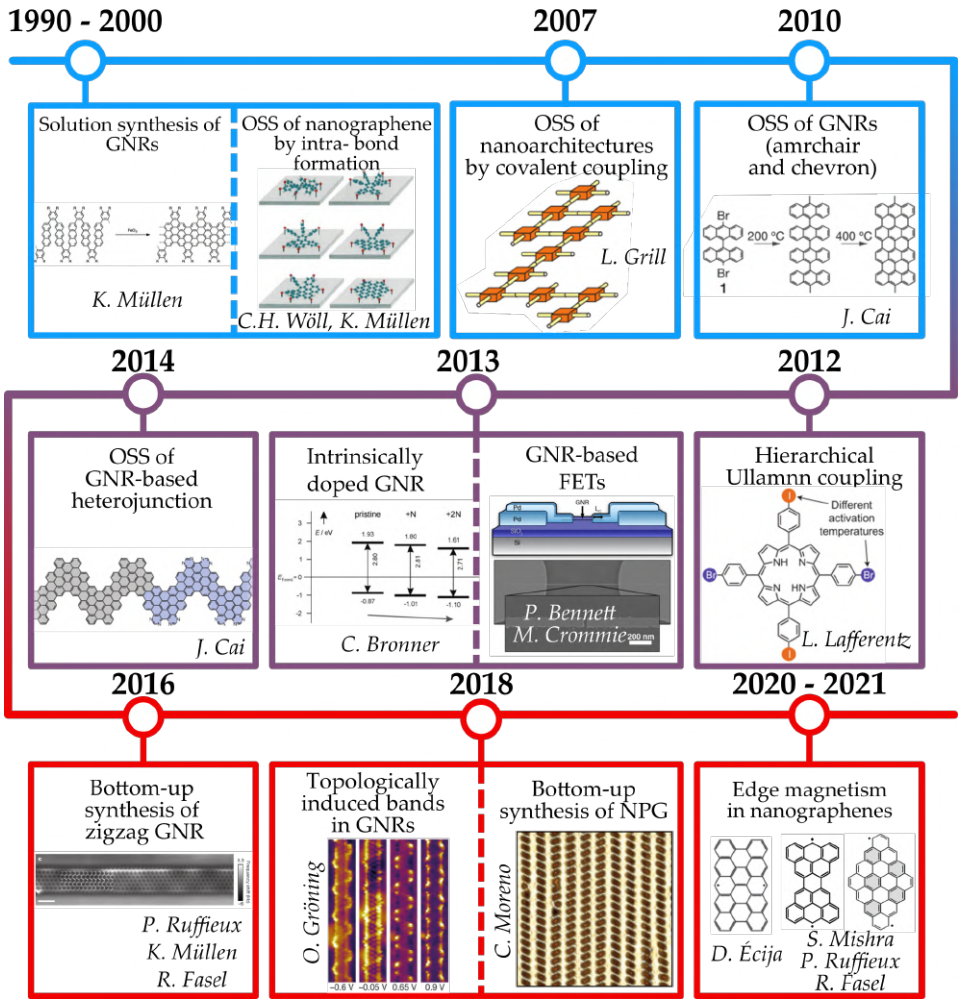

FIGURE 1.4: Graphene nanoarchitectonics timeline since the 90s.

synthesis of graphene nanoribbons, is the optimization of the synthesis conditions involving, among others, the precursor design, the catalytic surface choice, the temperature, the pressure, the surface coverage, etc [35]. Herein the three more relevant variables will be explained in more detail.

Tools for the on-surface reaction of 1D graphene nanoribbons

The effect of the precursor type

The rational design, of the molecular precursor will determine the characteristics of the final graphene nanoribbon. The particular structure will determine the width and lateral edge shape, and hence on the electronic properties (Figure 1.5 c) [6, 36, 37, 81].

The electronic structure of GNRs derives from that of the graphene honeycomb lattice, which is represented by two equivalent sublattices A and B (blue and red circles in Figure 1.5 a) and the lattice vectors a_1 and a_2:

$$a_1 = \frac{a}{2}(3, \sqrt{3}) \tag{1.10}$$

$$a_2 = \frac{a}{2}(3, -\sqrt{3}) \tag{1.11}$$

where a is the carbon-carbon bond distance (1.42 Å). The respective reciprocal lattice vectors are b_1 and b_2:

$$b_1 = \frac{2\pi}{3a}(1, \sqrt{3}) \tag{1.12}$$

$$b_2 = \frac{2\pi}{3a}(1, -\sqrt{3}) \tag{1.13}$$

Of particular importance in the reciprocal space are the high symmetry points (indicated in Figure 1.5 b): Γ, or the center of the Brillouin Zone (BZ) and **K** and **K'**, which are the Dirac Points.

The resulting electronic properties are unveiled by tight binding approximation [83] considering the first nearest neighbours, δ_1, δ_2 and δ_3, and one electron per carbon atom, which in reality is the valence electron of the p_z orbitals (the π bands), represented as a function of the lattice vectors:

$$\delta_1 = \frac{a}{2}(1, \sqrt{3}) \tag{1.14}$$

$$\delta_2 = \frac{a}{2}(1, -\sqrt{3}) \tag{1.15}$$

$$\delta_3 = -a(1, 0) \tag{1.16}$$

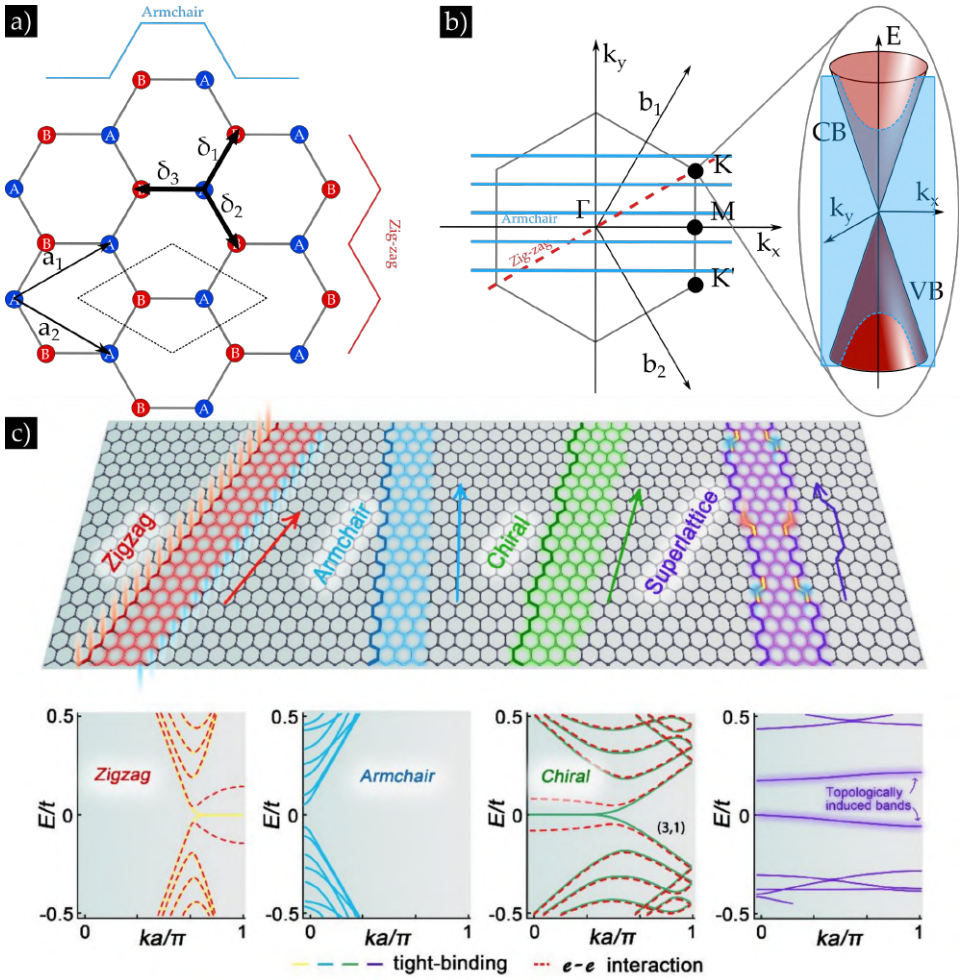

FIGURE 1.5: [Quantization of band structure in GNRs. a) Real space scheme of monolayer graphene, indicating the lattice vectors (a_1, a_2) and the nearest neighbours (δ_1, δ_2, δ_3). b) Momentum space scheme of the monolayer graphene and the quantization upon confinement into armchair GNRs. K Dirac point has been shown in 3D, cut by the plane of the graphene confinement and the respective parabolas of the valence and conduction bands. c) Different GNRs and their most representative electronic band structure by tight binding approximation [82].

The resulting energy dispersion in the infinite monolayer graphene can be expressed, after some approximations [83], as:

$$E_{\pm}(q) = \pm v_F |q| + O[(q/K)^2] \tag{1.17}$$

and the Fermi velocity:

$$v_F = 3ta/2 \tag{1.18}$$

where **q** is the momentum measured relatively to the **K-K'** Dirac points (**q** = k - **K**), t is the hopping term (generally t =2.7 eV) and v_F is the Fermi velocity ($v_F = 1 * 10^6$ m/s). The solution shows that the energy dispersion relation is linearly proportional to the k space. Therefore, the velocity does not depend on the energy and electrons are massless. Since the π bands, which provide two electrons per unit cell, are connected by the gapless Dirac cone (Figure 1.5 b) and half-filled, the graphene is semimetallic.

The 1D GNRs quantized the Dirac cones by intersecting them with discrete planes in the direction of the confinement (Figure 1.5 b)The most extensively studied GNR has been the armchair (AGNR), due to the easy tunability of the band gap and the stability out of the ultra high vacuum conditions. It has been demonstrated that AGNRs possess an open and direct band gap, as the Dirac cones turn into parabolic bands. The band gap opens as the width of the GNRs increases. However, the absolute value does not have a monotonic variation, since its value oscillates depending on the family the AGNRs belong due to the coincidence of a quantized level with the Dirac point. Considering that N = number of carbon atom across the ribbon, and p as an integer, the AGNRs can be distinguished in three families, where the band gap varies as $\Delta_{3p+1} > \Delta_{3p} > \Delta_{3p+2}$.

For other particular edge structures, additional states may arise within the π band gap. For instance, zigzag GNRs host p_z dangling bonds at the edges that lead to localized spin split states at the Fermi level [84].

Very recently, a novel strategy for band engineering regarding this oscillating behaviour has been exploited to create superlattices with topologically-induced bands [74]. An example with the 7-, 8- and 9- AGNR is represented in Figure 1.6. 7-AGNR belongs to the 3p+1 family and the 9- AGNR to the 3p, both semiconducting. According to tight binding calculations, 8- AGNR, which belong to the 3p+2 family, is a gapless ribbon. Therefore, designing a ribbon which combines both 7- and 9- AGNR components with an 8- AGNR like interface will close the band gap at that point. However, the symmetry

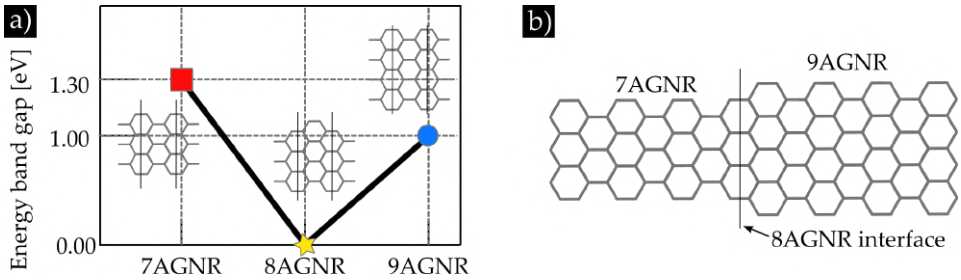

FIGURE 1.6: Electronic band gap and emergence of in-gap states. a) Tight binding calculation of the absolute value of the band gap in 7-AGNR, 8-AGNR and 9-AGNR. b) Schematic representation of a 7-9 AGNR junctions showing a (metallic) 8-AGNR-like interface.

of both components at this interface is a key parameter in order to induce the presence of in-gap bands with a determined topological phase [74]. In this thesis dissertation we study a synthetic route to create a topological 7-9 AGNR superlattice.

The effect of the configuration of active sites via Ullmann coupling

Although there are many other inter- molecular reaction strategies, the Ullmann coupling has been the most extensively used [35, 85] due to its simplicity and controllability. Therefore, it will be used here as example of the effect of the configuration of the active sites on the inter- molecular coupling. This reaction features the homocoupling of two radical carbon atoms after undergoing a halogen-carbon bond scission. Chlorine, bromine and iodine have been all proposed for the surface version of the Ullmann coupling reaction. Depending on the polarizability of the carbon - halogen bond, the cleavage will take part at a determined temperature window (Figure 1.7 a). This characteristic has been used to grow hierarchical nanostructures, by controlling at which step of the reaction the cleavage is promoted [68].

As commented previously, the position of the halogen atoms in the molecule can play a role in the final product characteristics [38, 86] (Figure 1.7 b). In general, a two-fold halogenated precursor is neccesary to grow graphene nanoribbons, otherwise 0D nanographenes (single- halogenated) or 2D covalent organic frameworks (many-fold halogenated) will be built. The two halogens can be distributed in the molecule in a *para-*

a)

C - X	Dissociation energy
C - F	5.51 eV
C - Cl	4.21 eV
C - Br	3.64 eV
C - I	2.84 eV
C - H	4.89 eV

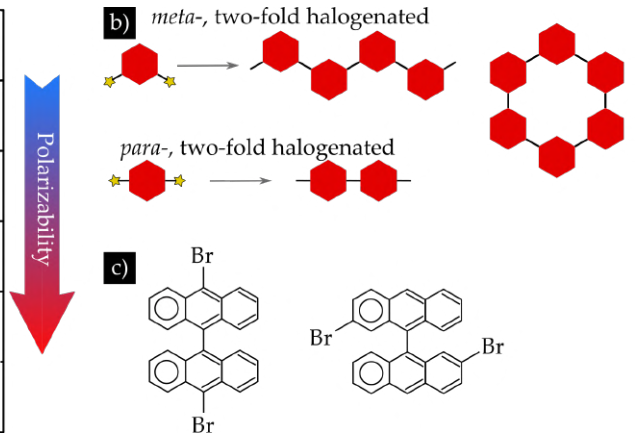

FIGURE 1.7: Choosing the halogen type and halogen distribution geometry. a) Table with the carbon-halogen dissociation energies (in gas-phase), compared to the carbon-hydrogen dissociation energy; b) schematics of two possible geometric distributions of two-fold halogenated molecular precursors: *para-* and *meta-*; c) *para-* two-fold substituted DBBA precursor in different positions.

like or *meta-* like configuration (Figure 1.7 b). The former will always give GNRs, whereas the latter could give either 0D nanographenes or GNRs. Furthermore, the absolute position of the two-fold halogenated precursors with *para-* distribution in the precursor is also important: for instance dibromo bianthracene molecular precursor can grow either armchair or chiral graphene nanoribbons depending on the positions of the halogen atoms (Figure 1.7 c) [87].

Halogen atoms also play a critical role in the yield of the final product when they are cleaved from the precursor monomers and adsorbed in the catalytic substrate. As it has been demonstrated from surface-sensitive techniques, halogen atoms generally desorb from the surface in the form of hydrogenated molecule [88–90]. Since the required hydrogen atoms can a priori only come from graphene nanoribbons, their desorption is a hint of the cyclodehydrogenation of these systems. In this thesis dissertation, the signature of the halogen-metal bond during the dehalogenation procedure will be critical to obtain the graphene nanoarchitectures.

The catalytic effect of the substrate and the templating effect of the superstructures

The choice of the different catalytic surfaces depends on the one hand on the compromise between the molecule mobility over the surface ad the adsorption energy. A second very important ingredient determined by the substrate is the separation of the actiivation temperatures of each reaction step. Also this temperature have to be not too high to avoid undesired side reactions, but high enough to promote diffusion. Graphene nanoribbons have been grown generally on coinage metals: gold, silver and copper. Gold facets are the most employed surfaces to grow as their lower reactivity leads to well separated reaction windows for each step, all above room temperature. The increasing reactivity for silver and copper does not only lead to an overlap of reaction thermal windows, but it also hampers diffusion, hindering the synthesis. The choice of the different catalytic surfaces depends, on the one hand, on the compromise between the molecule mobility over the surface and the adsorption energy. It also affects the activation of the molecule precursors into their intermediate products. These variables make that different products from the same precursor could be obtained [91–97].

Besides the reactivity of the different metals, each of them can induce local reactivity depending on their reconstruction. For the case of the Au(111) facet, which will be the most employed in this thesis, it is well known it shows a 22 X $\sqrt{3}$ reconstruction with a herringbone-like pattern [98], where face-centered cubic (fcc) and hexagonal close-packing (hcp) crystallographic structures alternate due to point dislocations. Predicted theoretically and evidenced experimentally, the adsorption energy at the fcc sites is lower in comparison to the hcp sites [98], which makes the Au(111) herringbone reconstruction behave as a nanotemplate. The first to describe the GNRs alignment into a rectangular grid by means of the nanotemplate created by the herringbone was demonstrated by our group [96] (Figure 1.8 left).

Other more rigid nanotemplates can also be used, such as the parallel arrays of monoatomic steps found in vicinal surfaces (Figure 1.8 right). It is known that in these cases ribbons grow parallel to the steps of the terraces, thus facilitating their characterization with surface-sensitive techniques, like polarized Raman, or ARPES [99–105]. An important difference with respect to the weaker template offered by the herringbone reconstruction is that the steps confine ribbons at each terrace. In this thesis dissertation, we use a curved vicinal Au(111) surface to confine graphene nanoribbons in

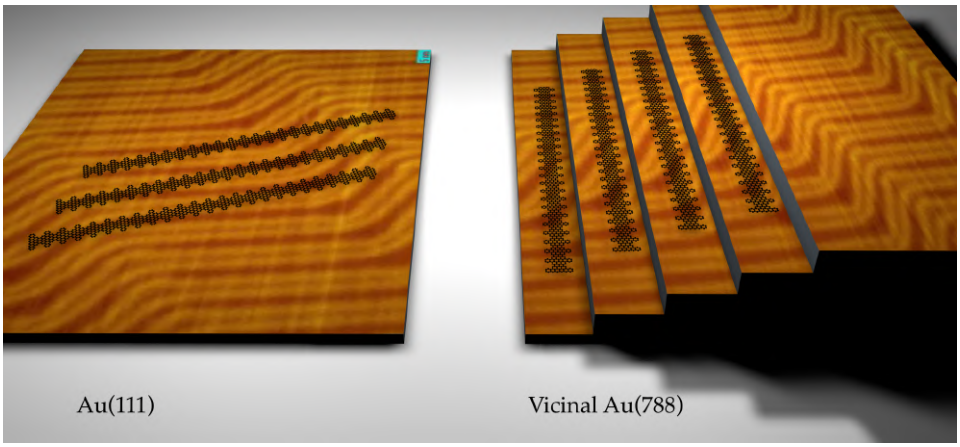

FIGURE 1.8: Gold facets as nanotemplates: the herringbone reconstruction of the Au(111) facet guides the growth of DPDBBA ribbons and the vicinal Au(788) (artificially represented) hosts the ribbons at each single gold terrace.

order to induce a specific type of reaction.

1.2.3 2D nanoporous graphene. The introduction of nanopores in a graphene matrix

Single layers of nanoporous graphene have been generally achieved from a top-down approach by chemical etching, ion bombardment or template assisted techniques, among others [25, 106, 107]. Its multiple properties, such as the sieving and filtering effect of atoms, ions, molecular gases, proteins or DNA [22–24, 106–112], and the electronic [113, 114] and sensing [107] applications have been demonstrated so far. The top-down strategy is nowadays competing with the bottom-up protocol, since the latter provides access to subnanometer structuring with atomic control on the pores edge shape and dopant distribution. However, there are still challenges concerning the introduction of these bottom-up synthesized nanoporous graphenes into applications which are reachable by the top-down synthesized systems, since one of the major challenges is the long range order.

The most obvious and explored method is the direct coupling of building blocks in 1D porous graphene nanoribbons or 2D covalent organic

Type	Coupling	Network characteristics	Halogen atom	Catalytic substrate	Band gap [eV]	Ref.
Porous GNRs	Organometallic intermediate Ullmann coupling	N-doped	Br	Ag(111)	2.20	[130]
Porous GNRs	Organometallic intermediate Ullmann coupling	GNRs	Br	Ag(111)	-	[53]
Porous GNRs	Organometallic intermediate Ullmann coupling	QDs	Br	Ag(111)	-	[52]
Porous GNRs	Ullmann coupling (hierarchical)		Br, Cl	Au(111)	1.95	[131]
Lateral fusion of GNRs	Dehydrogenative cross coupling	Short-range order	CDH*	Au(111)	-	[115]
Lateral fusion of GNRs	Dehydrogenative cross coupling	Short-range order	CDH*	Au(111)	-	[117]
Lateral fusion of GNRs	Dehydrogenative cross coupling	Short-range order	-	Au(111)	2.49 (GNR)	[116]
Lateral fusion of GNRs	Dehydrogenative cross coupling	Long-range order	CDH*	Au(111)	1.00	[96, 118]
Lateral fusion of GNRs	Dehydrogenative cross coupling	Long-range order	CDH*	Au(111)	2.70	[132]
Porous graphene/ COF	Ullmann coupling	-	I	Ag(111)	-	[133]
COF	Organometallic intermediate Ullmann coupling	N-doped	Br	Au(111)	1.90	[134]
COF	Organometallic intermediate Ullmann coupling	N-doped/kagome	Br	Ag(111)	2.45	[135]
COF	Ullmann coupling (hierarchical)	-	Br, I	Au(111)	-	[136]
COF	Organometallic intermediate Ullmann coupling	-	Br, I	Cu(111)	-	[137]
COF	Ullmann coupling (hierarchical)	-	Br	Au(111), Ag(111)	-	[86]
COF	Alkynyl cyclotrimerization) (No Ullmann)	N-doped/COF	-	Au(111)	3.41eV (theory)	[138]
COF	Organometallic intermediate Ullmann coupling	-	Br, Cl	Au(111), Ag(111), Cu(111)	-	[139]

*CDH stands for cyclodehydrogenation, which is the strategy the GNRs follow to laterally couple and form NPG.

TABLE 1.1: Graphene-based nanoporous structures grown by on-surface synthesis.

frameworks (COFs). The inherent difficulties are related to the irreversibility of the covalent bonds [86] and the high probability of creating defects in the synthesis of a covalent structure in 2D. An alternative is the sequential growth, ignited by L. Grill and coworkers [68]. The concept can be applied to Nanoporous graphene by growing 1D GNR building blocks first, avoiding the formation of defects. Then, the long, flawless GNRs couple laterally. This last step is the more challenging, as the parallel alignment of the ribbons is highly required [115–117]. Whereas most of previous literature has shown to carry out this strategy, succeeding in creating NPG of few GNR units, our group demonstrated it could be extended to the long range order

[96, 118]. Table 1.1 lists the most representative examples of bottom-up graphene-based nanoporous networks.

The synthesis of a long-range order nanoporous graphene structure featuring atomically precise, 1 nm scale stripes and pores [118, 119] was a notorious breakthrough in the realization of bottom-up 2D graphene nanoarchitectures [120–122]. The electron confinement in nanometer scale stripes leads to an electronic band gap is 1.0 eV, appropriate for the room temperature operation of a field-effect transistor [114, 118]. Additionally, the highly anisotropic structure imprinted by the weakly coupled GNRs that form the nanoporous graphene gives rise to highly anisotropic mechanical, electronic, optical and thermal properties [123, 124], and interesting quantum effects such as the electronic Talbot effect [125, 126]. Finally, promising applications have also been predicted related to the presence of nanometer scale pores, such as selective gas filtering [127, 128] or anodes for ion-based batteries[129]. Inspired by this work, this thesis goes a step beyond in the synthesis of nanoporous graphene by introducing dopants at the pore edges, and providing a method to synthesize NPG structures that electronically behave as superlattice heterostructures.

1.3 Multiple components in graphene-based nanoarchitectures

Up to now, the polymerization strategy has been achieved (i) by using the same precursor (homo-coupling) and (ii) by symmetrical coupling. However, this coupling can be further exploited so that in one single ribbon different components are combined, which is referred to "copolymers" [140] (Figure 1.9). Two strategies can be followed: in a first scenario, different molecular precursors can be randomly combined and connected via heterocoupling. This creates 'statistical' copolymers, which has been the proof of concept of GNR-based Type-I and Type-II heterojunctions [71–73, 141–145]. In a second scenario, precursors can be designed in advance with a non-symmetrical structural configuration, what is denominated 'alternating' copolymers. The strategy induces the formation of GNR-based superlattices [74–80, 146].

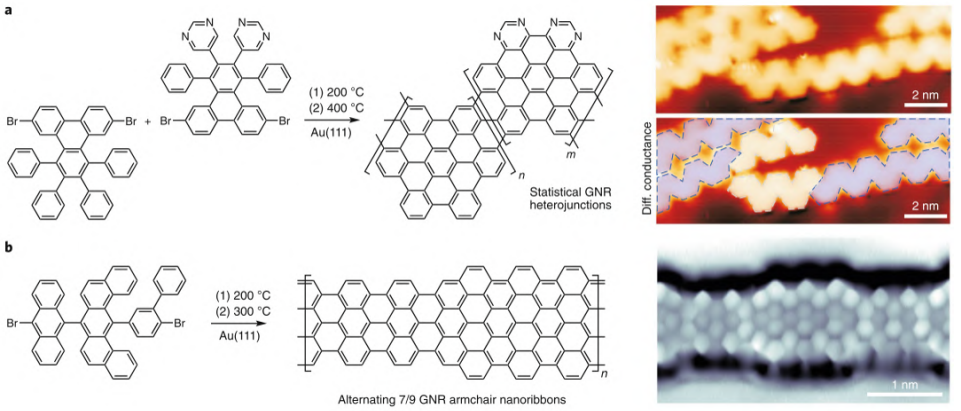

FIGURE 1.9: GNR heterostructures. Top: Random GNR heterojunction formed by statistical copolymerization [71]; bottom: GNR superlattice obtained by the alternating copolymerization strategy by using dicomponent precursors [76]. Figure taken from Ref. [140].

Alternatively to 1D copolymerization, it can be extended to 2D [147]. However, there is not so much reported literature about on-surface synthesis of 2D copolymers. The few examples that demonstrate it mostly show short-range order [68], or a huge number of defects [148]. As a consequence, it is needed a novel strategy where 2D copolymers can be built, and novel functionalities, such as the anisotropy observed in the NPG can be reached. This will be achieved in this thesis dissertation.

1.4 Transfer of chirality in the on-surface synthesis

The term chirality, which derives from the Greek name 'hand', was coined by Kelvin in 1904 and firstly evidenced by Pasteur in 1848 by the separation of sodium ammonium tartrate crystals. It is a structural property of an object that cannot be superimpose with its mirror image and are therefore called enantiomers. As a example, proteins and sugars are chiral and are present in nature in only one of their two enantiomers. Chirality is hence a topic of great scientific interest in biology, pharmacology, but also in chemistry, material science and optics.

Although it has been studied for more than a century for 3D bulk crystals, the expression of chirality in 2D has become of importance during the past 20 years [149], mainly due to studies of molecular systems on surfaces. Expression of chirality on surfaces is important as it can be used for light polarization [150], or to catalyze chiral-dependent reactions [151, 152].

When deposited on a surface, molecules retain their conformational chirality. In addition, the surface adsorption can induce chirality by inhibiting 3D transformations, what is called prochirality. Enantioselective interactions can transfer the conformational chirality to the molecular self-assembly, inducing the so-called organizational chirality [153–156] (Figure 1.10). This organizational chirality can be constituted by heterochiral or homochiral assemblies, leading to 2D racemates or conglomerates respectively. Interestingly, not only conglomerates [153], but also racemates [154] can express organizational chirality.

Recently, the research on chiral transfer has gone beyond the mere self-assembly in order to study the chiral dependence of on-surface reactions (Figure 1.10) [156]. It has been observed that on-surface reactions could be selective to the chirality of their molecular precursors. This enables the transfer of chirality from the organization of the precursors to the synthesis. Thus, one can transfer chirality from conformational to organizational, and to the on-surface synthesis by controlling chiral interactions at different levels (Figure 1.10).

It has been evidenced to take place for the formation of 0D nanographenes [157], 1D graphene nanoribbons [158, 159], and 2D COFs [52, 53, 160]. Concerning the formation of 0D nanographenes, chirality can be expressed via the intra- molecular formation [157], or it can direct certain types of inter-molecular formation [161, 162]. Besides, the axial chirality of the molecular precursors towards the formation of GNRs is transferred via inter-bond formation [158, 159]. Chirality is also present in the on-surface synthesis of COFs [52, 53, 160]. The flexible conformation of the molecular precursors on surface can induce different prochiral adsorption geometries that favour certain types of reactions towards different desired products [52, 53]. However, there have been very few reported cases where chirality has been transferred in the synthesis of the final 2D covalent product [160]. In other cases, the chirality, transferred from conformational to organizational, fails to be transferred to the covalent structure during the synthesis. Thus, it is of importance to track the evolution of chirality expressed in each reaction

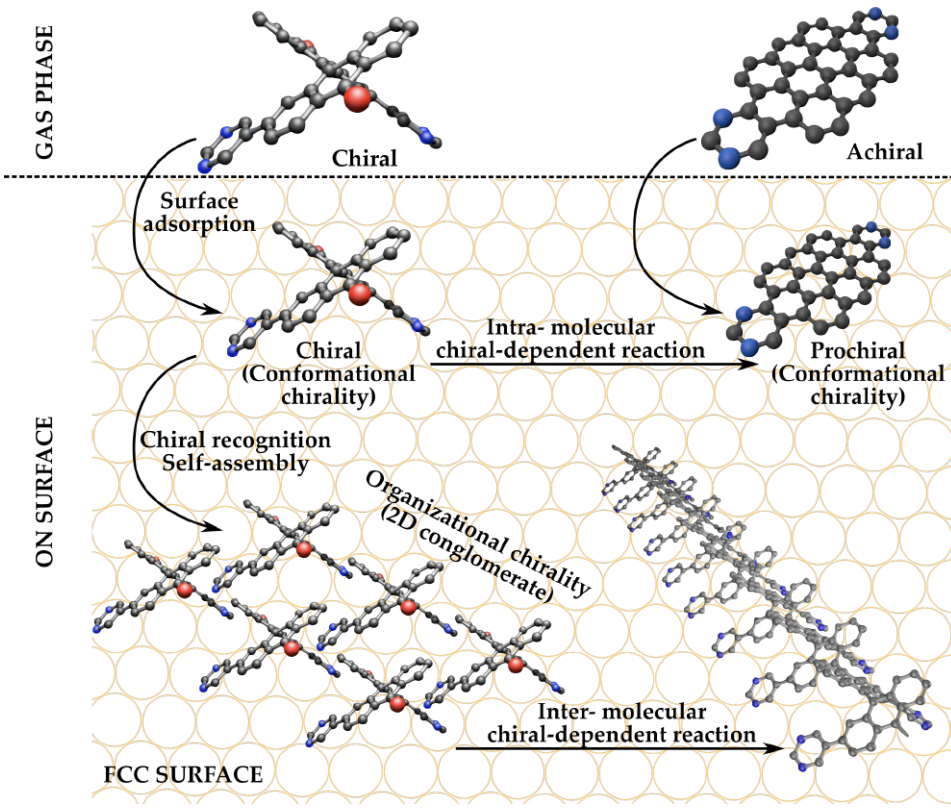

FIGURE 1.10: Chiral-dependent on-surface processes. Intrinsic chiral molecules in gas phase maintain their chiral character on the surface and achiral molecules become prochiral (conformational chirality). Upon molecular arrangement, chiral interactions can transfer conformational to organizational chirality, which can promote inter-molecular chiral-dependent reactions.

step, as it will be addressed in this thesis.

1.5 Thesis outline

The main aim of this thesis dissertation is to shed light into the understanding of on-surface synthesis of graphene nanoarchitectures in order to advance in the complexity by introducing heterocomponents, chirality, and by doing so in 2D nanoarchitectures, as well as the characterization of their

advanced electronic functionalities.

Chapter 2 is devoted to the description of the experimental techniques used to characterize the graphene nanoarchitectures: the Scanning Tunneling Microscopy (STM) and Spectroscopy (STS), the X-Ray Photoelectron Spectroscopy (XPS), and the Density Functional Theory (DFT) and the Tight Binding (TB) calculations.

Chapter 3 presents a systematic study of the reaction pathway towards the on-surface synthesis of a prochiral, nitrogen-doped nanoporous graphene: the chiral-dependent intermolecular interactions and reactions, and the structural characteristics of the products at each step. The study of the electronic properties upon nitrogen doping and the formation of nanopores is also assesed.

Chapter 4 is focused on a novel synthetic strategy to grow a nitrogen-doped nanoporous graphene. The strategy, based on the interdigitation of doped and undoped GNRs, imprints in the nanoporous graphene a type II superlattice heterostructure with the sharpest possible band discontinuities, in the limit of a single carbon-carbon bond.

Chapter 5 is dedicated to the synthesis of prochiral, nitrogen-doped nanographenes, in particular pyrimidine-annelated ovalene nanographenes. We demonstrate how, by controlling deposition coverage and temperature, one can promote the cyclodehydrogenation reaction before the Ullmann polymerization that leads to GNRs, inhibiting this reaction path and leading to self-assembled ovalenes that can later couple in 1D chains.

Chapter 6 studies internal transformations of graphene nanoribbons at temperatures beyond their formation as a way to achieve more complex nanostructures. We have focused the attention on two different kinds of intra- ribbon transformations happening at temperatures beyond the cyclodehydrogenation that leads to the initial GNRs: on the one hand, the partial or total cleavage of the nitrogen-containing functional groups which leads to a GNR superlattice of non-trivial topology that hosts topological superlattice bands. On the other hand, the phenyl migration and closure of a carbon ring that leads to graphene nanoribbons with annulene-like pores at the edges.

Chapter 2

Experimental techniques

In this Chapter 2, I present the main experimental techniques which have been employed during this thesis. The first section is dedicated to Scanning Tunnelling Microscopy (STM), the technique that allows us to track *in-situ* and with submolecular resolution the morphology of the different intermediate states and final products through the on-surface reaction pathways, as well as their electronic properties.

The second section is devoted to the X-Ray Photoelectron Spectroscopy (XPS), which complements the STM and have been used to characterize the molecular chemical composition at every reaction step. Finally, the third section briefly describes the DFT ab-initio calculations, which helps on the interpretation of our experimental results.

2.1 Scanning Tunnelling Microscopy

Scanning Tunneling Microscopy (STM) is a surface sensitive technique that, since its development in the 80s, has enabled the study of surfaces at the atomic scale [163]. STM was invented and developed by Gerd Binnig and Heinrich Rohrer in 1981 at IBM Zürich (Switzerland), who obtained the Physics Nobel Prize in 1986 for their work together with Ernst Ruska (TEM).

In the seminal lecture of the annual American Physical Society meeting in 1959, R. Feynman already envisioned that we could soon b able to see and manipulate matter at the atomic scale, giving birth to the field that later in 1974 was coined as Nanotechnology by Norio Taniguchi in his work 'On the basic concept of Nanotechnology'. The STM gave the eyes and the hands Feynmann was trying to explain in 1959, in the sense that it provides resolution down to the atomic scale, and allows to manipulate with precision

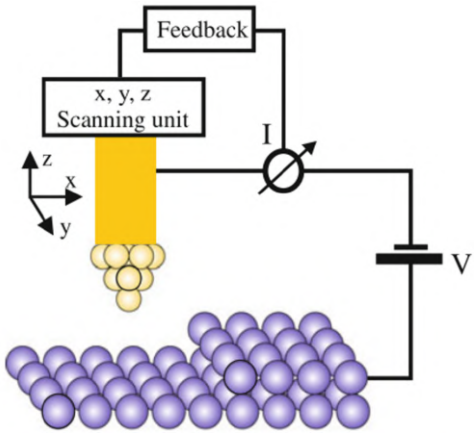

FIGURE 2.1: Schematics of the main elements in STM: a voltage bias is applied between the tip and the surface in order to obtain a current. The feedback can be used to correct the tip-sample distance during the scan.

single atoms and molecules. 40 years after, STM is today a tool extensively used world wide to go down and reach the nanoworld.

The basic operation of an STM consists on a conductive sample surface and a local metallic probe, ideally terminated by a single atom, and separated about 10 Å (Figure 2.1). At this tip-sample distance and under an applied voltage, a current is collected, generated by the quantum tunnelling effect. One can generate an image by using the tunneling current as sensing parameter and scanning over the surface.

An STM operates mainly in two modes: i) the constant current mode (CC), which adjusts the height difference between the tip and the surface by a feedback loop that maintains a fixed current value; and ii) the constant height mode (CH), which does not require a feedback loop because the tip collects the variation in tunnelling current between the tip and sampled as it maintains the same z piezo position.

2.1.1 STM Working principle

The working principle of the STM is based on electronic quantum tunnelling. In classical mechanics, for a finite potential barrier, a particle with cannot cross if this is higher than the particle energy (Figure 2.2, top image).

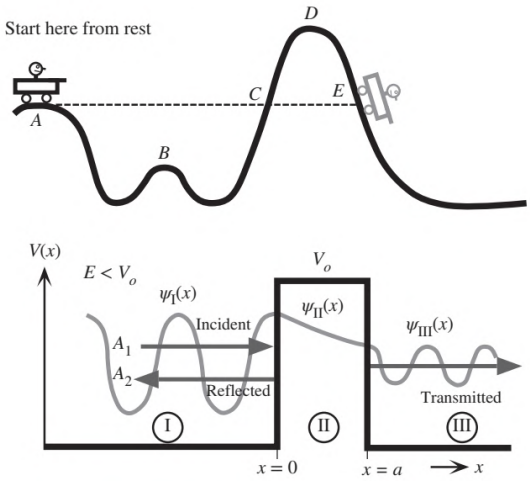

FIGURE 2.2: STM working principle: the classical versus the quantum version. In classical mechanics, for a given potential barrier, an object cannot overpass it unless its energy is bigger than the barrier. In quantum mechanics, the particle is described by probabilities and can tunnel the potential barrier, even if its energy is lower than the barrier V_o. In this scenario, there is the incident and the reflected wave Ψ_I(x) at one side of the barrier, the evanescent wave inside the potential barrier Ψ_2(x) and the transmitted wave Ψ_3(x) at the other side.

However, in quantum mechanics, the objects are not defined by a precise position and momentum since they are expressed as probabilities (Figure 2.2, bottom image). They can cross the barrier, as there is a certain probability of appearing at the other side of the barrier.

The propagation of an electron through an energy barrier can be calculated with the one-dimensional square potential barrier model (Figure 2.2, bottom image), using the 1D stationary Shrödinger equation [164]:

$$\frac{-\hbar^2}{2m}\frac{\delta^2}{\delta^2 x}\Psi(x) + V(x)\Psi(x) = E(x)\Psi(x) \tag{2.10}$$

The solution, for an electron with energy lower than the potential barrier $E < V_o$, is composed by the equations 2.11, 2.12 and 2.13 in the spatial regions I, II and III respectively. Equation 2.11 corresponds to the incident and

reflected sinusoidal wavefunctions, which are present outside the barrier (x < 0):

$$\psi_I(x) = A_1 e^{ikx} + A_2 e^{-ikx} \tag{2.11}$$

Equation 2.12 describes the behaviour of the electrons inside of the potential barrier (0 < x < a), which have an evanescent character:

$$\psi_{II}(x) = B_1 e^{-\chi x} + B_2 e^{\chi x} \tag{2.12}$$

Equation 2.13 describes the transmitted electron wavefunction outside the potential barrier (x > a), also with sinusoidal character:

$$\psi_{III}(x) = C_1 e^{ikx} \tag{2.13}$$

Parameters k and Ξ in the equations above refer to:

$$k = \frac{\sqrt{2mE}}{\hbar} \tag{2.14}$$

$$\chi = \frac{\sqrt{2m(V_o - E)}}{\hbar} \tag{2.15}$$

Considering the boundary conditions of the system and the flowing direction, the transmission coefficient can be obtained (detailed explanation can be found in Ref. [164, 165]):

$$T = \frac{|\psi_{transmitted}|^2}{|\psi_{incident}|^2} \propto e^{-2\chi a} \tag{2.16}$$

The flowing current is proportional to the transmission T:

$$I \propto T \propto exp[-(\frac{\sqrt{2m(V_o - E)}}{\hbar})a] \tag{2.17}$$

With this equation we observe that the tunnelling current decreases exponentially with the tip-sample distance a and with the square-root of V_o-E. For this simplified model, E is close to the Fermi level and V_o is the work function Φ_o. Considering that E « V_o, and that the typical value of the workfunctions in metals is Φ_o= 5 eV, the decay constant takes a value of χ = 11.4 nm $^{-1}$. That means that the tunneling current decays almost by one order of magnitude for every increase of 0.1 nm in the tip-sample distance [164].

Tersoff and Hamann [166–168] presented a more realistic model based on the first-order perturbation theory introduced by Bardeen [169], which is called the Bardeen Transfer Hamiltonian (BTH).

The BTH model has three terms: the Hamiltonians of the tip and the sample (H_t and H_s), plus the addition of a new Hamiltonian that depends on the overlap between the tip and the sample (the transfer Hamiltonian H_T). The Hamiltonian of the system is:

$$H = H_t + H_s + H_T \tag{2.18}$$

The transmission probability from the tip to the sample is based on a variant of Fermi's golden rule:

$$T_{ts} = \frac{2\pi}{\hbar}|M_{ts}|^2\delta(E_t - E_s) \tag{2.19}$$

where:

$$M_{ts} = < \psi(x)_t \left| H' \right| \psi(x)_s > \tag{2.20}$$

$$H' = H_t + H_T \tag{2.21}$$

Considering the sum over all pairs of initial and final states, the total current is:

$$I = I_{t\to s} - I_{s\to t} = \frac{4\pi e}{\hbar}\sum_{t,s}[f(E_t,T) - f(E_s - eV_b,T)]\,|M_{ts}|^2\,\delta(E_t - E_s + eV_b) \tag{2.22}$$

where $f(E_t,T) - f(E_s - eV_b,T)$ is the Fermi-Dirac distribution of both the tip and the sample.

The summation over all the electrons can be substituted by the integral over the density of states:

$$I = \frac{4\pi e}{\hbar}\int_{-\infty}^{\infty}[f(E_F+\epsilon) - f(E_F+\epsilon - eV_b)]\,|M_\epsilon|^2\,\rho_s(E_F+\epsilon - E_s - eV_b)$$
$$\rho_t(E_F+\epsilon)d\epsilon \tag{2.23}$$

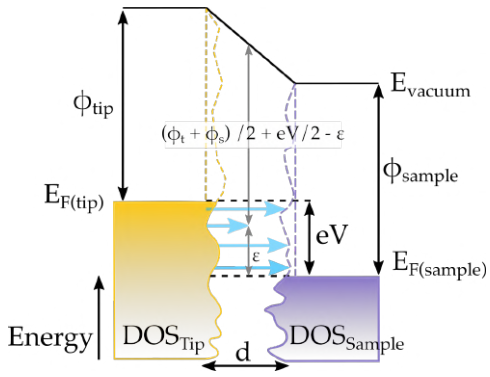

FIGURE 2.3: Energy diagram of the tunneling between the tip and the sample. When a bias is applied between the tip and the sample, the electrons with energy within this range from the Fermi level tunnel from the occupied to the unoccupied DOS. The tunneling depends on the tip-sample distance d and the average potential barrier $(\Phi_t + \Phi_s)/2$, where Φ_t and Φ_s are the work functions of the tip and sample respectively.

being M_ϵ the transmission factor. Considering small kT values, the Fermi-Dirac distribution can be simplified to a step function and the resulting equation of the current is:

$$I = \frac{4\pi e}{\hbar} \int_{EF}^{EF+eV} M_\epsilon \rho_s(E_F + \epsilon - eV_b)\rho_t(E_F + \epsilon)d\epsilon \tag{2.24}$$

For small tunneling voltages, (eV « Φ) the energy dependent term of the Transmission factor M_ϵ) can be replaced by an average energy, indicated in Figure 2.3: (EF (tip) + EF (sample))/2 = eV/2. Hence, the tunneling current has two components, the constant average energy and the distance dependent exponential function:

$$I \propto \frac{4\pi e}{\hbar} e^{-2\chi a} \int_0^{eV} \rho_s(E_F + \epsilon - eV_b)\rho_t(E_F + \epsilon)d\epsilon \tag{2.25}$$

where χ expressed in eq. 2.15 is now rewritten as:

$$\chi = \frac{\sqrt{2m(\Phi_t + \Phi_s/2)}}{\hbar} \tag{2.26}$$

2.1.2 Scanning Tunnelling Spectroscopy (STS)

In the model of the Bardeen's Transfer Hamiltonian, the tunnelling current is directly proportional to the integral of the local density of states, and the differential conductance can be expressed making the derivative of eq. 2.25 and considering the simplest approximation, i.e. that the LDOS of the tip and the transmission factor are voltage independent:

$$\frac{dI}{dV} \propto \rho_s(\vec{r}, E) \tag{2.27}$$

This equation can be used to do spectroscopy. dI/dV signal can be acquired as the bias voltage is swept to obtain ρ_s as a function of the energy, providing the same spatial resolution as for imaging, allowing to take ρ_s maps. Generally, a modulation technique is used in order to obtain the derivative signal dI/dV as a function of the voltage with high signal to noise ratio, what is called the lock-in technique [165].

STS acquisition method: the lock-in amplifier

Figure 2.4 describes the steps followed to obtain the filtered lock-in signal of the tunneling current. The red plot in Figure 2.4 is the tunneling current detected when sweeping a bias voltage on a bare Au(111) surface at constant height. The blue plot is the corresponding lock-in signal. A sinusoidal voltage modulation ($V_{mod} = v_o \cdot sin(w_r t)$) is added to the bias voltage at every point of the voltage sweep (step **1**). Two random points **A** and **B** are shown as an example in order to highlight that the resulting tunneling current modulation amplitude is directly proportional to the slope, thus to the dI/dV signal.

The modulated tunneling current, I_{signal} is converted to an input voltage V_{in} through the I-V conversion amplifier (step **2**). The V_{in} has three components: the DC signal related to the DC bias voltage, the modulation, and the noise:

$$V_{in} = V^I_{sig} \cdot sin(w_r t + \theta_{sig}) + V^I_{DC} + V^I_{noise}(t) \tag{2.28}$$

The first operation of the lock-in amplifier is the phase-sensitive detection (PSD) (step **3**). Here the input signal V^I_{in} is multiplied by a reference signal: $V_{ref} = V_{mod} \cdot sin(w_r t + \theta_{ref})$

$$V_{psd} = V_{in} \cdot V_{ref} \tag{2.29}$$

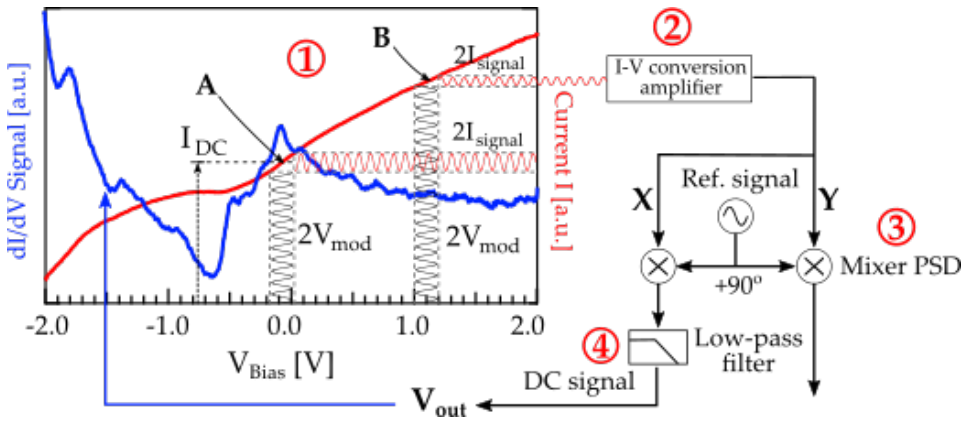

FIGURE 2.4: Lock-in technique procedure. Step **1**: a modulation voltage stimulates the output signal, giving a modulated tunneling current that is proportional to the slope (to the dI/dV). Step **2**: the modulated tunneling current is converted to voltage. Step **3**: the modulated voltage is multiplied by the reference signal; Step **4**: the product signal of the two components is passed through a low-pass filter, getting only DC output signal.

Considering that $sin(\alpha) * sin(\beta) = \frac{1}{2}[cos(\alpha - \beta) - cos(\alpha + \beta)]$, and that $\alpha = \beta$ should be fulfilled, the result is:

$$V_{psd} = V_{DC}^{I} \cdot V_L(t) + V_{noise}(t) \cdot V_L(t) + \frac{1}{2} |V_{in}| \left|V_{ref}\right| cos(\theta_{sig} - \theta_{ref}) -$$

$$\frac{1}{2} |V_{in}| \left|V_{ref}\right| cos(2w + \theta_{sig} + \theta_{ref}) \tag{2.30}$$

The output of the PSD (step **4**) passes through a low-pass filter, leaving only the DC components:

$$V_{out} = \frac{1}{2} |V_{in}| \left|V_{ref}\right| cos(\theta_{sig} - \theta_{ref}) \tag{2.31}$$

If $\theta = \theta_{sig} - \theta_{ref} = 90$, the V_{psd} is the V_{signal} times a constant, considered the V_{out}.

In the Tables below, commonly used parameters for STM (topography) and STS (spectroscopy) data acquisition are listed:

Lock-in parameters: dI/dV spectrum at CH:

- Modulation amplitude: 20-30 mV
- Time constant (τ): 1 - 3 ms
- Sweeping time: 5 - 10 s/V
- Sensitivity: 100 - 200 mV/nA
- Maximum tunnel current reached: 0.8 - 1.0 nA
- Frequency: 2.5 KHz or 3.0 KHz

The modulation amplitude is the lock-in reference signal amplitude that is added to the bias voltage to stimulate a current modulation. The smaller the voltage amplitude, the better the energy resolution, but the smaller the signal to noise ratio. The time constant (τ) is directly related to the low-pass filter: τ = RC in the circuit. By increasing the time constant, the output becomes more steady as the signal-to-noise ratio increases (the band width of the filter gets narrower), but it takes more time to reach to a stationary output value. As a consequence, there is always a compromise between the time constant and the acquisition time.

STS measurements protocol

The protocol to acquire dI/dV spectra has been systematic by checking the clean Au(111) surface reference STS signal before and after measuring our system to track any tip modification during the experiment. dI/dV spectra and images may be influenced by the density of states of the tip, drastically modifying or even hindering the dI/dV features when the tip is not perfectly metallic.

Commonly, single dI/dV spectra is taken at the edges of the GNR and the corresponding stripes that form the NPG. This is because at this point there is a lack of cancellation between the positive and the negative wavefunctions [170], generated by the finite size oft he tip, that probes both phases simultaneously. If a line scan is taken across the GNR (in the transversal direction) the maxima appear at both side, becoming minimum in the centre [100].

STS measurements can be performed at either constant height (CH) or constant current (CC). Generally, to track the density of states close to the

Fermi level, STS at CH is preferable. However, the electric field generated at CH for a suitable distance to have good resolution may induce the damage of the GNRs when the bias voltage overpasses 2 V. As a consequence, in order to preserve the resolution the CC mode is carried out, since the distance between the tip and the sample varies and hence the electric field does not change so abruptly.

2.1.3 Submolecular resolution with STM functionalized-tip

To obtain submolecular resolution in our STM images, the tip is functionalized with a single specific molecule. The technique is called bond-resolved STM (BR-STM), since it allows to obtain local information about the molecular bonds of our specimen.

In 2005, J. Repp and coworkers demonstrated this evidence by observing the molecular orbitals of a pentacene molecule with a bare metallic that was functionalized with a single pentacene molecule [171]. Indeed, they realized that picking up a pentacene molecule with the STM apex was enhancing the spatial resolution of the inspected molecules. That is because decorated tips with single atoms or molecules with well-defined p-type orbitals can give access to detailed information about the chemical structure in STM images [172] . Even if the first proof was made with H_2 molecules (and that is why this technique is generally known as STHM) it was rapidly extended to other molecules such as CO, CH_4, Xe. In 2009, L. Gross and coworkers [173] demonstrated high resolution with non-contact AFM, evidencing that the submolecular resolution is attained to the Pauli repulsion and lateral relaxation of the molecule tip with respect to the atom or bond of the surface [174] , the Probe Particle (PP) model, which can be also extended to STM. In addition to this, in 2014 Chiang and coworkers demonstrated that submolecular resolution is obtained by means of Inelastic Electron Tunnelling Spectroscopy (IETS) [175]. Intramolecular information can be obtained from the shift of the CO-hindered translational vibrational energy when approached towards different parts of the inhomogeneous surface potential of the studied. This made AFM, STM and IETS the three techniques to acquire bond-resolved resolution (Figure 2.5 a-c) [176].

In this thesis, CO-functionalized STM tips have been used to obtain bond-resolved STM images. The CO gas is dosed through a leak valve at a pressure of $5*10^{-7}$ mbar for 30 seconds with the cryoshield doors of

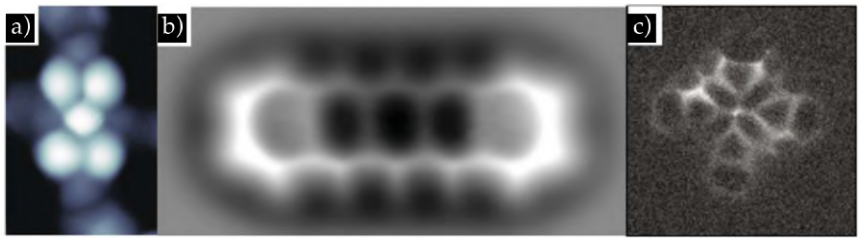

FIGURE 2.5: Functionalized STM tips. a)Bond-resolved STM image of PTCDA molecule on Au(111) with a CO-functionalized tip, b) Bond-resolved nc-AFM image of a pentacene molecule with CO-functionalized tip, c) constant height IETS-STM image of CoPc molecule with CO-functionalized tip. a)-c) images have been taken from Ref. [177].

the STM open. In this proccess, the STM head and cryoshielding, which are at 5 K in standard working conditions, increase the temperature up to 12K during 30 seconds of CO evaporation. Fortunately, this temperature increase is below the CO desorption temperature. In the STM images after CO dosing, CO molecules appear assemble in 2D clusters that nucleate at the elbows of the fcc sites of the Au(111) herringbone reconstruction. STM tip is functionalized by a gentle indentation onto one of these CO clusters, or spontaneously by using a relatively small tip-sample distances (low voltages). We recognize the tip has been functionalized after a significant enhancement of the image resolution. Whereas a very diluted coverage makes the picking up process difficult, a high density of CO molecules over the surface makes impossible to scan properly and carry out the experiment. The optimum CO coverage (for our purposes, i.e. tip functionalization) should be around 5-10%.

2.1.4 STM Experimental setup

The STM equipment used in this thesis is based on a design by G. Meyer and commercially available from Createc Fischer and Co GmbH Berlin, Germany. This STM works in ultra high vacuum conditions ($p < 10^{-11}$ mbar) and at 5 K thanks to a liquid Helium cooling tank from which the STM hangs. This He tank is surrounded by another concentric tank which is filled with liquid Nitrogen, preserving the inner cryostat at the temperature of liquid He for five days. The STM head is isolated from vibrations due to four external dampers, three incorporated springs that let the head hang

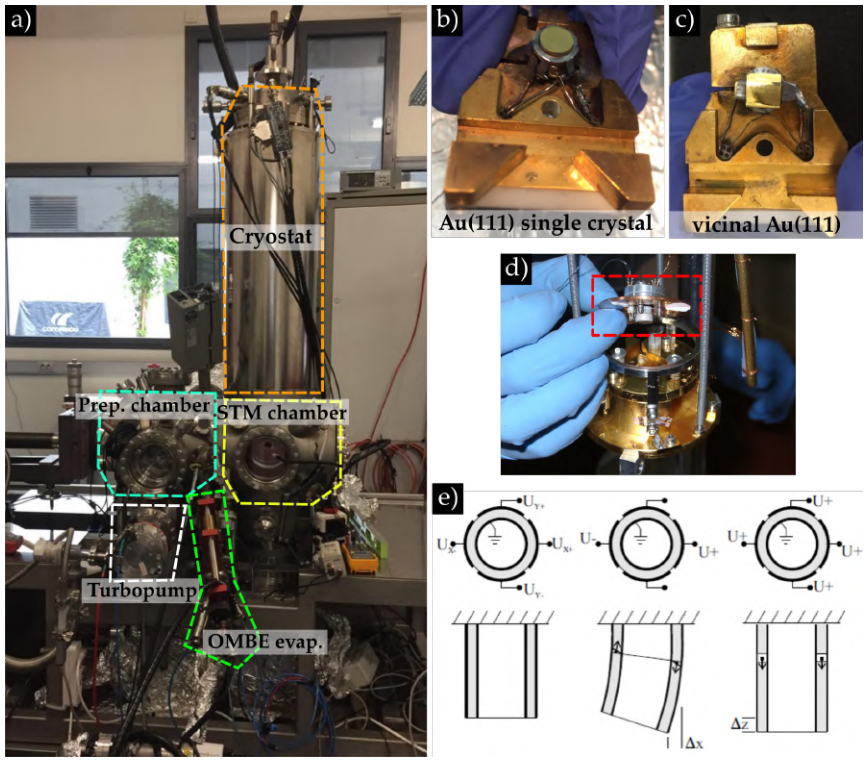

FIGURE 2.6: STM setup. a) Photo of the STM setup highlighting some of the principle components: the preparation and the analysis (STM) chamber, the turbopump of the preparation chamber, the OMBE evaporator and the cryostat. b)-c) Used crystals for the experiments. b) Flat Au(111) single crystal, c) curved vicinal Au(111) single crystal. d) Besocke-type STM head [178]; e) Scanning mechanism by the main piezos of the STM.

freely, and an eddy current damping system.

The microscope itself is a Besocke-beetle-type [178] (dashed, red square in Figure 2.6 d). This design consists on four identical piezoelectic actuators: three of them fixed in the STM head in a 3-fold configuration, and are used for the coarse xyz motion of the tip. They move a ramp-plate where the fourth piezo, which acts as the scanner, is mounted (Figure 2.6 e).

On the other hand, there is a preparation chamber which is separated from the STM chamber by a built-in gate valve and only open when transferring the samples with a rigid manipulator. The preparation chamber is

hold at room temperature, and contains a manipulator that can be cooled down, a mass spectrometer (RGA), a sputter gun, an LEED (low-energy electron diffraction) and the molecular evaporators.

Both chambers are preserved at ultra high vacuum conditions thanks to a system of primary, secondary and ion pumps. The UHV conditions are maintained in the STM chamber by a Titanium ionic pump, apart from the cryo-pumping of the cryostat. The preparation chamber reaches pressures around $10^{-10} mbar$ due to the incorporation of a primary Scroll pump and a secondary turbomolecular pump connected in series, plus another Titanium ionic pump. The latter one runs independently, and once UHV conditions are reached, the turbomolecular pump and the Scroll are switched off in order to reduce the vibrational noise.

2.1.5 Sample preparation

During this thesis, two types of Au(111) substrates have been used: a flat, hat-shaped single crystal (Figure 2.6 b) and a curved vicinal single crystal (commercially available from Bihur Crystals, shown in Figure 2.6 c). Flat Au(111) single crystal has been the most used substrate, whereas the curved vicinal Au(111) was employed for graphene nanoribbon alignment.

The substrates were cleaned by repeated cycles of ion sputtering and postannealing. Typically, the 10 min sputtering takes place under an Argon pressure in the preparation chamber of 10^{-6} mbar that forms plasma Ar+ after applying high voltages (1-2KV for Au(111) single crystal and 0.5 KV for curved crystal), generating a current through the sample of 3.0 μA. After the surface is sputtered, and in order to reconstruct the surface, they are postanneal at around 450ºC and a pressure of few 10^{-6} mbar, reaching large and atomically flat gold terraces.

Precursor monomers were sublimated from a four-fold Knudsen-cell type evaporator (OMBE from Dodecon) with a beam directly focused towards the Au(111) substrate. The sublimation temperature and time needed depending on the surface coverage for every precursor used in this thesis is listed in the Table below.

Precursor	Rate (ML/min)	Temperature (ºC)
DPDBBA	0.075	270ºC
BDPDBBA	> 0.025	320ºC
DPyrDBBA	> 0.013	320ºC
DClPyrDBBA	0.005	320ºC
BClDPBA	< 0.050	360ºC

TABLE 2.1: Surface deposition conditions of the molecular precursors studied in this dissertation.

The precursors have been synthesized in CiQUS (Centro Singular de Investigación en Química Biolóxica e Materiais Moleculares), in Santiago de Compostela (Spain) by our collaborators, Dr. J. Vilas-Varela, Dr. J. Castro-Esteban and full Prof. D. Peña.

In the Table 2.1 DPDBBA is 10,10'-dibromo-2,2'-diphenyl -9,9'-bianthracene [96, 118, 179], DBPDBBA is 10,10'-dibromo-2,2'-di(bisphenyl) -9,9'-bianthracene, DPyrDBBA is 10, 10'-dibromo - 2,2'-dipyrimidine- 9, 9'-bianthracene, DClPyr-DBBA is 10, 10'-dibromo - 2, 2'-di(4-Chlorine)pyrimidine- 9, 9'-bianthracene and DBClDPBA is 2,2'-di(bis 4-chloro-phenyl) -9,9'-bianthracene.

The precursor deposition and reaction sequence for the synthesis of the nanostructures are performed in the preparation chamber. Afterwards, the sample is cooled down to liquid nitrogen temperature through the manipulator,then transferred into the STM analysis chamber, and kept inside until it thermalized down in LHe temperature (5 K) before measurements take place, for at least 8 hours.

2.2 X-Ray Photoelectron Spectroscopy

XPS is a spectroscopic technique that probes the core electronic levels of the atoms, providing information about elemental composition and their chemical environment. It was first performed by H. Hertz and W. Hallwachs in 1887 without knowing what an electron was [180]. A. Einstein in 1905 described it with a quantum theoretical explanation of the photoelectric effect, coining the term 'quanta' to refer, in this case, to the smallest non-divisible unit of light, the photon, and how it is able to interact with an atom and

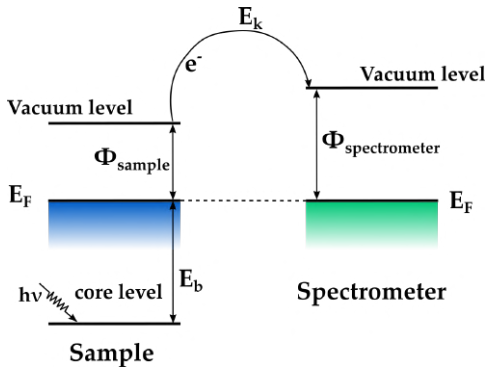

FIGURE 2.7: Schematics of the X-ray photoelectron spectroscopy principle. A photon with energy $h\nu$ is absorbed by an electron from the core level of one atom in the sample. If the electron is close enough from the surface to avoid inelastic scattering with other electrons, it will be ejected at a kinetic energy E_k. The E_k, when measured with the spectrometer, is equal to the sum of the binding energy $E_b$and the workfunction of the sample ϕ_{sample}.

ionized it.

2.2.1 XPS working principle

The photoelectric effect consists in ejecting electrons from the sample surface under illumination with photons. There is a threshold in energy below which light, regardless of intensity, fails to eject electrons from a surface, which is the workfunction of the material (Φ_{sample} in Figure 2.7). Just above this threshold photon energy only the highest energy electrons located at the Fermi level will be ejected. Core level electrons bounded to and atom will need an additional energy, called binding energy (E_b in Figure 2.7, also known as BE), in order to be ejected. The kinetic energy E_k that will be measured for a given photoelectron of initial BE is described following the equation:

$$E_{kin} = h\nu - E_b - \Phi_{sample} - (\Phi_{spectrometer} - \Phi_{sample}) = h\nu - E_b - \Phi_{spectrometer} \tag{2.32}$$

Since the escape depth of photoelectrons that reach the detector afterwards is of few nanometers, it is sensitive to the composition of the first surface layers of our sample. This sensitivity makes XPS an ideal technique

to track the evolution of the chemical composition of surface species during the stepwise reactions.

2.2.2 Identifying chemical environments by binding energy shifts

A careful deconvolution into the corresponding element environments implies the binding energy (BE) assignment to a specific electronic transition and the chemical shifts. Chemical shift is directly related to the effective charge an electron has. If, for instance, a single atom is bonded to another one more electronegative, the charge will be displaced from the former to the latter, and the former will have a more positive charge. This positive charge will be measured as an increase in the binding energy. This example can be extended to any changes in the chemical environment of the atom, are directly manifested in the XPS spectrum not only as peak shifts, but also in peak width and shape.

A way to assign the different chemical environment to a specific BE is by the difference in electronegativity: an electron charge removal implies an increase on the BE, whereas the electron charge addition decreases the BE value. Hence, a carbon atom surrounded by chlorine will have a higher BE than when surrounded by a hydrogen atom. With the same trend, a carbon with a double bond will be placed at higher BE in comparison to a carbon atom with a single bond.

However, there is controversy about the peak assignment of $C[C_3]$, $C[C_2H]$ for graphene-based nanomaterials [93, 119] since they have similar binding energy (the Pauli electronegativity of both carbon and hydrogen atoms is very similar, 2.5 and 2.1 respectively) and they overlap in the XPS signal.

C 1s core level spectra is the only one showing multiple components overlapping in a single experimental peak. In the particular case of this dissertation, the molecular precursor **3** contains four different chemical species for the C 1s core level peak depending on the sp^2 hybridized bonds: $C[C_3]$, $C[C_2H]$, $C[C_2Br]$, $C[CNH]$ and $C[CN_2H]$ as it has been described in Figure A.1. The molecular precursor **4** has another one, $C[N_2Cl]$, whose nominal stoichiometry has been described in Figure A.2. In these both cases the environment $C-Au$, although likely to happen, is not considered in

the peak convolution [94, 95]. Even though the peak is at low BE and placed in the tail of the convoluted peak, it is well fitted without this components, suggesting the contribution is very low. In the procedure of identifying each peak, we start by fixing the areas with the nominal ratio while the binding energy is free, with some constraints (for example, we know that the $C[C_2Br]$ peak should be at higher binding energy than the $C[C_2H]$ peak.)

Regarding the controversy given by the peaks $C[C_3]$, $C[C_2H]$ we found the best approximation to their fitting by considering a single peak overlapping both. As a result, we estimate the binding energies of each component is given:

$$C[N_2Cl] > C[CNH]/C[CN_2H] > C[C_2Br] > C[C_2H]/C[C_3]$$

2.2.3 XPS fitting procedure

Fitting XPS data is not straightforward when dealing with small signal-to-noise ratio or deconvolution of peaks into a many-fold of components as it occurs in our case [181]. Generally, main error sources in the fitting procedure involve: using a too narrow binding energy range; using an incorrect background type or incorrectly adjusting the background to a noisy signal; assigning peak components to very noisy signal; and convoluting a peak into several components with no scientific reason or adding components that do not fit the convoluting peak. In this section it will be explained how we have overcome these issues during the XPS peak fitting.

Firstly, we consider a broad BE range of ± 3 eV between the peak tails, although in the Figures of the manuscript we have reduced the range for simplicity. Background subtraction has been performed in an active mode, that is, adjusted at the same time the peak is fitted and has been approximated in most of the cases to a linear slope. Even if a linear background in XPS has no physical meaning, is a simple and convenient strategy. Among all the fitted species, the doublet Br 3d $_{3/2}$ - Br 3d $_{5/2}$ has been the unique exception where a linear background has not been used for fitting since it is located at the tail of the prominent Au 4f $_{5/2}$ - Au 4f $_{7/2}$ doublet.

Last but not least, for the fitting procedure we consider the fitting line shape as a linear combination of Gaussian and Lorentzian function in order

to approximate a Voigt profile [182]. In particular, the components have a different weight in the linear contribution, so a Gauss-Lorentz ratio of 0.3 is used in our analysis. On the other hand, matching raw data points with the fitting functions has intrinsic associated errors, and that will affect perturb the information obtained from it.

All the issues considered above will determine the error in the fitting, and hence the information we derive from it, such as the atomic concentration.

The fitting of the XPS core levels have been performed with the XPST macro (Martin Schmid) of the program Igor Pro (wavemetrics.com) and the constraint parameters are listed in the following Tables. Among the considered core level peaks (C 1s, N 1s, Br 3d, Cl 2p, Au 4f), C 1s core level peak has been deconvoluted into the specific carbon environments due to the specific structure and different carbon bonds.

2.2.4 XPS atomic concentration calculation

XPS is a quantitative technique in the sense that the number of collected photoelectrons for a given transition is proportional to the number of atoms our sample has, so that information about the atomic concentration can be obtained, that is, the ratio of the peak area of each element and the total peak area of every core level of all the elements in the measurement.

To understand how the atomic concentration is obtained, we have to know all the components encapsulated in the intensity signal:

$$dI = \varphi * \sigma * N * k * exp(\frac{-x}{\lambda * cos\theta}) * dx \tag{B.10}$$

where:

φ is the X-ray flux, σ is the photoionisation cross section, N is the number of atoms per unit area (density), k is the instrument factor, λ is the inelastic mean free path and θ is the angle between the existing electrons and the surface orthogonal axis.

When integrating equation B.10 for an infinitely thick sample, the standard formula of the core level peak intensity is obtained:

$$I^{\infty} = \varphi * \sigma * N * k * \lambda * cos\theta \tag{B.11}$$

Equation B.11 must be solved for N:

$$N = \frac{I}{T(E_i) * R_i * E_i^n} \tag{B.12}$$

where I is the raw intensity; T(E) is the transmission function, an energy-dependent variable; R is the Scofield's Relative Sensitivity Factor (also known as RSF) and E^n is related to the inelastic mean free path (IMFP), where n factor is the scape depth correction. The RSF factor is the primary fundamental parameter to obtain the peak intensity, and it represents the probability of a given photon to ionize an electron from a given atom in the surface sample, relative to the C 1s peak [183].

Although the RSF values are universal and tabulated [183], and the transmission function can be obtained also from the measured signal, it is not so easy to understand the origin of the inelastic mean free path, since our sample is not an infinite thick film with an identified penetration depth. However, the error that accompanies the accuracy of IMFP for different components [184] is very low in comparison with the error associated to the fitting procedure.

The current program we use to fit XPS data (the XPST macro for the program Igor Pro) is limited in the sense that the given area of the convoluted peaks is the raw integrated area after background removal, without taking into consideration any correction factor. As a result, we generally complement the fitting analysis with the program Casa XPS. This program provides a way to obtain the different correction factors needed to have the corrected area: the transmission function $T(E_i)$, the Relative Sensitivity Factor (RSF) R_i and the Inelastic Mean Free Path (IMFP) E_i^n.

All things considered, the atomic concentration of any component of our system is the percentage of the corrected area of each of them divided by the corrected area of all the species:

$$\%At.Conc. = \frac{A_i}{A_{all}} \tag{B.13}$$

In our analysis, for the atomic concentration calculation, we proceed with four random measurements (sampling N = 4) of the fitted regions for the chemical species C 1s, N 1s, Br 3d, Cl 2p and Au 4f in the as-deposited monomer **3** and **4** by varying the bracketing region while maintaining a linear-type background.

2.2.5 XPS set up

The XPS set-up is shown in Figure 2.8. It consists on a hemispherical Phoibos 150 Analyser (indicated with a red arrow in Figure 2.8), an X-Ray source WR50 M equipped with aluminium and silver targets (green square), and a FOCUS 500 X-Ray Monochromator (yellow square), all commercially available by SPECS GmbH Berlin (Germany). The photon energy used for the XPS experiments is of 14886.6 eV, obtained from the AlK_α line, emitted from the Al target.

The sample growth was performed in-situ in the preparation chamber. Molecules were evaporated using the same OMBE evaporator employed in the STM experiments. Then, with the manipulator, the sample is transferred to the analysis chamber. The sample was prepared below 10^{-8} mbar of base pressure and heated at the desired temperature, whereas it was measure in the analysis chamber at a pressure $<10^{-9}$ mbar and at room temperature (although it can be cooled down by an external LN tank in contact with the sample holder).

2.3 Theoretical simulations

Most of the theoretical calculations were performed by our collaborators P. Febrer and J. M. A. Pruneda from the Theory and Simulation group in ICN2 and by A. García-Lekue, from Donostia International Physics Center (DIPC), in San Sebastian. DFT ab-initio calculations have been used as the tool complement the experimental results and study deeper certain aspects of the properties of our new materials. The code that has been used in both cases is SIESTA [185–187].

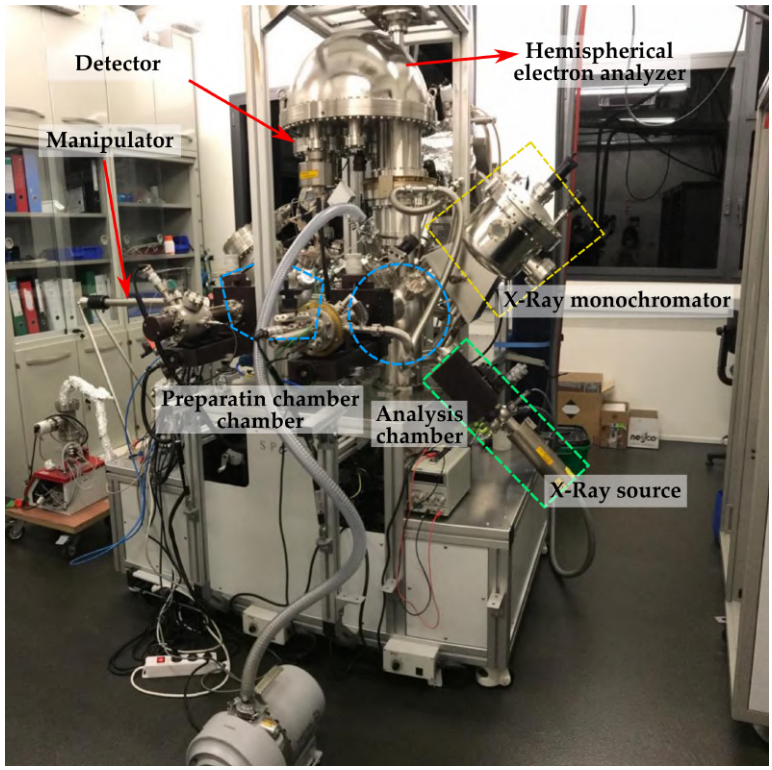

FIGURE 2.8: The XPS setup. The analysis chamber (dashed, blue circle) is separated from the preparation chamber (dashed, blue square), where the sample is grown in-situ. The X-Ray light is generated by the X-Ray source (dashed, green square) and filtered by the X-Ray monochromator (dashed, yellow square). The signal is collected at the detector, after the electrons are sorted by the hemispherical electron analyser.

The results obtained by our collaborators were post-processed by using SISL python package [188]. SISL is a Python library that enables the manipulation and analysis of the DFT output data. In particular, electronic bands of the structures can be plotted within a determined energy range and in a determined momentum path. The PDOS can be visualized for the whole system or at a specific (x,y,z) position.

Furthermore, group velocity, effective mass and eigenvalues can directly be extracted. It also allows to construct low dimensional systems in order to run it into the SIESTA code or inside the SISL library by using a code based on the tight binding approximation. Wavefunctions of specific bands can be

extracted into 3D grids and visualized afterwards with the program VESTA [189], and the natural structure of the system is visualized employing the program Avogadro.

Those calculations that were not computed by DFT (most of them in Chapter 6) were obtained by tight binding simulations using the program 'quantum lattice', developed by Dr. J. Lado (Aalto university, Finland), or with SISL itself, that allows to obtain the energies from a given Hamiltonian.

Chapter 3

Towards nitrogen-doped nanoporous graphene.

Introduction

Adding heteroatoms to the edges of nanopores provides new interesting properties that increase the range of potential applications as compared to an undoped NPG. Firstly, doped nanopores tune the electronic properties of the semiconducting NPG [8, 118, 190]. Regarding the nanosieving functionality, the presence of heteroatoms at the pore edges can also be used to taylor the effctive pore radii and the affinity to specific targets [107], very interesting for gas separation [23] and rare-earth filtering [24] or water treatment (purple panel in Figure 3.1) [25]. Furthermore, the presence of heteroatoms at the edges can be exploited for photocatalysis (i.e. water splitting) [17, 191]; electrocatalysis [192] or as a single metal complexant of heavy metal atoms to support other reactions [17] (red panel in Figure 3.1). It has been also observed that the binding ability of alkaline atoms to the doped nanoporous graphene is better than with the undoped counterpart (green panel in Figure 3.1), making the former a candidate for ion-based batteries [129, 193], for electrochemical double layer capacitors [25, 107] and as supporting layer for the active materials in batteries and solar cells [25].

Despite all the aforementioned advantages, heteroatom doping in a controlled manner is still a major challenge. Reported results show typically a post-process addition of nitrogen with no control on the dopant location, where the initial pristine pore structure is already irregular in shape and distribution [24, 193]. Currently, controlling both, the pore structure and the dopant content and bonding configuration remains therefore a difficult task.

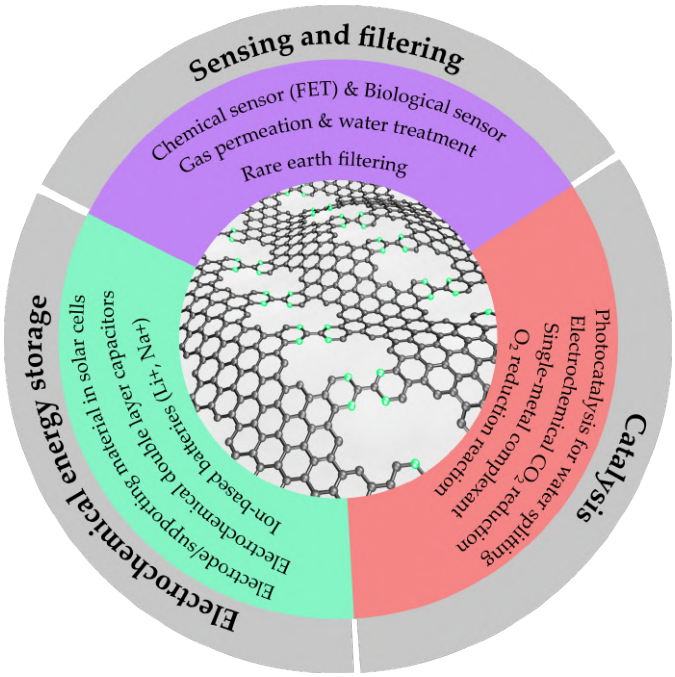

FIGURE 3.1: Enhanced properties of doped nanoporous graphene in comparison to the undoped one, and potential applications.

Bottom-up methods such as the on- surface synthesis and the use of specifically designed molecular precursors can offer a solution to simultaneously control both the atomic structure and chemical composition of the pores, as well as their distribution. The best example is the bottom-up synthesis of graphene nanoribbons (GNRs), where heteroatoms can in principle be introduced with the same atomic precision as the rest of the structural parameters [36]. Figure 3.2 a) shows that on-surface synthesis of doped/functionalized GNRs (green histogram) is rather scarce in comparison to the vast literature of bottom-up synthesis of graphene nanoribbons (blue histogram) [9, 33, 81]. We understand, as it will be discussed in this Chapter, that this is probably because the dopant moieties would perturb the hierarchical reactivity towards the formation of GNRs, achieving disordered graphene-based structures. Table 3.1 summarizes the literature on the on-surface synthesis of doped or functionalized GNRs.

On the one hand, the substitution of carbon by heteroatoms can take place in the backbone of GNRs (Table 3.1 and Figure 3.2 a). Typically, boron

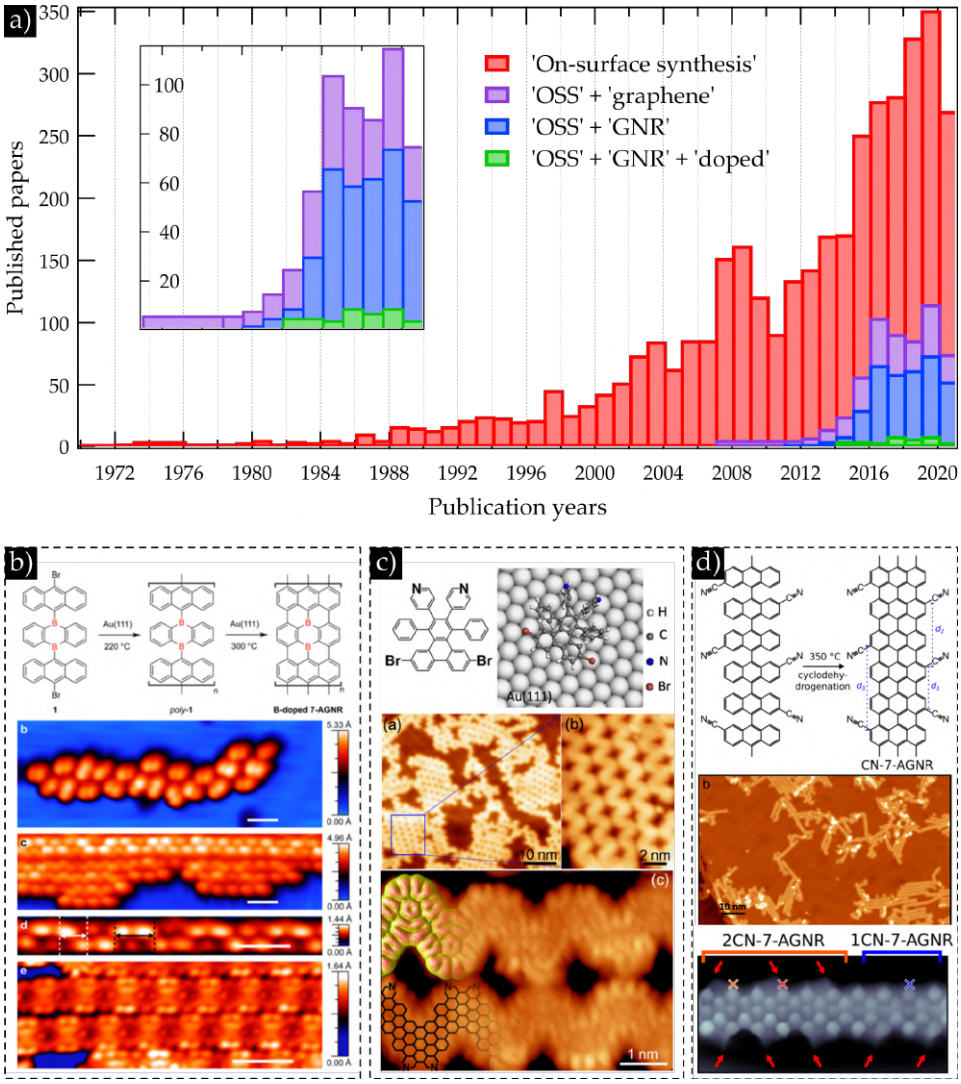

FIGURE 3.2: Literature about on-surface synthesis of graphene nanoribbons. a) Literature research from the database Web of Science using different keywords filtering. b)-d) Representative examples of heteroatom doping and functionalization of graphene nanoribbons depending on the location. b) Backbone doping with boron atoms [194]; c) substitutional edge doping with nitrogen atoms [195]; d) and peripheral chemical functionalization with cyanide groups [196].

has been the most used heteroatom for doping armchair graphene nanoribbons [142, 194, 197, 198, 211], tuning profoundly the electronic properties

GNR type	Dopant location	Dopant type	Electronic band gap	Band shift	Ref.
Armchair (7-AGNR)	Backbone	B (x2)	2.4 eV* (<)	No shift	[194, 197]
Armchair (7-AGNR)	Backbone	B, N (x1)	2.3 eV* (=)	+0.4 eV	[198]
Armchair (3-AGNR)	Edge doping	N (x1, x2)	3.3 eV (=)	-0.35 eV (Nx2)	[199]
Armchair (9-AGNR)	Edge doping	N (x2)	2.7 eV (>)	NA	[130]
Armchair (7-13-AGNR)	Edge doping	N (x4)	1.4 eV (>)	-0.4 eV	**This work**
Armchair (13-AGNR)	Edge doping	S (x2)	1.4 eV (<)	No shift	[200]
Zig-zag (16-ZGNR)	Edge doping	B, NH	1.50 eV (NBN-ZGNR1) 0.90 eV (NBN-ZGNR2)	NA	[201]
Chiral (8-cGNR)	Edge doping	B, O	3.33 eV (>)	NA	[202]
Chiral	Edge doping	N (x2)	NA	NA	[203]
Fjord	Edge doping	N (x2)	2.04 eV (theoretical)	NA	[204]
ChevGNR	Edge doping	N (x2, x4)	2.8 eV for N (=) 2.7 eV for 2N (<)	-0.1 eV (2N) -0.2 eV (4N)	[69]
Chevron	Edge	N (x8)	2.0 eV (=)	-0.6 eV	[71]
ChevGNR	Edge doping	N (x4)	1.02 eV	NA	[195]
ChevGNR	Edge doping	N (x8)	1.9 eV	NA	[205]
ChevGNR	Edge doping	N (x4)	NA	NA	[206]
ChevGNR	Edge doping	NH (x1)	2.2 eV (<)	+0.15 eV**	[207]
Chevron	Edge doping	O (x1)	2.3 eV (<)	No shift**	[207]
ChevGNR	Edge doping	S (x1)	2.2 eV (<)	+0.06 eV**	[207]
ChevGNR	Edge doping	CO (x1)	2.33 eV (<)	Downshift	[141]
ChevGNR	Edge doping	S (x4)	From 1.28 eV to 1.78 eV	NA	[208]
ChevGNR	Edge doping	NH, N (x2)	2.3 eV	-0.4 eV (N vs NH)	[144, 145]
Chiral (8-ChGNR)	Edge functionaliz.	NH2 (x2)	0.37 eV (<)	+0.8 eV	[209]
Armchair (7-AGNR)	Edge functionaliz.	CN (x2)	1.36 eV (<)	-0.4 eV	[196]
ChevGNR	Edge functionaliz.	F (x4)	1.3 eV (=)	-0.2 eV (theoretical)	[210]

*The gap refers to delocalized frontier orbitals, without considering the presence of possible impurity bands introduced by the boron heteroatoms. **The band shift for systems with different gap has been identified for the VBM.

TABLE 3.1: Summary of on-surface synthesized doped graphene nanoribbons. Experimental band gaps have been listed (it is indicated if theoretically obtained). Negative (positive) value of the band shift refers to downshift (upshift) of electronic bands. '=', '>' and '<' correspond to 'same', 'bigger than' and 'smaller than' the electronic band gap of the undoped counterpart.

[198] or adding some other functionalities such as magnetism [211, 212].

On the other hand, heteroatoms can be present at the edges of the GNRs, offering a way to not only tune the electronic properties but also modify the edge chemical affinity with the surrounding environment, very interesting for metal complexation, catalysis and sensing [17, 19, 20, 213, 214]. Two different scenarios can be considered: (i) edge heteroatom doping (i.e. dopants substitute edge carbon atoms, Table 3.1 and Figure 3.2, b) and (ii) edge functionalization (i.e. dopants substitute edge hydrogen atoms, Table

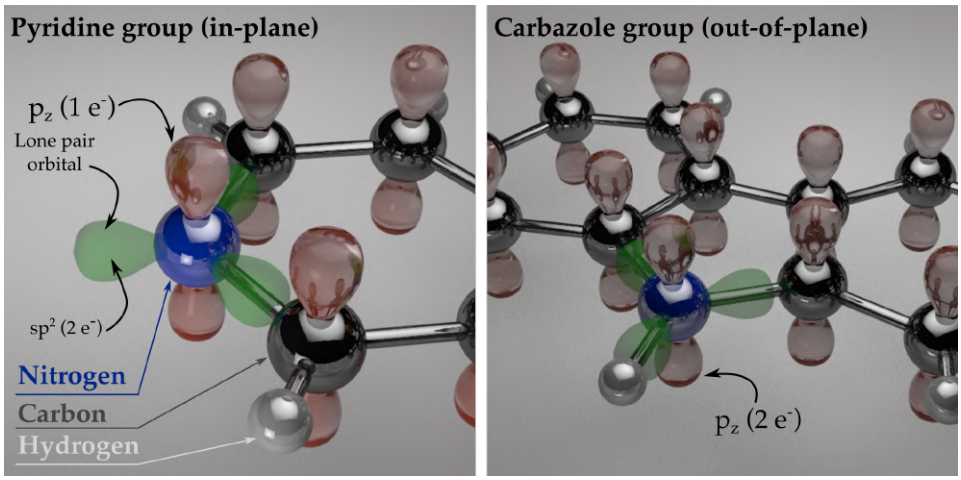

FIGURE 3.3: 3D schematic representation of a pyrimidine- (left) and carbazole- (right) based group. bluem black and silver spheres correspond to nitrogen, carbon and hydrogen atoms respectively; p_z orbitals have been colored in red, and nitrogen in-plane orbitals, in green color.

3.1 and Figure 3.2, c).

The most studied edge heteroatom doping in GNRs is by far nitrogen, either in the form of pyridine [130, 199], phenanthridine or carbazole [144, 145, 207] (Figure 3.3). Depending on the local configuration of the nitrogen atom, it can have an impact on the modification of the electronic properties of the entire ribbon.

Carbazole-based groups have a nitrogen atom in a five-atom aromatic system (Figure 3.3, right image). The nitrogen is not only covalently connected to the carbon atoms by sigma bonds, but also to one hydrogen atom. As a consequence, the lone pair orbital with two electrons (in this case is a p_z) is fully out-of-plane and then conjugated to the other p_z orbital from the carbon atoms (which contain only one electron per p_z orbital) [145, 207], contributing to add more electrons to the conjugated extended π-system of GNRs. This characteristic not only shifts the bands of the ribbon, but also modify the absolute value of the band gap [207].

In the pyridine-annelated groups (Figure 3.3, left image), the nitrogen atom is covalently connected by sigma bonds (sp^2) to two carbon atoms,

and has an in-plane lone pair orbital (sp^2) that does not conjugated to the p_z out-of-plane electronic cloud of the carbon atoms. As a consequence, the lone pair electrons behave as localized impurities and the p_z orbital only contributes with one electron to the aromatic cloud in contrast to the carbazole group. This doping configuration modifies the electronic properties through inductive effects, shifting rigidly the bands of narrow enough ribbons and preserving in most of the cases the absolute value of the band gap [212].

Apart from the electronic properties, the geometrical localization of the heteroatoms inside the graphene nanostructure can also modify the overall symmetry of the system, and then also influence their final properties [205, 208]. Chirality is generally imprinted in the final product by transferring it from the original molecular precursor by means of enantioselective interactions and reactions at the surface [156]. These interactions may favor enantiopure (conglomerate) or mixed (racemates) domains, whic can trigger or inhibit reaction steps. Enantioselective interactions may be critical for the formation of the 2D nanoarchitecture, even when the final product is not chiral [215]. The combination of on-surface synthesis and STM characterization is particularly useful to study this transfer of chirality in each reaction step and understand the role of enantioselective interactions in the synthesis of the final product.

In this chapter we will overcome the challenges related to edge doped armchair graphene nanoribbons with nitrogen atoms by using a pyrimidine functional group that fuses to the armchair backbone, leading to an N-doped 7-13 AGNR structure. We further demonstrate how the pyrimidine units can survive the whole reaction path towards the formation of atomically precise nitrogen-doped graphene nanopores by the lateral coupling of the doped GNRs. The crucial point to achieve that will be the decrease of the reaction temperatures below the decomposition threshold of the pyrimidine. The local structure and electronic properties have been studied by means of STM and STS combined with DFT ab-initio calculations. In addition to this, XPS has been used to track the chemical composition during the reaction mechanisms, in particular the cleavage of the halogen atoms involved and the stability of the nitrogen dopants.

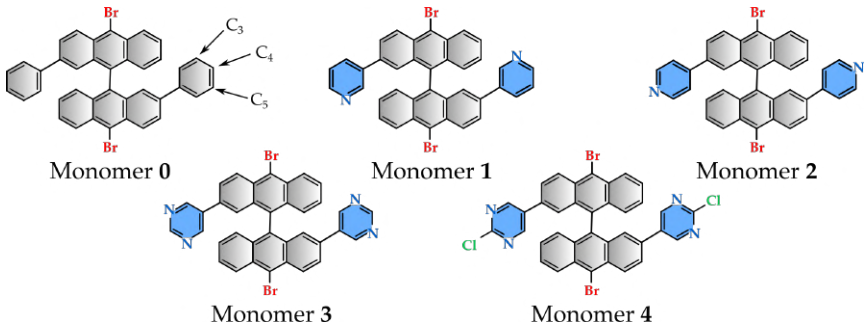

FIGURE 3.4: Molecular precursors explored for the on-surface synthesis of nitrogen-doped nanoporous graphene: monomer **0** is the phenyl-functionalized DBBA or DPDBBA [96, 118, 179]; monomer **1** and **2** are pyridinic-functionalized DBBA, and monomer **3** and **4** are pyrimidinic-functionalized DBBA. Precursors containing nitrogen atoms have their functional groups coloured in blue for clarity.

3.1 Introducing the molecular precursors under study

In the task of synthesizing N-doped GNRs we have been testing several precursors that are presented here. Attempts on functionalizing DPDBBA with nitrogen-containing groups showed that the position of nitrogen atoms inside the outer phenyl rings of monomer **0** (10,10′-dibromo-2,2′-diphenyl -9,9′-bianthracene or DPDBBA [96, 118, 179]) plays a critical role in succeeding to sublimate our molecular precursors in UHV conditions. We have found that nitrogen atoms in either position C_3 or C_4 in these phenyl rings (monomer **1** and monomer **2** in Figure 3.4 respectively) polymerize in the powder phase in the crucible before sublimation, most likely due to the nucleofilic attack of the nitrogen to the carbon atom bonded to the bromine. However, we realize that the monomer gains stability upon sublimation when the outer phenyl rings are substituted by pyrimidine functional groups instead of pyridine (two nitrogen atoms per phenyl rings instead of one). The molecular precursors we use for our on-surface study are described in Figure 3.4 as monomer **3** and monomer **4** (2,2′-pyrimidine 10, 10′-dibromo 9, 9′-bianthracene and 2, 2′-di(4-Chlorine)pyrimidine 10, 10′-dibromo 9, 9′-bianthracene respectively). We note that all four precursors explored in this chapter, as well as its undoped counterpart, are chiral.

In the following section we will address the thermally-induced on-surface reactions towards the synthesis of nitrogen-doped nanoporous graphene by using the two pyrimidine containing precursors, and how

the thermal instability of functional groups and enantioselective interactions and reactions may alter the chemical route and consequently the yield of the expected 2D graphene nanostructure.

3.2 On-surface synthesis of N-doped graphene nanoribbons

Firstly, we track the reaction mechanism for monomer **3** (Figure 3.5 a) with both STM and XPS and compare it to the pristine DPDBBA. After its deposition on the Au(111) surface at room temperature, large-area close-packed islands of self-assembled precursors are formed (Figure 3.5 b, overview), denoting a high diffusivity and substantial intermolecular interactions of this molecule on Au(111).

Looking more in detail this initial stage, in STM images we observe that the as-deposited monomer **3** possesses the same 3D conformation as the previously described dibromo bianthracene derivatives [51, 96]: the bisanthracene units tilt in a scissor-like conformation due to the steric hindrance of the confronted hydrogen atoms in both anthracene groups, providing axial chirality to the molecule. The lateral distance between brightest lobes in the STM contrasts of Figure 3.6 b) is 7.4 Å and the height profile is 2.3 Å (Figure 3.6 c), elucidating that the bisanthracene subunits are pointing upwards and the N-containing phenylenes are towards the surface, like in the undoped monomer **0** [96].

Even though the mixture upon deposition is racemic, enantioselective interactions (which we presume could be weak forces such as van der Waals, hydrogen bonding and $\pi - \pi$ stacking) lead to a phase separation into 2D conglomerates. Each enantiopure domain forms a chiral unit cell of size 1.65 X 1.15 nm (Figure 3.6, b), confirming the transfer from conformational to organizational chirality.

Upon annealing the precursors at 150ºC, molecular precursors undergo homolythic C-Br bond cleavage to condensate into 1D polymers via the Ullmann coupling reaction [51]. In Figure 3.5 c), we observe that the average length of the polymer chain is smaller than the characteristic size of the initial precursor island. In contrast to the up to 100 nm long polymeric chains obtained for its undoped counterpart [179], these polymers have

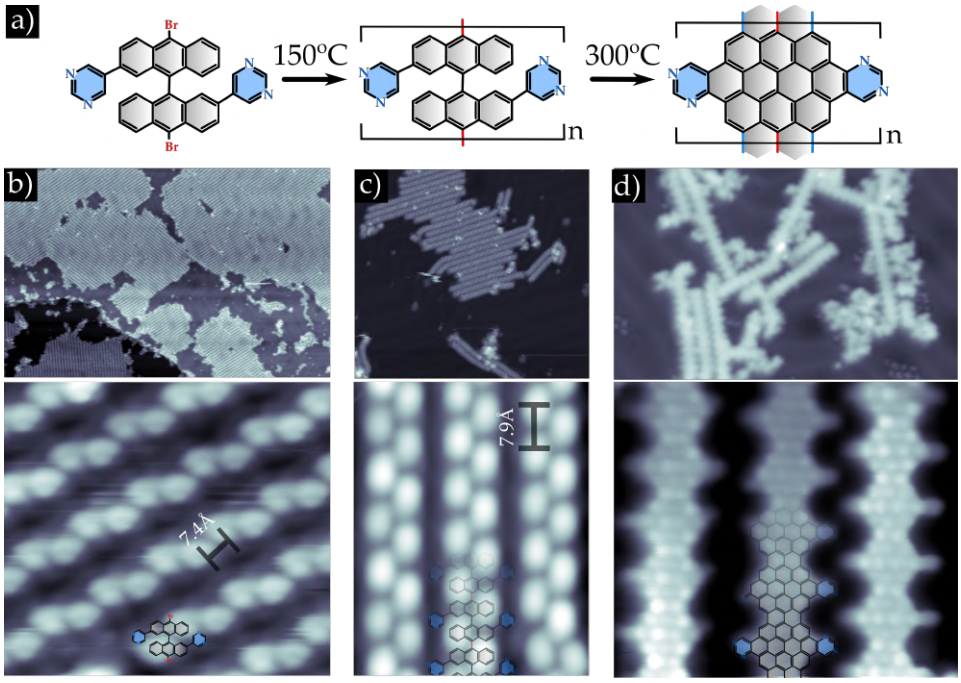

FIGURE 3.5: On-surface synthesis of N-doped 7-13 AGNR. a) Schematic representation of the temperature-dependent reaction pathway. b) STM images of a representative overview and closeview of the as-deposited monomer **3** on Au(111). c) STM images of a representative overview and closeview of the polymeric phase upon 150°C of postannealing. d) STM images of a representative overview and close view of the nitrogen-doped GNR after undergoing a 300°C postannealing. 2D schematics of intermediate steps have been superimposed for clarity.

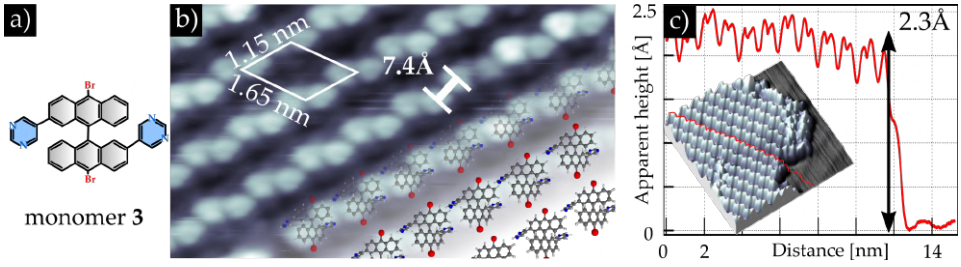

FIGURE 3.6: Pyrimidine functionalized bisanthracene molecular precursors. a) 2D schematics of monomer **3**. b) STM image with an superimposed 3D composition of the self-assembled organic precursors and the unit cell indicated; c) the Z-profile of the as-deposited monomers and the respective STM image.

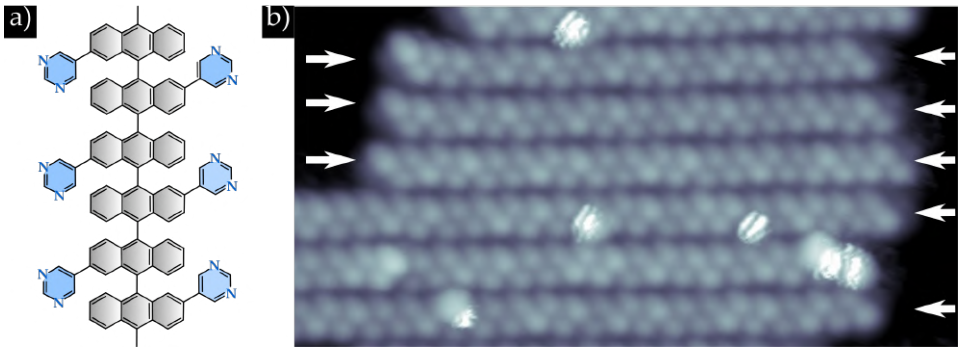

FIGURE 3.7: Homochirality in a bunch of polymers. a) 2D schematic illustration of the pyrimidine functionalized polymer. b) STM image of a bunch of polymers. White arrows point the termini of the polymers, indicating they belong to the same axial chirality.

an average length of 18 $\pm$8 nm. This value is close to the length of linear fcc/hcp tracks between a pair of elbow dislocations, indicating that the limiting factor for the growth of polymers might be the strong interaction with the underlying herringbone template.

In addition to this, the staggering of alternating anthracene units favor the polymerization between the same enantiomers (opposite enantiomers confront anthracenes with the same tilt, which suffers strong steric repulsion), leading to homochiral polymers. The interaction between the polymers also seems to favour the formation of enantiopure domains, similar to that found for the monomers. The chiral correlation of interacting polymers can be tracked by following the zigzag alternation of protrusions in the images shown in Figure 3.7. This homochiral preorganization will be relevant for the possible formation of a chiral NPG by the coupling of GNRs.

When further postannealed to 300ºC, chiral polymers cyclodehydrogenate into *pro-* chiral nitrogen-doped graphene nanoribbons. The non-superposable ribbons, separated by a dashed line which represents a mirror plane, have been depicted schematically in Figure 3.8. We confirm this trend by the BR-STM images of the single graphene nanoribbon in Figure 3.8 and two interacting GNRs in Figure 3.9.

The chirality of the single graphene nanoribbons is directly manifested in the contrast of the BR-STM image displayed in Figures 3.8 b) and c). In

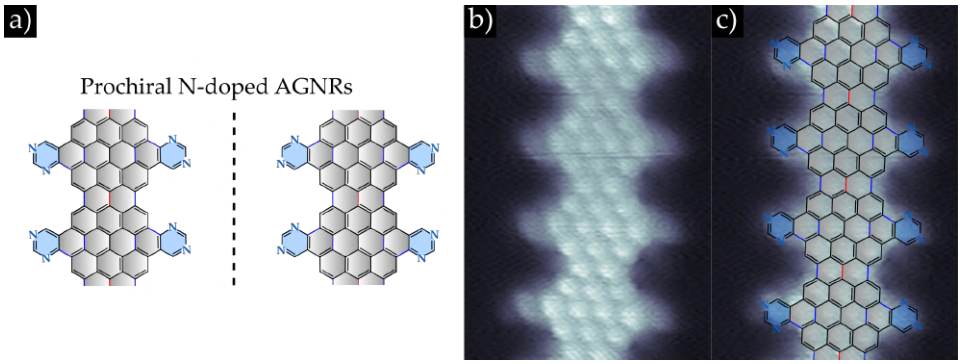

FIGURE 3.8: STM contrast signatures of pro- chirality in nitrogen-doped graphene nanoribbons obtained after postannealing at 300ºC. a) 2D schematics of the two possible homochiral ribbons, separated by a dashed line that represents a mirror plane; b) BR-STM image of a single nitrogen-doped GNR. c) Same BR-STM image with the proposed 2D scheme of the pro- homochiral GNR.

this image we notice that the lateral extensions in the GNR (13-carbon-atoms periodic segments) display a subtle asymmetry that originates from a decrease of the contrast in those locations of the rings where there is nitrogen. As a consequence, one can directly relate the asymmetry of the pyrimidine groups along the two edges with the position of the nitrogen atoms and conclude that chirality is transferred from the polymers to the GNRs.

Another indirect prove to elucidate the prochiral character of the ribbons is in their interaction, as shown in Figure 3.9. Whereas for the undoped GNR the distance between them was of few nanometers of separation [179] in diluted samples due to repulsive interactions, here we notice that ribbons tend to pack as close as possible in a particular manner. As a consequence, the weak interactions driving the packing of the ribbons is attractive, more specifically driven by hydrogen bonding due to the nitrogen atoms at the edges. We propose a zig-zag zipping model to explain the stereoselective interaction of prochiral ribbons (Figure 3.9 a). By superimposing homo and heterochiral GNR pairs to the STM image of Figure 3.9 c), we find that only the homochiral configuration (Figure 3.9 a) is stabilized by such H-N bonds. This model agrees with the faint but sizeable assymmetry that can be distinguished in the pyrimidine rings in the BR-STM image of Figure 3.9 c).

The prochirality of the GNRs and their homochiral interactions at this

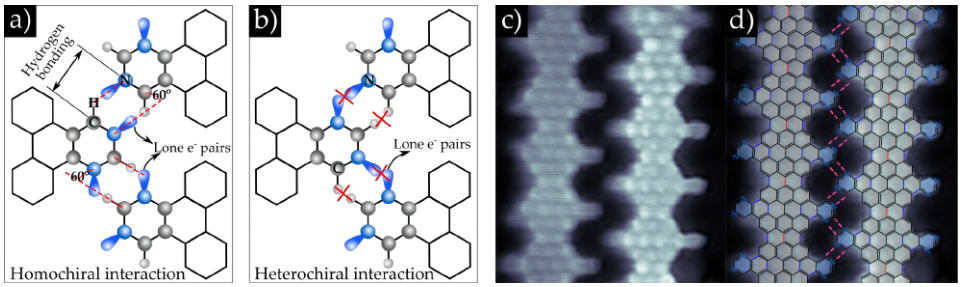

FIGURE 3.9: Interacting N-doped GNRs by hydrogen bonding. a) Homochiral pyrimidine rings interacting by hydrogen bonding with a zig-zag zipping scenario. b) Hypothetical case heterochiral pyrimidine rings interact. c) Bond-resolved STM image of two interacting GNRs. d) Overlapped 2D scheme of the proposed zig-zag zipping scenario.

stage of the reaction are critical to obtain a good yield for the subsequent lateral connection of the ribbons to grow nanoporous graphene. Unfortunately, when we increase the postannealing temperature up to 400ºC in order to induce the lateral fusion of the ribbons by dehydrogenative cross coupling, pyrimidine rings start to cleave, triggering the formation of 7-9 armchair graphene nanoribbons instead of the expected NPG (which will be further described in Chapter 6). Therefore, although we have demonstrated the transfer of homochirality upon the whole reaction path up to the GNRs, a critical aspect in the synthesis of the chiral N-doped NPG that we aimed at, we still have to address the issue of functional group degradation by looking for other strategies (it will be seen in Section 3.3).

Complementary to STM, XPS measurements were carried out to study the chemical composition at different temperature conditions: as-deposited at room temperature (RT), after a postannealing to 150ºC and after 300ºC. We analyze the spectra of carbon C 1s (Figure 3.10, b), bromine doublet Br 3d $_{5/2}$ and 3d$_{3/2}$ (Figure 3.10, c), and nitrogen N 1s (Figure 3.10, d) as they are the traceable elements comprised in monomer **3**. As explained in Chapter 2, in the case of the C 1s core level fit, its multiple overlapping components result in too many degrees of freedom, so we impose some stoichiometry constraints by assuming the structures inferred from the STM analysis. The fitting parameters are detailed in the Appendix A.

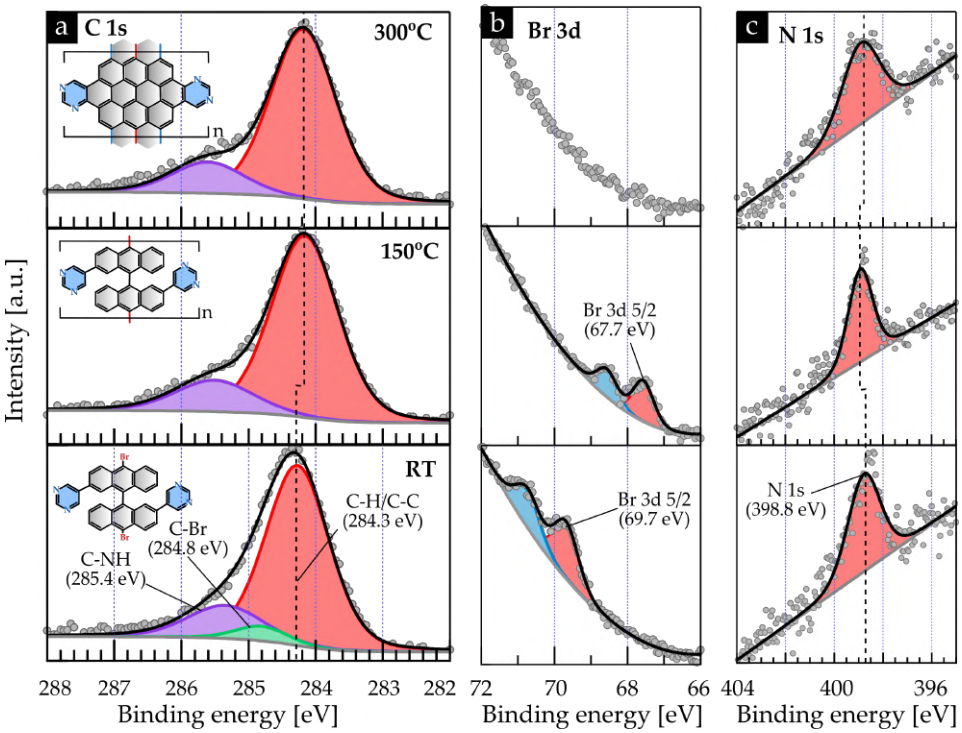

FIGURE 3.10: Tracking on-surface reactions of molecular precursor **3** by XPS. a) C 1s XPS core level spectra and the corresponding convoluted components with the 2D schematic representation of each intermediate step; c) Br 3d XPS core level spectra and d) N 1s core level spectra at RT, 150ºC and 300ºC. XPS fitting constraints and parameters are listed in Tables A.13, A.14, A.15.

The different components and corresponding ratios used to fit the multicomponent C 1s core-level spactra obtained at room temperature correspond to the stoichiometry of the monomer (for increasing binding energy): $C[C_2H]/C[C_3]$:$C[C_2Br]$:$C[CNH]/C[CN_2H]$ = 28:2:6, which are defined herein as C-H/C-C, C-Br and C-NH. Both $C[CNH]$ and $C[CN_2H]$ have been considered in a single 'C-NH' for simplicity, since the environment is quite similar. Performing the peak fitting under these parameter constraints, the fitted contributions of C-H/C-C and C-Br binding energies have been set as 284.3 and 284.8 eV respectively, very similar values of those of the undoped precursor [96] when it is deposited intact at room temperature, and C-NH has been set at 285.4 eV, characteristic of pyridine groups [216, 217].

The Br 3d core-level spectra at RT display a double peak corresponding to the spin-orbit split $3d_{5/2}$ - $3d_{3/2}$ doublet at 70.7 and 69.7 eV (Figure 3.10 b). From the binding energy, the doublet can be assigned to C-bonded Br [96], confirming that the monomer is still brominated upon deposition [218]. The N 1s core-level spectrum shows a single peak with the maximum at 398.8 eV (Figure 3.10 d), which agrees with the experimental values of pyridinic nitrogen species [27].

The main modification of the spectra after annealing at 150ºC is related to the Br 3d core level. The doublet shifts 2.1 eV to lower BE, indicating that Br-C cleavage has taken place at this temperature, being the Br atoms chemisorbed on the gold surface, as expected for DBBA derivatives on Au(111) [119, 218].

Based on the full debromination, indicated by the Br core-level shift, and considering that the carbon radical is saturated by the Ullmann C-C coupling that leads to the polymers, as found by STM, the C 1s core level spectrum is fitted with stoichiometry constraints $C[C_2H]/C[C_3]$:$C[CNH]/C[CN_2H]$ = 30:6. The C-Au component is not considered in this case since the signal to noise ratio achievable with our lab source in reasonable times does not allow to univocally discern such small peaks, overlapped with the main one. From the fit, we note that the C-C and C-ÇH components shift by 0.2 eV to lower BE, something that has already been observed when Br atoms are present on the surface, and has been attributed to a halogen-induced change of the work function [96, 137, 218, 219].

Last, the area and energy positions of the N 1s core level spectrum do not vary upon annealing, revealing stability of the functional groups during the formation of the polymers.
Finally, upon further annealing at 300ºC, and by comparing with the STM images of Figure 3.5 d), N-doped GNRs have already grown at this temperature. The new corresponding stoichiometry of its chemical environments that we used to fix ratios is therefore $C[C_2H]/C[C_3]$:$C[CNH]/C[CN_2H]$ = 30:6. In line with results obtained for the undoped GNR [119], there is also a shift back of the C-C and C-H contribution again to BE.

The combined disappearance of the Br signal and the good fit of the C core level with the GNR stoichiometry indicate that the desorption of the Br adatoms from the metallic substrate take place simultaneously with

the cyclodehydrogenation process in the temperature range from 150ºC to 300ºC. A similar correlation was made for the undoped case, though in this case they were occurring at higher temperature, between 300ºC and 400ºC [96]. The correlation, observed in many reported cases [88–90, 220, 221] has been attributed to the fact that Br only desorbs after forming HBr by the residual H atoms provided by cyclodehydrogenation. By comparing the undoped and doped cases, it can be concluded that the presence of pyrimidine rings reduces the cyclodehydrogenation temperature.

The N 1s core level spectrum broadens after this last annealing step. We ascribe it to the progressive degradation at 300ºC of the pyrimidine rings into other groups, such as cyanide groups [144, 196]. At this temperature the STM reveals only a partial degradation of some of the rings (Figure **??** d). Since the peak area is conserved, we believe that the other fraction remains at the surface. More details on the intermediates of this progressive degradation will be given in the analysis of Chapter 6, where we deliberately cleave the pyrimidines to give rise to new GNR structures. The main conclusion here is that the XPS analysis corroborates the STM observation, that the onset of the degradation of pyrimidine rings occurs already at 300ºC, which inhibits the formation of N-doped NPG.

3.3 Interribbon coupling and formation of prochiral N-doped graphene nanopores

In order to facilitate the lateral coupling at lower temperatures and preserve the integrity of pyrimidine rings, we have rationally design the monomer **4**, which was introduced in Figure 3.4. This molecular precursor contains chlorine atoms in the C_4 position of the pyrimidine rings, which is otherwise hydrogenated in the molecular precursor **3**.

Large areas of close-packed molecular islands of the same enantiomer are observed in Figure 3.11, a), creating 2D conglomerates as happens with the monomer **3**. Monomer **4** also possesses the same 3D conformation as monomer **3**: the bisanthracene units tilt in a scissor-like 3D geometry. The lateral distance between brightest lobes in the STM contrasts of Figure 3.11 is also the same for both molecules (7.4) whether they have chlorine atoms or not. The presence of the added halogen atoms in in the pyrimidine

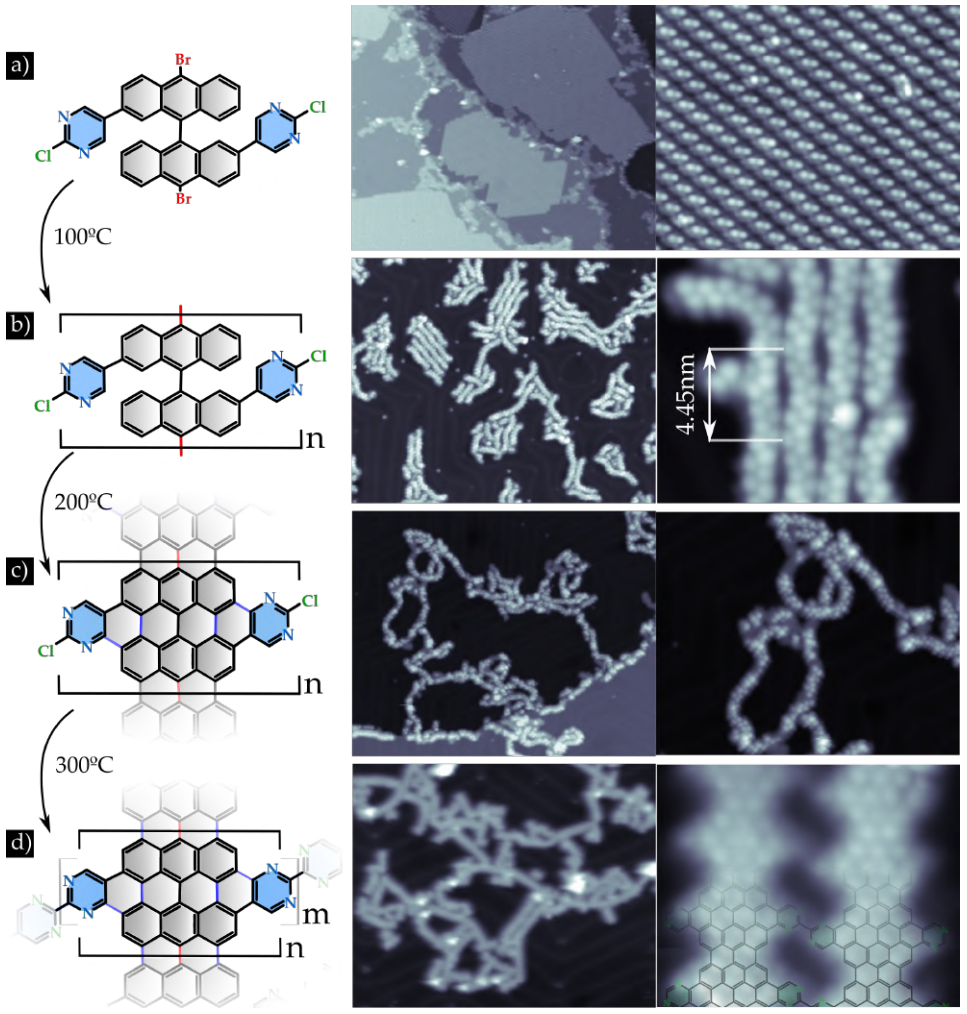

FIGURE 3.11: On-surface synthesis of N-doped graphene nanopores from monomer **4**: 2D schematics, overview and closeview of every temperature-dependent step. Pyrimidine rings have been colored in blue for clarity. 'm' and 'n' subscripts indicate the repeating units at both transversal and longitudinal directions; a) As-deposited monomers ; b) Polymers ; c) Intermediate step with partial cyclodehydrogenated segments; and d) nitrogen-doped graphene nanopores.

increases its apparent height to 2.9, higher than the 2.3 of monomer **3**.

At 100ºC of postannealing and during low coverage conditions, the homolythic cleavage of the C-Br and further polymerization into 1D chains

takes place. However, the large areas of close-packed molecular precursors islands disaggregate and rearrange into smaller bunches of few polymers on the face-centered cubic (fcc) area of a strongly distorted herringbone reconstruction. Indeed, the polymers modify significantly the fcc-hcp areas of the surface, maximizing the fcc ones. Similar behaviour has also been observed for the adsorption of a brominated molecular precursor to grow chiral graphene nanoribbons [159], whose bromine atoms are in close proximity with the gold surface. This indicates that the herringbone distortion depends on the strength of the physical adsorption of the halogen atoms with surface, that will eventually depend on the relative distance that separate them, directly related to the 3D conformation of the molecule. The preference for the fcc stacking is in close agreement with a scenario of halogen dominated interactions with the surface, since the fcc regions are indeed the most stable adsorption sites for halogen atoms on Au(111) [98].

Taking a closer look to any of the cluster of polymers, it can be seen that they interact with each other bending with a snake-like shape. The meanders have a periodicity of 4.45 nm (5 units), labelled in Figure 3.11 b). Since it is known that chlorine atoms interact so strongly with the gold atoms from the surface that they lift them up [222], this scenario could be understood as a creation of organometallic hybrids [221, 223, 224]. However, one cannot discard that the combination of hydrogen and halogen bonds can be strong enough to induce such conformational distortions by themselves [225].

A further postannealing to 200ºC starts to induce the planarization of the 1D polymers. Alteration of the fcc regions decreases at this step, so we understand chlorine atoms do not interact so intensely as compared to the polymer phase. This could be explained by the new conformation acquired by the planarized segments, where the Cl atoms now would be lying parallel to the aromatic backbone instead af facing down to the surface. Taking monomer **3** as reference, this decrease in the planarization temperature can only be explained if the chlorine atoms still remain at the edges of the ribbon, as evidenced by I.Swart and coworkers [91], so planarization takes place before chlorine cleavage. On the other hand, this phase triggers a random distribution of the created ribbons, and hence does not facilitate the ordered formation of 2D extended porous graphene structures with a high yield in the long-range order.

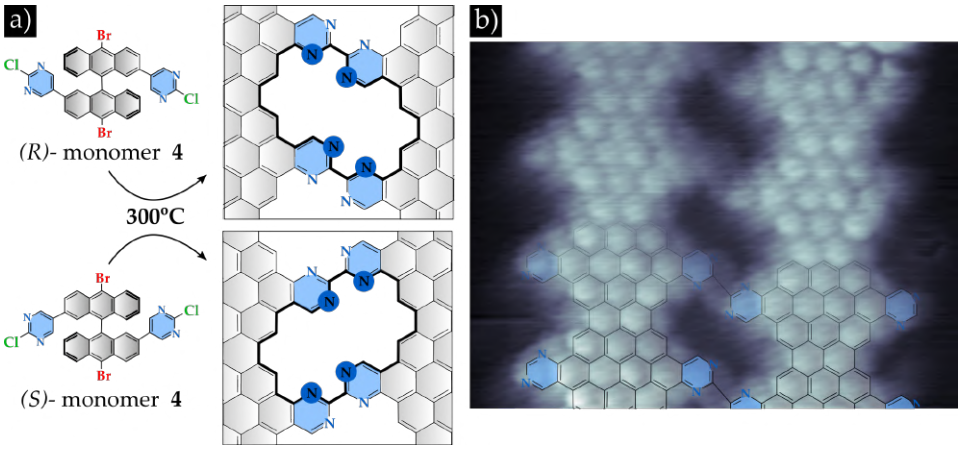

FIGURE 3.12: Prochirality of N-doped nanoporous graphene. a) Molecular precursor **4** in its two possible enantiomer conformations, either *(R)-* or *(S)-*, with the subsequent *pro- (R)-* or *pro (S)-* chiral nanopore. b) BR-STM image with an overlapped Laplacian filter to enhance the contrast of the graphene nanopores. The 2D structure has been added on top to locate the position of the pyrimidine rings.

Finally at 300ºC, we find that all chains are fully planarized. At the same time, couples of ribbons appear laterally fused. This is shown in Figure 3.12, where the prochiral nature of the nanopores acquired from the molecular precursors is also represented. As expected for a highly connected and disordered distribution ensemble of GNRs, the yield for the lateral fusion is low as compared to the undoped NPG [118]. However, the already observation of few areas with N-NPG indicates that the use of rationally-designed precursor containing chlorine atoms allows to decrease the formation temperature of N-NPG by 100ºC, preventing the cleavage or transformation of pyrimidine rings.

To complement the STM analysis, we have performed also XPS experiments to the same monomer **4**, summarized in Figure 3.13. We carry out the sublimation with the Au(111) substrate held at the polymerization temperature since, in contrast to the case of RT deposition, the formation of GNRs is independent on the coverage (see Chapter 5 for more details). The fitting parameters are listed in Appendix A.

The Br 3d core level spectra, which gives us information about the formation of the 1D polymeric chains, are depicted in Figure 3.13, c). At 100ºC

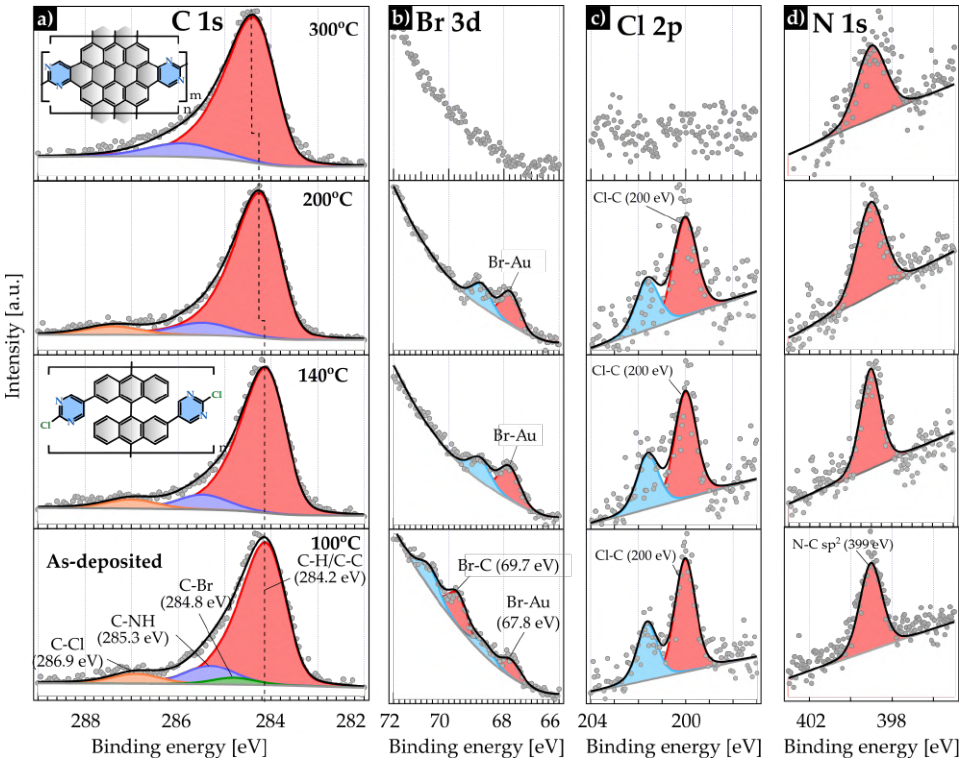

FIGURE 3.13: Tracking on-surface reactions of monomer**4** by XPS. a) C 1s core-level peak; b) Br $3d_{5/2}$ and Br $3d_{3/2}$ doublet; c) Cl $2p_{3/2}$ and Cl $2p_{1/2}$ doublet; d) N 1s, N-C sp^2 core level peak.

there are two doublets, indicating that there are bromine atoms still bonded to the molecule (Br-C 69.66 eV and 70.69 eV for Br 3d $_{5/2}$ and Br 3d $_{3/2}$ respectively), and bromine atoms that have already left the molecule to adsorb on the gold surface (Br-Au 67.72 eV and 68.72 eV for Br 3d $_{5/2}$ and Br 3d $_{3/2}$ respectively). In contrast, the Cl 2p doublet binding energies (200.0 eV and 201.6 eV) correspond to the C-Cl bond [226], indicating that the chlorine atoms are both preserved in the monomers and the polymers.

The C 1s core level peak measured for the monomers deposited at 100ºC has been deconvoluted into the different chemical environments: $C[C_2H]/C[C_3]$, $C[C_2Br]$, $C[CNH]/C[N_2H]$, $C[N_2Cl]$. Both $C[CNH]$ and $C[N_2H]$ contributions have been merged into a single peak for simplicity, and no $C-Au$ signal has been identified [93, 95]. A new component has been added in comparison to precursor **3**, the $C[N_2Cl]$, due to the addition

of chlorine atoms at the pyrimidine rings. The stoichiometry constraints have been set according to the Br-C/Br-Au ratio described before, and free between the atomic concentration ratio of the monomeric phase (C-H/C-C : C:Br : C-NH : C-Cl = 28 : 2 : 4 : 2) and the polymeric phase (C-H/C-C : C-NH : C-Cl = 30 : 4 : 2) (see Appendix A, Figure A.2). We obtain a good fit by setting the BE of C-H/C-C and C-Br at 284.2 eV and 285.15 eV respectively [96]; the C-NH at 285.55 eV [216, 217]. The new component, C-Cl, has been set at 287.0 eV [226].

By subsequently annealing to 140ºC, we observe a complete debromination (no Br-C component Br 3d doublet at 69.7 eV - 70.7eV) and chemisorption of the bromine atoms on the Au(111) surface, same as for the monomer **3**. This unveils that the polymerization has been completed at this step. The area of the peaks doublet at this temperature is the same as the sumation of the two doublets at 100ºC, indicating that the hierarchical reactions are well separated in temperature so far. On the other hand, both the area and the binding energy of the Cl 2p doublet have been preserved, showing that polymers do not dechlorinate during 1D polymerization. Regarding the N 1s peak, no changes are observed, evidencing the preservation of the pyrimidine rings at this temperature. With these changes considered, the C 1s deconvolution has been set by taking into account the polymeric phase: C-H/C-C : C-NH : C-Cl = 30 : 4 : 2. Binding energy shifts at these stages are not noticeable as for the case of the precursor **3** since the experiment has started at the polymerization step, with bromine atoms already chemisorbed on the Au(111) surface.

At 200ºC, Br 3d and Cl 2p doublets are kept intact, as well as the total area of the N 1s peak. This indicates that the polymers are preserved at this stage. Finally at 300ºC, neither the Br-Au doublet nor the Cl-C doublet are observed. Combining these results with the corresponding STM images, we can conclude that the cyclodehydrogenation has been completed at this temperature, so the new stoichiometry used in the C 1s core level fit is C-H/C-C : C-NH/C-N_2 = 30 : 6. For the case of the $C-NH/C-N_2$ we keep it unconstrained because we have observed from the N 1s peak a subtle broadening that could indicate the starting temperature which is promoting pyrimidine transformation into different N species.

We note that there is a coincidence of both the cyclodehydrogenation and the Cl Ullmann. This indicates that the planarization of polymers into

ribbons and their lateral couping take place at very similar temperatures. However, it is not possible from our analysis to know wether we couple polymers that then planarize into GNRs or viceversa.

The are of the N 1s peak at 300ºC slightly broadens, which may be related with the fact that most GNRs cannot fuse laterally, and therefore the pyrimidine rings are prone to be degraded. The XPS analysis does not allow to proof the chemical state of pyrimidines in the coupled GNRs versus does isolated or degraded. Hence, the C 1s peak is deconvoluted according to the new stoichiometry: C-H/C-C : C-NH - C-NCl = 30 : 6.

3.4 Electronic properties of N-doped graphene nanoribbons.

As it has been explained in the introduction of this Chapter, the presence of heteroatoms in graphene-based nanostructures may alter their local electronic properties depending on the exact location and bonding configuration of the dopants. Therefore, it is essential to study the electronic properties of these nitrogen-doped graphene nanoarchitectures so that we can assess the applicability in different types of (opto)electronic devices. In this section we study the electronic properties of both single and coupled graphene nanoribbons experimentally by means of STS, and we interpret the results by combining it with DFT calculations of the respective infinite systems. The effect of doping is specifically addressed byb comparing these results with those obtained for the undoped 7-13 AGNR and the NPG [118].

The analysis of the electronic properties will be detailed as follows: we will start by describing the bands close to the Fermi level (frontier bands), followed by the analysis of higher energy lying bands that do not disperse along the ribbon (transversal bands), to finish with the description of localized states or flat bands identified at both negative (pyrimidine-related) and positive (bay, pore- related) energies.

Frontier bands (valence and conduction bands)

Figure 3.14 a) displays the STS spectra acquired around the Fermi level for three systems: the undoped 7-13 AGNR (red spectrum), the N-doped

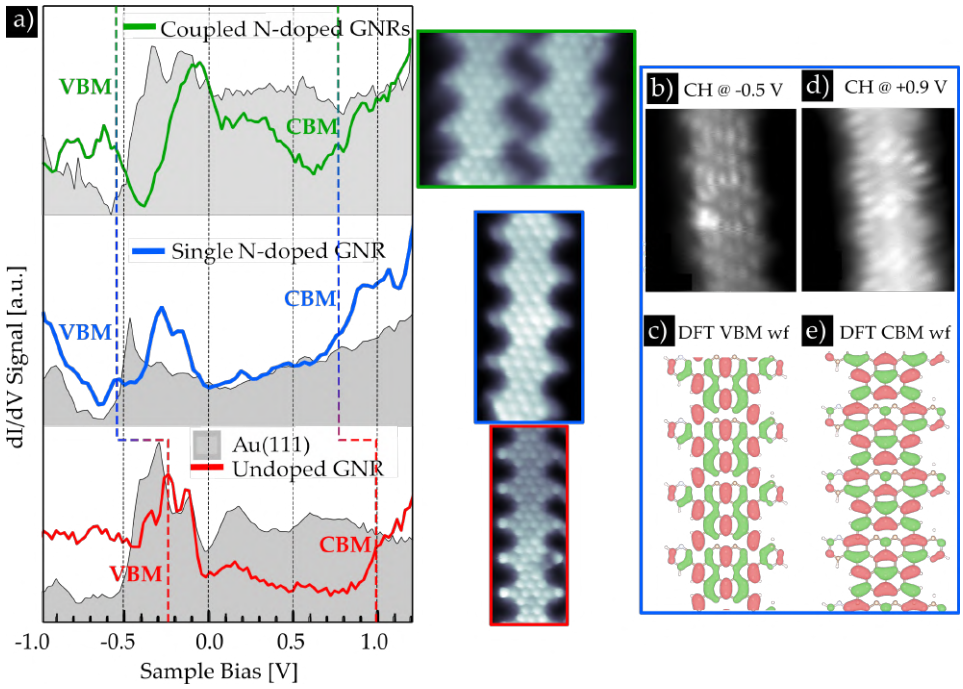

FIGURE 3.14: Experimental electronic properties of N-doped GNRs. a) Experimental frontier bands of the undoped GNR (red spectrum), the N-doped GNR (blue spectrum) and a pair of coupled N-doped GNRs (green spectrum) with the corresponding BR-STM images. b) Constant height conductance maps of the N-doped GNR at -0.5 V, with the respective c) DFT wavefunction of the valence band at Γ point. d) Constant height conductance map of the N-doped GNR at 0.9 V, with the respective e) DFT wavefunction of the conduction band at Γ. The DFT wavefunctions have been represented with a red-green colour contrast, corresponding to $+/-$, both with an isovalue of 0.05 $Å^{-3}$.

7-13 AGNR (blue spectrum) and two coupled N-doped 7-13 AGNRs (green spectrum), with their respective BR-STM images. In these STS spectra, the frontier bands can be identified: the valence band maximum (VBM) and the conduction band minimum (CBM), which correspond to the onset of the local density of states (LDOS) of 1D bands.

The CBM of the doped systems (blue and green plots) was recognized as an onset at 0.75 V, which is 0.25 V downshifted with respect to the undoped GNR (red plot). To confirm it, this CBM has been tracked for the single N-doped AGNR with a constant height conduction map at 0.9 V (Figure

3.14 d), whose pattern is in close agreement with the symmetry of the wavefunctions given by DFT calculations in Figure 3.14 e).

The valence band maximum (VBM) is more difficult to track as it can interfere with the signal coming from the Shockley surface state (SS) of the Au(111). The onset of the SS is at approximately -0.47 V [227], but due to the presence of the ribbons, shifts by 0.20 V to higher energies [228, 229] (only below the ribbons) due to an interaction between the two. To avoid such features, our Au(111) references have always been taken far from a GNR area just to be sure we avoid this shift and we collect the original signature of the Au(111) SS. Besides, the scattering of the SS of the Au(111) with the GNRs modulate the LDOS giving rise to resonances that may be taken misleadingly as GNR band onsets. A further complication is the fact that for some small band gap the VBM is pinned to the Au(111) Fermi surface, lying very close to the shifted SS onset [230]. Because of that, we double check our peak assignment by comparing STS maps with DFT wavefunctions. After these considerations, the VBM of the N-doped 7-13 AGNR is identified as a very subtle peak at -0.55 eV, which has been also confirmed by the constant height conductance map of Figure 3.14 b), in agreement with the symmetry of DFT valence band wavefunction in Figure 3.14 c).

The effect of doping and interibbon coupling on the frontier bands has been also studied by DFT calculations (Figure 3.15). Since they are responsible of the electronic conductance along the ribbon backbone, we refer to them as longitudinal, **L** (highlighted in yellow). The undoped GNR (red plot) possesses a band gap of 0.76 eV (Δ_U^{GNR} in Figure 3.15, a), as demonstrated previously [118]. When adding nitrogen dopants to the edges of the ribbon (blue plot), the absolute value of the band gap (Δ_D^{GNR}) remains the same, as well as the symmetry of the VBM and CBM wavefunctions (Figure 3.15 b), while the bands rigidly shift downwards by 0.54 eV (Δ_{offset}), which is of the order of the value observed experimentally for the valence band (0.40 eV). Besides, the doping affects the band width of the bands ($BW_{\Gamma X}$), which decreases by 15% for the case of the conduction bands, while the valence bands do not experience almost any change. This parameter gives a qualitative estimation of the dispersive character of the conductive electrons through the **L** bands. Another relevant electronic property is the electron effective mass, which does not vary upon doping, neither for the valence or the conduction bands (m*(CB) = 0.138 m_o and m*(VB) = 0.134 m_o, being m_o the mass of the free electron).

Bandwidth	Undoped NPG	N-doped NPG
L bands (ΓY)	0.694 m_e	0.672 m_e
L bands (ΓX)	-0.168 m_e	-0.187 m_e
Anisotropy **L** bands (ΓX / ΓY)	4.13	4.6

TABLE 3.2: Effective masses and anisotropy of both undoped and N-doped NPG

Furthermore, the DFT calculations allow to track the effect of the lateral coupling of GNRs on the electronic properties by analyzing the band structure of the N-doped NPG structure (Figure 3.15 e). Doping the NPG (green plot) somehow increases the absolute value of the band gap (Δ_D^{NPG} = 0.92 eV) and the frontier bands downshift is not so acute as compared to the ribbons (Δ_{offset} = 0.32 eV). Besides, the symmetry pattern of the **L** bands is not perturbed by the doping (Figure 3.15 f).

The comparison of the effective masses in the ΓX and ΓY directions for both undoped and N-doped systems give an estimation of the electronic anisotropy [114]. Listed in Table 3.2, the ratio of the effective masses for both the VBM and CBM in the undoped NPG is around 4, as also calculated recently [114]. Upon doping, this ratio does not vary indicating that the nitrogen addition does not affect this characteristic.

Beyond frontier bands: transversal bands

Transversal bands have been defined as those wave functions that conjugate across the GNR backbone and do not disperse longitudinally. Whereas for single GNRs they are not relevant for transport properties (Figure 3.15 b), it does have an impact in the NPGs, since it is directly related to the transversal conductance across the GNRs components. Unfortunately, they cannot be resolved experimentally due to the fact that they lie high in energy and coexist with the longitudinal bands, so their LDOS contribution cannot be isolated.

In the band structure of Figure 3.15 b), we find for T bands the same qualitative behaviour as for L bands: they are downshifted upon doping.

Looking in more detail, we see that the shift (Δ^{T}_{offset}) is larger than for the **L** bands (Δ^{CBM}_{offset}). This can be explained by the localization of the nitrogen at the same 13 C atom wide stripes where the T bands are localized, which makes the inductive, local gating effect stronger for these bands. Considering both the doping and the lateral coupling of the ribbon together, the transversal band approaches the CBM (energy offset Δ_T), from an energy difference of 1.27 eV in the undoped GNR and of 0.8 eV in the N-doped NPG. The latter is very relevant since it facilitates the access to T bands in transport, and modulate for instance the electronic anisotropy by switching the on/off transport with a gate [118].

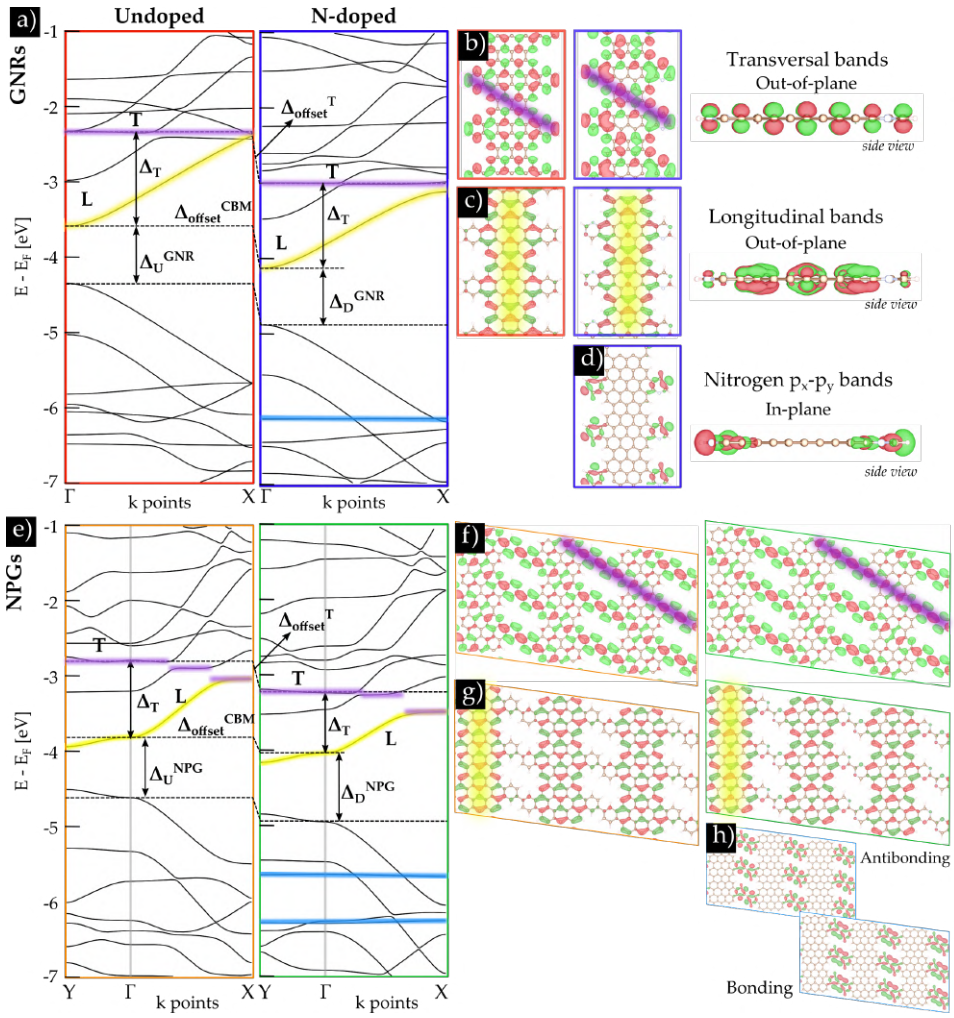

FIGURE 3.15: Theoretical electronic properties of N-doped GNR and NPG. a) DFT electronic band structure of undoped GNR (red plot), N-doped GNR (blue plot); b)-d) DFT wavefunctions of b) transversal, c) longitudinal and d) nitrogen px-py bands for undoped and doped systems, with both top and side views; e) DFT electronic band structure for undoped (orange) and N-doped (green) NPGs; f)-h) DFT wavefunctions of the f) transversal, g) longitudinal and h) nitrogen px-py bands. **T** bands, **L** bands and **N** bands have been highlighted in purple, yellow and blue respectively, and the bandwidth energies ($BW_{\Gamma X}$) can be indicated with red and blue rectangles for undoped and N-doped GNRs, and in orange and green (darker for $BW_{\Gamma X}$ and lighter for $BW_{\Gamma Y}$) for undoped and N-doped NPGs respectively.

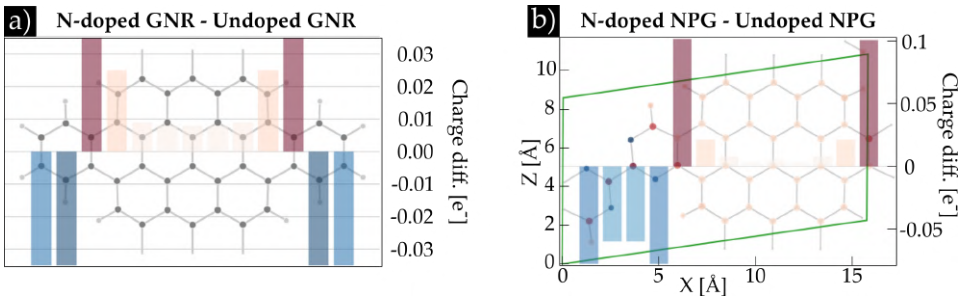

FIGURE 3.16: Hirshfeld plot of the N-doped GNR (left) and N-doped NPG (right). Every atom has been colored depending on the charge difference between the doped system and the undoped peer. Red color means more positive, whereas blue color refers to negative charge difference. The color bars represent the total charge difference accumulated per plane, taking them parallel to the longitudinal axis.

To understand the rigid shift of the bands for both theoretical and experimental results, we have plot the charge difference by Hirshfeld plots for both infinite 1D N-doped GNR and 2D N-doped NPG, shown in Figure 3.16. This plot shows the charge difference between the doped GNR/NPG and the undoped counterpart. As it can be noticed, there is extra charge accumulated by the pyrimidine sites, withdrawing it from the backbone. Since now the backbone is more electropositive, it behaves as a local gating, which downshift the bands (the electrons feel an increased attractive Coulomb interaction and their energy decreases). This takes place due to the inductive effects of the nitrogen atoms [207], located at the edges of the ribbon.

Beyond frontier bands: nitrogen flat bands

We now focus on nitrogen related flat bands or localized states that can be detected below the VBM. In the band structures of doped GNR and NPG of Figure 3.15 we observe flat bands at energies below the Fermi level (marked as blue). By plotting the DFT wavefunctions at this energy, we notice that they belong to the in-plane nitrogen orbitals p_x and p_y. Due to their in-plane character, it has been particularly challenging to track them via experimental methods. The tunnelling probability is low due to the weak overlap of tip-molecule wavefunctions, also observed for other systems with in-plane orbitals [231]. Generally, very close tip-sample distances are needed in order to achieve a sizeable overlap, which translates into high tunnelling currents.

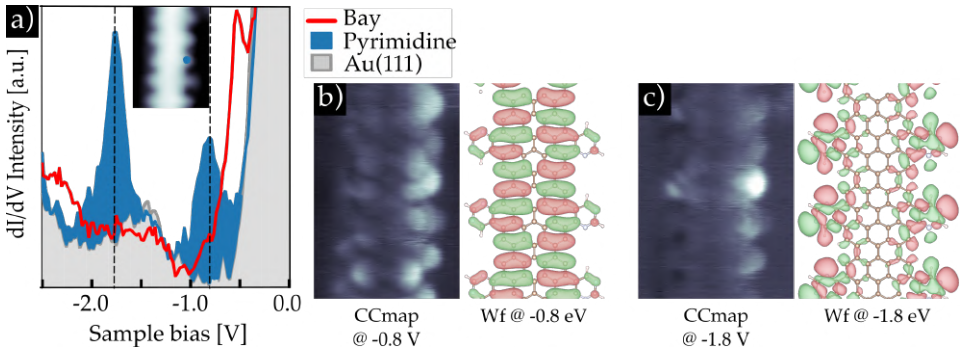

FIGURE 3.17: In-plane p_x and p_y orbitals of the nitrogen atoms in the N-doped GNR. a) STS spectra at constant current on the GNR bay (red) and on the pyrimidine ring (blue), taking bare Au(111) as reference (grey). b) constant current conductance maps of the same GNR at -0.8 V, with the respective DFT wavefunction. c) constant current conductance map at -1.8 V with the respective DTF wavefunction. Red-green contrast belongs to positive-negative sign of the orbitals, with an isovalue of 0.035 $Å^{-3}$.

In order to avoid damaging the sample, the STS has been performed at constant current.

Luckily, sometimes the accidental modification of the tip apex [232], what can be called a 'funky tip', allows for a more efficient hybridization with the in-plane orbitals of the sample. This is shown in Figure 3.17. A constant current spectrum was performed from -0.2 V to -2.5 V at a pyrimidine ring (blue spectrum), and it was compared to a single spectrum at the bay of the ribbon (red color). As it can be observed, there are two prominent peaks at both -0.8 V and -1.8 V. Checking their relative position with respect to the VBM, something that can be quite reliably done with the DFT band structure, the peak at -0.8 eV can be assigned to the VBM-1 (the VBM can be observed in the red spectrum, taken at the bay of the GNR), whereas we presume that the peak at -1.8 eV belongs to the in-plane p_x and p_y orbitals of the nitrogen atoms, corroborated with constant current conductance maps.

Beyond frontier bands: bay and pore states

A different type of localized state has also been identified at the unoccupied energy range by following the same CC spectroscopy strategy to reach

higher energy values without affecting the system (Figure 3.18). From the STS maps we can see that these states are localized at the bays of the ribbon and at the pores of coupled GNRs. These type of localized states, also found in the undoped counterpart [118], are originated from the lateral confinement of image potential states that are trapped between the ribbon and the vacuum [233]. The edge structure originate lateral quantum wells in the image potential, giving rise to the localized states at the bay.

Figure 3.18 shows the spectra taken at positive bias for both single and coupled GNRs. Figure 3.18 a) shows the STS of a single GNR, where one can distinguish the CBM at 0.9 eV, the CBM+1 at 1.5 eV, as well as the prominent bay state at 2.1 eV. We confirm this assignment by the constant current height map of Figure 3.18 b) and the corresponding DFT wavefunction pattern. When fusing together the GNRs, in DFT we observe that the bay state now splits in two new states, which we called the bonding and antibonding pore state (Figure 3.18 e). Experimentally, when we measure a series of spectra along a line that crosses a couple of GNRs (Figure 3.18 c-d), we find a bay state at 2.3 eV at the edges, and a double peak at the pores, at 1.95 eV and 2.30 eV. The localization of the states at the bay/pores is confirmed by acquiring STS maps at these energies (Figure 3.18 f). We attribute the lower lying peak at the pore site to the bonding pore state. The second peak could be in principle the antibonding counterpart, though DFT estimates a significantly larger splitting of 0.62 eV. Alternatively, this second peak could be related to **L** or **T** bands (note that these bands appear more intense at the edges when performing CC dI/dV maps [170], and therefore not so straightforward to distinguish them from pore localized states).

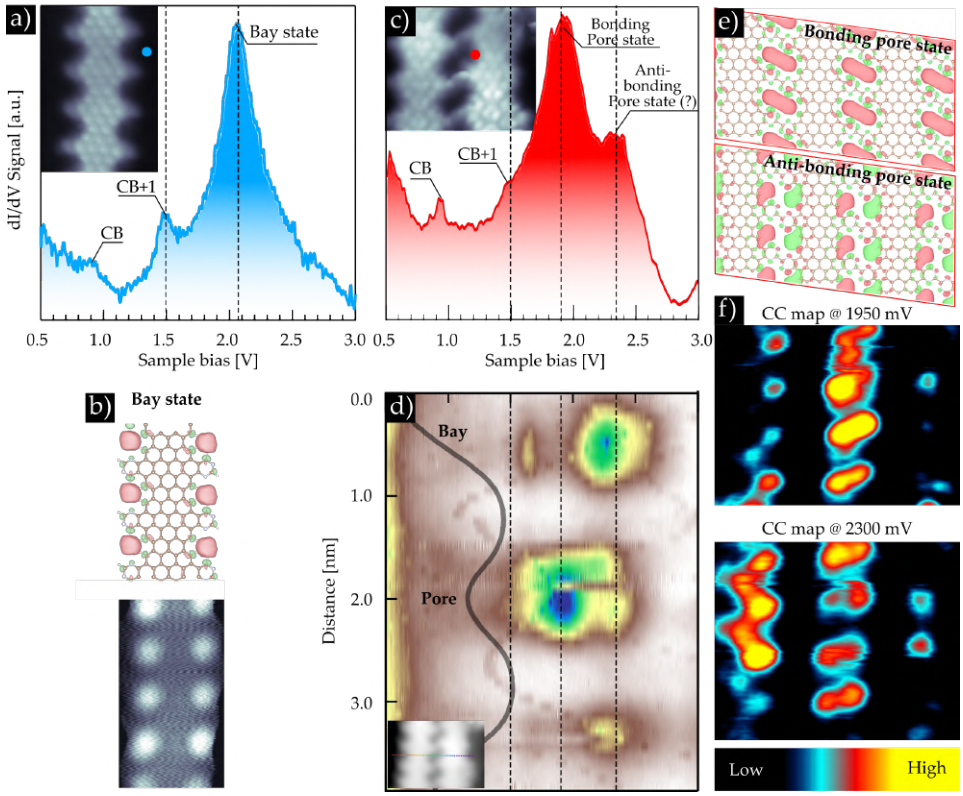

FIGURE 3.18: Bay and pore state in single N-doped GNRs. a) dI/dV signal at constant current from 0.5 V to 3.0 V on a single N-doped GNR. The inset shows the BR-STM of the ribbon at 7 mV. b) Constant current condutance map at 2.2 V and the corresponding DFT wavefunction showing the bay state; c) wavefunction of the bonding pore state in an infinite NPG (isosurface value: 0.05). d) dI/dV signal at constant current on coupled N-doped GNRs; e) 2D color map of a line scan at constant current. The line scan crosses transversally a pair of coupled GNRs by the pore site (inset). f) BR-STM image of the scanned coupled ribbons; g) constant current conductance maps at 1950 mV and 2300 mV.

In summary, we have studied the electronic properties of the N-doped single and coupled GNRs and infinite NPGs and compare them with the undoped counterpart. These properties are modified in several aspects due to the presence of the nitrogen atoms: although the absolute value of the band gap remains the same, the frontier bands are rigidly shifted due to the inductive effects given by the nitrogen atoms at the edges of the studied structures. The shift is also observed in the transversal bands by

means of DFT calculations, becoming more accessible for the transport in this direction upon gating. The effective masses barely change upon doping, hence maintaining the anisotropic character of the 2D networks. We have studied the presence of localized states at energies below the VBM, that correspond to the nitrogen in-plane orbitals, and how they split upon lateral coupling. We have also describe the bay and pore states for the doped systems: even if the bonidng state appears at the same energy for both the undoped and the N-doped systems, we suggest that the extra peak in the N-doped NPG to a decrease in energy of the antibonding state.

3.5 Conclusions and future perspectives

In this Chapter, we have systematically studied the on-surface reactions towards the formation of a nitrogen-doped nanoporous graphene. During the process, particular focus has been dedicated to these several aspects: (i) the position of the nitrogen atoms inside of the molecule to enable their sublimation, (ii) the thermal instability of the functional groups throughout the whole reaction sequence to achieve laterally coupled GNRs and (iii) the effect of enantioselective interactions in the synthesis of each intermediate and the final product.

The first issue was overcome by substituting the pyridine rings that were originally designed and inhibited the sublimation by pyrimidine functional groups, which are more stable than the pyridine rings during the sublimation. Concerning the second issue, the thermal instability of the pyrimidine functional groups during the thermally-induced lateral coupling of GNRs was controlled by adding chlorine atoms at the *para-* positions of these moieties. This modification allowed to induced a Cl Ullmann coupling, that requires less energy and hence less temperature to make it happen in comparison to the cyclodehydrogenation, preventing the functional groups from being cleaved out of the ribbon backbone.

Lastly, concerning the third issue, we demonstrate how, in each of the reaction steps, enantioselective interactions give rise to enantiopure domains, which facilitates the synthesis of the next step. We also observe how an enantioselective catalysis leads to chiral structures, starting from chiral polymers, to prochiral GNRs, and finally to the homochiral coupling of GNRs, which leads to prochiral pore structures. Chirality is transferred this way from the conformation of the molecules, to the organization, and finally

to the synthesis.

However, the addition of chlorine atoms alters the arrangement of intermediate products on the surface, leading to a randomly distributed and highly connected networks of GNRs, form which it is difficult to achieve a long-range order in the lateral coupling needed for the synthesis of extended NPG. This issue is overcome in Chapter 4, where the undoped 7-13 AGNR is used as a dynamic template to guide the growth of the more reactive nitrogen-doped GNR.

Bond-resolved STM has allowed to distinguish the features coming from the presence of nitrogen atoms in the 13 C wide segments as compared to the undoped counterpart, and directly visualized the chiral structure of the GNR. The XPS analysis has allowed to study the chemical composition at each step, confirming at which temperature the debromination, dechlorination and cyclodehydrogenation were taking place, confirming a hierarchical Ullmann coupling and an almost simultaneous dechlorination and planarization.

Considering the electronic properties of the nitrogen-doped systems, the presence of dopants by the edges keeps the absolute value of the band gap almost intact and close to 1 eV, while shifting bands rigidly downwards, hence keeping the semiconducting character.

Additionally, the doped structures have different types of localized states: on the occupied region, a single level related to the nitrogen p_x-p_y lone pair orbitals is split in two when GNRs couple. On the other hand, at the unoccupied side we find states localized at the pores and bays that originate from the confinement of image potential states. Both these types of localized states could participate in interactions with guest molecules, relevant for sensing and catalysis applications.

Chapter 4

N-doped NPG with built-in superlattice heterojunctions.

Introduction

In the previous chapter we found several issues that impeded the synthesis of extended N-doped NPG, related to undesired intermolecular and molecule-surface interactions. These interactions were driven by the component we needed for the doping and the synthesis of the doped structures (for the activation of interribbon cross-coupling at low enough temperatures). Finding molecular designs that allows us to control the dopant site of the final product, the stability of the doped unit, and the intermolecular interactions and reactions during the synthesis is an enormous challenge that, if overcome from some particular design, will surely be limited by the choice of the precursor. Here we present an alternative strategy consisting on using two components to form the NPG: an undoped component that is used as template to guide, and a second component that is grown interdigitated with the template formed by the first one. This strategy does not only overcome the problem of growing doped NPG structures, but it opens new doors for the synthesis of lateral heterostructures. We will demonstrate that the different electronic properties of both components simultaneously lead to a lateral superlattice heterostructure of type-II junctions.

Combining materials with distinct properties on a covalently bonded, one-atom thick layer is a configuration that can be very attractive for optoelectronics [234] and photo/electro catalysis [235] among other applications. Different types of such lateral heterostructures have already been realized by following several in-situ [32, 236–238] and prepatterning [239] methods. However, despite the plethora of new 2D materials that have been

HJ type	GNR type	Dopant type	Dopant location	GNR connection	Reference
Type I	Armchair (7-AGNR + 13-AGNR)	-	-	Longitudinal (intra-GNR)	[72]
Type I	Armchair (5-AGNR + 7-AGNR)	-	-	Longitudinal (intra-GNR)	[143]
Type I	Chevron (chevGNR + binaph-cGNR)	-	-	Longitudinal (intra-GNR)	[73]
Type I	Armchair (7-AGNR + B- 7-AGNR)	B	Backbone	Longitudinal (intra-GNR)	[142]
Type II	Chevron (chevGNR + 4N- cGNR)	N	Substitutional edge doping	Longitudinal (intra-GNR)	[71]
Type II	Chevron (chevGNR + CO- cGNR)	CO	Substitutional edge doping	Longitudinal (intra-GNR)	[141]
Type II	Chevron (N- chevGNR + NH- cGNR)	N, NH	Substitutional edge doping	Longitudinal (intra-GNR)	[144, 145]
Type II	Armchair (7-13-AGNR + 4N- 7-13-AGNR)	N	Substitutional edge doping	**Transversal (inter-GNR)**	**This work**

TABLE 4.1: List of graphene-based heterojunctions.

recently synthesized [236–238, 240] their combination is severely limited by the epitaxial matching and chemical stability at the interface [238]. Besides, although methods to fabricate high-density heterostructure arrays have already been proposed [236–239], scaling them to the nanoscale and with atomic precision is beyond their limit.

A natural solution for the aforementioned challenges can be found in the bottom-up, on-surface synthesis of graphene-based nanostructures. From the vast pool of on-surface synthesized GNRs demonstrated in the literature, it can be assumed that different molecular precursors can be polymerized to form heterocomponents with tailor designed properties. In contrast to that happening with 2D materials such as transition metal dichalcogenides (TMDs), GNR components share the same graphene backbone structure which should lead to chemically stable, epitaxial, and covalent interfaces. In one dimension, different types of graphene-based heterojunctions have been realized by codeposition of the two molecular building blocks [71–73, 143], or chemical transformation of functional groups [145], all listed in Table 4.1. These strategies, however, albeit defining each component with atomic precision, lead to a random distribution [71, 72, 143, 145, 241, 242] or a small number of heterojunctions [73, 243], and are hard to be extrapolated to two dimensional structures.

Control in the order along the GNR longitudinal direction can be achieved by substituting the two precursors co-deposition method by a single monomer that contains both components [75–78]. However, for these cases, the flexibility of selecting components, in particular introducing doping, is limited (described more in detail in Chapter 6).

Extending the recently proposed on-surface method to synthesize nano porous graphene (NPG) [118], in this Chapter we report a novel synthetic strategy to fabricate atomically precise, lateral superlattice heterojunctions built in a nitrogen-doped nanoporous graphene structure.

The strategy consists on a double templating effect, that guides the growth of the NPG intermediate products. A first graphene nanoribbon (the undoped 7-13 AGNR, refer here as **GNR1**) component grows in parallel arrays guided by the static template provided by the substrate [179]. In a second step, the **GNR1** array acts as a dynamic template, defining reactor nanochannels for the synthesis of the second nanoribbon component (**GNR2**), and fusing with the latter to form [**GNR1-GNR2**]n superlattice heterojunctions. The strategy of interdigitating GNRs triggers the formation of an N-doped NPG that now we refer as a hybrid NPG (h-NPG). Our methodology can be extended to the synthesis of other type of nanometer scale, graphene-based lateral hybrid superlattices.

The different electronic properties of both components simultaneously lead to a lateral superlattice heterostructure of type-II junctions, where the potential gradient is localized at the periodic array of heterogeneous nanopores within the ultimate carbon carbon bond limit. The combined atomic precision in structure and band discontinuity, the latter unprecedented in lateral heterojunctions, enable the realization of a few atom size lateral heterostructures where well-defined pristine properties of each component coexist with emergent interfacial quantum properties.

4.1 On-surface synthesis of a hybrid NPG by sequential templating

The main steps of the process are summarized in Figure 4.1. The first component, **GNR1**, is the 7-13-AGNR that can be synthesized using **0** diphenyl

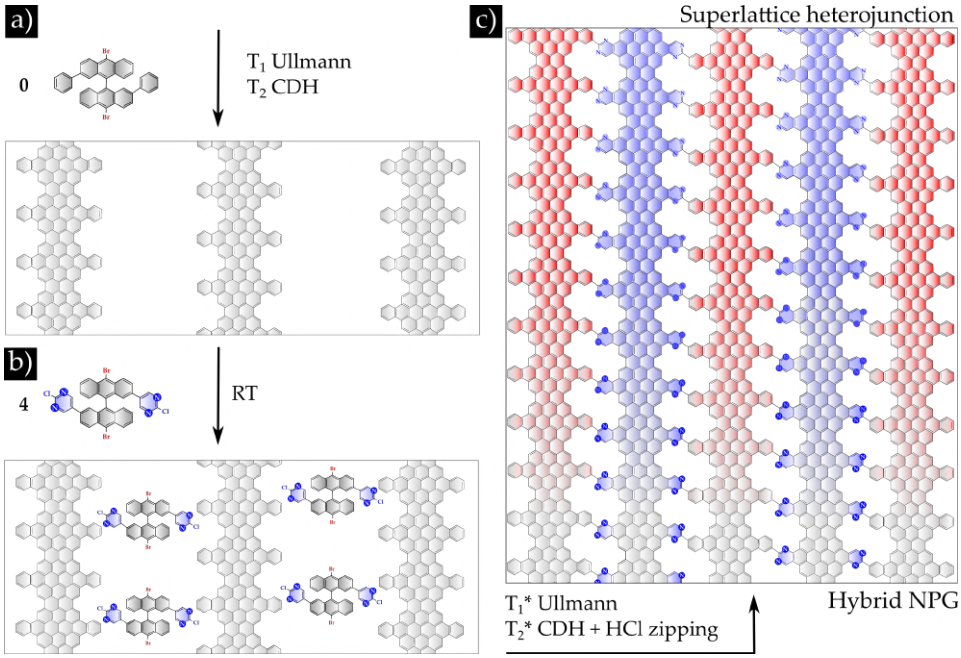

FIGURE 4.1: Schematic illustration of the bottom-up fabrication of the superlattice heterojunction (red-blue) built-in a hybrid nanoporous graphene (grey). a) First the array of **GNR1** is synthesized by depositing precursor **1** on Au(111) at room temperature and following the Ullmann polymerization and cyclo-dehydrogenation (CDH) steps at T_1 = 200ºC and T_2 = 400ºC respectively, as previously reported in Ref. [179]. b) The parallel array of **GNR1** serve as a template to host precursor **4** on the empty Au(111) tracks and guide the synthesis of **GNR2**. Ullmann polymerization of **4** occurs at $T_1* = 150$ ºC, and at $T_2* = 300$ ºC both the CDH of **poly-2** into **GNR2** and the interribbon HCl zipping are simultaneously triggered. c) The resulting interdigitated, cross-coupled ribbons can be seen as a hybrid nanoporous graphene with heterogeneous pore structure and a built-in **[GNR1-GNR2]**$_n$ superlattice heterojunction.

–10,10'- dibromo-9,9'-bianthracene, previously introduced in Chapter 3 (Figure 3.4) as monomer **0**, and following the widely used two-step Ullmann polymerization and cyclodehydrogenation (CDH) reaction path [96, 118, 179]. The corresponding onsets for the two thermally induced reactions are T_1 = 200ºC and T_2 = 400ºC.

As previously reported, the potential grid formed by the herringbone reconstruction of the Au(111) surface guides the synthesis of this GNR into

periodic arrays [179] (see Figures 4.2). This prealignment, besides being critical for the lateral fusion, also promotes the synthesis of long GNRs, with an average length around 70 nm (though GNRs up to 200 nm can be found). As evidenced in ref. [179], first the polymer bunches are pinned by the kink dislocations, helping to aligning them along the zigzag direction. Then, upon planarization, the attractive intermolecular forces of the polymer bunches are replaced by a stronger interaction with the substrate gets stronger, resulting in an ordered dispersion of GNRs, in positions that maximize the contact with the fcc regions. The separation between the parallel aligned ribbons can be tuned according to the coverage: three different periods, d_1=7.8 nm, d_2=3.8 nm, and d_3=1.9 nm can be obtained for 0.25 ML, 0.25 ML, and 1 ML respectively (1 ML corresponds to the saturation of the d_3 phase by definition).

In the preparation of Figure 4.3 a), these three distances have been identified from the profile in green color. The forth distance, d_2*= 3.0 nm, is given as a result of a combination between d_2 and d_3 phases. In the limit of a very diluted sample (< 0.5 ML), N-doped polymers can interact with each other, forming irregular clusters, similar to that observed on the bare surface (Chapter 3), and disrupting the **GNR1** pattern (see Figure **??**). On the contrary, for a very saturated sample, there is no room to allocate the new incoming precursors. The optimal **GNR1** density is therefore defined by an intermediate coverage containing the d_2 and d_3 phases, i.e. between 0.5 ML and 1 ML. We therefore use a coverage in this range to create the **GNR1** template where we deposite the precursor for the second component, monomer **4**, or 2, 2'-di(4-chlorine)pyrimidine 10, 10'-dibromo 9, 9'-bianthracene.

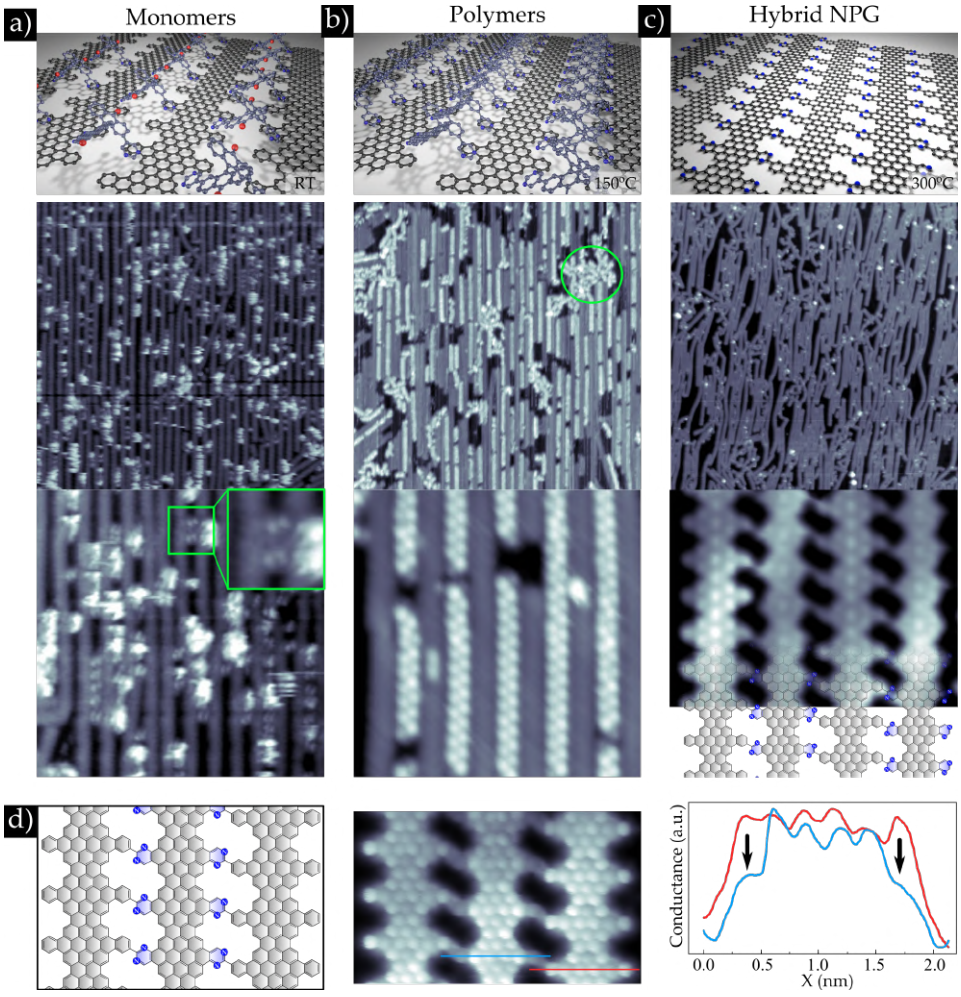

FIGURE 4.2: On-surface synthesis of h-NPG. (**A-C**) Synthesis of the second component (**GNR2**) within the aligned **GNR1** array that has been pre-synthesized as reported in Ref. 20. The STM topographic images show: (**A**) intercalated monomers of precursor **2** after deposition at room temperature. The inset in the bottom image shows a pair of monomers. (**B**) Formation of **poly-2** chains interdigitated within the **GNR1** array after annealing at $T_1* = 150C$. (C) Simultaneous cyclodehydrogenation (CDH), which converts **poly-2** chains into **GNR2**, and interribbon cross-coupling, which leads to **[GNR1-GNR2]**$_n$ superlattice heterostructures, after annealing at $T_2* = 300C$. (**D**) BR-STM of a **[GNR1-GNR2-GNR1]** triplet obtained with a CO-functionalized tip. The image unveils clear chemical contrast between the bridging pyrimidine rings of the N-doped **GNR2** (center ribbon) and the benzene rings of the undoped **GNR1** (side ribbons). The significantly lower contrast of the pyrimidine rings are clearly visualized at the transversal profiles (bottom figure) obtained at the lines marked in the schematic model (middle figure). All STM imaging parameters are detailed in Appendix A Table A.4.

As already explained in the previous Chapter, monomer **4**, being isostructural to **0**, bears two important differences: the pyrimidine group that substitutes the phenyl of **0**, and its para chlorination. The pyrimidine introduces chemical heterogeneity to the nanopores, and modifies the electronic band structure of the final **GNR2**, and consequently of the whole h-NPG. Pyrimidinic N is an isoelectronic substitution that does not introduce additional charges, but its higher affinity results in a local charge accumulation and the corresponding inductive band shift [71, 207]. The role of the chlorine substituents, on the other hand, is to reduce the temperature of the final interribbon lateral cross-coupling in order to assure the survival of the pyrimidine group throughout all the reaction path.In the homocoupling of N-doped GNRs studied in Chapter 3 the dehydrogenative path that requires temperatures of 450ºC [118], high enough to cleave or decompose edge functional groups [209, 210], was substituted by a second Ullmann coupling that could be triggered at 300ºC simoultaneously to the CDH reaction. For the hybrid structure, the heterocoupling between GNR1, with fully hydrogenated edges, and **GNR2**, with Cl at the C sites between the two N of the pyrimidine, is carried out by a novel HCl zipping mechanism that emulates the recently reported HF zipping [215].

The STM image of Figure 4.2 shows that precursors deposited at room temperature already intercalate in the interibbon channels. By annealing to T_1* = 150ºC, precursor **4** already undergoes Ullmann polymerization, exhibiting the characteristic chain of alternating lobes that can be seen in Figure 4.2 b) [96]. Besides some marginal regions where short, meandering poly-2 chains cluster (see circle in Figure 4.2 b), the surface is covered with an interdigitated [**GNR1**-(**poly-2**)]$_n$ superlattice. The longer, straight, **poly-2** chains found in the interdigitated region suggest that the reactor nanochannels provided by the **GNR1** superlattice can be employed as a general strategy to assist polymerization of precursors that lead to undesired intermolecular interactions on a 2D template, as is the case of many functionalized molecules. The single periodicity of 2.5 nm measured by STM for the interdigitated superlattice indicates that GNR1-(poly-2) interactions unpin the **GNR1** superlattice from the herringbone template (see Figure 4.3 e-f).

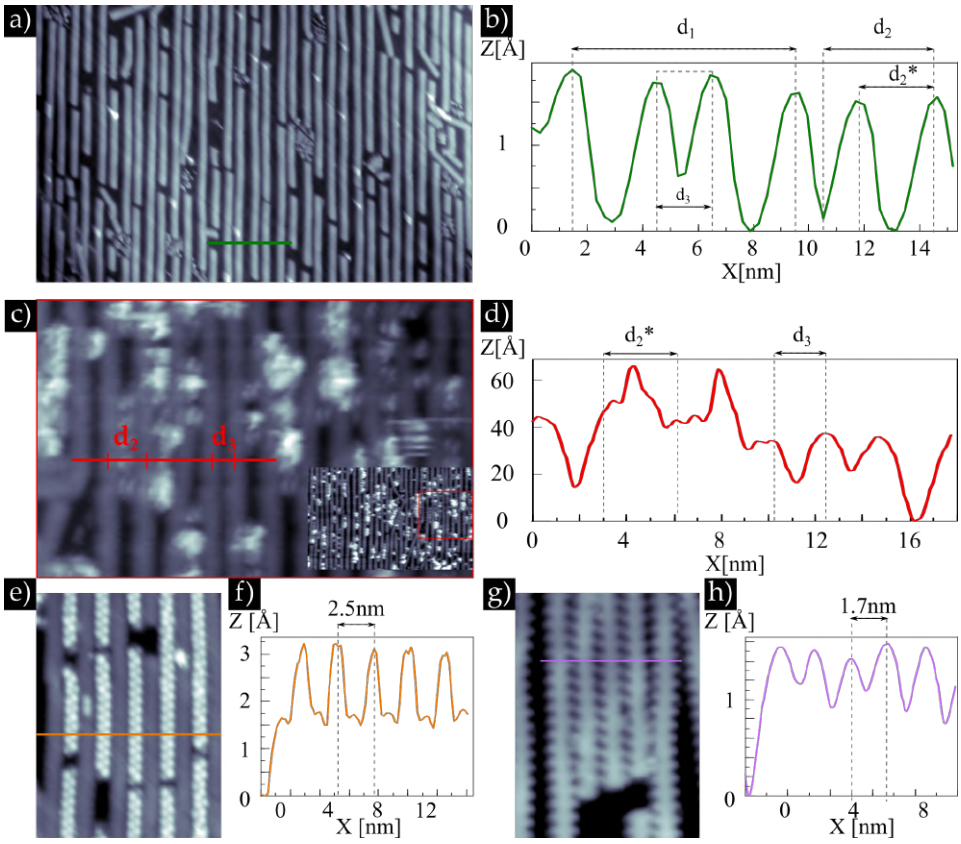

FIGURE 4.3: **GNR1** lateral distance analysis at different stages of the hierarchical on-surface reaction to grow h-NPG. (**A**): STM image of the undoped **GNR1** on Au(111). The green line depicts a profile in (**B**), revealing at 75% of coverage the lateral distances d_1 = 7.8nm and d_3 = 1.9nm, and an intermediate of both close to d_2 = 3.8 (d_2* = 3.0nm). (**C**): STM image of as-deposited precursor **2** on an already-grown superlattice of **GNR1**. (D) Lateral distances depicted in the profile between undoped **GNR1** are maintained upon precursor **2** deposition. As-deposited precursors lay in the d_2* bare stripes. (**E**): Superarray of **GNR1 - Poly 2**, with its respective orange line profile shown in (**F**). Lateral distance between **GNR1** shrinks upon **Poly 2** formation towards 2.5 nm. (G): As-grown superarray **GNR1 - GNR2**, with the purple line representing a profile, which has been shown in (**H**). This is the narrowest distance between ribbons and agrees with the densest scenario. I-V conditions are collected in Appendix A Table A.5.

The optimization of the h-NPG needs not only the right coverage for the template but also for component 2. Fortunately, we find that this can be tuned in sequential growth steps. Figure 4.4 shows one example where,

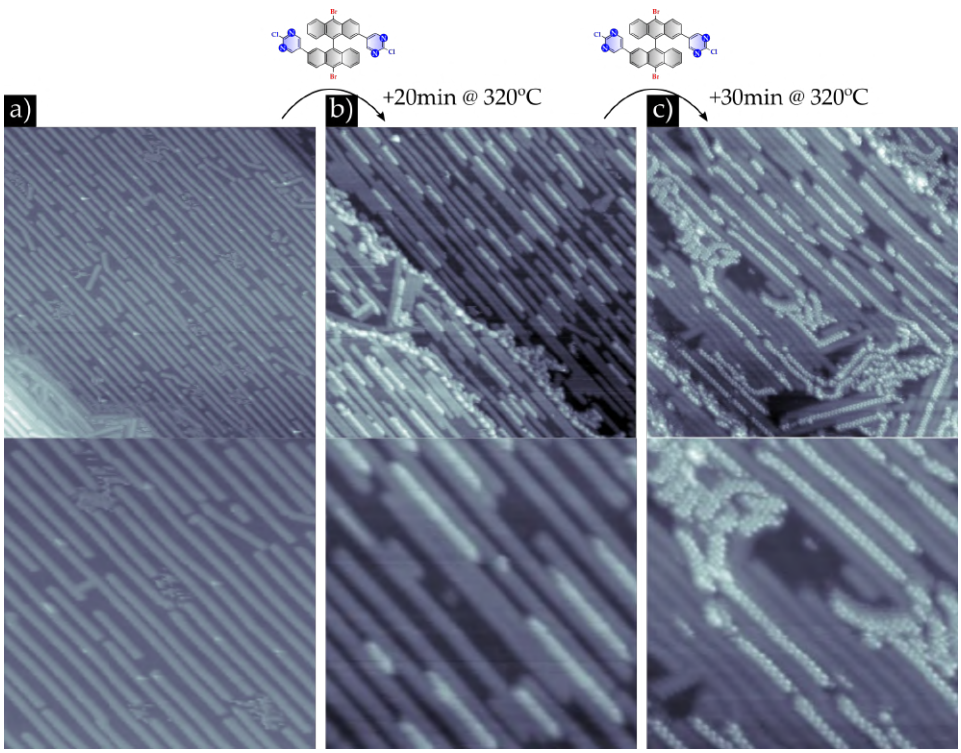

FIGURE 4.4: Dose tuning of precursor **4** with the GNR template. a) As-grown undoped **GNR1** at 75% of coverage; b): subsequent molecular deposition of precursor **4** at a temperature of 320ºC during 20 minutes and further postannealing to 150ºC to grow **Poly 2**; c): additive deposition of precursor **4** during 30 minutes (total time of sublimation: 50 minutes) with a further postannealing to 150ºC to grow **Poly 2**.

monomer **4** was sublimated on a **GNR1** template in two steps, on of 20 minutes and a second of 30 minutes. The sample is annealed to 150ºC after each deposition in order to obtain the **GNR1-Poly-2** superlattice. By comparing the two samples we can see that the increase in coverage of **poly-2** is proportional to the increase in deposition time, and more importantly, that the polymer chains in the second step are longer than in the first, indicating that the polymer can be sequentially grown.

Similar to what has been found for the homocoupling of pairs of N-doped GNRs, we find that at T2*=300 ºC, the planarization of **poly-2** into **GNR2** occurs simultaneously with the interibbon coupling (Figure 4.2 c), meaning that the novel HCl cross coupling mechanism is as effective as the Ullmann. The difference is of course the longer order obtained in the latter

case due to the preorganization of the **GNR1** template and its role in guiding the polymerization of the second component. BR-STM images acquired with a CO-functionalized tip as the one shown in Figure 4.2 d) demonstrate the coupling of adjacent GNRs, and enable the direct visualization of the chemically heterogeneous nanopores defining the junctions by revealing clear chemical contrast between the bridging units of the two components, as illustrated by the line profiles of Figure 4.2 c).

4.2 Electronic properties of the h-NPG

The dI/dV spectra of Figure 4.5 a) reveal pairs of peaks that can be assigned to the VMB and CBM of each component. Similar to what we find for each decoupled ribbon (see Chapter 3), our analysis leads to similar band gaps of 1.24 eV for the undoped **GNR1** and 1.47 eV for the N-doped **GNR2**, with the VBM and CBM respectively downshifted by 0.41 eV and 0.18 eV for **GNR2**. The magnitude of the valence and conduction band offsets is well captured by a similar shift of 0.42/0.41 eV found for the VBM/CBM in the DFT band structure shown in Figure 4.5 c).

The assignment of the experimental VBM/CBM of each component is supported by the onset of the corresponding LDOS in dI/dV maps, displayed in Figure 4.5, and cross-checked by acquiring a set of dI/dV maps around these energies. Figure 4.6 shows an example of a series of maps obtained at the occupied energy range in order to determine the two VBM. The system considered is a group of four interconnected ribbons: [**GNR1-GNR2-GNR1-GNR2**], (as in Figure 4.5) with two non connected **GNR1** at both sides to also compare the maps. The first map at -100 mV shows a weak modulated signal at connected and disconnected **GNR1**, overlapped with a long wavelength modulation that extends over the whole surface and is related to the scattered Au(111) surface state. At -200 mV the more intense pattern at **GNR1** stands out of the surface state modulation background, with its pattern resembling that simulated by DFT for the VBM (see Figure 4.5 d). The VBM signal of **GNR1** vanishes at -300 mV, and is replaced by a weaker signal of different pattern at -400 mV, which may arise from the VBM-1. At -500 mV, the weak signal at **GNR1** persists, and a pattern starts to arise at **GNR2**. The latter become more intense at -600 mV, showing the same VBM as that found for GNR1 at -200 mV. The signal is progressively decreasing at lower bias voltage. As a summary, the most intense signals

that can be related to the VBM are found at -200 mV for **GNR1** and at -600 mV for **GNR2**, confirming our assignment of the dI/dV spectra.

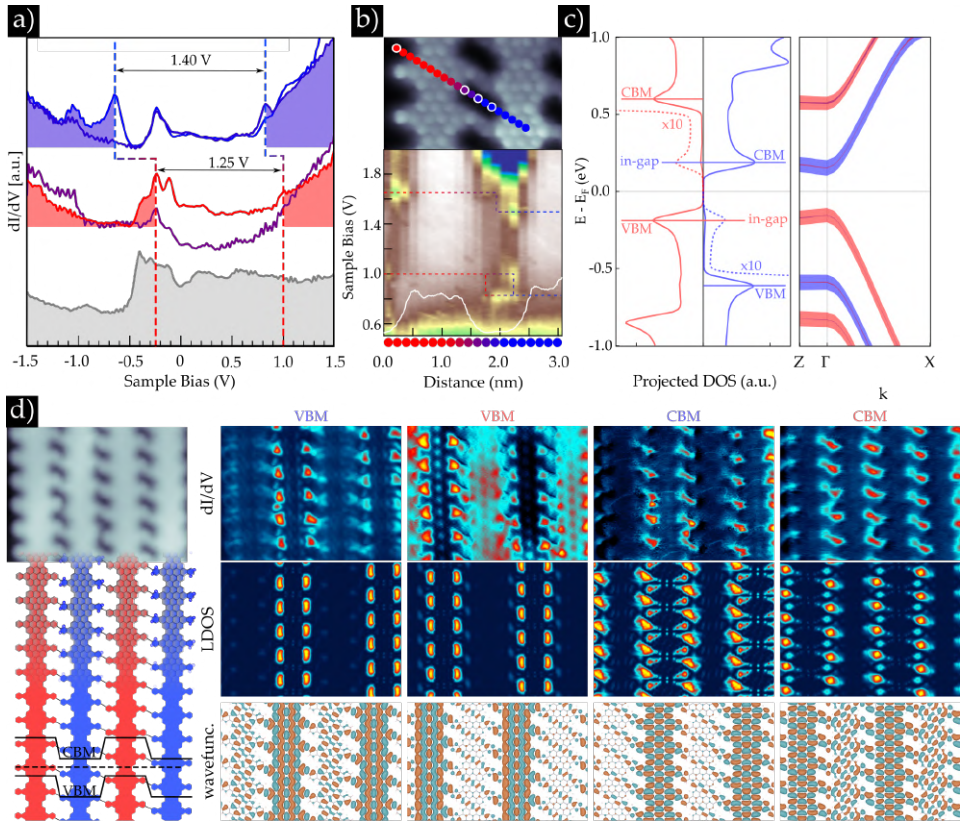

FIGURE 4.5: Electronic band structure of h-NPG. a) Representative dI/dV spectra of **GNR1** and **GNR2**, where the VBM and CBM are marked with dashed vertical lines (positions of the selected spectra are highlighted with white outline in the series of Fig. 3b). The corresponding band gap is indicated. A spectra acquired on Au(111) is included as reference (shadowed grey line). b) Color plot of a series of constant current dI/dV spectra acquired along a line that crosses a GNR1-GNR2 pair within the triplet shown in Figure 4.2 b). The topographic profile along the spectroscopic series is overlaid as white line. c) Band structure in the longitudinal (ΓX) and transversal (ΓZ) directions. Colored fat bands represent the projection onto **GNR1** (red) and **GNR2** (blue). The DOS of each heterocomponent is added on the left. d) Constant current dI/dV maps acquired on a **[GNR1-GNR2]**$_n$ superlattice at the energies of the VBM and CBM of both GNRs, together with LDOS cuts obtained by DFT at VBM and CBM energies, at the height of h= 0.3 nm, and the corresponding wave functions at Gamma. The topographic image where the maps were acquired, overlapped with a schematic illustration, are shown at the left.

The substantial band discontinuity exerts an effective confinement of

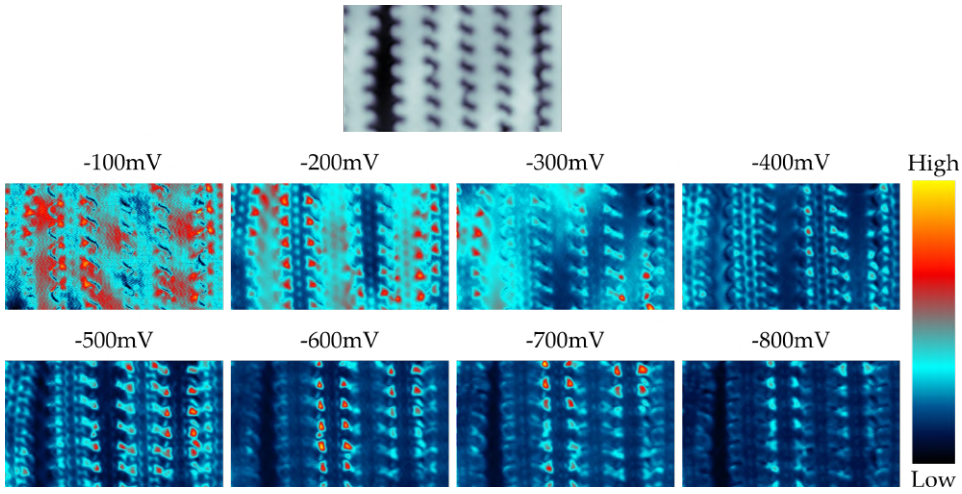

FIGURE 4.6: Constant current conduction maps at energies below the Fermi level on a group of four inter connected ribbons: **[GNR1-GNR2-GNR1-GNR2]** with other non connected **GNR1** at both sides for comparison. Significant contrast can be observed for the **GNR1** components at -200 mV, while it is at -600 mV for **GNR2**. STM image I-V conditions are listed in Appendix A Table A.8.

the frontier bands of each heterocomponent, as can be visualized in the constant current dI/dV maps and constant height LDOS cuts shown in Figure 4.5 d). However, the corresponding wave functions of the interdigitated components do not completely vanish at adjacent GNRs (Figure 4.5E e). In particular, the VBM of the undoped **GNR1** and CBM of the N-doped **GNR2** are interconnected via diagonal stripes, even if these states are located at the forbidden gap region of the adjacent GNRs. We attribute it to the tunnelling of these states across the junction, which can also be perceived in the DOS for high enough amplification (dashed lines in Figure 4.5 c). The in-gap states arising from tunnelling are not detected in the STS maps due to fact that their weak signal is further attenuated by the faster decay of the wavefunction into the vacuum at the backbone of GNRs [170], resulting in the amplification of the signal at the edges observable in the STS and LDOS maps of Figure 4.5 d).

In-gap tunneling states have been predicted to exist in well-defined heterojunctions with atomically sharp potential steps [244]. In a more detailed analysis of our experimental and theoretical data, we find evidences for both, the atomically sharp potential steps and the presence of tunnelling

states.

Figure 4.5 b) shows a series of constant current dI/dV spectra acquired across a **GNR1-GNR2** interface. Here, the CB+1 maxima exhibit a sharp discontinuity at the interface within the step size of 0.15 nm, a single C-C bond, used in the spectroscopic series. This value is about a factor of 5-10 smaller than the already narrow band bending region found in 0D heterojunctions in graphene nanoribbons [71]. The CBM of both components also show constant energy levels, separated by ∼0.2 eV, but in this case they interpenetrate across the interface, which we attribute to tunneling. The decay of the tunneling tail can be better studied in simulated LDOS scans, displayed in logarithmic scale in Figure 4.7 for a [**GNR1-GNR2-GNR1**] triplet. The finite segment allows to simultaneously visualize the decay of CBM states of **GNR2** within the **GNR1** region, and the strong overlap of the tails of the VBM of **GNR1** coming from each heterojunction into the central **GNR2** region. This overlap is the origin of the "stripes" that connect the VBM/CBM wave functions in the periodic superlattice of Figure 4.5 e).

In order to study the evolution of the overlap with the period of the superlattice, in Figure 4.7 b) we analyze squared wavefunction profiles for [(**GNR1**)$_m$-(**GNR2**)$_m$]$_n$ heterojunctions of different periodicity w = m x d (d = 1.6 nm is the inter-ribbon distance in the superlattice). For the superlattice that we synthesized, the m = 1, a small but finite overlap of the in-gap tails within the single ribbon components (blue line sections) can be clearly perceived. For superlattices with wider heterocomponents (m > 1), the distance between junctions is enough to prevent any significant overlap, leading to an effective disconnection of the interdigitated GNRs. Notably, the bridges that couple **GNR2** units introduce step discontinuities that further attenuate the decay. This is evident for m = 3, where the in-gap state abruptly decays to negligible values when entering the central **GNR2** unit (follow guiding green line sections in Figure 4.7 b).

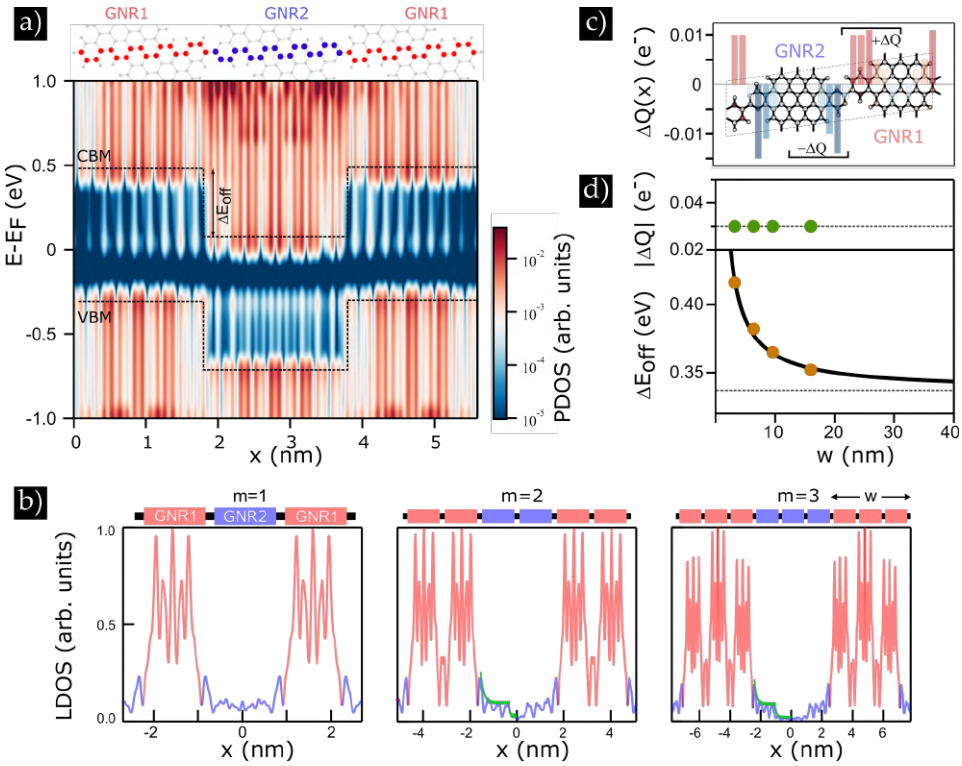

FIGURE 4.7: In-gap states and quantum dipoles. a) Simulated LDOS scan across a **GNR1-GNR2-GNR1** triplet. The path of the scan line is indicated with colored atoms on the schematic on top. The color plot is in log scale to enhance in-gap states within the gap. b) Wave function profiles of the VBM of **GNR1** averaged along the ribbon direction for m = 1-3 superlattices, showing the evolution of the decaying in-gap tail at **GNR2**. The green line is an envelope guideline. c) Hirshfeld charge difference with respect to individual **GNR1** and **GNR2**, averaged in columns along the ribbon direction. The sum over half segments of the ribbons define the dipolar charge Q. The charge difference at each atom is also depicted in red/blue (+/-) color scale. d) Evolution of the dipolar charge and band offset with the superlattice period. The band offset data is fitted with the inverse law model of [170]. The dashed line in the top graph refers to dipolar charge of the m = 1 superlattice, and in the bottom graph to the band shift of the infinite superlattice.

Interfacial in-gap states are inherently associated with a charge redistribution, which can induce significant band realignment [244]. Unlike conventional bulk heterostructures, the interfacial dipole potential of 1D (lateral) heterojunctions decays logarithmically with the distance from the junction. In superlattice heterostructures with periodicity w larger than the

interfacial dipole, the potential decays as 1/w. Consequently, for periods smaller than the characteristic decay length, which can be as large as 30 nm for semiconductor heterojunctions such as MoS_2/WS_2 [245], the band offset is size-dependent. In narrow superlattices the interaction between adjacent dipoles can also lead to charge redistributions that induce additional shifts [145]. These two factors demand an accurate control on the superlattice quality for a homogenous, well-controlled band offset. In order to discern the different mechanisms for band realignment, we tracked the evolution of both the dipole charge and band offset with respect to the superlattice period.

Figure 4.7 d) shows that the dipole charge $|\Delta Q|$, as obtained from the Hirshfeld charge difference integrated in half segment of each type of ribbon (see Figure 4.7 c), remains nearly constant down to the narrowest superlattice m = 1. This is a further manifestation of the strong localization of the quantum dipoles that characterize these heterojunctions, estimated to be within two carbon bond-lengths from the interface, well below the narrowest superlattice period of 1.6 nm. This result is in contrast with the significant charge redistribution found for 0D heterojunctions of similar width within single GNRs [145]. Confirming the rigid dipole scenario, the band realignment evolution follows the inverse scaling down to m = 1 (see Figure 4.7 d). The fit of the data results in a decay length of 7.8 nm, measured as the period where the band offset deviates 10% from the asymptotic value of 0.34 eV of the infinite superlattice.

In summary, the lateral connection of ribbons in the h-NPG keeps qualitatively their electronic properties constant as compared to the same isolated system (i.e. the absolute value of the band gap is the same and the frontier bands rigidly downshift in the doped component). Interestingly, the connection do not totally confined the frontier bands, but induce a faint tunnel into the neighbour component across the junction, creating in-gap states. We have demonstrated that these tunnelling states overlap, perturbing the subsequent band offset of the frontier bands. By simulating heterojunctions with wider periodicities we have observed that the in-gap states do not overlap and hence do not change the band offset, unveiling it is size dependent. This is the consequence of a constant charge accumulation at the junction due to the tunneling, and therefore the presence of highly localized interface quantum dipoles.

4.3 Conclusions and future perspectives

In this Chapter we propose a strategy based on a templating effect to grow an N-doped nanoporous graphene with 2D long range order. We claim this strategy can be generalized to other GNRs that can act as second component, including other doped or functionalized 7-13 AGNR, setting a new path for engineering nanopores with atomic precision. Our system consists on alternating undoped and doped 7-13 AGNR which we demonstrate it behave as a 2D superlattice heterojunctions with atomically sharp, well-defined step potentials and with nanometer scale periods that are well below the screening length of the interfacial dipole. The band offset is controlled by the atomic scale design of the components and the strong localization of the interfacial quantum dipoles. Relevant applications of the h-NPG can be foreseen in, for instance, photocatalysis, since the pores can be used to immobilize the reactant right at the heterojunction. Likewise, it could be interesting for sensing, since target molecules at the nanoporous heterojunctions would affect optical transitions, in particular the interribbon absorption peak.

The sharp band discontinuity, together with the presence of tunneling states at both sides of the junction, is expected to promote interlayer excitons and efficient charge separation that can be relevant for optoelectronic and excitonic solar cells applications [246].

This is demonstrated theoretically in Figure 4.8, where we present the absorption coefficient of both undoped and doped GNRs (top row), and NPGs, as well as the hybrid NPG (bottom row) for in-plane (longitudinal transversal directions) polarized light. The first two visible peaks in GNRs and pure NPGs are at 0.98 eV and 1.48 eV, in agreement with that found in a previous study [123]. These peaks, which belong to the near IR region, correspond to the longitudinal and transversal band gap of the systems, and do not appear for pristine graphene. For the hybrid NPG, both peaks are preserved, while a new peak at 0.4 eV appears. This peak belongs to **inter**-ribbon transition, whereas the other two already mentioned correspond to **intra**- ribbon transition. The **inter**- ribbon transition is possible, but with much less probability than the intra- ribbon exciton transitions. As a consequence, we presume that the excitation would take place in each of the components of the h-NPG separately and then the electron-hole pair separation would take place as soon as the exciton approaches to the

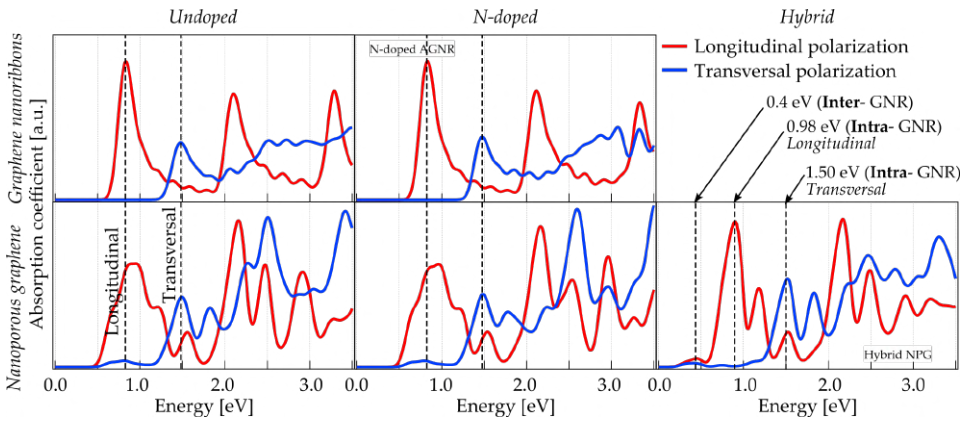

FIGURE 4.8: Absorption coefficient of undoped and N-doped GNRs (top row), undoped, N-doped and hybrid NPGs (bottom row). Red and blue color plots correspond to longitudinal and transversal light polarization, respectively.

interface connecting both components, as commonly observed for organic solar cells [247].

As a future perspective, we aim to try the optoelectronic properties of this material experimentally. Furthermore, the characteristic of the nanopores makes this graphene-based nanomaterial particularly attractive for photocatalytic applications such as water splitting [191].

Chapter 5

On-surface synthesis of ovalene derivatives

Introduction

As described in the introduction of this thesis dissertation, nanographenes, also known as graphene quantum dots or molecular graphene [15, 32, 46, 248], are zero dimensional systems with an sp^2 configuration that have been demonstrated to possess specific quantum properties depending on their size, edge topology and heteroatom content. This condition arises from the lateral quantum confinement given to electrons by nanostructuring with atomic precision [33], giving rise to multiple different optical [13, 14, 16, 249], electronic [7] and optoelectronic [15, 249, 250] properties. Likewise, this quantum confinement may also generate sublattice imbalance or the destabilization of Kekulé structures, emerging magnetic properties [11].

As considered previously for one dimensional graphene nanoribbons, doping or introducing heterocycles to 0D nanographenes is a feasible strategy to tune their electronic, optical, catalytic or magnetic properties, i.e. introducing electrochemical and biological activity, charge polarization, or the capability to realize p-n junctions, complexate with metal atoms, and manipulate spin ground states [251].

The best option to acquire these desired functionalities is, as commented in the introduction, by the bottom-up method. However, albeit the vast literature related to doped or heterocyclic nanographenes in solution [251], there are not so many works regarding the surface-assisted synthesis of these nanographenes [49, 252–257]. These are mostly involved in modifying the so-studied hexabenzocoronene (HBC) [49, 252, 255–257], or passivating

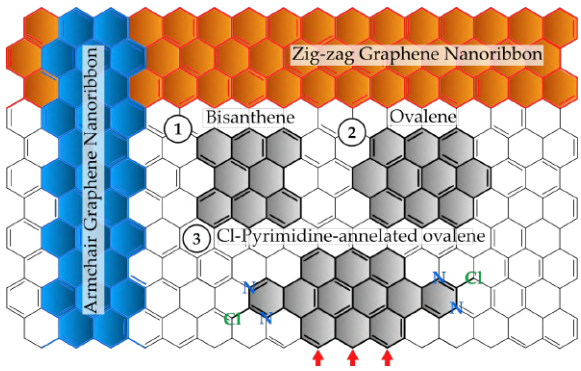

FIGURE 5.1: Graphene cutout into the ovalene derivative studied in this Chpater. 1D armchair and zigzag graphene nanoribbons have been coloured in blue and orange respectively. The 0D nanographenes, in grey color, are listed as: (1) bisanthene, (2) ovalene and (3) Cl-pyrimidine-annelated ovalene. Red arrows point to the zig-zag edges.

unstable zigzag edges in periacenes[254].

Here in this Chapter, we demonstrate the on-surface synthesis of a 0D nanographene with embedded pyrimidine heterocycles and also featuring zigzag edges. We present a comprehensive study of the on-surface reaction pathway of a planar ovalene-derivative nanographene (Figure 5.1, number **3**) named chloro-pyrimidine-annelated ovalene. Ovalenes (Figure 5.1, number **2**) have in common their 'oval' shape, and originate from bisanthenes (Figure 5.1, number **1**) with two annelated rings in the narrowest benzene row. These types of nanographenes present both zig-zag and armchair edges, and ca be easily compared to the respective graphene nanoribbons (infinite 1D GNRs coloured in blue and orange in Figure 5.1). Among the on-surface routes previously described to grow 0D nanographenes, the one employed here consists on an intra-molecular reaction that turns the non-planar precursor into a planar 0D nanographene.

Moreover, we demonstrate that the intrinsic chirality of the molecular precursors and their organization on surface, as described in Chapter 3, also plays a pivotal role in the yield towards the final product. Whereas in Chapter 3 we studied how the chirality is transferred through the **inter-** molecular reactions, in this Chapter we focus on the effect the chiral-dependent molecular interactions have in order to guide the chemical route towards the anticipated **intra-** molecular reactions. STM will be the tool to study the

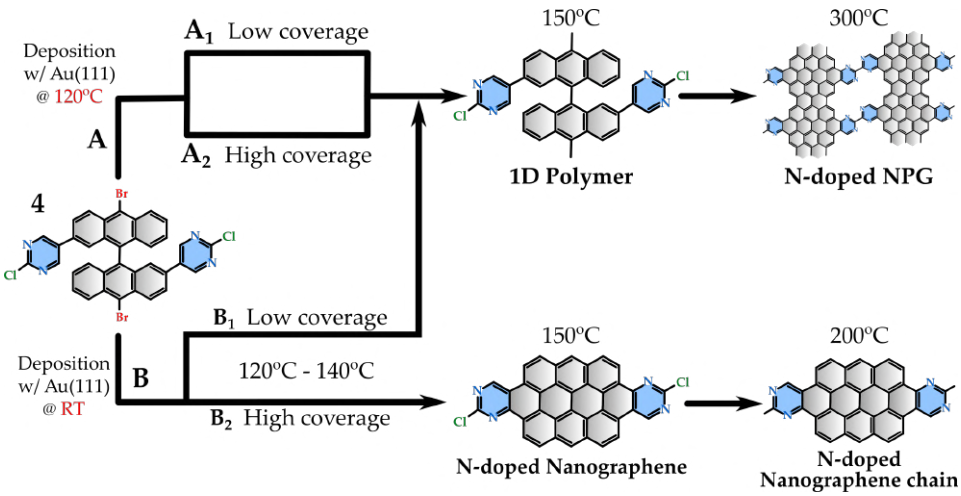

FIGURE 5.2: Two alternative routes can be followed when the molecular precursor **4** is deposited on Au(111) at different conditions. Reaction pathway **A** takes place with the substrate held at 120º, and it does not depend on the surface coverage conditions. If the substrate is held at room temperature during molecule deposition (route **B**), the synthesis diverges into two routes depending on the surface coverage.

intermediate steps at the single-molecule level, and will be complemented with XPS.

5.1 On-surface synthesis of a pyrimidine substituted ovalene.

As previously described in Chapter 3, deposition of monomer **4** at low coverage and postannealing to 120ºC (Figure 5.2, path B_1) or the direct deposition with the substrate held a 120ºC at any coverage (Figure 5.2, paths A_1 and A_2), trigger the reaction path towards the two-step Ullmann + CDH needed for the synthesis of GNRs / NPGs. Instead, when a high coverage is deposited at RT, the reaction path is different from the prior, as depicted in Figure 5.2 (route B_2). In this section it will be shown how these deposition conditions can lead to the synthesis of chloro-pyrimidine annelated ovalenes. The different intermediate reaction steps necessary for the obtention of the planar nanographenes will be described in the following.

The different structures obtained when deposited at low and high coverage deposition at RT (B_1 and B_2 routes) are shown in Figure 5.3. After postannealing to 100ºC, in the low coverage case (Figure 5.3 a-b), the precursor islands found at RT are replaced by small clusters of linear polymer chains resulted from the Ullmann coupling. As mentioned in Chapter 3, the size of the clusters seems to be limited by the fact that the polymers prefer to be at fcc regions of the Au(111) surface reconstruction [98], regions that can only locally distort to accommodate the as-formed polymers at the empty surface regions.

On the contrary, for high coverage conditions, the surface annealed at 100ºC (Figure 5.3 c-d) still hosts well-ordered, non-polymerized molecular units. We notice that molecular islands lose building blocks from their periphery and diffuse to empty Au(111) terraces regions, most probably locating at fcc regions. Thus, we conclude that the polymerization is kinetically promoted only when the molecular building blocks are able to diffuse to nearby Au(111) regions. But in locally saturated regions, the polymerization is kinetically hindered and molecular islands persist.

We now follow this step of chemical route B_2 with more detail by paying particular focus on the chiral-dependent interactions (Figure 5.4). Before postannealing, we observe that the conformational chirality of the non-planar single molecular precursors has been transferred to a 2D conglomerate organizational chirality [156] (Figure 5.4 a). These enantioselective interactions most probably happen due two factors: intrachain interactions (along the shortest intermolecular direction) mediated by chloropyrimidine-anthracene $\pi - \pi$ stacking (T-shape [258, 259]) and interchain interactions (along the longest intermolecular direction), driven by Br-H bonding (Figure 3.6).

When looking closer into one of the fully covered areas of Figure 5.4 b) after 100ºC of postannealing, we notice that the as-deposited molecular precursors in the 2D conglomerate co-exist with a new rearrangement. Molecules in the same row have lost their distinct homochiral pattern to be substituted by a kinked row, but the double protrusion pattern indicate that the configuration of the individual molecules has been preserved from the initial phase.

To study deeper what has happened, we have taken a closer look into

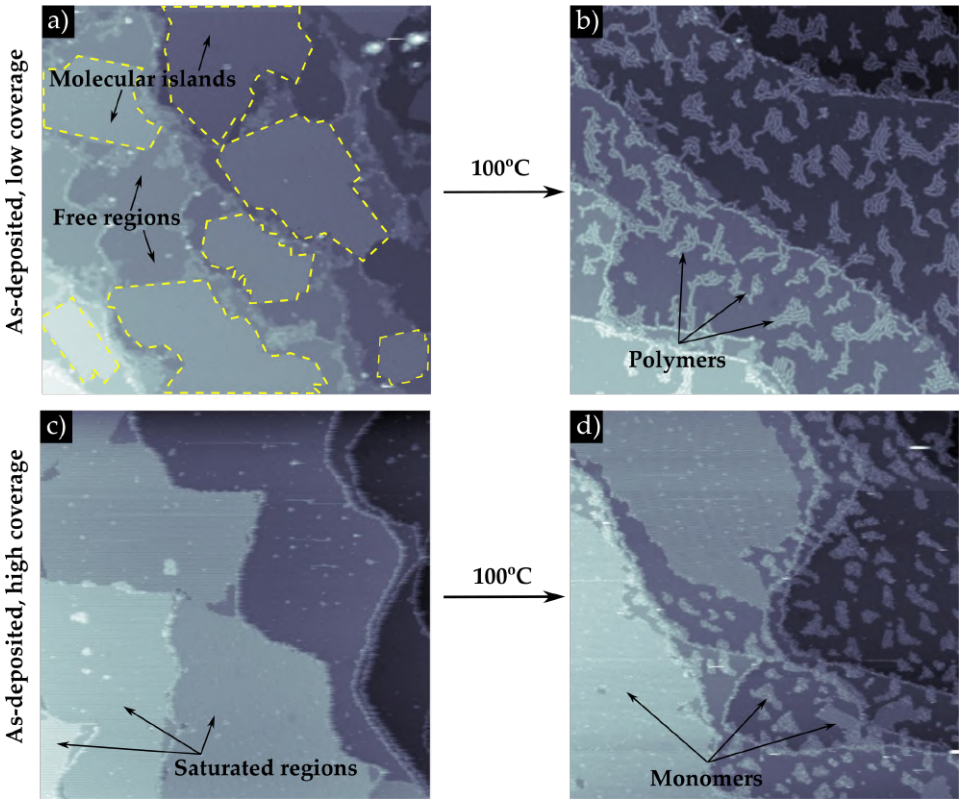

FIGURE 5.3: Molecular deposition of precursor **4** at different surface coverages. a) and c) STM images of as-deposited molecules at low (a) and high (c) coverage regimes. Molecular islands in a) are framed with dashed yellow line. Saturated regions in c) have been pointed out with black arrows.

the boundaries of the two domains so that we can compare them, an example represented in Figure 5.4 c) - e). 2D FFT patterns have been extracted from the two different periodic regions to analyze the different size and shape of the unit cell parameters. For the case of the 2D conglomerate (blue dashed line square in Figure 5.4 c), each unit cell of dimensions 1.65 nm x 1.15 nm and α = 75° hosts one monomer. The new morphology (green dashed line square in Figure 5.4 d) has two monomers per unit cell, with dimensions of 2.20 nm x 1.40 nm and α = 72°. Figure 5.4 e) shows a zoom of the new morphology, where lobes now show a slight modulation of the contrast, which can be induced to avoid the steric interactions of the new organization. In addition to this, the lobes are now grouped in series

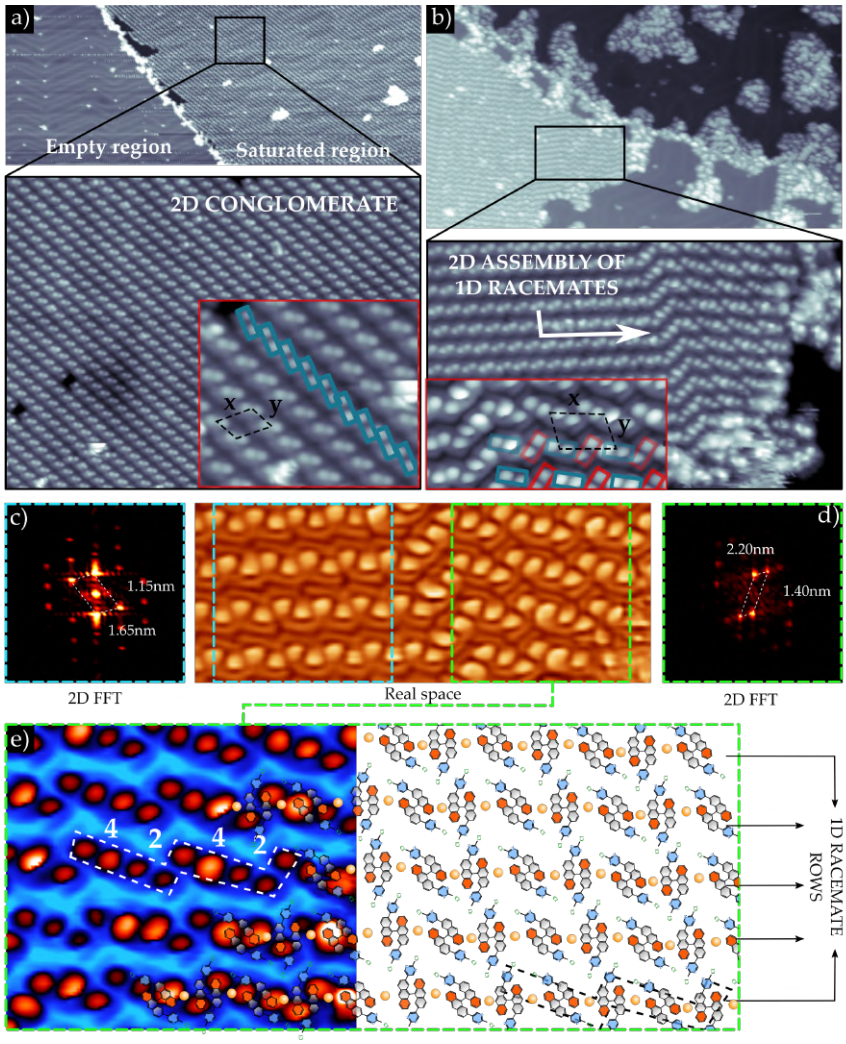

FIGURE 5.4: 2D molecular assemblies: as-deposited versus postannealed. a) STM image of as-deposited molecular precursors at high surface coverage. The zoom shows the 2D assembly corresponds to a 2D conglomerate. b) STM image of molecules after postannealed to 100ºC. The Zoom shows the boundary between a 2D racemate moiety and a 2D assembly of 1D racemates. c)-d) 2D FFT pattern of these two different moieties. e) Zoom STM image of the region framed by green dashed line. The zigzag pattern given by the alternating monomers with different chirality combines 4 or 2 aligned rows, indicated in white dashed lines on the STM image and in black dashed lines in the 2D schematics.

of 4 (dashed, white frame) that form a kinked, zigzag structure which is different from the initial as-deposited 2D conglomerate. We propose this is a consequence of an heterochiral distribution that has happened due to a chiral phase transition of every two monomers in the same molecular island. By overlapping the 2D schematics of monomer **4** with an heterochiral distribution on the STM image, we find the structure of the new domain agrees with a scenario of rows of 1D racemates.

Now the question is what has driven the route towards the chiral phase transition. The scenario of intermixing between different 2D conglomerates by diffusion is very improbable since their size almost saturates terrace regions completely. Under this premise, the new scenario could be an intramolecular chiral phase transition. To make it happen, molecules have to undergo a flip upside down plus a rotation of both bisanthracene subunits, which has been theoretically predicted to be very costly in energy [260], at least in gas phase. Moreover, it has been demonstrated experimentally that chiral molecules belonging to bisanthracene derivatives preserve their enantiomeric conformation upon the different steps of the reaction [159]. As a consequence, we propose that the energetic barrier to overcome this modification can be reduced by the formation of organometallic hybrids. In particular, we propose bonds are formed between the gold surface atoms and the debrominated carbon radical (proposed structures in Figure 5.4 e). This would also explain the similar chiral phase transformation observed for the DP-DBBA on Ag(111) [96].

When heating at 120ºC, molecular islands suffer an even more significant reduction of their size, having their periphery decorated with short and randomly dispersed polymers, as observed in Figure 5.5 a). On the other hand, the molecular units within the island start to experience a planarization [91], as it can be seen in Figure 5.5 b). We speculate that the planarization at this such a low temperature is induced by the presence of chlorine atoms in the molecular structure [91] (it will be further demonstrated via XPS) and promoted by the hindering of the diffusion along the terraces. The formation of organometallic hybrids could also play a role, as proposed in other cases [95]. It is remarkable to notice that this planarization is only promoted in 2D conglomerate domains, where all molecules have the same chirality, and the intra- molecular transformation happens in cascade along the direction along which the molecules are most packed (green arrow in Figure 5.5). The planarization of a single molecule seems to reduce the

barrier for the CDH of adjacent molecules within the same chain but not the ones at adjacent chains. This CDH of individual molecules resembles that found in the CDH wihtin the DBBA polymer chains that lead to 7-AGNRs [261].

At 140ºC, molecules planarize completely forming prochiral islands. Observing the decreasing size of the islands at this step, we suggest that only central molecules, still experience kinetic hindrance, experience planarization. Focusing at the remaining 2D conglomerates, we estimate from the STM contrast that the bromine is not bonded to carbon atoms (indicated with a red arrow in Figure 5.5, and supported by XPS measurements that will be described later). On the other hand, the Cl atoms are still present in the molecule, as shown by the prochiral appearance of the nanographenes in high resolution STM images such as Figure 5.5 and supported also by XPS measurements. It is worth noting that the self-assembled nanographenes, more specifically chloro-pyrimidine annelated ovalenes, contain two oposite zig-zag edges. The stabilization of nanographenes with zig-zag edges is considered a challenge due to the edge reactivity and the consequent tendency for cross-coupling during the surface-assisted formation. We propose this stabilization has been promoted by the low temperature needed to grow this type of nanographenes, which we attain to the presence of the chlorine atoms [91]. At this stage, the ovalenes form a 2D assembly that interacts by the hydrogen bonding with nitrogen atoms along the chain and by C-H···Cl interactions [225] between chains, depicted in Figure 5.5. We discard the formation of Cl···Cl bonds since their axial conformation lead to repulsive interactions [225]. The average distance between the chlorine atom and the two opposite carbon atoms in the meso- positions of the zig-zag edges is approximately 0.4 nm, which is in agreement with previous works [225].

We analyze this new 2D conglomerate and compare it with previous stages. Firstly, by the 2D FTT pattern we determine the unit cell, comprised of one molecule, with dimensions of 1.35 mn X 1.20 nm (Figure 5.6 a-b). The area of this unit cell is bigger than the as-deposited monomer and the 100ºC postannealed phases (all parameters are listed in Table 5.1), which is a consequence of the increasing size of every single molecule upon losing the 3D tilting conformation and planarized into nanographenes.

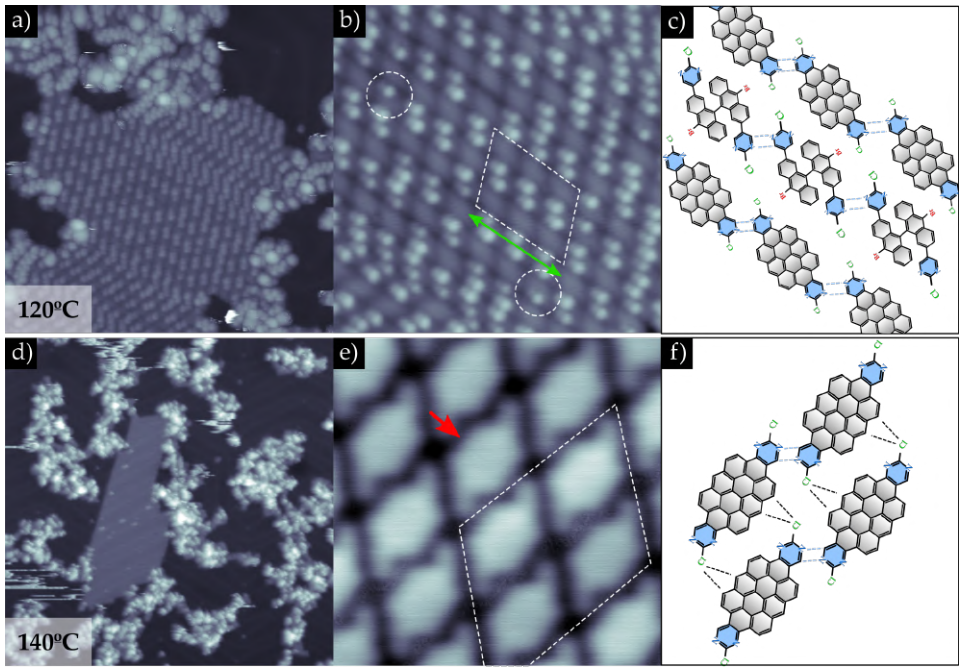

FIGURE 5.5: Postannealing to 120ºC and 140ºC. a) STM overview, b) closeview and c) 2D schematics of the intermolecular interaction of precursor **4** at 120ºC of postannealing. Square with white dashed lines in b) frames the schematics in c); d) STM overview, e) closeview and f) 2D schematics of the nanographene platelets interactions after the molecular precursor **4** undergoes 140ºC of postannealing. Square with white dashed lines of e) frames the schematics depicted in f).

	N*	x (nm)	y (nm)	α	Molecular density**
As-dep RT	1	1.65	1.15	75º	2.00
100ºC	2	2.20	1.40	72º	2.00
140ºC	1	1.35	1.21	65º	1.45

TABLE 5.1: Unit cell dimensions at every reaction step. *N = number of molecules per unit cell; **Molecules per nm^2, considering = $(cos(\alpha) * x * y/Z)^{-1}$

From the 2D conglomerate, we made an approximated estimation of the macroscopic distribution of the islands having as a reference the crystallographic orientations of the Au(111). Although we cannot obtain atomic resolution in these images, the Au(111) lattice orientation was determined by using the herringbone reconstruction (Figure 5.6 c). As a result, molecular rows in the 2D assembly form an angle of approximately $\pm 12^{o}$ with

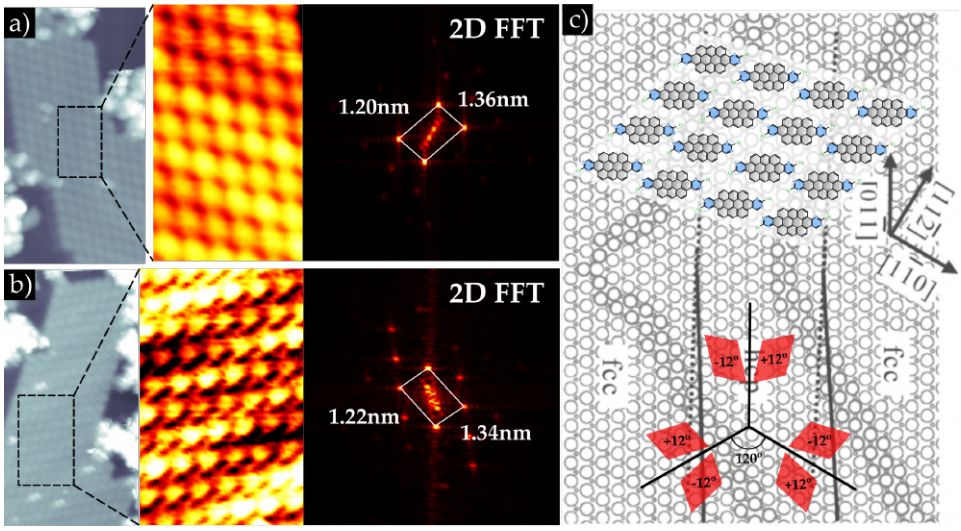

FIGURE 5.6: Organizational chirality in chloro-pyrimidine annelated ovalene arrangements. a)-b) mirror 2D assemblies of nanographenes, with their respective zoom and 2D FFT pattern. c) 2D schematic representation of one molecular arrangement (top) and the subsequent three-fold double mirror 2D assemblies (bottom), orientated with respect to the [0, 1, -1] main axis of the Au(111) substrate.

the [1 -1 0] main axis and replicate in a mirror-like tendency along the three main directions of the Au(111) surface. This demonstrates that the prochirality of the single nanographenes has been imprinted to the prochiral nanographene islands, as was also described in Chapter 3.

In a final step, postannealing temperature was elevated 10º degrees more to 150ºC, which promoted the covalent interconnection of ovalenes into 1D nanographene chains. We presume it happens due to an Ullmann coupling reaction of already cleaved C-Cl bonds. This would confirm that the ovalenes had the chlorine atoms still bonded to the carbon core at the previous annealing step at 140ºC. The connection into chains, depicted in Figure 5.7 takes place 150ºC below the Ullmann coupling to grow the nitrogen-doped NPG using the same precursor (described in Chapter 3). We suggest this low temperature limits the covalent connection between nanographenes only by the C-Cl sites, minimizing for instance, a HCl zipping with the zig-zag edges. Yet, some non-selective coupling seems to occur, based on the meandering, interconnected morphology of the chains.

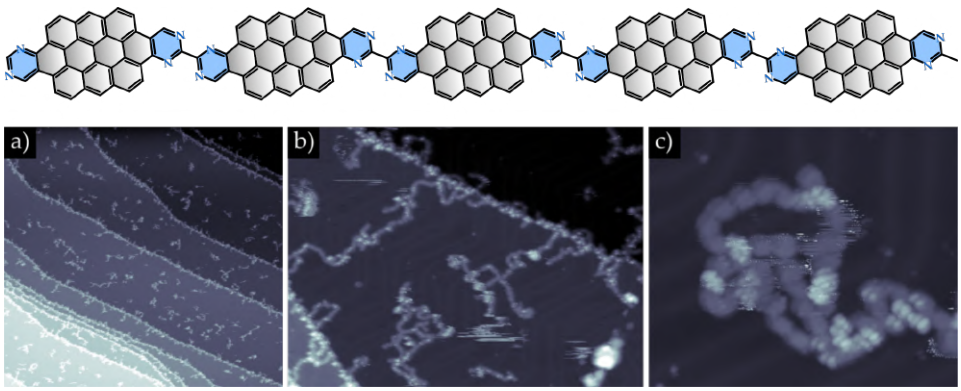

FIGURE 5.7: Nanographenes after postannealing at 150ºC. a) STM overview image; b) a closer view at one of these terraces shows the connection among the nanographenes and c) STM closer view of the nanographene chains. Top scheme represents a chain formed by five connected nangraphenes.

As a summary (Figure 5.8), we interpret that the racemic mixture deposited at room temperature segregates on the Au(111) surface into 2D conglomerates due to enantioselective interactions. Upon annealing to 100ºC (T1), some of these regions undergo a chiral phase transition into a 2D assembly of 1D racemate chains, which we propose that it is formed by the conformational chiral switch of every two molecules. Under annealing to T2, those molecular arrangements forming the 1D racemate rows are unstable and aggregate into amorphous cluster, while the 2D conglomerates undergo intra- molecular cyclodehydrogenation and form the 0D ovalene nanographenes. The last step, that takes place at a temperature T3, involves the connection of the planar nanographenes by their chlorine atoms to grow 1D chains.

In order to complement the STM analysis we have performed XPS, where we have tracked C 1s, Br 3d, Cl 2p and N 1s XPS core level spectra, presented in Figure 5.9. We compare it with the results obtained to grow the N-doped NPG and identify the hints needed in order to distinguish which of the two reaction paths is taking place.

RT spectra provides the starting point: Br 3d and Cl 2p split into the spin-orbit coupling components: Br 3d $_{3/2}$ and Br 3d $_{5/2}$ at 70.9 eV and 69.9 eV respectively [119, 218], and Cl 2p $_{1/2}$ and Cl 2p $_{3/2}$ at 201.8 eV and 200.2 eV respectively [226]; and N 1s at 399.3 eV [27, 262]. For the case of the C

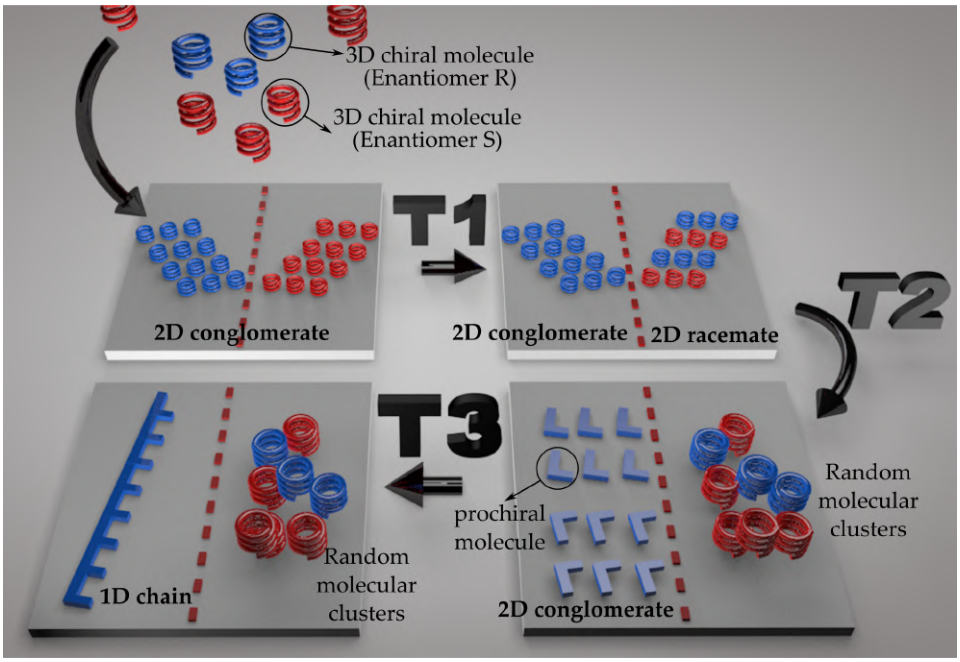

FIGURE 5.8: 3D schematic representation of the surface-assisted synthesis of chloro-pyrimidine annelated ovalenes.

1s peak, we consider the ensemble of carbon environments: $C[C_2H]/C[C_3]$, $C[C_2Br]$, $C[CNH]/C[N_2H]$, $C[N_2Cl]$ with the stoichiometry 28 : 2 : 4 : 2 and the binding energies 284.47 eV, 285.0 eV, 285.7 eV and 287.3 eV respectively. Comparison of these BE values with those obtained from the literature indicate that the molecules remain intact upon deposition on Au(111).

At 100ºC, where we expect to have the chiral phase transition, around the 70% of the molecules are still brominated, no dechlorination takes place and the N 1s peaks are almost not shifted. We estimate, as far as we have been able to check in the STM images, that the other 30%, present as Br-Au bond component, is related to the racemic phase that might be formed by organometallic interactions between a debrominated radical carbon atom and one gold atom uplifted from the surface. This would explain the slight shift of 0.1 eV of the C-H/C-C component at this temperature. Besides, Cl 2p and N 1s spectra preserve the area during the annealing to 100ºC, confirming that the molecule preserves the chloro-pyrimidine functional groups.

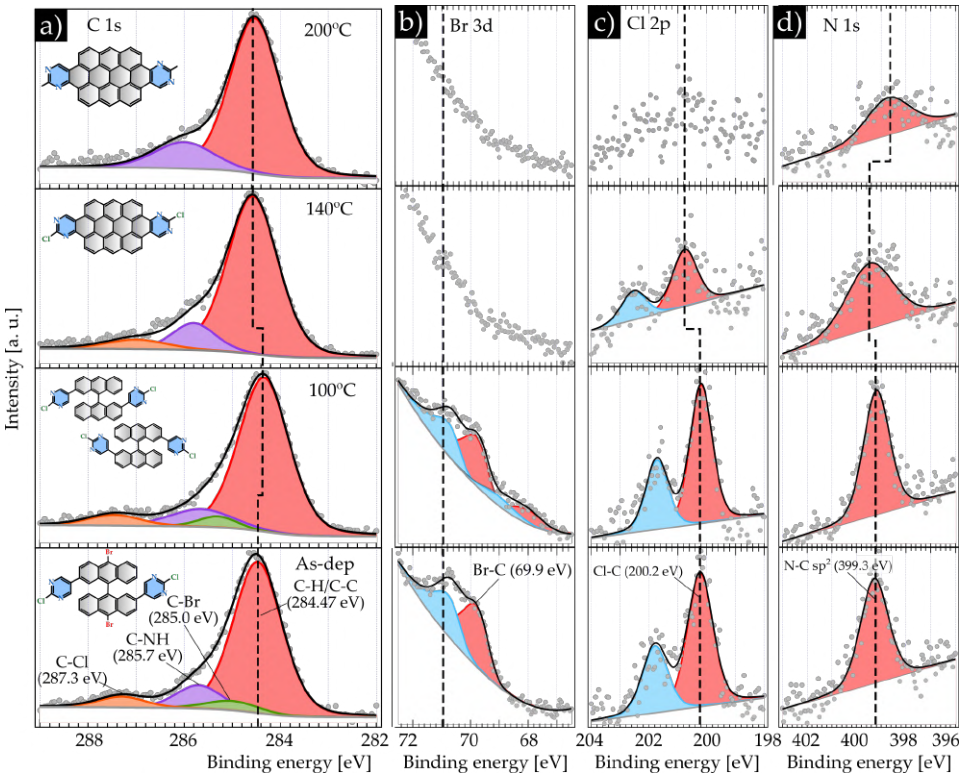

FIGURE 5.9: XPS analysis of the monomer **4** deposited on Au(111) at room temperature and higher surface coverages. a) 2D schematics of the on-surface reactions happening when the monomer **4** is deposited on the metallic surface at RT and high coverages. b)-e) C 1s, Br 3d, Cl 2p and N 1s core level spectra at RT, 100ºC, 140ºC and 200ºC of postannealing.

At 140ºC all Br 3d components vanish after annealing, in contrast to that found in the reaction path that leads to GNRs/NPGs (discussed in Chapter 3). Same as other examples in literature [89], we correlate the absence of the Br signal to the hydrogenative desorption of Br, which is in turn a fingerprint of the onset of the cyclodehydrogenations that planarized the monomers. The residual hydrogen is also expected to passivate the debrominated radical carbon atom at the zig-zag edges, which is crucial for the stability of nanographenes.

The C-H/C-C component of the C 1s core level spectrum shifts back by

0.20 eV at this step, a consequence of the Br desorption. The stoichiometry of all the components is C-H/C-C : C-NH : C-Cl = 30 : 4 : 2.

Regarding the Cl 2p doublet, we observe a decrease to the 60% at this temperature, showing that the majority of the planarized monomers are still chlorinated at this temperature, confirming the proposed 2D schematic representation of planar and chlorinated nanographenes of Figure 5.5 e) and f). The lack of Cl-Au component indicates that the cleaved Cl, the other 40%, directly desorbs, as expected when residual hydrogen is available. This estimation has been made considering that, during the cyclodehydrogenation, each molecule cleaves out eight hydrogen atoms: two of them bond to bromine and desorb in the form of HBr, other two passivate the radical carbon, leaving four additional hydrogen atoms on the surface which could be binding to chlorine. At this point of the reaction, the Cl 2p doublet suffers a shift of 0.5 eV towards higher energies upon nanographene formation. This shift, not observed for precursor **4** during GNR/NPG formation, could be related to the reduced screening due to the decrease of the Cl-Au interaction upon planarization.

Finally, at 200ºC the remaining Cl signal totally vanishes, meaning that all molecules are dechlorinated and Cl has desorbed from the surface. This is in agreement with the 1D nanographene chains observed in the STM images above 150ºC, as shown in Figure 5.7. The C-H/C-C component of the C 1s core level spectrum does not shift at this step, indicating there has not been a change in the value of the workfunction upon chlorine cleavage, confirming there is no adsorption of the halogen atom in the gold surface. At this temperature, considering the formation of nanographene chains, the stoichiometry considered is C-H/C-C : C-NH = 30 : 6.

Interestingly, the shift of the C 1s main peak differs from those observed for the formation of N-doped GNR/NPG (Figure 5.10). A shift of 0.4 eV and 0.3 eV is present when comparing the peaks after undergoing a postannealing to 140ºC and 200ºC. This is related to the change in the work function of the Au(111) when the bromine atoms adsorb on the surface [137], that take place at lower temperatures for the case of the nanographenes.

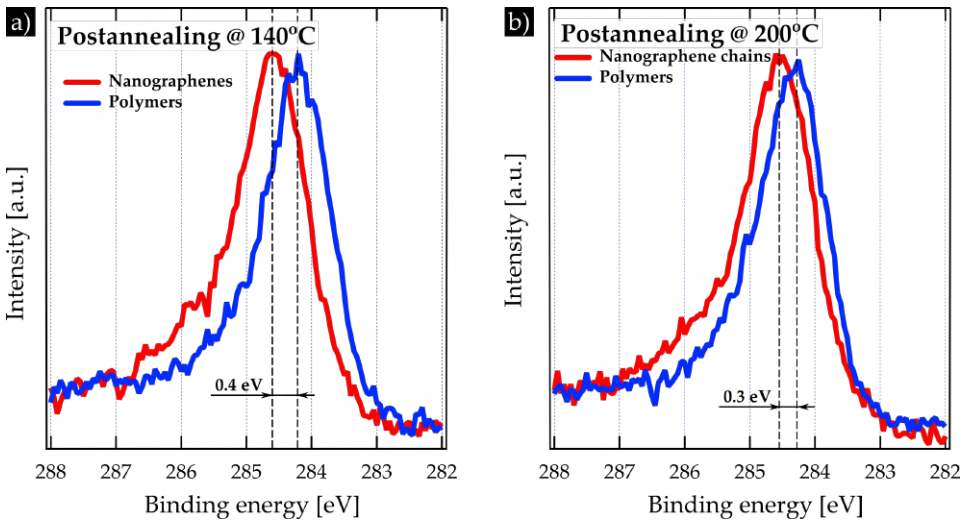

FIGURE 5.10: C 1s XPS core level spectra comparison between the reaction pathway A (route towards the synthesis of nitrogen-doped nanoporous graphene) and reaction pathway B (route towards the synthesis of nitrogen-doped nanographene platelets) at a) 140ºC and b) 200ºC of postannealing.

These results are in clear contrast to that obtained in the formation of N-doped GNR/NPG. The most representative differences can be seen for the Cl 2p and the Br 3d (Br-Au) doublets (Figure 5.11). The Cl 2p area keeps constant upon annealing for the synthesis of the N-NPG up to 200ºC, whereas its area becomes 0 at 200ºC for the synthesis of N-doped nanographenes. Furthermore, the Br-Au component is present in the synthesis of the N-NPG up to 200ºC of postannealing. On the contrary, the signal is much lower for the synthesis of the nanographenes. With these results we have demonstrated we can track with XPS the differences between the two reactions.

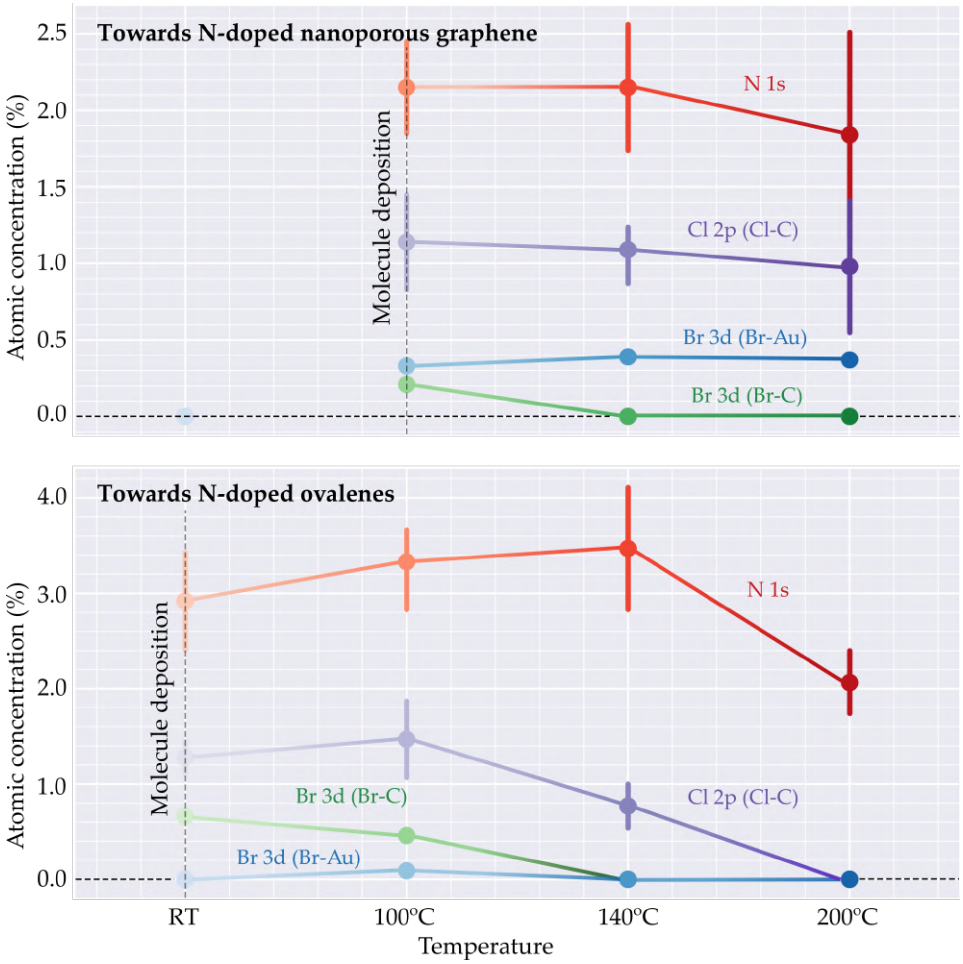

FIGURE 5.11: Atomic concentration of the chemical species N 1s, Cl 2p (Cl-C), Br 3d (Br-C and Br-Au) upon N-doped nanoporous graphene formation (left) or N-doped ovalene formation (right). The errors bars have been taken from the standard deviations of the Tables in the Appendix A.

As a summary, Figure 5.12 shows the temperature onsets and thermal windows for every step of the reactions from the results obtained with STM and XPS. Initially, from the deposition of the precursors at room temperature (25ºC) until the first performed annealing to 100ºC, we assume they do not change their conformation (indicated as "monomer" in Figure 5.12). We consider the postannealing to 100ºC is the onset for the debromination and the chiral phase transition. Then, there is presumably a thermal window

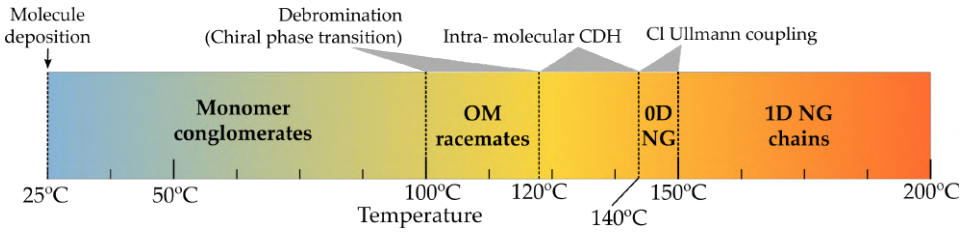

FIGURE 5.12: Temperatures and thermal windows for the synthesis of N-doped nanographene chains

of 20ºC (between 100ºC and 120ºC) where the homochiral 2D conglomerates colive with and the heterochiral 1D racemate rows. We identify the postannealing to 120ºC as the onset for the intra- molecular cyclodehydrogenation (CDH in Figure 5.12), where the precursors start to planarize. This step. Finally, postannealing to 150ºC is, as demonstrated by both STM and XPS, the onset for the dechlorination and formation of nanographene chains.

5.2 Conclusions and future perspectives

In this Chapter we have systematically studied the on-surface formation of a specific type of nanographene: a chloro-pyrimidine annelated ovalene exhibiting two parallel zigzag edges. We have been able to find the specific surface conditions to favour this kinetic reaction pathway versus the thermodynamic route towards N-doped NPG. We claim the factor to hinder the polymerization needed to lead to the N-doped GNRs and NPG is the formation of a condensed, saturated phase where the lack of diffusion and configurational degree of freedom, together with intermolecular reactions, seem to promote CDH at the same energy window of debromination, passivating the carbon radicals before the Ullmann coupling can take place.

We compare this reaction pathway in Figure 5.13 with the formation of nitrogen doped GNR and NPG by STM images and XPS spectra. This schematic summary clearly shows how the CDH is anticipated in the case of the high coverage system, and how it coexists in temperature window with the debromination. Likewise, we evidenced an earlier dechlorination (150ºC below) in these nanographenes as compared to the N-doped NPG, well below the dehydrogenative cross-coupling temperature, which

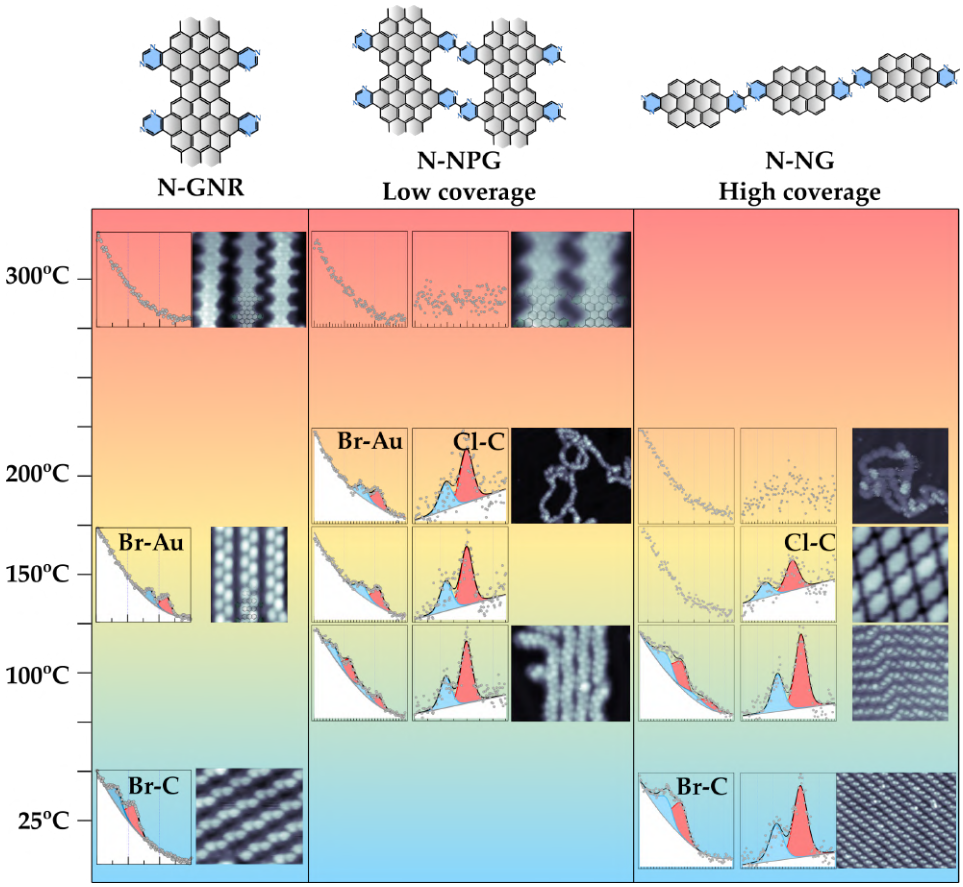

FIGURE 5.13: 2D temperature diagram to compare the three on-surface reaction pathways described in the Chapters 3 and 5. X axis shows, from left to right, reaction mechanism to grow through a bottom-up strategy: 1D nitrogen-doped graphene nanoribbons (N-GNR), 2D nitrogen-doped graphene nanopores (N-NPG) and 0D nitrogen-doped nanographenes (N-NG). Y axis indicate increasing temperatures from room temperature (25ºC) to 300ºC. At each temperature, STM image is shown combined with the respective XPS plot.

is crucial for a selective coupling and the formation of nanographene chains.

As far as we are concerned, periacene derivatives show open shell character depending on their size [263]. 2-periacene (perylene) and 3-periacene (bisanthene, which also includes our annelated ovalene) have shown to prefer the Kekulé structure as the most stable electronic configuration, whereas for 4-periacenes (peritetracene) and 5-periacenes (peripentacene) the most

stable configuration is the biradical one, showing antiferromagnetic inelastic excitations when performing measurements via STS. We envision this strategy to grow chains of periacenes at low temperature can be exploited for those systems showing an open shell character [59, 62].

Structurally, we have performed an analysis on the chiral dependent interactions towards the synthesis of the planar nanographenes. First, the chiral recognition among the as-deposited precursors leads to the formation of islands of the same enantiomer. Secondly, the large molecular 2D assemblies inhibit the Ullmann polymerization and partially undergo a chiral phase reaction of presumably organometallic hybrids. Finally, those moieties which did not experience the chiral phase transition planarize into 0D nanographenes and covalently connect after losing the chlorine atoms into 1D nanographene chains. Future ongoing work would be to sublimate on surface only one type of enantiomer [159], and confirm if the chiral phase transition still takes place.

Chapter 6

Post-synthesis transformation of graphene nanoribbons

Introduction

Once graphene nanoribbons have been grown on a metallic substrate, further on-surface reactions can take place if they are annealed at the last step of their formation. The induced a-posteriori structural transformations entail in many cases a degradation of the ribbon structure, but if done in a controlled way, it can also be a strategy to obtain GNR structures that are otherwise difficult to achieve.

GNR with functional moieties are particularly prone to be subjected to internal transformations (Figure 6.1). When annealing to temperatures around or above the formation of GNRs, the moieties can cleave [196, 209, 210] (Figure 6.1 b-c) or undergo a structural or chemical transformation [144, 145] (Figure 6.1 a-b). A common characteristic of these systems is that there is no control on the specific cleavage along the ribbon backbone, and generally systems with combined components in a random manner are observed. This leads to abrupt local changes of the electronic properties [145].

In this Chapter we analyze intra-ribbon edge transformations that lead to different types of ribbon structures that are beyond conventional GNRs (armchair, zigzag, chiral, chevron,etc). In the first strategy, illustrated in Figure 6.2 a) and b) , the N-doped 7-13 AGNR is overannealed undergoing a partial or total cleavage of the pyrimidine annelated moieties and giving rise to an undoped 7-9 AGNR (Figure 6.2 a) or a half doped 7-11 AGNR. This will depend, as already observed in Chapters 3 and 4 on whether they

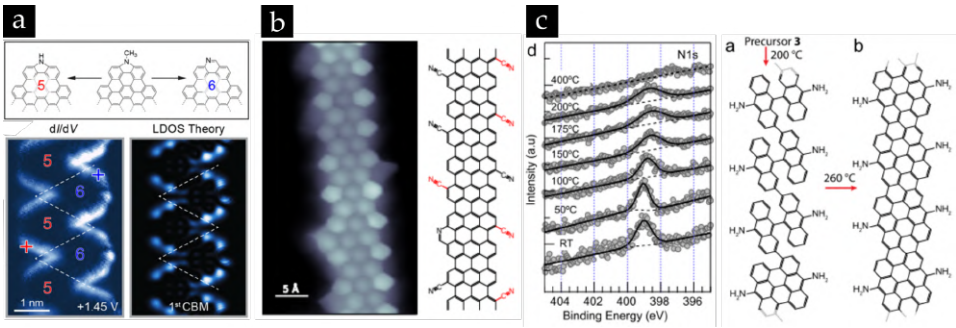

FIGURE 6.1: Examples in literature of graphene nanoribbon transformations. a) A methyl-pyrrole functionalized molecular precursor is transformed in either a carbazole or a phenanthridine group. Images taken from Ref. [145]. b) CN- functionalized 7-AGNR: the CN groups are cleaved our transformed into pyridine groups. Image taken from Ref. [196]. c) Amino-functionalized chiral GNR gradually lose NH_2- groups upon postannealing towards GNR formation and beyond [209].

feature hydrogen or chlorine atoms at the extremes of their pyrimidine rings.

We benefit from these on-surface reactions to modify the GNRs superlattices characteristics. It has been recently demonstrated that graphene nanoribbons composed of alternating GNR components of different widths into a 1D superlattice can generate frontier electronic bands with tunable band gap as a function of the periodicity and length of these components [74–79, 264, 265]. The key factor to create these in-gap bands is that the GNR components belong to different topological phases.

We propose a second strategy, illustrated in Figure 6.2 c), that demonstrates how overannealing a phenylated 7-13 AGNR leads to the migration of the phenyl and C-C ring closure with a neighbour one to form annulene nanopores at the edges of the ribbon. We succeeded on inducing this type of reaction at high yield by orienting the ribbons along the steps of a vicinal Au(111) surface.

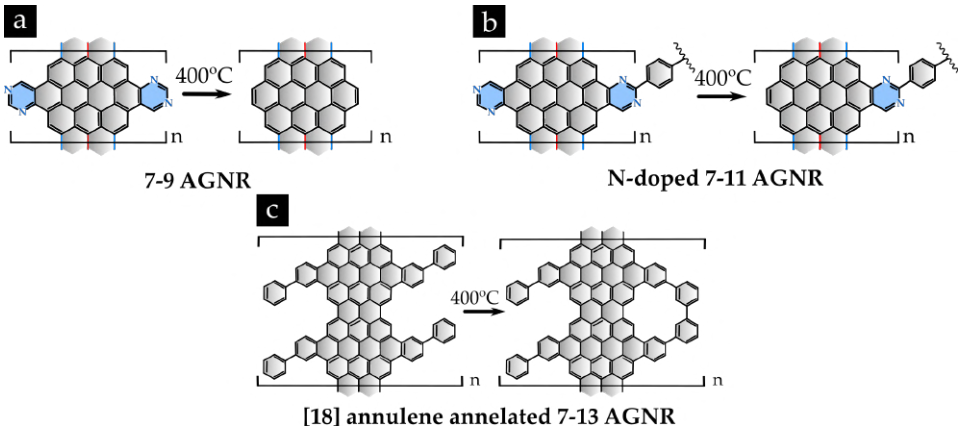

FIGURE 6.2: Introduction of the intra-ribbon transformations studied in this Chapter. a) Formation of an undoped 7-9 AGNR after total cleavage of the pyrimidine groups in the N-doped 7-13 AGNR. b) Formation of an asymmetric N-doped 7-11 AGNR after the partial cleavage of the pyrimidine groups only at one side of the ribbon. c) Formation of annulene groups in phenyl-decorated 7-13 AGNR.

6.1 Controlling partial or total cleavage of N-doped 7-13 AGNRs

Figure 6.3 displays the sequential degradation of the pyrimidine rings in N-doped 7-13 AGNRs by both STM and XPS. At 300ºC of postannealing (Figure 6.3 a), lateral extensions corresponding to the pyrimidine rings can be noticed, as already demonstrated in Chapter 3. When annealed towards 350ºC (Figure 6.3 b), these groups partially cleave (indicated with red arrows in Figure 6.3 b), most probably into cyano (CN-) groups to form CN-functionalized 7-AGNR [196]. At temperatures between 350ºC and 400ºC (Figure 6.3 c-e), we achieve a complete cleavage of all these nitrogen-containing moieties. At this temperature, since there is not a specific signal at the edges coming from the mentioned functional groups, neither localized radicals, we propose the surrounding hydrogen has passivated the carbon radical at the cleaving sites.

In Figure 6.3 d) we see the evolution of the N 1s core level peak tracked by XPS as a function of the postannealing temperature. For clarity, the Gaussian-like fit of the peak is obtained by using a linear background and the latter is extracted to better notice the variation of the XPS signal. After 300ºC of postannealing, the area of the N 1s component is preserved,

although the peak slightly broadens from a FWHM of 1.4 to 1.7 eV, most probably due to the internal transformation from the pyrimidine to the cyano functional groups, plus remaining HCN molecules cleaved out of the GNR. At 400ºC of postannealing, the N 1s peak experiences a decrease of the 30 %. We attribute the partial persistence of the pyrimidine N 1s component to two different mechanisms: i) the protection of this group by the inter-ribbon coupling, as shown in Figure 6.3 e). Here covalently coupled GNRs still show some irregular bridges that should be formed by the N-doped functional groups. ii) A minor contribution of N may also arise from the residual HCN molecules, cyano groups or itself transformed into pyridine rings by nitrile cycloisomerization, as proposed for the case of other cyano-functionalized GNRs [196].

We propose a reaction mechanism that explains the cleavage of the pyrimidine groups (Figure 6.4), passing from an intermediate product that we presume it is a cyano group (CN-functionalized 7-9 AGNR in Figure 6.4) [196]. In this scenario, at temperatures between 300ºC and 350ºC the C-H bonds of the pyrimidine rings, surrounded by a more labile C-N environment, are activated by the catalytic surface (step **I**). The radical sigma bonds promote the scission of the C-N bonds (step **II**), and a subsequent oxidation gives rise to the cyano group, while the other component of the ring totally leaves the ribbon as a HCN group, leaving a radical C at the edge that is passivated with residual hydrogen (step **III**). Subsequently, the remaining cyano group is also cleaved leaving a second radical carbon atom that is also passivated (step **IV**). We note that each cleavage step produces the hydrogen needed for passivation.

If the doped ribbon is connected by both lateral sides, then it becomes a hybrid NPG, explained previously in Chapter 4. However, if the protecting ribbon is bonded to only one side, it leads to an asymmetric system where one side is fully decorated with pyrimidine annelated rings whereas the opposite side is totally cleaved. The protection of the fused pyrimidine edges in N-doped 7-13 AGNRs by the lateral coupling of undoped GNRs has been demonstrated by using the molecular precursor **4** since, as explained in Chapter 3 and 4, adding chlorine atoms at the extremes of the pyrimidine rings that favours the lateral coupling before their cleavage. The coupling has been induced with the same N-doped AGNR and the undoped 7-13 AGNR. The latter case is represented in Figure 6.5 a), where a long nitrogen doped ribbon exhibit regions with pyrimidine groups fully

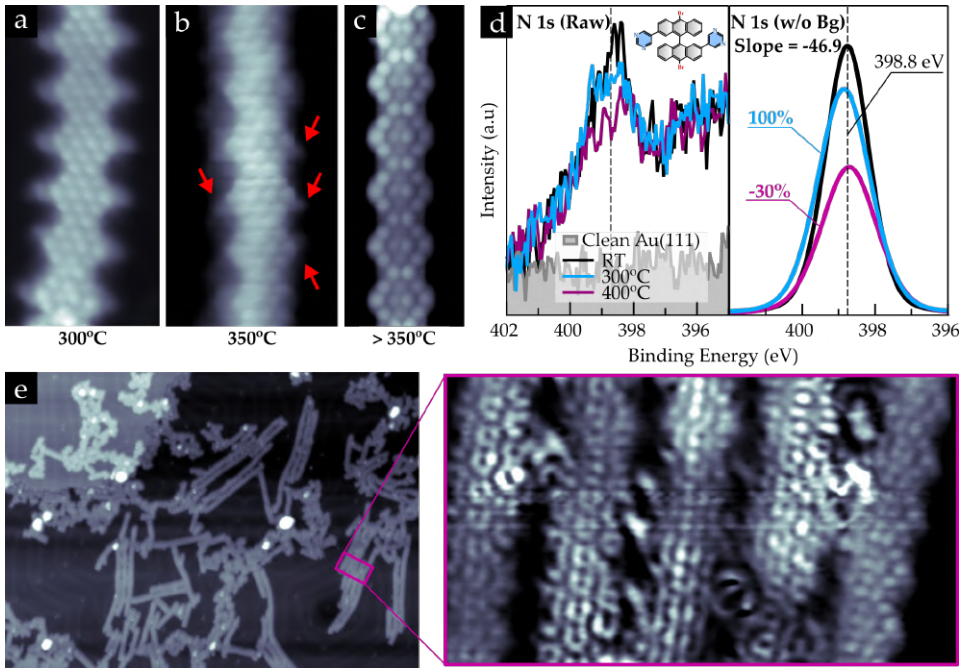

FIGURE 6.3: Cleavage of pyrimidine groups. a)-c) BR-STM images of an as-grown N-doped 7-13 AGNR after 300ºC of postannealing (a), 350ºC of postannealing (b) and 400ºC of postannealing (c). Red arrows in b) point partially degraded pyrimidine rings. d) N 1s XPS core level spectra raw data (left) and fitted without background (right), at different stages: before molecule deposition (grey), as-deposited (black), and after 300ºC and 400ºC of postannealing (blue and magenta respectively). e) Overview STM image of a sample after 400ºC of postannealing, and a zoom into a bunch of five interacting ribbons, showing degraded functional groups.

protected at both edges (lower part of the image) or a single edge (upper part of the image). To prove that the part of the ribbon that is not protected has lost the pyrimidine groups, we performed BR-STM imaging, as it can be seen in Figure 6.5 b). The image clearly shows bridges where pyrimidine rings are intact, and exposed edges that are totally cleaved, forming an asymmetrically N-doped 7-11 AGNR structure.

As a consequence, we demonstrate to be able to control the transformation of the 7-13 AGNR superlattice into either the half doped 7-11 AGNR or the fully undoped 7-9 AGNR superlattices depending on the characteristics

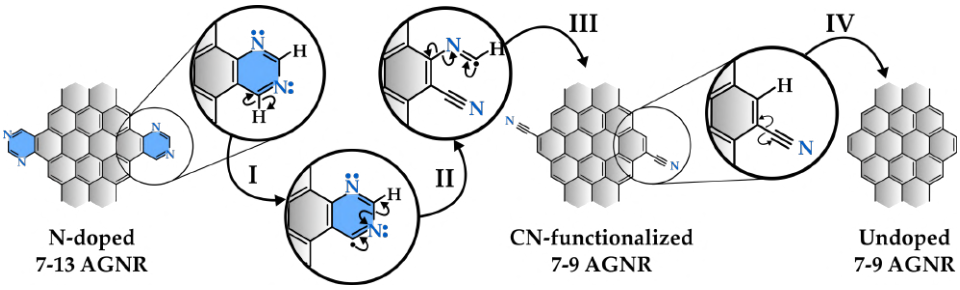

FIGURE 6.4: a) Reaction mechanism from the molecular precursor **3**, to the nitrogen-doped 7-13 AGNR, passing by the CN-functionalized 7-9 AGNR intermediate product from a partial cleavage of the pyrimidine ring, to end up with an undoped 7-9 AGNR.

of the molecular precursors. In the next sections, how these internal transformations affect the electronic properties of the ribbons will be studied.

6.2 Electronic properties of the series 7-9, 7-11 and 7-13 AGNRs

The electronic properties of the series of doped and undoped 7-13 AGNR, asymmetrically-doped 7-11 AGNR and undoped 7-9 AGNR have been studied by means of STS, DFT and tight binding (TB) approximations. The analysis has been divided in two subsections: the first one is devoted to the analysis of the electronic properties as a function of the doping level. The second is focused on the 1D superlattie of heterojunctions between different ribbon width, as they may host half-filled states at the interface.

6.2.1 Evolution as a function of structural transformations

Figure 6.6 shows the electronic properties of AGNR superlattices as a function of their doping content. Undoped 7-13 AGNR (red spectrum in Figure 6.6 a) shows its CBM as an onset at 1.0 eV whereas its VBM is pinned to the Fermi level of the Au(111) [230] at -0.25 eV [266], revealing and experimental absolute value of the band gap of 1.25 eV (The respective VBM/CBM conductance maps are shown in Chapter 4, Figure 4.5). The slight difference of the absolute value of the band gap as compared to the recently reported NPG [118] is due to the point where the CBM has been considered: in

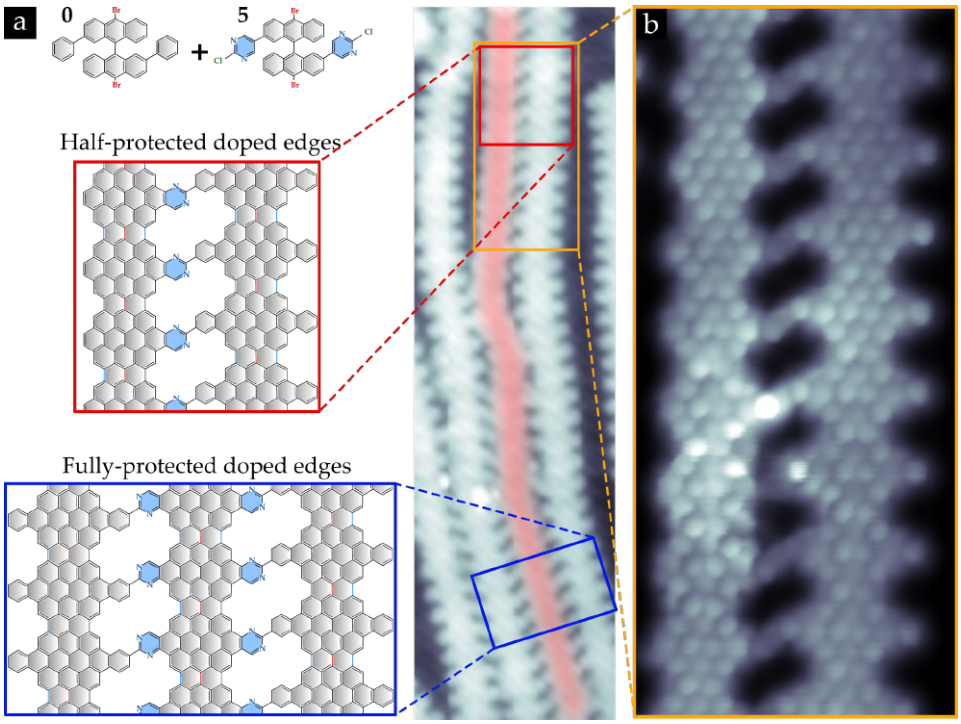

FIGURE 6.5: Lateral protection of the pyrimidine group by coupling to 7-13 AGNR. a) STM image of a N- doped ribbon coupled to two protecting pristine 7-13 graphene nanoribbons. Half and fully protected doped edges have been highlighted with red and blue squares respectively, and the 2D schematics have been added to the left. b) BR-STM image of the region of half-protected doped edges, resolves the edge and bridge structures of the asymmetric undoped 7-11 AGNR.

the recent report it was set at the threshold of the CBM, whereas in this work we set it at the maximum of the CBM. Although the spectrum has been obtained from a connected ribbon, we do not expect any band gap reduction due to delocalization in the connected GNRs (detailed in Chapter 4).

When the 7-13 AGNR contains four nitrogen atom per unit cell (blue-purple spectra in Figure 6.6 a), bands downshift 0.20 eV and 0.40 eV, also demonstrated in Chapters 3 and 4. In this particular case, two spectra obtained at different positions have been overlapped to maximize the VBM and CBM in each case.

The VBM and CBM for the asymmetric N-doped 7-11 AGNR are found

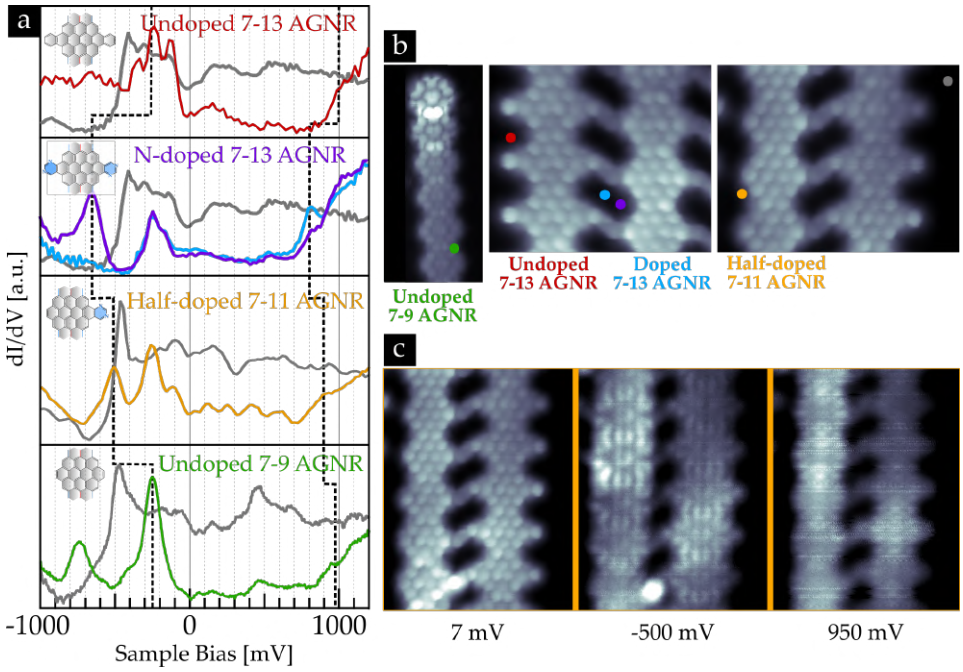

FIGURE 6.6: a) dI/dV spectra of: undoped 7-13 AGNR (red) ; doped 7-13 AGNR (overlapped blue and purple); half-doped 7-11 AGNR (yellow) and undoped 8-UC 7-9 AGNR (green). Each spectrum has its Au(111) reference signal in grey, and an inset with the unit cell of the specific system. b) BR-STM images of each system, with a dot of the same color at the exact location where the dI/dV spectra have been acquired. c) BR-STM images of the asymmetric N-doped 7-11 AGNR coupled to a undoped 7-13 AGNR: at mid-gap (7 mV), at the VBM (-500 mV) and at the CBM (950 mV).

at -0.5 V and 0.9 V respectively, consistent to the wavefunction patterns of the conductance maps shown in Figure 6.6 c). This results in corresponding shifts of 0.25 eV and 0.1 eV to lower energies, around half the value of that found in the fully doped GNR, and consistent with the fact that the number of nitrogen atoms per unit cells has been reduced to two instead of four [69]. Locally, the dI/dV spectrum in this specific case has been taken opposite to the doped site, confirming the non-local effects of the dopant [209].

Finally, the position of the VBM and CBM are restored in the spectrum of the fully cleaved structure, the 8-Unit Cell (8-UC) 7-9 AGNR (green spectrum in Figure 6.6 a). The measured band gap of 1.25 eV is the same as for the 7-13 AGNR, but we anticipate that this is a coincidence related to the

	Band gap	Reference
7 AGNR	2.37 eV	[170]
9 AGNR	1.40 eV	[266]
13 AGNR	1.40 eV	[267]
7-9 AGNR (INF/QD)	0.75/1.25 eV *	This work
7-13 AGNR	1.25 eV	This work

TABLE 6.1: Experimental absolute value of the electronic band gap for several armchair graphene nanoribbons which are in the family of 7, 9 and 13 carbon atom wide. 7-9 AGNR band gap has been experimentally observed by means of STS (QD), while for the infinite system (INF) an experimental value has been estimated from the DFT calculations (GGA-PBE functional, 0.73 eV for the infinite system and 0.47 for the finite one).

widening of the band gap of the 8-UC 7-9 AGNR due to quantization effects. We estimate, from the theoretical calculations and the experimental value of the finite ("QD" in Table 6.1) system, that the experimental band gap of the infinite 7-9 AGNR ("INF" in Table 6.1) should be around 0.75 eV. This will be described deeper in the following section.

As summary, the main findings ia that the doping does not alter the band gap and rigidly shifts down the bands proportionally with the doping density. We note that, as it is listed in Table 6.1 that the band gaps of the superlattices are smaller than the respective components. The origin of this reduction is related to the topology of the superlattices, and it will be explained in the following.

6.2.2 The topological origin of the band structure of GNRs

The series of ribbons studied in this Chapter have one characteristic in common: they possess alternating GNR segments of different width, generating a 1D superlattice of interfaces. These type of geometries have been elucidated to be a strategy for material engineering with atomic precision in graphene nanoribbons [75–77], apart from the control on their width, shape, and already described doping. It has been foreseen that depending on the topological phase associated to each of these components in the superlattice, the system can generate a 1D chain of half-filled states, which has potential interest as a band engineering strategy [75, 76], or the presence

of topological superconductivity for quantum computing.

In the following, we will demonstrate that internal selective transformations of GNRs by undergoing an over annealing is a strategy to modify the characteristics of their topological in-gap bands. This study has been performed experimentally by STS, complemented with tight binding calculations carried out with the program 'Quantum-lattice' developed by J. Lado (Aaldo University) and SISL library in python [188], developed by N.Papior (DTU, Technical University of Denmark). P. Febrer and M. Pruneda have carried out the DFT calculations.

Experimentally, we perform a series of constant current dI/dV spectra along the edge of the finite 8-unit-cell (8-UC) 7-9 AGNR with a 9th unit covalently connected to another oligomer by the terminus (Figure 6.7 a-d). Reference dI/dV spectrum in Au(111) has been performed prior to this experiment in order to guarantee a featureless metallic character of the tip (grey plot in Figure 6.7 g).

In the explored energy range we can identify signatures coming from the VBM and CBM. The bands appear split at discrete energy levels with the characteristic spatial modulations that correspond to quantum well states [268]. The modulation due to quantization is superimposed to another modulation that arises from the superlattice nature of the ribbon structure. The quantum well states are clearer for the VB, where the n=1-3 levels can be identified. The less clear modulation of the quantized states in the CB can be due to the energy hybridization with the metallic substrate plus the modulation of the ribbon structure.

Another important characteristic is the presence of localized states at the ribbon termination, labelled as **ES1** and **ES2**. The existence of such localized states is related to the topology of the ribbon's electronic structure, as it will be explained later. A-priori, these states should appear half-filled, degenerated at the Fermi level, although the p-type doping induced by the substrate can deplete the state and shift them above the Fermi level. The breaking of the degeneracy can be a consequence of interactions between the two end states [268]. However, DFT calculations of a 7-9 AGNR segment of the same length of 8-UC show two degenerate end states at the Fermi level, indicating that the ribbon is long enough to avoid interactions between the two terminations. This is consistent with other observations

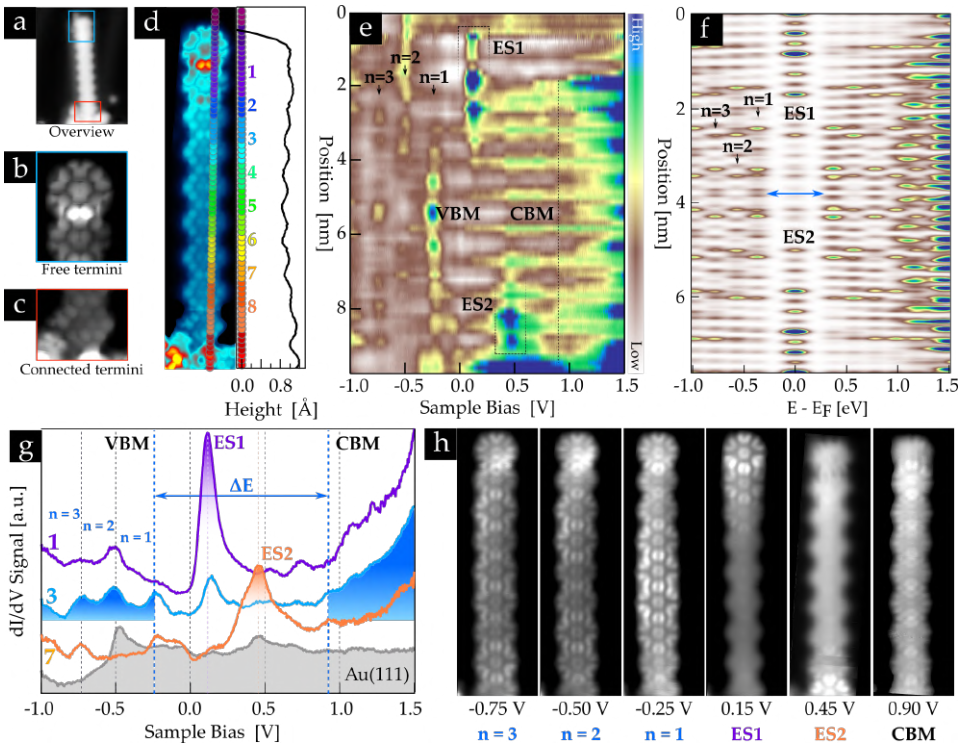

FIGURE 6.7: Electronic properties of a finite 8-UC 7-9 AGNR. a) STM scan overview of the GNR under study. b) BR-STM image of the GNR free termination. c) BR-STM image of the GNR connected termination. d) BR-STM image of the entire ribbon, with a 70-point line superimposed. e) Color plot of 70-point dI/dV constant height spectra taken along the line depicted in d). f) DFT PDOS 2D color map of a finite 8-UC 7-9 AGNR. g) dI/dV spectra at the 1st, 3rd and 7th bay of the finite 7-9 AGNR, indicating the VBM/CBM, the quantized states n = 1-3 and the end states **ES1** and **ES2**. h) Constant height conduction maps at the energy levels of interest.

where ribbons with similar band gap exhibit degenerate end states for this length. As a consequence, we attribute the splitting to a second mechanism: the asymmetric chemical environment of the two termini, which can split or even quench end states at terminations that are connected to other structures or molecular species [269]. Indeed, bond-resolved images show very different terminations, where the one hosting the **ES1** seems to be a free terminus passivated with H atoms [270, 271], whereas the one hosting **ES2** is connected to an unknown carbonaceous oligomer.

Before unveiling the origin of the end states **E1** and **E2**, a brief introduction to topology in the electronic structure of graphene nanoribbons is required.

What does topology mean?

Topology is the field of mathematics that studies geometrical properties of objects that are insensitive to smooth transformations (they can be transformed into another in a continuous way). In particular, in condensed matter physics two systems are considered of the same topology if their Hamiltonians are equivalent (they remain the same under an applied transformation).

More specifically, for semiconductor 1D systems, we can say they are topologically equivalent if their Hamiltonian can be transformed by keeping it semiconducting in the transformation process (without closing the gap, i.e. without making it metallic at some point). The topological character of the semiconductor 1D systems is characterized by the Zak phase or Berry phase [272], which will determine the symmetry-protected topological (SPT) character. A more direct way of calculating the SPT is by the $\mathbb{Z}_2$ invariant, which can acquire as values the integers 0 or 1 (called topologically trivial or non trivial insulator respectively), determined by the spatial symmetries of the systems [74]. The interface of semiconductors with different topological phase (different invariant $\mathbb{Z}_2$) and the lack of topological continuity implies the existence of metallic localized states at the junction, known sa the bulk boundary correspondence.

The clearest evidence of the trivial/non-trivial topology of a semiconducting armchair GNR in vacuum is the absence/presence of localized states at the termini. Since vacuum is a trivial insulator ($\mathbb{Z}_2$ will be always 0), the bulk boundary correspondence predicts localized states at the termini of non-trivial GNRs. Currently, as-grown 5-AGNR and 7-AGNR from known molecular precursors give topological non-trivial GNRs (Figure 6.8 a-b, left side). At the right side of Figure 6.8 a) we show the hypothetical case of a termini in a GNR with trivial topological phase. As far as we are concerned, there is no specific molecular precursor that can grow these kind of ribbons with the latter termination geometry.

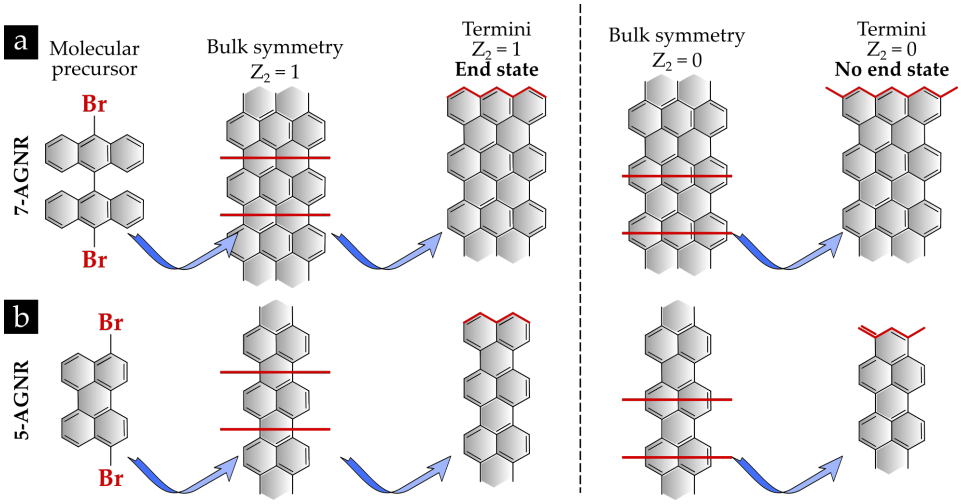

FIGURE 6.8: Identifying the topology character of the GNRs by their termini geometry. a) 2D schematics of the 7-AGNR with either invariant $\mathbb{Z}_2 = 1$ or $\mathbb{Z}_2 = 0$ depending on the termination geometry. b) 2D schematics of the 5-AGNR with either invariant $\mathbb{Z}_2 = 1$ or $\mathbb{Z}_2 = 0$ depending on the termination geometry.

Topology in a 1D superlattice

Topological boundary states can also be induced by fusing longitudinally two ribbons with different topological character. An example is depicted in Figure 6.9 a) with the 5-7 AGNR junction. For a non-symmetric junction, both 5-AGNR and 7-AGNR components are non-topological ($\mathbb{Z}_2 = 1$). This smooth transition with equal Zak phase does not show any in-gap state. On the contrary, for the symmetric junction, 5-AGNR component is trivial, whereas the 7-AGNR is not, generating a half-filled in-gap, boundary state at the interface.

Applying this analysis to our AGNR superlattices we can elucidate the existence or not of topological boundary states at the junctions, as shown in Figure 6.9 b). For the case of the symmetric 7-9 junction and the 7-13 junction, an interface state appears since each of the components belong to different topological phases. In the following, we will focus on the particular case of the symmetric 7-9 AGNR and compare it to the 7-13 AGNR.

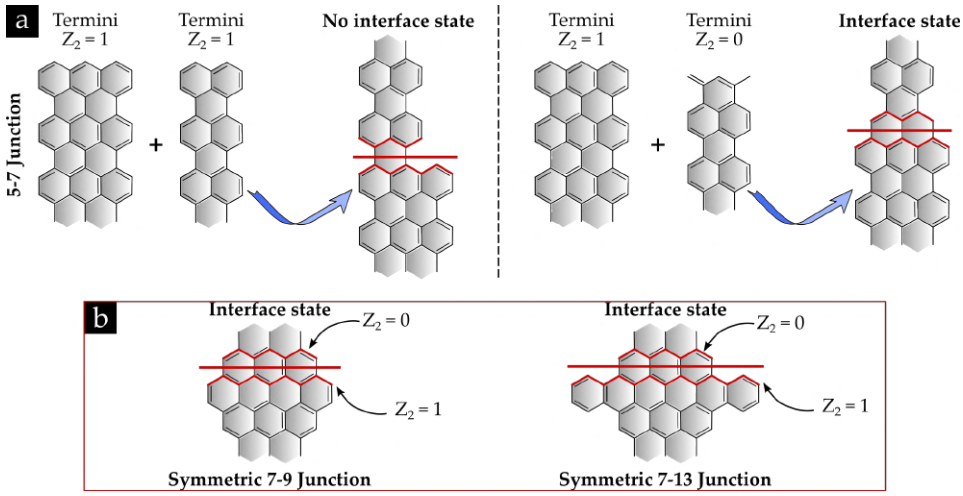

FIGURE 6.9: 2D schematics of examples either showing or not junction states depending on the symmetry the interface of each component. a) Example of a 5-7 AGNR junction with trivial character (left) and non-trivial character (right); b) Presence or absence of junction states in the systems studied in this work (from left to right): non-trivial 7-9 AGNR junction, trivial 7-11 AGNR junction and non-trivial 7-13 AGNR junction.

Unveiling the topologically-induced bands of 7-9 AGNR

7-9 AGNR is a superlattice of topological junctions, which give rise to the hybridization of the localized states, and hence to superlattice bands. To show the emergence of these bands due to the hybridization of junction states, we compare two 7-9 superlattices with either absence (Figure 6.10 a) or presence (Figure 6.10 b) of superlattice bands by TB calculations. In the prior case, both components have a $\mathbb{Z}_2 = 1$. As a consequence, no interface state appear. On the other hand, in the latter scenario, which is our work, the components have different SPT phase, hence generating interface states that communicate creating a superlattice with the corresponding topological-induced bands, which are located in the band gap, making it smaller.

The topological bands generated by the superlattice of the interface states (Figure 6.10, b), can be compared to a system with two coupling parameters, better represented with the Su-Schrieffer-Heeger model (SSH) [273] in Figure 6.11. This model consists of an infinite trans polytacetylene chain (Figure 6.11 a). The SSH model considers two atoms (**A** and **B**) per

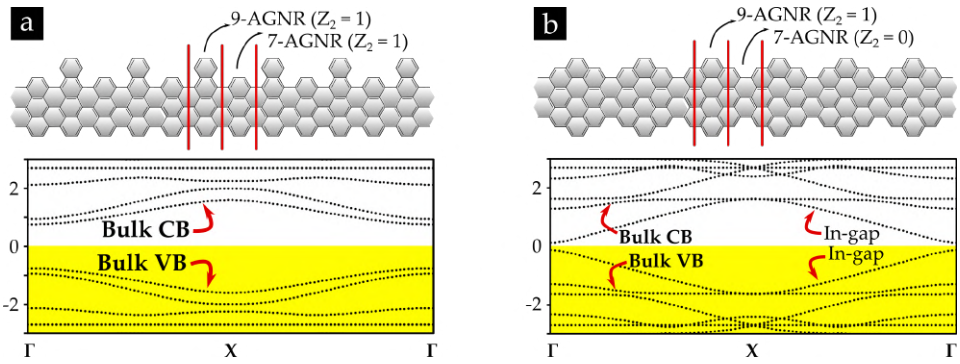

FIGURE 6.10: Tight binding approximations of a 7-9 AGNR superlattice with different interface geometry. a) 7-9 AGNR superlattice with no topological induced bands. b) 7-9 AGNR superlattice with topological induced bands. The calculations have been performed with the program *quantum lattice*, developed by J. Lado (Aaldo University, Finland) considering a hopping parameter t = -2.7 eV, a smearing of 0.03 eV and 100 k points.

unit cell interacting with the first nearest neighbour (1st NN), giving rise to two different hopping terms: the intracell t_1 and the intercell t_2. Considering a periodic system with no boundary states, the Hamiltonian is shown in equation 6.10.

$$H(k)_{1,2} = \begin{pmatrix} 0 & t_1 + t_2 e^{ik} \\ t_1 + t_2 e^{-ik} & 0 \end{pmatrix} \tag{6.10}$$

Solving the matrix Hamiltonian for E=0, the energy of this system is given by the equation 6.11.

$$E(k) = \pm\sqrt{t_1^2 + t_2^2 + t_1 t_2 cos(k)} \tag{6.11}$$

The energy solutions of the equation are represented in Figures 6.11 b) and c). When the intracell hopping has the same value as the intercell hopping, the bands have a point in common at energy E = 0, turning the system into metallic (red color). On the other hand, when the hopping parameters differ, a gap is open in the system, turning it into a semiconductor (black color). Since the equation 6.11 is symmetric, there is no distinction between t_1 and t_2 for an infinite system (Figure 6.11 a-c), only the k-point where the direct band gap generates, determined by the sign of the hopping

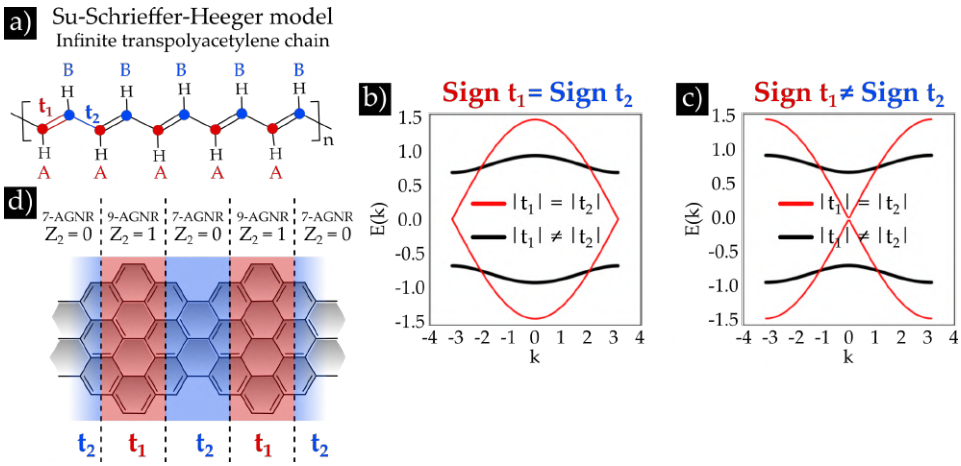

FIGURE 6.11: SSH model. a) SSH model for an infinite trans- polyacetylene chain. Every unit cell possesses two atoms, A and B, with only one electron and hopping terms t_1 and t_2. b) Energy solutions of the SSH model for t_1 and t_2 with the same sign, when they have same absolute value (red plot) or different (black). c) Energy solution of the SSH model for hopping parameters t_1 and t_2 with opposite sign, when they have the same absolute value (red plot) or different (black plot), d) Schematic representation of two unit cells of a periodic 7-9 AGNR system, determining every component of different colour depending on their topological phase.

parameters.

This model is applied to the 7-9 AGNR superlattice, shown in Figure 6.11 d): the interface states can be understood as the **A** and **B** atoms of the trans- polyacetylene chains. The 'intracell' hopping t_1 corresponds to the 9-AGNR segment, whereas the 'intercell' hopping t_2 corresponds to the 7-AGNR segment, and the different values of t_1 and t_2 will help to estimate the characteristics of the topologically-induced bands. We compute by DFT calculations the electronic bands of an infinite 7-9 AGNR and fit the respective VB and CB close to the Γ point with the SSH model (Figure 6.12, c). The resulting coupling parameters are listed in the Table 6.2 (7-9 AGNR (1,1)) and compared to a similar 7-9 AGNR whose interface states are more separated (7-9 AGNR (3,3)), recently demonstrated [76] (Figure 6.12 b).

For a very similar band gap, our system (7-9 AGNR (1,1)) has greater coupling parameters t_1 and t_2, as the interface states are closer (strongly

7-9 AGNR (m,n)	**Reference**	t_1 **(eV)**	t_2 **(eV)**	**Band gap (eV)**	**Band width (eV)**
(3,3)	[76]	0.33	-0.07	0.52	0.14
(1,1)	This work	0.61	-0.38	0.47	0.75
7-13 AGNR (m,n)	**Reference**	t_1 **(eV)**	t_2 **(eV)**	**Band gap (eV)**	**Band width (eV)**
(1,1)	This work	0.61	-0.28	0.76	0.51

TABLE 6.2: SSH model parameters of two 7-9 AGNRs depending on the periodicity length (m,n), and the 7-13 AGNR. The coupling terms t_1 and t_2 have been obtained from the SSH model fitting, the electronic band gap is the DFT band gap and the band width has been obtained from the SSH model: $|t_1| + |t_2| - \frac{E_g}{2}$.

coupled). This induces a wider band width and hence a more dispersing character. On the contrary, the 7-9 AGNR (3,3) [76] has smaller coupling parameters t_1 and t_2 because the interface states are further, thus weakly coupled, and the superlattice bands resemble more to localized flat bands. Compared to our 7-13 AGNR superlattice, the band gap is bigger but the bandwidth decreases.

However, albeit these parameters allow to compare similar 1D topological superlattices, it is not enough to unveil the topological character of the entire system. There exist two strategies that give an indirect result of the topological character of the ribbon (Figure 6.13). One can be done by focusing at the termini states of finite systems, as we had observed experimentally (and schematically illustrated with the SSH model in Figure 6.13 a). Another approach is by making a heterojunction with the ribbon to be explored and another one with known topology, as shown in Figure 6.13 b)-c). If boundary state arise at the junction, then both are of opposite topology. This has to coincide with the emergence of a termini state only at the non-trivial section. If both are trivial/non-trivial, no boundary state could emerge, and the two section will exhibit termini states only in the non-trivial case.

From the results, shown in Figure 6.13 b), we observe that there are two in-gap localized states at the termination of both 7-AGNR and the 7-9 AGNR. The absence of a third in-gap state in the junction between the 7-9

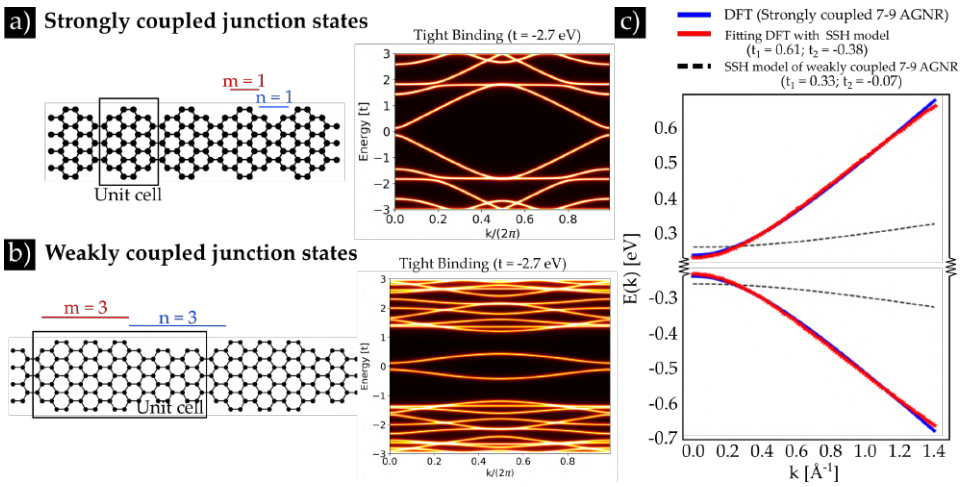

FIGURE 6.12: Comparison of the electronic bands of 7-9 AGNR superlattices depending on the periodicity conditions. a) Strongly coupled junction states (our work), with periodic terms m=1 and n=1, with the respective tight binding electronic band structure (1st nearest neighbour with a hopping parameter t = -2.7 eV); b) Weakly coupled junction states, from Ref. [76], with periodic terms m=3 and n=3 , and with the respective tight binding electronic band structure (1st nearest neighbours, t = -2.7 eV); c) Valence and conduction band of the strongly coupled interface states (blue) and the weakly coupled interface states (black dashed lines). Strongly coupled system has been simulated by DFT (P. Febrer and M.Pruneda), and fitted with the SSH model. Weakly-coupled system has been plotted with the SSH model considering t_1=0.33 eV and t_2=-0.07 eV.

AGNR superlattice and the 7-AGNR extension corroborates, knowing that the 7-AGNR is non trivial, that the connected 7-9 AGNR is also topological non trivial.

As a conclusion, we have demonstrated to be able to modify the superlattice characteristics of a (doped) 7-13 AGNR into a narrower (undoped) 7-9 AGNR. While preserving their topologically induced frontier bands due to the opposite Zak phase at the junctios, the different GNR geometries change other parameters as the band gap and the CBM band width.

6.3 Phenyl translocation and formation of annulene

In the previous section we have exploited the gradual cleavage of pyrimidinic functional groups of N-doped 7-13 AGNR as a strategy to gradually

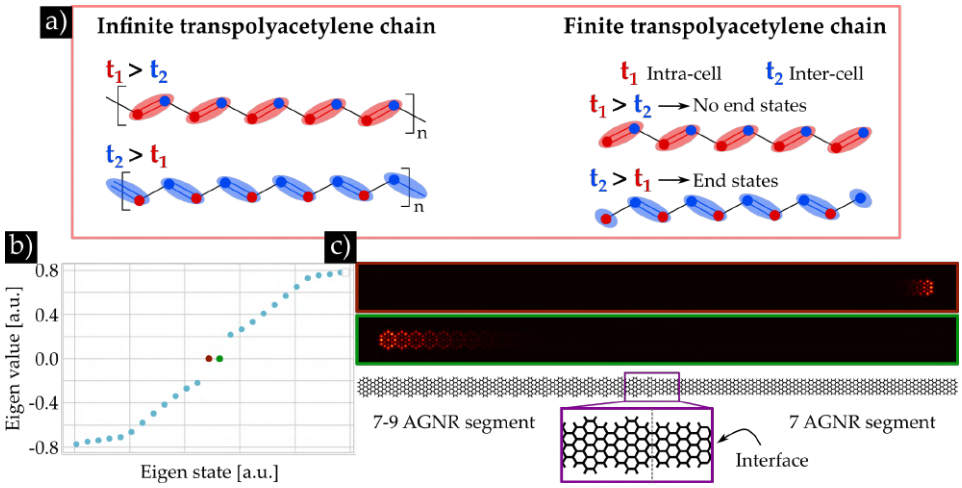

FIGURE 6.13: Strategies to unveil the topological character of topological GNR superlattices. a) SSH model schematic representation of both an infinite (left) and a finite (right) chain, showin end states depending on the value of the hopping parameters. b) Eigenvalues at 0 eV of 7-9 GNR superlattice with 7 AGNR extension. DFT eigenvalues close to the Fermi energy have been marked in red and green colors for clarity; b) the respective LDOS of the 7-9 AGNR superlattice with the 7-AGNR extension. A zoom of the interface between the 7-9 AGNR and the 7-AGNR components has been shown.

control de N doping and engineer the topological superarlattice bands. In this section, we describe another internal transformation that leads to a totally different GNR structure, a porous graphene nanoribbon that is obtained when the *para-* phenyl substituted 7-13 AGNR is annealed beyond its formation temperature.

There are some studies in the literature that have been focused in obtaining porous graphene nanoribbons [52, 130, 274]. In these examples, the synthesis has been carried out using the Ullmann coupling reaction. The lack of specificity in their bond configurations make the system difficult to extend in the long range order, and as a consequence, they adopt multiple configurations. Another important characteristic of these systems is that the nanopores are generated in the backbone of the ribbons, hence affecting the electron mobility. In contrast, the strategy we propose here leads to long-range ordered GNRs, where annulene-type pores are placed at the edges, minimizing perturbations the armchair backbone electron channel.

The molecular precursor under study in this section, the 2,2'-di(para-bisphenyl), 10,10'-dibromo, 9,9'-bianthracene, or DBP-DBBA, and the hierarchical reaction steps to create annulene rings embedded to the graphene nanoribbons are described in Figure 6.14. This molecular precursor adopts a 3D conformation, acquiring axial chirality. After Ullmann polymerization at 200ºC and cyclodehydrogenative aromatization at 300ºC, we obtain *para*-phenylated 7-13 AGNR, represented with red color in Figure 6.14 b). As for the case of the DPyrDBBA (Chapter 3), we find the chirality is transferred to the intermediate and final product, giving rise to prochiral GNRs.

The homochiral configuration is interrupted at 400ºC of postannealing. At this temperature, the system undergoes a phenyl migration between the C_2 and the C_3 at particular sites, illustrated in Figure 6.14, in blue color. If the adjacent unit cell in the same ribbon does not undergo this structural modification, two phenyl groups appear confronted. A planar confronted configuration would place the two phenyls only separated by an sp2 carbon-carbon distance. The phenyl pair could remain stable by tilting away from the GNR plane to avoid the steric hindrance but the system, very likely promoted by the interaction with the substrate, prefers to planarize by inducing a C-C ring closure that leads to the formation of embedded annulenes.

The main condition to induce this on-surface reaction is to avoid the lateral coupling between ribbons that impedes the phenyl migration [117, 230, 275–278]. A simple strategy is to immobilize GNRs by forming irregular covalent GNR networks. However, there is a more controlled and efficient strategy that also has the advantage of orienting the GNRs: assisting their growth by a vicinal Au(111) crystal, which exhibit a periodic array of monoatomic steps separating (111) terraces that work as a nanotemplate. There have been previous studies where vicinal surfaces were applied to guide the growth of GNRs, either to align them macroscopically for spatially averaging, angle-dependent measurements such as ARPES [101, 199], or to control the width of GNRs obtained from laterally fused PPP chains [99, 275]. Here by selecting particular vicinal angles that define terrace widths that can only host individual GNRs, we aim at inhibiting the lateral coupling of GNRs, in order to guide the reaction pathway towards the internal transformations. For that purpose, we have used a curved Au(111) crystal with cylindrical section from BihurCrystal (San Sebastian, Spain) as the nanotemplate, illustrated in Figure 6.15 g). This curved crystal is vicinal to the (111) surface, with a varying vicinal angle along the curvature. In other

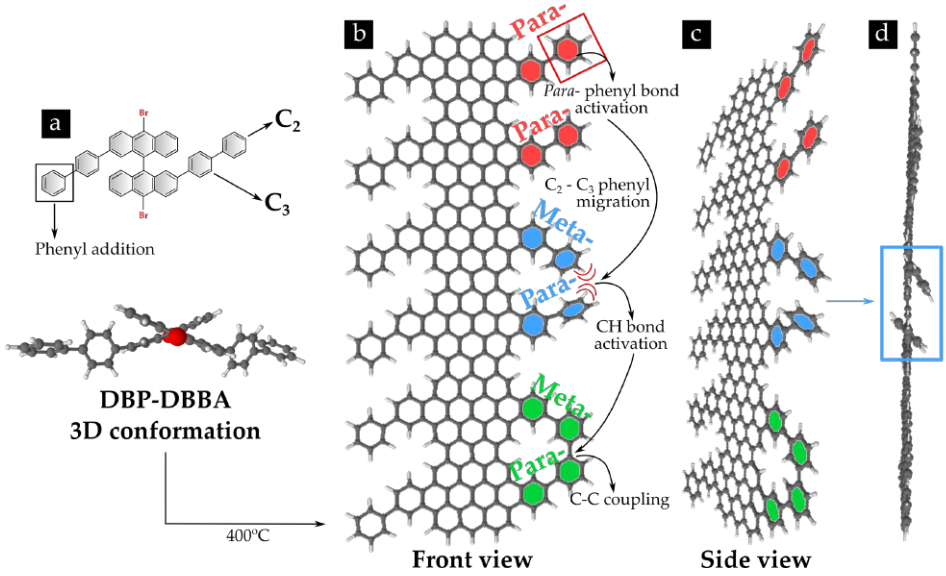

FIGURE 6.14: 3D schematic representation of the formation of an annulene group via phenyl translocation in the *para-* phenyl substituted 7-13 AGNR. a) 2D schematics and 3D conformation of the BDPDBBA monomer. b)-c) As grown ribbon in front view (b) rotated 45° (c) and 90° (d). The colors indicate the steps for the formation of the embedded annulene: red belongs to the initial step, with *para-* substitution configuration; blue represents the $C_2 - C_3$ phenyl migration and green corresponds to the final step of the ring closure.

noble metals this results in a continuous variation of step periodicity, and hence terrace widths. In Au(111) the interplay between step and the surface reconstruction results in specially stable widths of 2 and 4 nm, with varying distributions along the curvature [103].

The STM image of Figure 6.15 a) shows the parallel alignment of the as-grown graphene nanoribbons on the stepped surface after annealing to 300°C. When zooming in any of these terraces, (Figures 6.15 b-d), we found that there is only one ribbon per terrace for the $d_w \sim 4nm$ space width. Interestingly, the phenyl substituted extensions in contact with step edges overpass the terrace step, similar to that found for armchair GNRs [99]. We observed that for $d_n \sim 2nm$ the terraces are decorated with nanographene platelets and other oligomers (not shown here). It seems that the monomer diffusion is inhibited by the steps, most probably by anchoring the phenyl rings with the kins of the steps.

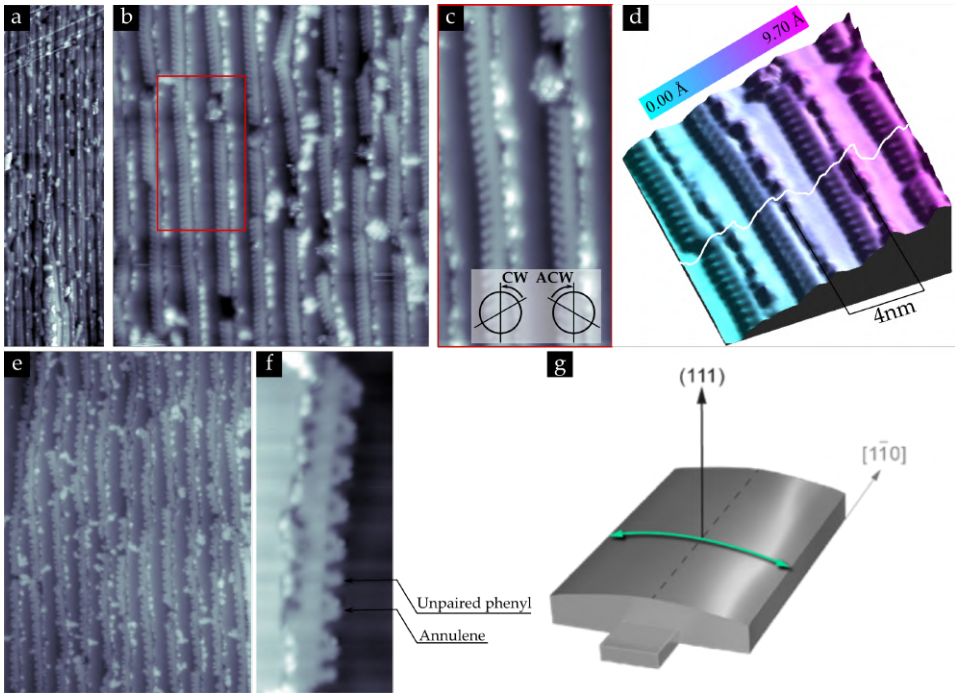

FIGURE 6.15: On-surface synthesis of annulene-embedded graphene nanoribbons. a) Overview STM image of as-grown phenyl substituted 7-13 AGNR on the vicinal Au(111) surface. b) Zoom in of the terraces. c) Closer look to a couple of GNRs showing the prochirality, indicated either with a clockwise (CW) or anticlockwise (ACW) label [279]. d) 3D STM image of a group of 4 ribbons pinned to the steps of 4 terraces. A line profile has been taken in white color to measure the terrace size, which is 4 nm wide. e) Overview STM image after 400ºC of postannealing. f) Zoom of a single ribbon, which is pinned to the step of the Au(111) terrace, and shows the formation of the annulenes. g) Schematics of the curved Au(111) surface, indicating the curvature and step directions.

After annealing to 400ºC, *para-* phenyl units randomly undergo migration, as shown in Figures 6.15 e) and f), followed by a subsequent C-C ring closure that leads to the annulene pores.

When analyzing the density of pores in this system, only considering the side that is not anchored to surface steps, we observe that the yield of production of annulene pores using the strategy of the stepped surface is of about 60%. The rest consists on single phenyls isolated between pairs of

annulenes or immobilized by bonding to other species such as platelets.

With these results, we demonstrate a strategy to grow nanoporous graphene nanoribbons by transforming edge functional phenyl groups into pores, where arrays of pores at the edges are combined with an uninterrupted graphene backbone. The hierarchical formation of the nanopores after the ribbon formation allows to grow long GNRs, and due to the factg that stepped surfaces are employed, we also assure a macroscopic alignment of themselves.

6.4 Conclusions and future perspectives

In this Chapter we have presented two different on-surface strategies by inducing further reactions beyond the formation of GNRs that lead to controlled internal transformations.

In the first case we show the study of GNR systems with partially or totally cleaved pyrimidine groups, to give rise to either asymmetric nitrogen-doped 7-11 AGNR or symmetric undoped 7-9 AGNR superlattices.

We have studied the electronic properties of the undoped symmetric 7-9 AGNR and 7-13 AGNR, the half-doped asymmetric 7-11 AGNR and the doped symmetric 7-13 AGNR by focusing at the doping content and the topology of the superlattices. Regarding the doping, we have demonstrated a gradual shift of the frontier bands to lower energies as the density of nitrogen dopants increase in the ribbon structure.

Regarding the topology of the superlattices, we have demonstrated that 7-9 AGNR possesses topological superlattice bands within the bulk band gap, reducing the overall band gap of the ribbon. DFT calculations also reveal that the superlattice bands have non-trivial topological order, which leads to the emergence of end states localized at the termini. The short period of the 7-9 and 7-13 AGNRs superlattices couple the interface states effectively, giving rise to highly dispersive topological superlattice bands [75, 76], with a larger band width and group velocity, making it more interesting for electron transport-based applications.

We have revised another superlattice that we grew along the course of this thesis, that are shown in Figure 6.16 b). In this case, a novel 1D graphene

nanoribbon superlattice is formed from the molecular precusor diphenyl-dibromo trianthracene (DPDBTA). The on-surface sysnthesis gives rise to a 7-10 AGNR superlattice. The interface at the heterojunction generates 7- AGNR and 10- AGNR components with the same $\mathbb{Z}_2$ invariant ($\mathbb{Z}_2 = 0$, trivial insulator). As a consequence, we would not expect topologically-induced bands when performing STS measurements, generating a bigger band gap than for the already known 7-13 AGNR.

Likewise, following the same strategy of the cleavage of pyrimidine groups (Figure 6.16 c), we propose two hypothetical molecular precursors with pyrimidine functional groups that would lead to the formation of two novel 7-9 AGNR superlattices, called 7- AGNR I(1,2) and 7-AGNR S(1,1), represented in Figures 6.16 d) and e). The 'I' and 'S' stand for 'In-line' and 'Staggered', a terminology used in previous publications [75]. We guess that the 7-AGNR I(1,2) will have a less coupled junction states and hence the band width of the induced topological bands will be narrower than the results of this work with 7-9 AGNR. We do not expect to observe in-gap superlattice bands in the 7-AGNR S(1,1), so a bigger band gap might emerge. In general, these are the strategies for band engineering of GNR structures that are obtained using similar molecular precursors via pyrimidine cleavage.

Furthermore, we have demonstrated the growth of isolated GNRs with [18]annulene pores at the edges. By using stepped surfaces to immobilize isolated GNRs in order to induce the internal transformations, we have been able to produce these ribbons at large scale, aligning them macroscopically. As future perspectives, we want to test the selective interactions of these pores with target molecules or atoms, and compare it with that of the NPG. Due to this fact, our collaborators computed the wavefunctions of an infinitely long annulene-decorated AGNR. Apart from the expected longitudinal bands along the ribbon backbone, we notice above 2.9 eV localized states surrounding the pore that communicate with the longitudinal bands placed at the backbone, which could promote the selective interactions at the pores, and enhance its electronic transduction by coupling localized and propagating states.

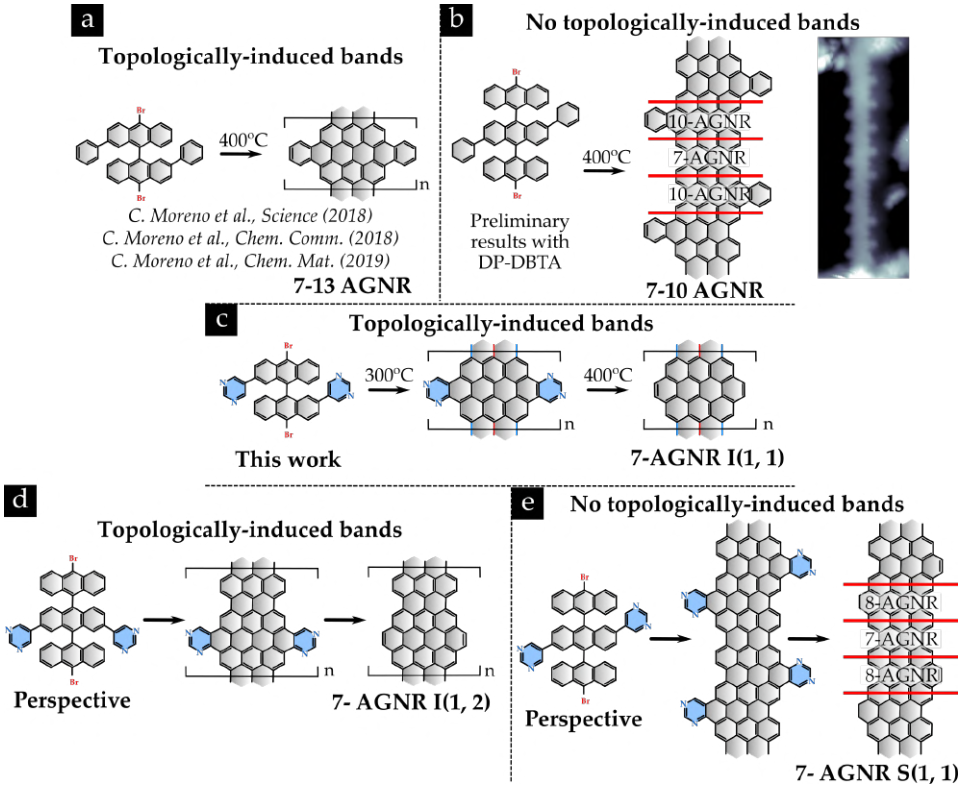

FIGURE 6.16: 2D schematics of already studied and hypothetical GNR superlattices. a) DPDBBA monomer gives rise to the 7-13 AGNR superlattice. b) Preliminary results of a novel phenyl-functionalized trianthracene monomer that grows 7-10 AGNR superlattice. c) Monomer **3** forms 7-9 AGNR superlattice with topological non-trivial character. d)-e) Hypothetical pyrimidine-functionalized trianthracene derivatives to form a 7-AGNR I(1,2) (d) and 7-AGNR S(1,1) superlattices.

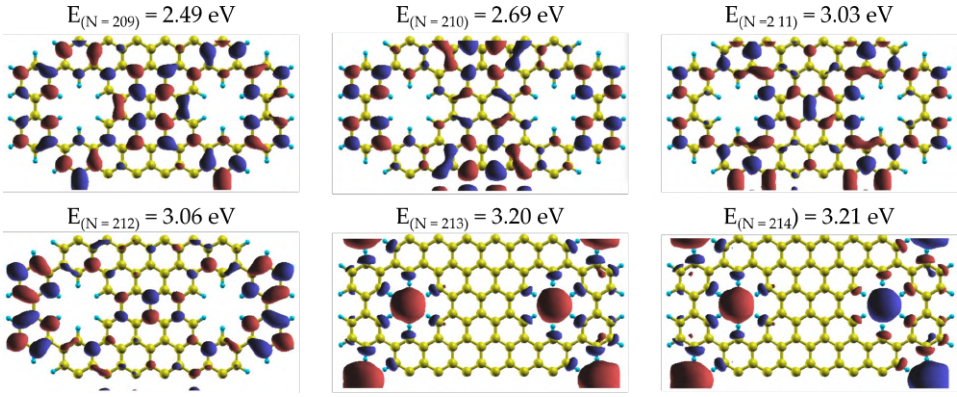

FIGURE 6.17: Wavefunctions of the annulene-decorated AGNR. The wavefunction have been taken from 2.49 eV to 3.21 eV, considering the Fermi level is in the gap and 0.2 eV above the VBM.

Chapter 7

Conclusions and future perspectives

This dissertation has been devoted to the bottom-up synthesis of 0D, 1D and 2D doped graphene-based nanoarchitectures and the study of the intermediate step reactions and electronic properties by means of STM, STS and XPS. It has covered a systematic analysis from the **intra-** molecular transformations (0D nanographenes or graphene QDs) to the **inter-** molecular coupling (1D nanographenes or GNRs), and to the **inter-** ribbon coupling (NPG and 2D superlattices), based on three main on-surface reactions: (i) Ullmann coupling, (ii) cyclodehydrogenation and (iii) H-Cl zipping.

In the first part of the results of this thesis we blaze a trail towards the bottom-up synthesis of a nitrogen-doped nanoporous graphene. The main challenge overcome in this study has been the stability of the pyrimidine group used to introduce N-dopants throughout the whole synthetic route. This is achieved by designing a proper molecular precursor with nitrogen containing functional groups that is stable among sublimation at ultra high vacuum conditions. Secondly, we found the best candidate to avoid the degradation of these functional groups upon annealing on the catalytic substrate. By adding chlorine atoms to the precursor, we have been able to demonstrate the decrease in temperature by 100ºC for the formation of N-doped NPG.

The problem of the long range order in N-doped NPG is overcome in the second part of the thesis, where we have dealt with a novel strategy to grow this 2D network. We have demonstrated that, by the combination of undoped and N-doped graphene components we can construct a 2D superlattice down to the nanoscale. This triggers the presence of interface

quantum dipoles, which are responsible for a highly confined charge redistribution, that enables the realization of heterojunctions whose interface are as narrow as one carbon-cabon bond.

In the third part, we demonstrate to alter the thermodynamic synthetic route to grow N-doped NPG and redirect it to the kinetic one, so that we grow 0D nanographenes with chlorine and nitrogen heteroatoms. The addition of these heteroatoms induces the simultaneous debromination and intra- molecular cyclodehydrogenation, assisted by the strong intermolecular interaction in a high surface coverage scenario. These results have also manifested it is possible that the molecules experience an in-situ chiral phase transition, most probably promoted by the creation of organometallic hybrids with the Au(111) surface. As far as we are concerned, it has not been reported so far. The presence of intact zig-zag edges upon formation of the nanographene chains at low temperature is a promising result in order to study the cooperative magnetism of the very probable unpaired electrons

The last part of the results of this thesis has been focused on inducing intra- ribbon transformations a high temperatures of postannealing. In a first scenario, we show how the controlled thermal-dependent degradation of pyrimidine functional groups in a 7-13 AGNR 1D superlattice with topologically induced bands triggers the transformation into an undoped 7-9 AGNR 1D superlattice with also topologically-induced bands. Thanks to the calculations made with DFT and tight binding, we have been able to finally elucidate the topological character of our systems by merging them with known ribbons. Due to the close proximity of the interface states, the induced topological bands are characterise by being dispersive and with a small charge carrier effective mass, as compared to the state-of-the-art 1D GNR-based topological superlattices.

Likewise, we also demonstrated on-surface annulene formation by phenyl translocation in phenylated 7-13 AGNRs by assisting this reaction with the growth on a vicinal curved Au(111) catalytic surface.

The milestones of this thesis can be listed in five items:

- The development of a strategy towards the synthesis of a nanoporous graphene with heteroatom doped pores and whose semiconducting electronic properties are preserved.

- The on-surface synthesis of an N-doped hybrid nanoporous graphene, which consist on an interdigitated pair of GNRs that result on a type II lateral superlattice heterojunction. This strategy can be generalized to other systems.
- The on-surface synthesis of the kinetically favourable synthetic route to grow N-doped nanographene chains featuring zig-zag edges at low temperatures of postannealing.
- The on-surface transformation of a doped topological superlattice into a narrower undoped topological superlattice.
- The on-surface transformation of a phenylated 7-13 AGNR into fused annulene 7-13 AGNRs.

As the outlook of this research, we expect to demonstrate the general application of our strategy to grow laterally connected multicomponent systems, inserting ones containing other functionalities.

Concerning the synthesis of the N-doped NPG, we aim to deposit on the as-grown system specific atoms to prove their functionalities: alkaline and heavy metal atoms for energy storage applications [280]; heavy metal atoms and lanthanides for catalytic and optical properties; and magnetic atoms (iron, cobalt) to study the coupling of their spin and how it is affected by the anisotropic character of the 2D network.

Concerning the nanographenes, we aim to find similar systems with an open shell character and, by following the same strategy, being able to grow chains at low temperature, hence avoiding undesired reactions and enabling the study of the coupling among the unpaired electrons.

Beyond the generation of fundamental knowledge on the on-surface synthesis, a potential outlook direction will be the study of the physical properties of the graphene nanoarchitectures outside the UHV conditions and on more technologically relevant substrates, such as insulators. In particular, it is interesting to study the strong anisotropy in the electronic properties of NPG, as it was recently predicted [114, 118]. That means conductivity strongly depends on the main axis of the NPG. The band width of the longitudinal bands (**L** in the Chapter 3) is six times bigger in the longitudinal direction than in the transversal direction. This anisotropy may induce Talbot interferences [125], opening up new opportunities for

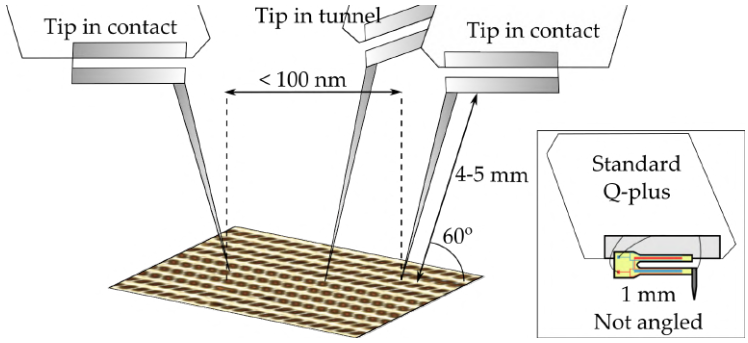

FIGURE 7.1: Schematic representation of the experiment to detect the Talbot interferences on the NPG by means on a Multiple Probe STM. Two tips are in physical contact with the NPG under an applied voltage bias, while the third tip scans the NPG area between the in-contact tips to track the Talbot intereferences. Specific characteristics of these type of microscopes has been indicated and compared to standard ones (bottom-right square).

future quantum electronic, computing or carbon nanocircuitry.

To experimentally probe the Talbot interferences, we propose the study of the NPG on an insulating substrate by means of a Multiple Probe STM/AFM [281]. The experiment would be feasible with three STM tips (shown in Figure 7.1): two of them are separated far away and into contact with the NPG (Tips 1 and 3), applying a bias voltage. The 'Tip 2', between the other tips, scans the area in tunnelling regime so that it collects the density of states coming from the Talbot effect.

We tried to do this experiment during a two-months internship in the National Institute for Materials Science (NIMS) in Tsukuba (Japan), under the supervision of Prof. T. Nakayama and Dr. Y. Shingaya, by means of a home made Quadruple-Probe Tuning-Fork-Type Atomic Force Microscopy (QP-AFM), commonly operated in frequency modulation (FM) mode. In order to have access to the 2D local properties of the NPG at short distances (<100 nm), the tips need specific characteristics (depicted in Figure 7.1): the length of the prongues is 4-5 times larger than the current ones, are tilted 60º with respect to the normal axis, and the radii of the probe has to be as thin as possible (generally standard tungsten tips are substituted by tungsten oxide nanorods [281, 282]).

Another future perspective beyond band engineering by means of width,

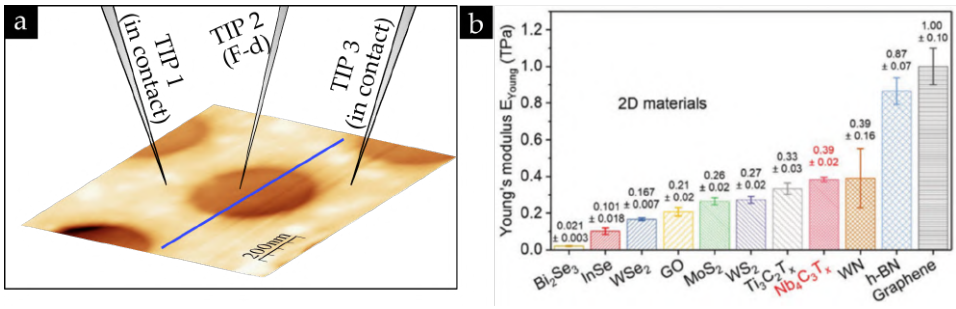

FIGURE 7.2: Mechanical properties of a free-standing NPG. a) Schematic representation of the proposed experiments in order to study the electronic properties of the NPG as a function of the applied strain; b) Young's modulus of some 2D materials, taken from Ref. [286].

shape modification, doping content or superlattice generation, is upon strain (a field called straintronics). It has been theoretically predicted that applied strain in graphene nanoribbons along their longitudinal direction affects on the total absolute value of the band gap [283, 284], inducing the change of their topological phase [285]. We propose its transfer on to a porous, insulating substrate, so that the Nanoporous graphene stands freely on it and the charge transfer is avoided. The experiment to know the variation of the electronic properties as a function of the strain is also proposed to be performed with a mutlitple probe AFM, as is shown in Figure 7.2 a): two tips are in contact with the supporting substrate (Tips 1 and 3) whereas the tip 2 is located inside the free-standing membrane, which will perform indentation measurements. It is known that the force applied by the AFM tip to the free-standing membrane can be known from the cantilever deflection. If the gap closes upon tip indentation, the current will increase and will be detected by the other two tips that are in contact with the system.

We were still able to determine the mechanical properties of the NPG with a single AFM tip, a key experiment before performing the proposed one. The resulting calculated Young's modulus is of the order of the MoS2 [286] (Figure 7.2).

We foresee with this experiment to also study the electronic band gap variation upon strain and how it is affected by the anisotropy of the network. Our aim is also to see the piezoconductivity properties, and how the excitonic and plasmon generation is altered [287, 288].

Appendix A

Experimental details

A.1 STM image parameters

Chapter 3 STM image parameters

FIGURE 3.5	Mode	Size (nm X nm)	I (nA)	V (mV)	V mod	Freq	Zoffset
3.5 b) Top	CC	150 x 95	0.028	1810	-	-	-
3.5 b) Bottom	CC	9.5 x 8.5	0.098	1132	-	-	-
3.5 c) Top	CC	100 x 75	0.078	1040	-	-	-
3.5 c) Bottom	CC	9.2 x 9.8	0.078	1040	-	-	-
3.5 d) Top	CC	38 x 23	0.046	786	-	-	-
3.5 d) Bottom	CH	6.0 x 5.0	-	7	3	2500	180
FIGURE 3.6	Mode	Size (nm X nm)	I (nA)	V (mV)	V mod	Freq	Zoffset
3.6 b)	CC	11 x 6	0.098	1130	-	-	-
FIGURE 3.7	Mode	Size (nm x nm)	I (nA)	V (mV)	V mod	Freq	Z offset
3.7 b)	CC	20 x 10	0.067	1900	-	-	-
FIGURE 3.8	Mode	Size (nm X nm)	I (nA)	V (mV)	V mod	Freq	Zoffset
3.8 b)-c)	CH	2.5 x 5.0	-	7	3	2500	330
FIGURE 3.9	Mode	Size (nm X nm)	I (nA)	V (mV)	V mod	Freq	Zoffset
3.9 c)-d)	CH	3.5 x 5.0	-	7	3	2500	180

TABLE A.1: I-V conditions in STM data acquisition for Figures 3.5, 3.6, 3.7; 3.8 and 3.9.

FIGURE 3.11	Mode	Size (nm X nm)	I (nA)	V (mV)	V mod	Freq	Zoffset
3.11 a) Left	CC	136 x 110	0.049	1500	-	-	-
3.11 a) Right	CC	17.8 x 14.4	0.13	1500	-	-	-
3.11 b) Left	CC	80.0 x 64.5	0.049	1132	-	-	-
3.11 b) Right	CC	15.0 x 11.4	0.051	1545	-	-	-
3.11 c) Left	CC	80.0 x 64.5	0.077	1800	-	-	-
3.11 c) Right	CC	40.0 x 32.0	0.077	1800	-	-	-
3.11 d) Left	CC	52.7 x 42.6	0.067	1256	-	-	-
3.11 d) Right	CH	5.1 x 4.1	-	30	3	2500	290
FIGURE 3.12	Mode	Size (nm X nm)	I (nA)	V (mV)	V mod	Freq	Zoffset
3.12 b)	CH	5.1 x 4.1	0.067 (1020 mV)	30	3	2500	290

TABLE A.2: I-V conditions in STM data acquisition for Figures 3.11 and 3.12.

FIGURE 3.14	Mode	Size (nm X nm)	I (nA)	V (mV)	V mod	Freq	Zoffset
3.14 a) Top	CH	5.1 x 4.1	-	30	3	2500	290
3.4 a) Middle	CH	2.5 x 5.0	-	7	3	2500	330
3.14 a) Bottom	CH	2.0 x 5.5	-	7	3	2500	0
3.14 b)	CH	2.5 x 3.0	-	-600	30	2500	0
3.14 d)	CH	2.5 x 3.0	-	900	40	2500	-50
FIGURE 3.17	Mode	Size (nm X nm)	I (nA)	V (mV)	V mod	Freq	Zoffset
3.17 a) Inset	CC	3.25 X 4.5	0.088	400	-	-	-
3.17 b)	CC map	3.5 X 5.0	0.75	-800	20	3000	120
3.17 c)	CC map	3.5 X 5.0	0.75	-1800	20	3000	120
FIGURE 3.18	Mode	Size (nm X nm)	I (nA)	V (mV)	V mod	Freq	Zoffset
3.18 a) Inset	CH	2.5 x 5.0	0.46 (200 mV)	7	3	2500	330
3.18 b)	CH	2.5 X 5.0	0.46 (200 mV)	2200	5	300	-500
3.18 c) Inset	CH	3.5 X 3.2	0.067 (-500 mV)	3	3	2500	230
3.18 f) top	CC map	4.5 X 3.5	0.067	1950	30	2500	-
3.18 f) bottom	CC map	4.5 X 3.5	0.067	2300	30	2500	-

TABLE A.3: I-V conditions in STM data acquisition for Figures 3.14, 3.17 and 3.18.

Chapter 4 STM image parameters

Figure 4.2	Mode	Size	I	V	V mod.	Freq.	Z offset
		[nm x nm]	[nA]	[mV]	[mV]	[Hz]	[pm]
a) Top	CC	80.0 X 80.0	0.05	2150	-	-	-
a) Bottom	CC	40.0 X 40.0	0.05	2150	-	-	-
b) Top	CC	200.0 X 200.0	0.035	2150	-	-	-
b) Bottom	CC	14.0 X 14.0	0.043	1750	-	-	-
c) Top	CC	150.0 X 150.0	0.056	1840	-	-	-
c) Bottom	CH	7.0 X 6.0	-	7	3	2500	190
d)	CH	5.50 X 3.25	-	7	3	2500	500

TABLE A.4: I-V conditions in STM data acquisition for Figure 4.2.

Figure 4.3	Mode	Size	I	V	V mod.	Freq.	Z offset
		[nm X nm]	[nA]	[mV]	[mV]	[Hz]	[pm]
4.3 a)	CC	85 X 50	0.06	1570	-	-	-
4.3 c)	CC	40 x 25 (80 X 50)	0.05	2150	-	-	-
4.3 e)	CC	14 X 20	0.043	1750	-	-	-
4.3 g)	CC	12 X 16	1.00	800	-	-	-

TABLE A.5: I-V conditions in STM data acquisition for Figure 4.3.

Figure 4.4	Mode	Size	I	V	V mod.	Freq.	Z offset
		[nm x nm]	[nA]	[mV]	[mV]	[Hz]	[pm]
4.4 a)	CC	100 X 100 50 X 50	0.06	1570	-	-	-
4.4 b)	CC	90 X 90 32 X 32	0.047	1940	-	-	-
4.4 c)	CC	60 X 60 36 X 36	0.043	1750	-	-	-

TABLE A.6: I-V conditions in STM data acquisition for Figure 4.4.

Figure 4.5	Mode	Size	I	V	V mod.	Freq.	Z offset
		[nm X nm]	[nA]	[mV]	[mV]	[Hz]	[pm]
4.5 b)	dI/dV CH map	3.8 X 3.0	-	7	3	2500	500
4.5 d) Left	CC	6.7 X 5.0	0.80	1100	-	-	-
4.5 d) (VBM) -600	dI/dV CC map	6.7 X 5.0	0.65	-600	40	2500	-
4.5 d) (VBM) -200	dI/dV CC map	6.7 X 5.0	0.25	-200	40	2500	-
4.5 d) (CBM) +850	dI/dV CC map	6.7 X 5.0	0.65	850	40	2500	-
4.5 d) (CBM) +1000	dI/dV CC map	6.7 X 5.0	0.82	1000	40	2500	-

TABLE A.7: I-V conditions in STM data acquisition for Figure 4.5.

Figure 4.6	Mode	Size	I	V	V mod.	Freq.	Z offset
		[nm X nm]	[nA]	[mV]	[mV]	[Hz]	[pm]
Top center	Topo CC	10.0 x 6.0	0.82	1100	-	-	-
-100	dI/dV CC map	10.0 x 6.0	0.1	-100	40	2500	-
-200	dI/dV CC map	10.0 x 6.0	0.25	-200	40	2500	-
-300	dI/dV CC map	10.0 x 6.0	0.25	-300	40	2500	-
-400	dI/dV CC map	10.0 x 6.0	0.25	-400	40	2500	-
-500	dI/dV CC map	10.0 x 6.0	0.65	-500	40	2500	-
-600	dI/dV CC map	10.0 x 6.0	0.65	-600	40	2500	-
-700	dI/dV CC map	10.0 x 6.0	0.65	-700	40	2500	-
-800	dI/dV CC map	10.0 x 6.0	0.65	-800	40	2500	-

TABLE A.8: I-V conditions in STM data acquisition for Figure 4.6.

Chapter 5 STM image parameters

Figure 5.3	Mode	Size	I	V	V mod	Freq	Zoffset
		[nm x nm]	[nA]	[mV]	[mV]	[Hz]	[pm]
5.3 a)	CC	200 X 200	0.05	1500	-	-	-
5.3 b)	CC	200 X 200	0.05	1130	-	-	-
5.3 c)	CC	275 X 275	0.04	1500	-	-	-
5.3 d)	CC	260 X 260	0.08	1500	-	-	-
Figure 5.4	Mode	Size	I	V	V mod	Freq	Zoffset
		[nm x nm]	[nA]	[mV]	[mV]	[Hz]	[pm]
5.4 a)-Top	CC	150 X 60	0.064	-3600	-	-	-
5.4 a)-Bottom	CC	40 X 30	0.049	1500	-	-	-
5.4 a)-Inset	CC	8.0 X 7.0	0.13	1500	-	-	-
5.4 b)-Top	CC	100 X 55	0.050	1500	-	-	-
5.4 b)-Bottom	CC	25 X 16	0.067	1500	-	-	-
5.4 b)-Inset	CC	9.0 X 4.0	0.067	1500	-	-	-
5.4 c) - b)	CC	15 X 6	0.067	1500	-	-	-
5.4 d)	CC	9 X 7	0.067	1500	-	-	-
Figure 5.5	Mode	Size	I	V	V mod	Freq	Zoffset
		[nm x nm]	[nA]	[mV]	[mV]	[Hz]	[pm]
5.5 a)	CC	40 X 40	0.035	1500	-	-	-
5.5 b)	CC	15 X 15	0.084	1500	-	-	-
5.5 d)	CC	90 X 90	0.04	1550	-	-	-
5.5 e)	CC	5 X 5	0.024	800	-	-	-

TABLE A.9: I-V conditions in STM data acquisition for Figures 5.3, 5.4 and 5.5.

Figure 5.6	Mode	Size	I	V	V mod	Freq	Zoffset
		[nm x nm]	[nA]	[mV]	[mV]	[Hz]	[pm]
5.6 a)	CC	20 X 32	0.035	1600	-	-	-
5.6 b)	CC	17.5 X 35	0.04	1550	-	-	-
Figure 5.7	Mode	Size	I (nA)	V (mV)	V mod	Freq	Zoffset
		[nm x nm]	[nA]	[mV]	[mV]	[Hz]	[pm]
5.7 a)	CC	300 X 280	0.05	-1740	-	-	-
5.7 b)	CC	80 X 60	0.035	1410	-	-	-
5.7 c)	CC	20 X 17	0.1	-1650	-	-	-

TABLE A.10: I-V conditions in STM data acquisition for Figures 5.6, and 5.7.

Chapter 6 STM image parameters

Figure 6.3	Mode	Size	I	V	V mod.	Freq.	Zoffset
		[nm x nm]	[nA]	[mV]	[mV]	[Hz]	[pm]
6.3 a)	CH	2.5 X 5.0	-	7	3	2500	220
6.3 b)	CH	2.8 X 5.6	-	7	3	2500	330
6.3 c)	CH	1.5 X 3.0	-	5	3	2500	330
6.3 e) Left	CC	100 X 60	0.064	750	-	-	-
6.3 e) Right	CH	8.0 X 5.0	-	7	3	2500	290
Figure 6.5	Mode	Size	I	V	V mod.	Freq.	Zoffset
		[nm x nm]	[nA]	[mV]	[mV]	[Hz]	[pm]
6.5 a)	CC	6.0 X 12.0	0.32	830	-	-	-
6.5 b)	CH	4.0 X 12.0	-	7	3	2500	400
Figure 6.6	Mode	Size	I	V	V mod.	Freq.	Zoffset
		[nm x nm]	[nA]	[mV]	[mV]	[Hz]	[pm]
6.6 b) Left	CH	1.5 X 3.0	-	5	3	2500	330
6.6 b) Middle	CH	4.0 x 4.0	-	7	3	2500	500
6.6 b) Right	CH	4.0 x 3.0	-	7	3	2500	400
6.6 c) Left	CH	4.0 x 5.5	-	7	3	2500	400
6.6 c) Middle	CH	4.0 x 6.0	-	-500	20	2500	130
6.6 c) Right	CH	4.0 x 6.0	-	950	20	2500	170
Figure 6.7	Mode	Size	I	V	V mod.	Freq.	Zoffset
		[nm x nm]	[nA]	[mV]	[mV]	[Hz]	[pm]
6.7 a)	CC	5.0 X 10	0.6	1200	-	-	-
6.7 b)	CH	1.5 x 2.0	-	3	5	2500	380
6.7 c)	CH	1.7 x 1.5	-	3	5	2500	470
6.7 d)	CH	2.0 x 9.2	-	3	5	2500	330
6.7 h) Middle	CH	2.0 x 9.0	-	-750,...,900	40	2500	[130, 800]

TABLE A.11: I-V conditions in STM data acquisition for Figures 6.3, 6.5, 6.6 and 6.7. All CC images have been taken without any tip functionalization. CH image has bond-resolved resolution due to the functionalization of the STM tip with a CO molecule.

Figure 6.15	Mode	Size	I	V	V mod.	Freq.	Zoffset
		[nm x nm]	[nA]	[mV]	[mV]	[Hz]	[pm]
6.15 a)	CC	40.0 X 140.0	0.075	1075	-	-	-
6.15 b)	CC	40.0 X 40.0	0.075	680	-	-	-
6.15 c)	CC	10.0 X 20.0	0.075	680	-	-	-
6.15 d)	CC	15.0 X 16.0	0.075	680	-	-	-
6.15 e)	CC	60.0 X 80.0	0.18	1180	-	-	-
6.15 f)	CC	6.0 X 16.0	0.057	5100	-	-	-
Figure 6.16	Mode	Size	I	V	V mod.	Freq.	Zoffset
		[nm x nm]	[nA]	[mV]	[mV]	[Hz]	[pm]
6.16 b)	CC	6.0 X 12.0	0.32	830	-	-	-

TABLE A.12: I-V conditions in STM data acquisition for Figures 6.15 and 6.16. All CC images have been taken without any tip functionalization. CH image has bond-resolved resolution due to the functionalization of the STM tip with a CO molecule.

A.2 XPS fitting parameters

Chapter 3 XPS fitting parameters

Each table of this section shows the BE, relative area and FWHM (full width at half maximum) variation of every core level spectra as a function of the postannelaing temperature. The BE is the energy of the center of the fitted peak, and the relative area is directly related to the stoichiometry of each of the different bonds.

Precursor 3, Au(111) - C 1s				
Temperature	**Component**	**Binding energy [eV]**	**Relative area**	**FWHM [eV]**
RT	C-H/C-C	284.3	78%	1.1
	C-Br	284.8	5%	0.9
	C-NH/C-CN	285.35	17%	1.3
150°C	C-H/C-C	284.16	83%	1.17
	C-NH/C-CN	285.5	17%	1.35
300°C	C-H/C-C	284.17	83%	1.14
	C-NH/C-CN	285.6	17%	1.25

TABLE A.13: C 1s core level XPS fitting condition parameters of the molecular precursor **3**, shown in Figure 3.10. The main peak has been deconvoluted in the different chemical environments: C-C/C-H, C-Br and C-NH/C-CN, that stand for $C[C_3]/C[C_2H]$, $C[C_2Br]$, $C[CNH]$, $C[CN_2H]$. The relative area corresponds to the stoichiometry at this step.

Precursor 3, Au(111) - Br 3d				
Temperature	**Component**	**Binding energy [eV]**	**Relative area**	**FWHM [eV]**
RT	Br-C (5/2, 3/2)	69.68, 70.74	100%	0.81, 0.81
150°C	Br-Au (5/2, 3/2)	67.57, 68.57	56%	0.67, 0.67

TABLE A.14: Br 3d core level XPS fitting condition parameters of the molecular precursor **3**, shown in Figure 3.10. The relative area corresponds to the area variation with respect to the area at RT.

Precursor 3, Au(111) - N 1s				
Temperature	**Component**	**Binding energy [eV]**	**Relative area**	**FWHM [eV]**
RT	N-C	398.8	100%	1.59
150°C	N-C	398.9	86%	1.19
300°C	N-C	398.9	97%	1.84

TABLE A.15: N 1s core level XPS fitting condition parameters of the molecular precursor **3**, shown in Figure 3.10. The relative area corresponds to the area variation with respect to the area at RT.

Precursor 4, Au(111) - C 1s (towards NPG)				
Temperature	**Component**	**Binding energy [eV]**	**Relative area**	**FWHM [eV]**
As-dep (100°C)	C-H/C-C	284.19	81%	1.21
	C-Br	284.8	3%	1.11
	C-NH/C-CN	285.3	11%	1.12
	C-Cl	286.9	5%	1.24
140°C	C-H/C-C	284.18	85%	1.19
	C-NH/C-CN	285.46	9%	1.29
	C-Cl	287	6%	1.29
200°C	C-H/C-C	284.32	85%	1.23
	C-NH/C-CN	285.46	9%	1.18
	C-Cl	287.39	6%	1.41
300°C	C-H/C-C	284.46	88%	1.34
	C-NH/C-CN	285.9	12%	1.84

TABLE A.16: C 1s core level XPS fitting condition parameters of the molecular precursor **4**. The main peak has been deconvoluted in the different chemical environments: C-C/C-H, C-Br, C-NH/C-CN and C-Cl, that stand for $C[C_3]/C[C_2H]$, $C[C_2Br]$, $C[CNH]$, $C[CN_2H]$ and $C[N_2Cl]$ shown in Figure 3.13. The relative area corresponds to the stoichiometry at this step.

Precursor 4, Au(111) - Br 3d (Towards NPG)				
Temperature	**Component**	**Binding energy [eV]**	**Relative area**	**FWHM [eV]**
As-dep (100°C)	Br-C (5/2, 3/2)	69.66, 70.68	65%	0.76, 0.76
	Br-Au (5/2, 3/2)	67.72, 68.72	35%	0.68, 0.68
140°C	Br-Au (5/2, 3/2)	67.68, 68.88	71%	0.89, 0.89
200°C	Br-Au (5/2, 3/2)	67.77, 68.81	58%	0.82, 0.82

TABLE A.17: Br 3d core level XPS fitting condition parameters and constraints of the molecular precursor **4** shown in Figure 3.13. The relative area corresponds to the area variation with respect to the area at RT.

Precursor 4, Au(111) - N 1s (Towards NPG)				
Temperature	**Component**	**Binding energy [eV]**	**Relative area**	**FWHM [eV]**
As-dep (100°C)	N-C	399.03	100%	1.27
140°C	N-C	399.03	85%	1.18
200°C	N-C	399.03	85%	1.57
300°C	N-C	399.00	90%	1.69

TABLE A.18: N 1s core level XPS fitting condition parameters and constraints of the molecular precursor **4** shown in Figure 3.13. The relative area corresponds to the area variation with respect to the area at RT.

Precursor 4, Au(111) - Cl 2p (Towards NPG)				
Temperature	**Component**	**Binding energy [eV]**	**Relative area**	**FWHM [eV]**
As-dep (100°C)	Cl-C (3/2, 1/2)	200.2, 201.6	100%	1.00, 1.00
140°C	Cl-C (3/2, 1/2)	200.00, 201.6	81%	1.1, 1.1
200°C	Cl-C (3/2, 1/2)	200.00, 201.62	63%	1.17, 1.17

TABLE A.19: Cl 2p core level XPS fitting condition parameters and constraints of the molecular precursor **4** shown in Figure 3.13. The relative area corresponds to the area variation with respect to the area at RT.

Chapter 5 XPS fitting parameters

Precursor 4, Au(111) - C 1s (towards NPG)				
Temperature	**Component**	**Binding energy [eV]**	**Relative area**	**FWHM [eV]**
As-dep (RT)	C-H/C-C	284.47	79%	1.20
	C-Br	285.0	5%	1.30
	C-NH/C-CN	285.7	11%	1.11
	C-Cl	287.3	5%	1.15
100°C	C-H/C-C	284.34	80%	1.24
	C-Br	285.3	4%	0.93
	C-NH/C-CN	285.64	11%	1.52
	C-Cl	287	5%	1.26
140°C	C-H/C-C	284.57	82%	1.24
	C-NH/C-CN	285.80	12%	1.04
	C-Cl	287.00	6%	1.44
200°C	C-H/C-C	284.54	83%	1.23
	C-NH/C-CN	284.54	17%	1.44

TABLE A.20: C 1s core level XPS fitting condition parameters of the molecular precursor **4**. The main peak has been deconvoluted in the different chemical environments: C-C/C-H, C-Br, C-NH/C-CN and C-Cl, that stand for $C[C_3]/C[C_2H]$, $C[C_2Br]$, $C[CNH]$, $C[CN_2H]$ and $C[N_2Cl]$ shown in Figure 5.9. The relative area corresponds to the stoichiometry at this step.

Precursor 4, Au(111) - Br 3d (Towards Nanographene)				
Temperature	**Component**	**Binding energy [eV]**	**Relative area**	**FWHM [eV]**
As-dep (RT)	Br-C (5/2, 3/2)	69.88, 70.85	100%	1.17, 1.17
100°C	Br-C (5/2, 3/2)	69.69, 70.87	81%	1.18, 1.18
	Br-Au (5/2, 3/2)	68.03, 69.00	19%	1.36, 1.36

TABLE A.21: Br 3d core level XPS fitting condition parameters and constraints of the molecular precursor **4** shown in Figure 5.9. The relative area corresponds to the area variation with respect to the area at RT.

Precursor 4, Au(111) - N 1s (Towards Nanographene)				
Temperature	**Component**	**Binding energy [eV]**	**Relative area**	**FWHM [eV]**
As-dep (RT)	N-C	399.28	100%	1.33
100°C	N-C	399.19	100%	1.25
140°C	N-C	399.46	100%	2.23
200°C	N-C	398.73	54%	2.1

TABLE A.22: N 1s core level XPS fitting condition parameters and constraints of the molecular precursor **4** shown in Figure 5.9. The relative area corresponds to the area variation with respect to the area at RT.

Precursor 4, Au(111) - Cl 2p (Towards Nanographene)				
Temperature	**Component**	**Binding energy [eV]**	**Relative area**	**FWHM [eV]**
As-dep (RT)	Cl-C (3/2, 1/2)	200.23, 201.79	100%	1.04, 1.04
100°C	Cl-C (3/2, 1/2)	200.19, 201.73	92%	0.91, 0.91
140°C	Cl-C (3/2, 1/2)	200.76, 202.53	41%	1.02, 1.02

TABLE A.23: Cl 2p core level XPS fitting condition parameters and constraints of the molecular precursor **4** shown in Figure 5.9. The relative area corresponds to the area variation with respect to the area at RT.

Atomic concentration calculation

The Atomic Concentration of each core level of the elements C 1s, Br 3d, N 1s, Cl 2p and Au 4f of monomer **4** for different reaction steps has been listed in the Tables below. The experimental ratio of the atomic concentration between different elements has been calculated to compare to the nominal stoichiometry.

C 1s Atomic concentration (%)			
Towards NPG		Towards Nanographene	
As dep @ 100ºC	21.51 ± 0.92	As dep @ RT	26.30 ± 0.35
Postanneal. 140ºC	21.74 ± 0.70	Postanneal. 100ºC	25.86 ± 0.35
Postanneal. 200ºC	21.49 ± 0.72	Postanneal. 140ºC	24.86 ± 1.10

TABLE A.24: C 1s atomic concentration for the two different reaction pathways (towards NPG and towards nanographene).

N 1s Atomic concentration (%)			
Towards NPG		Towards Nanographene	
As dep @ 100ºC	2.15 ± 0.30	As dep @ RT	2.92 ± 0.51
Postanneal. 140ºC	2.15 ± 0.41	Postanneal. 100ºC	3.33 ± 0.49
Postanneal. 200ºC	1.84 ± 0.67	Postanneal. 140ºC	3.47 ± 0.64

TABLE A.25: N 1s atomic concentration for the two different reaction pathways (towards NPG and towards nanographene).

Cl 2p (Cl-C) Atomic concentration (%)			
Towards NPG		Towards Nanographene	
As dep @ 100ºC	1.14 ± 0.31	As dep @ RT	1.28 ± 0.17
Postanneal. 140ºC	1.09 ± 0.22	Postanneal. 100ºC	1.47 ± 0.40
Postanneal. 200ºC	0.98 ± 0.43	Postanneal. 140ºC	0.77 ± 0.23

TABLE A.26: Cl 2p (Cl-C component) atomic concentration for the two different reaction pathways (towards NPG and towards nanographene).

Br 3d Atomic concentration (%)					
Towards NPG	Br-C	Br-Au	Towards Nanographene	Br-C	Br-Au
As dep @ 100ºC	0.21 ± 0.04	0.12 ± 0.04	As dep @ RT	0.66 ± 0.04	-
Postanneal. 140ºC	-	0.39 ± 0.004	Postanneal. 100ºC	0.46 ± 0.02	0.09 ± 0.01
Postanneal. 200ºC	-	0.37 ± 0.01	Postanneal. 140ºC	-	-

TABLE A.27: Br 3d atomic concentration for the two different reaction pathways (towards NPG and towards nanographene).

C 1s : N 1s Atomic concentration Ratio			
Towards NPG		Towards Nanographene	
As dep @ 100ºC	10.15 ± 1.37 (13.5%)	As dep @ RT	9.21 ± 1.70 (18.5%)
Postanneal. 140ºC	10.47 ± 2.63 (25.0%)	Postanneal. 100ºC	7.90 ± 1.07 (13.6%)
Postanneal. 200ºC	13.03 ± 5.11 (39.3%)	Postanneal. 140ºC	7.34 ± 1.39 (18.9%)

TABLE A.28: C 1s N 1s atomic concentration ratio for the two different reaction pathways (towards NPG and towards nanographene). Standard deviation has been also represented in percentage.

N 1s : Cl 2p (Cl-C) Atomic concentration Ratio			
Towards NPG		Towards Nanographene	
As dep @ 100ºC	2.01 ± 0.61 (30.3%)	As dep @ RT	2.31 ± 0.38 (16.3%)
Postanneal. 140ºC	2.05 ± 0.62 (30.4%)	Postanneal. 100ºC	2.38 ± 0.63 (26.5%)
Postanneal. 200ºC	2.07 ± 1.06 (51.3%)	Postanneal. 140ºC	4.89 ± 2.01 (41.0%)

TABLE A.29: N 1s : Cl 2p (Cl-C) atomic concentration ratio for the two different reaction pathways (towards NPG and towards nanographene). Standard deviation has been also represented in percentage.

XPS constraints binding energy of multicomponent peaks.

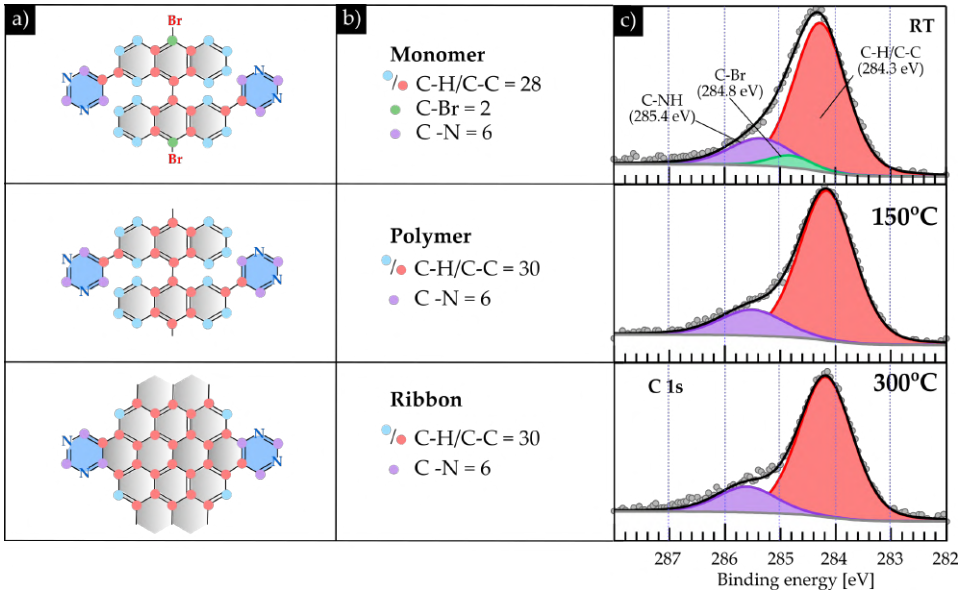

FIGURE A.1: Nominal stoichiometry and C 1s core level peak deconvolution into its different chemical bonds. a) Schematic representation of (from top to bottom): the molecular precursor **3**, a unit cell of the polymer, and a unit cell of the nitrogen-doped ribbon. Every atom has been identified with a circle and a color that represents the different chemical environment and it in accordance with the color of the convoluted peaks in c). b) Nominal stoichiometry of the precursor, intermediate species and final product. c) C 1s core level spectra, convoluted with the four different carbon environments determined from a): $C[C_3]/C[C_2H]$, $C[C_2Br]$, $C[CNH]$ and $C[CN_2H]$.

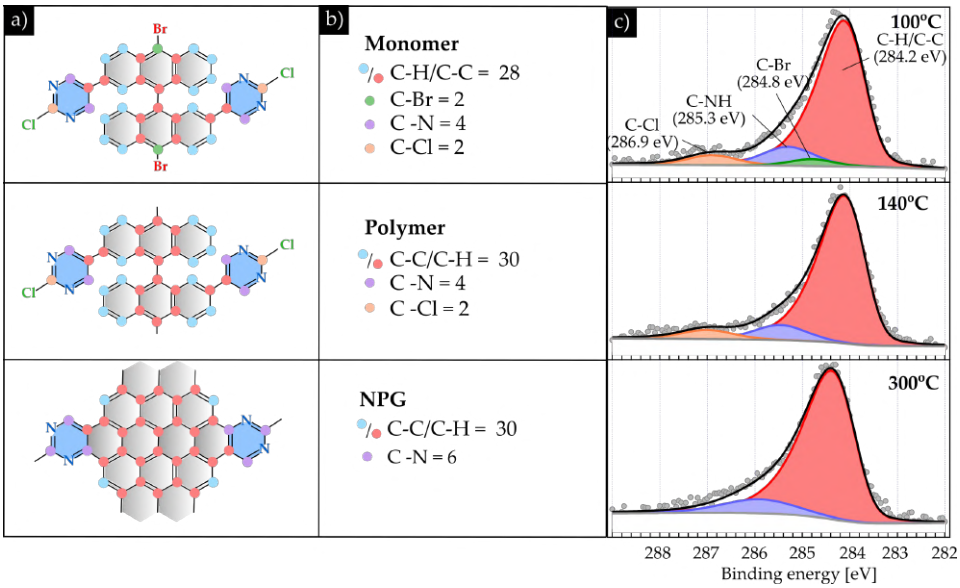

FIGURE A.2: Nominal stoichiometry and C 1s core level peak deconvolution into its different chemical bonds. a) Schematic representation of (from top to bottom): the molecular precursor **4**, a unit cell of the polymer, and a unit cell of the nitrogen-doped NPG. Every atom has been identified with a circle and a color that represents the different chemical environment and it is in accordance with the color of the convoluted peaks in c). b) Nominal stoichiometry of the precursor, intermediate species and final product. c) C 1s core level spectra, convoluted with the four different carbon environments determined from a): $C[C_3]/C[C_2H]$, $C[C_2Br]$, $C[CNH]$, $C[CN_2H]$ and $C[N_2Cl]$.

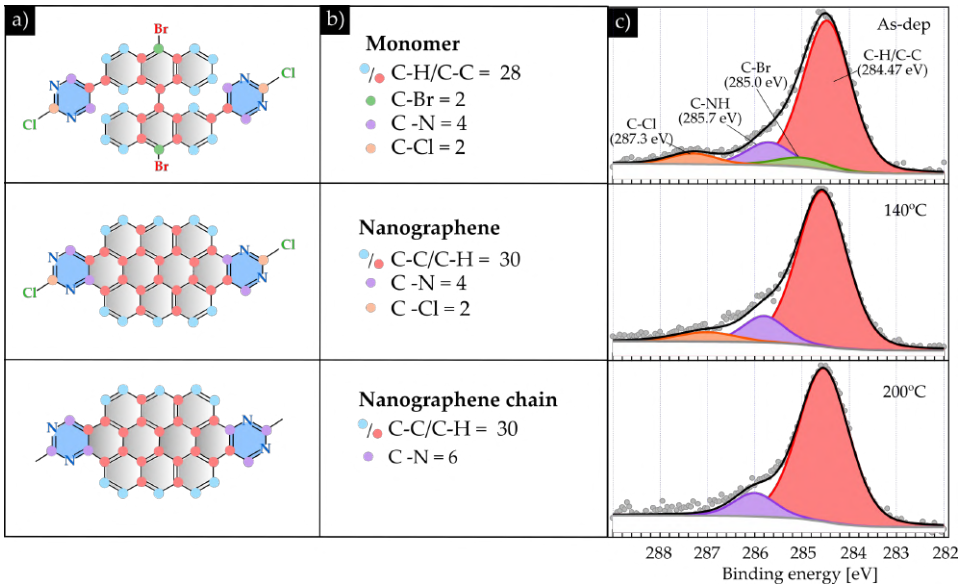

FIGURE A.3: Nominal stoichiometry and C 1s core level peak deconvolution into its different chemical bonds. a) Schematic representation of (from top to bottom): the molecular precursor **4**, a single nanographene, and a unit cell of the nanographene chain. Every atom has been identified with a circle and a color that represents the different chemical environment and it is in accordance with the color of the convoluted peaks in c). b) Nominal stoichiometry of the precursor, intermediate species and final product. c) C 1s core level spectra, convoluted with the four different carbon environments determined from a): $C[C_3]/C[C_2H]$, $C[C_2Br]$, $C[CNH]$, $C[CN_2H]$ and $C[N_2Cl]$.

Acknowledgements

Firstly, I would like to thank my thesis directors Aitor and César, from whom I've learnt so much these years. To Aitor, for being so didactic and for your contagious enthusiasm and motivation in research. To César, for mentoring me every single day, for making me feel valuable and feel equal to others. For transmitting me values like humility and patience, and for being so empathic.

Next I would like to thank Markos, the best office mate I could ever have: for your good advices, for making me think twice, for helping me to take my own decisions. To make my hardest days a bit less tough. To make me see the positive side of things, and to make me laugh. Also, to make me feel valuable, and to make me realize the value of the others.

Many thanks to Bárbara, who lighten the office with jokes and laughs since she arrived. Thank you for making this time so funny with you. There are still so many projects we have to do...! Thanks to all the current members of AMS group: Jose Ramón, and to the new office mates: Kevin, Serni and Esteve, I wish you succeed in your thesis and future projects.

I will not forget the former member of AMS group: Mercedes, Sergi, Alex, Nicolau, Jose Miguel, Dominik, Amina, Miguel. It was really grateful to share the office and the lab with you. Specially I would like to mention the new Doctors: Marc GC and Michele, ... It brings me so good memories when you were here...!

Thank you Marc Vila for being there since university, for helping me in the bachelor, the master, and the PhD. I hope you enjoy a lot your postdoc in Berkeley. And I hope next time we see each other again is in the dance floor!

Thank you Marta (Delgà) for your support, for listening me both professionally and personally, and for counting on me for your experiments. It has been a nice experience to share the lab with you, and I hope it will not be the last time. Thank you also to Pilar and Elisa, for so many good moments!

I would also like to mention the collaborators during these four years: the theoreticians Miguel Pruneda, Pol, and Aran. Many thanks specially to Aran, who welcomed me during one week in DIPC; the chemists, Diego, Jesús and Manuel, to listen to our discussion and new proposals of molecules to synthesize; the people from the ICN2 support division, scientists and technicians: Gustavo Ceballos, Marc Maymó, Roque and Rafa. To Guillaume for helping me in the XPS and Elena del Corro with Raman experiments.

To the JPhD2019 community from UAB: Noe, Miguel Ángel, Jan, Sole, Cris, Martí, Ivan, Artur and Juri. It was a really nice experience to meet you all out of the lab.

Then, I would like to thank Adrián Diaz, for his help, support and good advices in Tsukuba. You help me to understand the Japanese culture and their so strange way of living, in all the aspects. Of course thank you Prof. T. Nakayama, for hosting me in NIMS during two months. Thank you also to Shingaya and Tanaka for helping me in the lab during the experiments. Thank you Kawai, Kewei, Li Qiao, Nobuhiro for making my visit to Japan so pleasant. Arigato gozaimasu!

I would also like to make part of these messages of gratitude to my former teacher of Quantum Mechanics Jordi Pascual. Without your advice I would have never met Aitor and César and hence would not have made this trip of the PhD with them. Thank you Marta González, also one of my former Physics teacher during the bachelor and now my tutor for four years.

Moltes gracièss a la Societat Catalana de Nanociència i Nanotecnologia. Gràcies a vosaltres i a l'activitat que es fa he pogut portar la ciència al costat més social, reivindicatiu i humà. Vaig començar amb vosaltres alhora que vaig començar el doctorat, i m'hi heu acompanyat durant aquests quatre anys. Gràcies per estar al meu costat!

Gracias a Alex, por todo el apoyo y la paciencia que has tenido conmigo durante este proceso, por darme un punto de vista más imparcial de lo que se me atascaba en el trabajo, por enseñarme a hacerme valer, y por confiar en mi durante todo este tiempo.

And last but not least, thank you to all the support I have received from my family. Thanks a lot to my parents and brother (I know they

will appreciate the acknowledgement in English) for putting faith in my decisions and being so close even from so far. For being so proud of me. Also to my grandparents, for being so interested and concerned of my work.

List of publications

- C. Moreno, M. Panighel, M. Vilas-Varela, G. Sauthier, **M. Tenorio**, G. Ceballos, D. Peña, A. Mugarza. "Critical Role of Phenyl Substitution and Catalytic Substrate in the Surface-Assisted Polymerization of Dibromobianthracene Derivatives". In: *Chemistry of Materials* 31 (2019), pp:331-341. DOI: 10.1021/acs.chemmater.8b03094

- **M. Tenorio**, C. Moreno, P. Febrer, J. Castro-Esteban, P. Ordejón, D. Peña, M. Pruneda, A. Mugarza. "Atomically sharp superlattice heterojunctions built-in nitrogen-doped nanoporous graphene". In: *Advanced Materials (under review)*

- **M. Tenorio**, C. Moreno, P. Febrer, J. Castro-Esteban, D. Peña, M. Pruneda, A. Mugarza. "Towards bottom-up synthesis of prochiral nitrogen-doped nanoporous graphene" *(under preparation)*

- **M. Tenorio**, C. Moreno, P. Febrer, J. Castro-Esteban, D. Peña, M. Pruneda, A. Mugarza. "On-surface transformation of topologically-induced graphene nanoribbon 1D superlattices" *(under preparation)*

- **M. Tenorio**, C. Moreno, J. Castro-Esteban, D. Peña, A. Mugarza. "kinetically-induced bottom-up synthesis of nitrogen-doped ovalenes" *(under preparation)*

Bibliography

[1] K.S. Novoselov et al. "Electric Field in Atomically Thin Carbon Films". In: *Science* 306.5696 (2004), pp. 666–669. DOI: 10.1126/science.1102896. URL: https://www.science.org/doi/10.1126/science.1102896.

[2] Changgu Lee et al. "Measurement of the Elastic Properties and Intrinsic Strength of Monolayer Graphene". In: *Science* 321.July (2008), pp. 385–388.

[3] K. I. Bolotin et al. "Ultrahigh electron mobility in suspended graphene". In: *Solid State Communications* 146.9-10 (2008), pp. 351–355. ISSN: 00381098. DOI: 10.1016/j.ssc.2008.02.024. arXiv: 0802.2389.

[4] K S Novoselov et al. "Room-Temperature Quantum Hall". In: *Science* 315.5817 (2007), pp. 1379–1379. URL: https://www.science.org/doi/10.1126/science.1137201.

[5] Alexander A. Balandin et al. "Superior thermal conductivity of single-layer graphene". In: *Nano Letters* 8.3 (2008), pp. 902–907. ISSN: 15306984. DOI: 10.1021/nl0731872.

[6] Zhenliang Hao et al. "Tuning the Electronic Properties of Atomically Precise Graphene Nanoribbons by Bottom-Up Fabrication". In: *ChemNanoMat* 6.4 (2020), pp. 493–515. ISSN: 2199692X. DOI: 10.1002/cnma.201900706.

[7] Klaus Müllen and Jürgen P. Rabe. "Nanographenes as active components of single-molecule electronics and how a scanning tunneling microscope puts them to work". In: *Accounts of Chemical Research* 41.4 (2008), pp. 511–520. ISSN: 00014842. DOI: 10.1021/ar7001446.

[8] Jingwei Bai et al. "Graphene nanomesh". In: *Nature Nanotechnology* 5.3 (2010), pp. 190–194. ISSN: 17483395. DOI: 10.1038/nnano.2010.8.

[9] Zongping Chen, Akimitsu Narita, and Klaus Müllen. "Graphene Nanoribbons: On-Surface Synthesis and Integration into Electronic Devices". In: *Advanced Materials* 32.45 (2020), pp. 1–26. ISSN: 15214095. DOI: 10.1002/adma.202001893.

[10] Klaus Müllen and Xinliang Feng. *From Polyphenylenes to Nanographenes and Graphene Nanoribbons*. Vol. 278. 2017, pp. 1–32. ISBN: 9783319641706. DOI: 10.1007/978-3-319-64170-6. URL: https://books.google.de/books?id=7YM0DwAAQBAJhttp://link.springer.com/10.1007/978-3-319-64170-6.

[11] Shaotang Song et al. "On-surface synthesis of graphene nanostructures with π-magnetism". In: *Chemical Society Reviews* 50.5 (2021), pp. 3238–3262. ISSN: 14604744. DOI: 10.1039/d0cs01060j.

[12] C. Toninelli et al. "Single organic molecules for photonic quantum technologies". In: *Nature Materials* (2021), pp. 1615–1628. ISSN: 14764660. DOI: 10.1038/s41563-021-00987-4. arXiv: 2011.05059.

[13] Víctor Bonal et al. "Solution-processed nanographene distributed feedback lasers". In: *Nature Communications* 10.1 (2019), pp. 1–10. ISSN: 20411723. DOI: 10.1038/s41467-019-11336-0. URL: http://dx.doi.org/10.1038/s41467-019-11336-0.

[14] Qiang Chen et al. "Dibenzo[hi, st]ovalene as Highly Luminescent Nanographene: Efficient Synthesis via Photochemical Cyclodehydroiodination, Optoelectronic Properties, and Single-Molecule Spectroscopy". In: *Journal of the American Chemical Society* 141.41 (2019), pp. 16439–16449. ISSN: 15205126. DOI: 10.1021/jacs.9b08320.

[15] Giuseppe Maria Paternò et al. "Large Polycyclic Aromatic Hydrocarbons as Graphene Quantum Dots: from Synthesis to Spectroscopy and Photonics". In: *Advanced Optical Materials* (2021), pp. 1–18. ISSN: 2195-1071. DOI: 10.1002/adom.202100508. URL: https://onlinelibrary.wiley.com/doi/10.1002/adom.202100508.

[16] Enquan Jin et al. "A Highly Luminescent Nitrogen-Doped Nanographene as an Acid- and Metal-Sensitive Fluorophore for Optical Imaging". In: *Journal of the American Chemical Society* 143 (2021), pp. 2–11. DOI: 10.1021/jacs.1c04880.

[17] E. F. Holby and C. D. Taylor. "Control of graphene nanoribbon vacancies by Fe and N dopants: Implications for catalysis". In: *Applied Physics Letters* 101.6 (2012), pp. 1–4. ISSN: 00036951. DOI: 10.1063/1.4742890.

[18] Di Wu et al. "High-performance porous graphene from synergetic nitrogen doping and physical activation for advanced nonradical oxidation". In: *Journal of Hazardous Materials* 381.August 2019 (2020), pp. 1–10. ISSN: 18733336. DOI: 10.1016/j.jhazmat.2019.121010.

[19] Kyeong Min Cho et al. "Edge-Functionalized Graphene Nanoribbon Chemical Sensor: Comparison with Carbon Nanotube and Graphene". In: *ACS Applied Materials and Interfaces* 10.49 (2018), pp. 42905–42914. ISSN: 19448252. DOI: 10.1021/acsami.8b16688.

[20] Juan Amaro-Gahete et al. "Luminescent Graphene-Based Materials via Europium Complexation on Dipyridylpyridazine-Functionalized Graphene Sheets". In: *Chemistry - A European Journal* 25.27 (2019), pp. 6823–6830. ISSN: 15213765. DOI: 10.1002/chem.201900512.

[21] T. S. Sreeprasad and Vikas Berry. "How do the electrical properties of graphene change with its functionalization?" In: *Small* 9.3 (2013), pp. 341–350. ISSN: 16136810. DOI: 10.1002/smll.201202196.

[22] Stephanie J. Heerema and Cees Dekker. "Graphene nanodevices for DNA sequencing". In: *Nature Nanotechnology* 11.2 (2016), pp. 127–136. ISSN: 17483395. DOI: 10.1038/nnano.2015.307. arXiv: arXiv:1011.1669v3. URL: http://dx.doi.org/10.1038/nnano.2015.307.

[23] De-en Jiang, Valentino R Cooper, and Sheng Dai. "Porous graphene as the ultimate membrane for gas separation". In: *Nano letters* 9.12 (2009). ISSN: 1530-6992. DOI: 10.1021/nl9021946. URL: http://www.ncbi.nlm.nih.gov/pubmed/19995080.

[24] Hongxin Tan et al. "Nitrogen-doped nanoporous graphene induced by a multiple confinement strategy for membrane separation of rare earth". In: *iScience* 24.1 (2021), pp. 1–11. ISSN: 25890042. DOI: 10.1016/j.isci.2020.101920. URL: https://doi.org/10.1016/j.isci.2020.101920.

[25] Yuanyuan Zhang, Qijin Wan, and Nianjun Yang. "Recent Advances of Porous Graphene: Synthesis, Functionalization, and Electrochemical Applications". In: *Small* 15.48 (2019). ISSN: 16136829. DOI: 10.1002/smll.201903780.

[26] Jun Yang et al. "Graphene nanomesh: New versatile materials". In: *Nanoscale* 6.22 (2014), pp. 13301–13313. ISSN: 20403372. DOI: 10.1039/c4nr04584j.

[27] Petr Lazar, Radim Mach, and Michal Otyepka. "Spectroscopic Fingerprints of Graphitic, Pyrrolic, Pyridinic, and Chemisorbed Nitrogen in N-Doped Graphene". In: *Journal of Physical Chemistry C* 123.16 (2019), pp. 10695–10702. ISSN: 19327455. DOI: 10.1021/acs.jpcc.9b02163.

[28] Melinda Y. Han et al. "Energy band-gap engineering of graphene nanoribbons". In: *Physical Review Letters* 98.20 (2007), pp. 1–4. ISSN: 00319007. DOI: 10.1103/PhysRevLett.98.206805. arXiv: 0702511 [cond-mat].

[29] Akimitsu Narita et al. "Synthesis of structurally well-defined and liquid-phase-processable graphene nanoribbons". In: *Nature Chemistry* 6.2 (2014), pp. 126–132. ISSN: 17554330. DOI: 10.1038/nchem.1819.

[30] Akimitsu Narita et al. "New advances in nanographene chemistry". In: *Chemical Society Reviews* 44.18 (2015), pp. 6616–6643. ISSN: 14604744. DOI: 10.1039/c5cs00183h.

[31] Akimitsu Narita, Xinliang Feng, and Klaus Müllen. "Bottom-up synthesis of chemically precise graphene nanoribbons". In: *Chemical Record* 15.1 (2015), pp. 295–309. ISSN: 15280691. DOI: 10.1002/tcr.201402082.

[32] Xiao Ye Wang, Xuelin Yao, and Klaus Müllen. "Polycyclic aromatic hydrocarbons in the graphene era". In: *Science China Chemistry* 62.9 (2019), pp. 1099–1144. ISSN: 18691870. DOI: 10.1007/s11426-019-9491-2.

[33] Zijie Qiu, Akimitsu Narita, and Klaus Müllen. "Spiers Memorial Lecture: Carbon nanostructures by macromolecular design-from branched polyphenylenes to nanographenes and graphene nanoribbons". In: *Faraday Discussions* 227 (2021), pp. 8–45. ISSN: 13645498. DOI: 10.1039/d0fd00023j.

[34] Katsuhiko Ariga et al. "Nanoarchitectonics: A new materials horizon for nanotechnology". In: *Materials Horizons* 2.4 (2015), pp. 406–413. ISSN: 20516355. DOI: 10.1039/c5mh00012b. URL: http://dx.doi.org/10.1039/C5MH00012B.

[35] Sylvain Clair and Dimas G. de Oteyza. "Controlling a Chemical Coupling Reaction on a Surface: Tools and Strategies for On-Surface Synthesis". In: *Chemical Reviews* (2018). ISSN: 0009-2665. DOI: 10.1021/acs.chemrev.8b00601. URL: http://feedproxy.google.com/{~}r/acs/chreay/{~}3/qVtiV5-Ewa0/acs.chemrev.8b00601.

[36] Leopold Talirz, Pascal Ruffieux, and Roman Fasel. "On-Surface Synthesis of Atomically Precise Graphene Nanoribbons". In: *Advanced Materials* 28.29 (2016), pp. 6222–6231. ISSN: 15214095. DOI: 10.1002/adma.201505738.

[37] Qiang Sun et al. "On-Surface Synthesis of Carbon Nanostructures". In: *Advanced Materials* 30.17 (2018), pp. 1–12. ISSN: 15214095. DOI: 10.1002/adma.201705630.

[38] R. S. Koen Houtsma, Joris de la Rie, and Meike Stöhr. "Atomically precise graphene nanoribbons: interplay of structural and electronic properties". In: *Chemical Society Reviews* (2021), pp. 6541–6568. ISSN: 0306-0012. DOI: 10.1039/d0cs01541e.

[39] Andreas Stabel et al. "Diodelike Current-Voltage Curves for a Single Molecule. - Tunneling Spectroscopy with Submoleculaar Resolution of an Alhylated, pero-condensed hexabenzocoronene." In: *Angewandte Chemie - International Edition* 34.15 (1995), pp. 1609–16011.

[40] Klaus Weiss et al. "Template-mediated synthesis of polycyclic aromatic hydrocarbons: Cyclodehydrogenation and planarization of a hexaphenylbenzene derivative at a copper surface". In: *Angewandte Chemie - International Edition* 38.24 (1999), pp. 3748–3752. ISSN: 14337851. DOI: 10.1002/(SICI)1521-3773(19991216)38:24<3748::AID-ANIE3748>3.0.CO;2-0.

[41] Qigang Zhong et al. "Benzo-Fused Periacenes or Double Helicenes? Different Cyclodehydrogenation Pathways on Surface and in Solution". In: *Journal of the American Chemical Society* 141.18 (2019), pp. 7399–7406. ISSN: 15205126. DOI: 10.1021/jacs.9b01267.

[42] Niko Pavli et al. "Synthesis and characterization of triangulene". In: *Nature Nanotechnology* 12.April (2017), pp. 308–312. DOI: 10.1038/nnano.2016.305.

[43] Matthias Treier et al. "Surface-assisted cyclodehydrogenation provides a synthetic route towards easily processable and chemically tailored nanographenes". In: *Nature Chemistry* 3.1 (2011), pp. 61–67. ISSN: 17554330. DOI: 10.1038/nchem.891.

[44] Thorsten G. Lohr et al. "On-Surface Synthesis of Non-Benzenoid Nanographenes by Oxidative Ring-Closure and Ring-Rearrangement Reactions". In: *Journal of the American Chemical Society* 142.31 (2020), pp. 13565–13572. ISSN: 15205126. DOI: 10.1021/jacs.0c05668.

[45] Jeremy Hieulle et al. "On-Surface Route for Producing Planar Nanographenes with Azulene Moieties". In: *Nano Letters* 18.1 (2018), pp. 418–423. ISSN: 15306992. DOI: 10.1021/acs.nanolett.7b04309.

[46] Biao Yang, Bin Dong, and Lifeng Chi. "On-Surface Intramolecular Reactions". In: *ACS Nano* 14.6 (2020), pp. 6376–6382. ISSN: 1936086X. DOI: 10.1021/acsnano.0c03766.

[47] Rafal Zuzak et al. "Building a 22-ring nanographene by combining in-solution and on-surface syntheses". In: *Chemical Communications* 54.73 (2018), pp. 10256–10259. ISSN: 1364548X. DOI: 10.1039/c8cc05353g.

[48] Rafal Zuzak et al. "Synthesis and reactivity of a trigonal porous nanographene on a gold surface". In: *Chemical Science* 10.43 (2019), pp. 10143–10148. ISSN: 20416539. DOI: 10.1039/c9sc03404h.

[49] Xiushang Xu et al. "On-surface synthesis of dibenzohexacenohexacene and dibenzopentaphenoheptaphene". In: *Bulletin of the Chemical Society of Japan* 94.3 (2021), pp. 997–999. ISSN: 13480634. DOI: 10.1246/BCSJ.20200382.

[50] Marco Di Giovannantonio et al. "Large-Cavity Coronoids with Different Inner and Outer Edge Structures". In: *Journal of the American Chemical Society* 142.28 (2020), pp. 12046–12050. ISSN: 15205126. DOI: 10.1021/jacs.0c05268.

[51] Jinming Cai et al. "Atomically precise bottom-up fabrication of graphene nanoribbons". In: *Nature* 466.7305 (2010), pp. 470–473. ISSN: 00280836. DOI: 10.1038/nature09211.

[52] Maximilian Ammon, Tim Sander, and Sabine Maier. "On-Surface Synthesis of Porous Carbon Nanoribbons from Polymer Chains". In: *Journal of the American Chemical Society* 139.37 (2017), pp. 12976–12984. ISSN: 15205126. DOI: 10.1021/jacs.7b04783.

[53] Maximilian Ammon et al. "On-Surface Synthesis of Porous Carbon Nanoribbons on Silver : Reaction Kinetics and the Influence of the Surface Structure". In: *ChemPhysChem* 111 (2019), pp. 2333–2339. DOI: 10.1002/cphc.201900347.

[54] Jeremy Hieulle et al. "On-Surface Synthesis and Collective Spin Excitations of a Triangulene-Based Nanostar". In: *Angewandte Chemie - International Edition* 60.48 (2021), pp. 25224–25229. ISSN: 15213773. DOI: 10.1002/anie.202108301. arXiv: 2107.02198.

[55] Jingcheng Li et al. "Uncovering the Triplet Ground State of Triangular Graphene Nanoflakes Engineered with Atomic Precision on a Metal Surface". In: *Physical Review Letters* 124.17 (2020), p. 177201. ISSN: 10797114. DOI: 10.1103/PhysRevLett.124.177201. URL: https://doi.org/10.1103/PhysRevLett.124.177201.

[56] Shantanu Mishra et al. "Topological Defect-Induced Magnetism in a Nanographene". In: *Journal of the American Chemical Society* 142.3 (2020), pp. 1147–1152. ISSN: 15205126. DOI: 10.1021/jacs.9b09212.

[57] Shantanu Mishra et al. "Topological frustration induces unconventional magnetism in a nanographene". In: *Nature Nanotechnology* 15.1 (2020), pp. 22–28. ISSN: 17483395. DOI: 10.1038/s41565-019-0577-9. URL: http://dx.doi.org/10.1038/s41565-019-0577-9.

[58] Shantanu Mishra et al. "Collective All-Carbon Magnetism in Triangulene Dimers". In: *Angewandte Chemie - International Edition* 59.29 (2020), pp. 12041–12047. ISSN: 15213773. DOI: 10.1002/anie.202002687.

[59] Shantanu Mishra et al. "Observation of fractional edge excitations in nanographene spin chains". In: *Nature* 598.7880 (2021), pp. 287–292. ISSN: 14764687. DOI: 10.1038/s41586-021-03842-3. arXiv: 2105.09102.

[60] Shantanu Mishra et al. "Synthesis and characterization of [7]triangulene". In: *Nanoscale* 13.3 (2021), pp. 1624–1628. ISSN: 20403372. DOI: 10.1039/d0nr08181g.

[61] Shantanu Mishra et al. "Large magnetic exchange coupling in rhombus-shaped nanographenes with zigzag periphery". In: *Nature Chemistry* (2021). DOI: 10.1038/s41557-021-00678-2.

[62] Ana Sánchez-Grande et al. "Unravelling the Open-Shell Character of Peripentacene on Au(111)". In: *Journal of Physical Chemistry Letters* 12.1 (2021), pp. 330–336. ISSN: 19487185. DOI: 10.1021/acs.jpclett.0c02518.

[63] Jie Su et al. "On-Surface Synthesis and Characterization of [7]Triangulene Quantum Ring". In: *Nano Letters* 21.1 (2021), pp. 861–867. ISSN: 15306992. DOI: 10.1021/acs.nanolett.0c04627.

[64] Elia Turco et al. "On-Surface Synthesis and Characterization of Supernonazethrene". In: *The Journal of Physical Chemistry Letters* 12.34 (2021), pp. 8314–8319. ISSN: 1948-7185. DOI: 10.1021/acs.jpclett.1c02381.

[65] Yuqiang Zheng et al. “Designer spin order in diradical nanographenes”. In: *Nature Communications* 11.1 (2020), pp. 1–7. ISSN: 20411723. DOI: 10.1038/s41467-020-19834-2. URL: http://dx.doi.org/10.1038/s41467-020-19834-2.

[66] Leonhard Grill et al. “Nano-architectures by covalent assembly of molecular building blocks”. In: *Nature Nanotechnology* 2.11 (2007), pp. 687–691. ISSN: 17483395. DOI: 10.1038/nnano.2007.346.

[67] Sebastian Thussing et al. “Reaction Pathway toward Seven-Atom-Wide Armchair Graphene Nanoribbon Formation and Identification of Intermediate Species on Au(111)”. In: *Journal of Physical Chemistry C* 124.29 (2020), pp. 16009–16018. ISSN: 19327455. DOI: 10.1021/acs.jpcc.0c04596.

[68] L. Lafferentz et al. “Controlling on-surface polymerization by hierarchical and substrate-directed growth”. In: *Nature Chemistry* 4.3 (2012), pp. 215–220. ISSN: 17554330. DOI: 10.1038/nchem.1242.

[69] Christopher Bronner et al. “Aligning the band gap of graphene nanoribbons by monomer doping”. In: *Angewandte Chemie - International Edition* 52.16 (2013), pp. 4422–4425. ISSN: 14337851. DOI: 10.1002/anie.201209735.

[70] Patrick B. Bennett et al. “Bottom-up graphene nanoribbon field-effect transistors”. In: *Applied Physics Letters* 103.25 (2013), pp. 1–5. ISSN: 00036951. DOI: 10.1063/1.4855116.

[71] Jinming Cai et al. “Graphene nanoribbon heterojunctions”. In: *Nature Nanotechnology* 9.11 (2014), pp. 896–900. ISSN: 17483395. DOI: 10.1038/nnano.2014.184. URL: http://dx.doi.org/10.1038/nnano.2014.184.

[72] Yen Chia Chen et al. “Molecular bandgap engineering of bottom-up synthesized graphene nanoribbon heterojunctions”. In: *Nature Nanotechnology* 10.2 (2015), pp. 156–160. ISSN: 17483395. DOI: 10.1038/nnano.2014.307.

[73] Christopher Bronner et al. “Hierarchical On-Surface Synthesis of Graphene Nanoribbon Heterojunctions”. In: *ACS Nano* 12.3 (2018), pp. 2193–2200. ISSN: 1936086X. DOI: 10.1021/acsnano.7b08658.

[74] Ting Cao, Fangzhou Zhao, and Steven G. Louie. "Topological Phases in Graphene Nanoribbons: Junction States, Spin Centers, and Quantum Spin Chains". In: *Physical Review Letters* 119.7 (2017), pp. 1–5. ISSN: 10797114. DOI: 10.1103/PhysRevLett.119.076401. arXiv: 1702.02674.

[75] Oliver Gröning et al. "Engineering of robust topological quantum phases in graphene nanoribbons". In: *Nature* 560.7717 (2018), pp. 209–213. ISSN: 14764687. DOI: 10.1038/s41586-018-0375-9. arXiv: 1805.06635.

[76] Daniel J. Rizzo et al. "Topological band engineering of graphene nanoribbons". In: *Nature* 560.7717 (2018), pp. 204–208. ISSN: 14764687. DOI: 10.1038/s41586-018-0376-8. arXiv: 1805.06470. URL: http://dx.doi.org/10.1038/s41586-018-0376-8.

[77] Qiang Sun et al. "Evolution of the Topological Energy Band in Graphene Nanoribbons". In: *The Journal of Physical Chemistry Letters* (2021), pp. 8679–8684. ISSN: 1948-7185. DOI: 10.1021/acs.jpclett.1c02541.

[78] Qiang Sun et al. "Massive Dirac Fermion Behavior in a Low Bandgap Graphene Nanoribbon Near a Topological Phase Boundary". In: *Advanced Materials* 32.12 (2020), pp. 1–8. ISSN: 15214095. DOI: 10.1002/adma.201906054.

[79] Qiang Sun et al. "Coupled Spin States in Armchair Graphene Nanoribbons with Asymmetric Zigzag Edge Extensions". In: *Nano Letters* 20.9 (2020), pp. 6429–6436. ISSN: 15306992. DOI: 10.1021/acs.nanolett.0c02077. arXiv: 2005.02147.

[80] Xiushang Xu et al. "On-surface activation of benzylic C-H bonds for the synthesis of pentagon-fused graphene nanoribbons". In: *Nano Research* 12.1 (2021), pp. 1–6. ISSN: 19980000. DOI: 10.1007/s12274-021-3419-2.

[81] Vivek Saraswat, Robert M. Jacobberger, and Michael S. Arnold. "Materials Science Challenges to Graphene Nanoribbon Electronics". In: *ACS Nano* 15.3 (2021), pp. 3674–3708. ISSN: 1936086X. DOI: 10.1021/acsnano.0c07835.

[82] Haomin Wang et al. "Graphene nanoribbons for quantum electronics". In: *Nature Reviews Physics* (2021), pp. 791–802. ISSN: 25225820. DOI: 10.1038/s42254-021-00370-x.

[83] A. H. Castro Neto et al. "The electronic properties of graphene". In: *Reviews of Modern Physics* 81.1 (2009), pp. 109–162. ISSN: 00346861. DOI: 10.1103/RevModPhys.81.109. arXiv: 0709.1163.

[84] Pascal Ruffieux et al. "On-surface synthesis of graphene nanoribbons with zigzag edge topology". In: *Nature* 531.7595 (2016), pp. 489–492. ISSN: 14764687. DOI: 10.1038/nature17151.

[85] Dong Han and Junfa Zhu. "Surface-assisted fabrication of low-dimensional carbon-based nanoarchitectures". In: *Journal of Physics: Condensed Matter* 33 (2021), pp. 1–36.

[86] M. Lackinger. "Surface-assisted Ullmann coupling". In: *Chemical Communications* 53.56 (2017), pp. 7872–7885. ISSN: 1364548X. DOI: 10.1039/c7cc03402d.

[87] Néstor Merino-Díez et al. "Hierarchy in the Halogen Activation During Surface-Promoted Ullmann Coupling". In: *ChemPhysChem* 20.18 (2019), pp. 2305–2310. ISSN: 14397641. DOI: 10.1002/cphc.201900633.

[88] Christopher Bronner, Jonas Björk, and Petra Tegeder. "Tracking and removing br during the on-surface synthesis of a graphene nanoribbon". In: *Journal of Physical Chemistry C* 119.1 (2015), pp. 486–493. ISSN: 19327455. DOI: 10.1021/jp5106218.

[89] Maryam Abyazisani, Jennifer M. MacLeod, and Josh Lipton-Duffin. "Cleaning up after the Party: Removing the Byproducts of On-Surface Ullmann Coupling". In: *ACS Nano* 13.8 (2019), pp. 9270–9278. ISSN: 1936086X. DOI: 10.1021/acsnano.9b03812.

[90] Kewei Sun et al. "Low-Temperature Removal of Dissociated Bromine by Silicon Atoms for an On-Surface Ullmann Reaction". In: *Journal of Physical Chemistry C* 124.36 (2020), pp. 19675–19680. ISSN: 19327455. DOI: 10.1021/acs.jpcc.0c06188.

[91] Peter H. Jacobse et al. "Aryl Radical Geometry Determines Nanographene Formation on Au(111)". In: *Angewandte Chemie - International Edition* 55.42 (2016), pp. 13052–13055. ISSN: 15213773. DOI: 10.1002/anie.201606440.

[92] Peter H. Jacobse et al. "One Precursor but Two Types of Graphene Nanoribbons: On-Surface Transformations of 10,10'-Dichloro-9,9'-bianthryl on Ag(111)". In: *Journal of Physical Chemistry C* 123.14 (2019), pp. 8892–8901. ISSN: 19327455. DOI: 10.1021/acs.jpcc.8b12209.

[93] Konstantin A. Simonov et al. "Effect of substrate chemistry on the bottom-up fabrication of graphene nanoribbons: Combined core-level spectroscopy and STM study". In: *Journal of Physical Chemistry C* 118.23 (2014), pp. 12532–12540. ISSN: 19327455. DOI: 10.1021/jp502215m.

[94] Konstantin A. Simonov et al. "From Graphene Nanoribbons on Cu(111) to Nanographene on Cu(110): Critical Role of Substrate Structure in the Bottom-Up Fabrication Strategy". In: *ACS Nano* 9.9 (2015), pp. 8997–9011. ISSN: 1936086X. DOI: 10.1021/acsnano.5b03280.

[95] K. A. Simonov et al. "Synthesis of armchair graphene nanoribbons from the 10,10-dibromo-9,9-bianthracene molecules on Ag(111): The role of organometallic intermediates". In: *Scientific Reports* 8.1 (2018), pp. 1–12. ISSN: 20452322. DOI: 10.1038/s41598-018-21704-3.

[96] César Moreno et al. "Critical Role of Phenyl Substitution and Catalytic Substrate in the Surface-Assisted Polymerization of Dibromobianthracene Derivatives". In: *Chemistry of Materials* 31.2 (2019), pp. 331–341. ISSN: 15205002. DOI: 10.1021/acs.chemmater.8b03094.

[97] Dimas G. De Oteyza et al. "Substrate-Independent Growth of Atomically Precise Chiral Graphene Nanoribbons". In: *ACS Nano* 10.9 (2016), pp. 9000–9008. ISSN: 1936086X. DOI: 10.1021/acsnano.6b05269.

[98] Felix Hanke and Jonas Björk. "Structure and local reactivity of the Au(111) surface reconstruction". In: *Physical Review B - Condensed Matter and Materials Physics* 87.23 (2013), pp. 1–6. ISSN: 10980121. DOI: 10.1103/PhysRevB.87.235422.

[99] Néstor Merino-Díez et al. "Switching from Reactant to Substrate Engineering in the Selective Synthesis of Graphene Nanoribbons". In: *Journal of Physical Chemistry Letters* 9.10 (2018), pp. 2510–2517. ISSN: 19487185. DOI: 10.1021/acs.jpclett.8b00796.

[100] Pascal Ruffieux et al. "Electronic structure of atomically precise graphene nanoribbons". In: *ACS Nano* 6.8 (2012), pp. 6930–6935. ISSN: 19360851. DOI: 10.1021/nn3021376.

[101] S. Linden et al. "Electronic structure of spatially aligned graphene nanoribbons on Au(788)". In: *Physical Review Letters* 108.21 (2012), pp. 23–27. ISSN: 00319007. DOI: 10.1103/PhysRevLett.108.216801.

[102] Vikram Passi et al. "Field-Effect Transistors Based on Networks of Highly Aligned, Chemically Synthesized N = 7 Armchair Graphene Nanoribbons". In: *ACS Applied Materials and Interfaces* 10.12 (2018), pp. 9900–9903. ISSN: 19448252. DOI: 10.1021/acsami.8b01116.

[103] M. Corso et al. "Electronic states in faceted Au(111) studied with curved crystal surfaces". In: *Journal of Physics Condensed Matter* 21.35 (2009). ISSN: 09538984. DOI: 10.1088/0953-8984/21/35/353001.

[104] Sihan Zhao et al. "Optical Imaging and Spectroscopy of Atomically Precise Armchair Graphene Nanoribbons". In: *Nano Letters* 20.2 (2020), pp. 1124–1130. ISSN: 15306992. DOI: 10.1021/acs.nanolett.9b04497.

[105] Afaf El-Sayed et al. "Synthesis of Graphene Nanoribbons on a Kinked Au Surface: Revealing the Frontier Valence Band at the Brillouin Zone Center". In: *Journal of Physical Chemistry C* 124.28 (2020), pp. 15474–15480. ISSN: 19327455. DOI: 10.1021/acs.jpcc.0c02801.

[106] Pengzhan Sun, Kunlin Wang, and Hongwei Zhu. "Recent Developments in Graphene-Based Membranes: Structure, Mass-Transport Mechanism and Potential Applications". In: *Advanced Materials* 28.12 (2016), pp. 2287–2310. ISSN: 15214095. DOI: 10.1002/adma.201502595.

[107] Albert Guirguis et al. "Applications of nano-porous graphene materials-critical review on performance and challenges". In: *Materials Horizons* 7.5 (2020), pp. 1218–1245. ISSN: 20516355. DOI: 10.1039/c9mh01570a.

[108] Kyaw Sint, Boyang Wang, and Petr Král. "Selective ion passage through functionalized graphene nanopores". In: *Journal of the American Chemical Society* 130.49 (2008), pp. 16448–16449. ISSN: 00027863. DOI: 10.1021/ja804409f.

[109] Chengzhen Sun, Boyao Wen, and Bofeng Bai. "Application of nanoporous graphene membranes in natural gas processing: Molecular simulations of CH4/CO2, CH4/H2S and CH4/N2 separation". In: *Chemical Engineering Science* 138 (2015), pp. 616–621. ISSN: 00092509. DOI: 10.1016/j.ces.2015.08.049. URL: http://dx.doi.org/10.1016/j.ces.2015.08.049.

[110] Kyoungjun Choi et al. "Multifunctional wafer-scale graphene membranes for fast ultrafiltration and high permeation gas separation". In: *Science Advances* 4.11 (2018), pp. 1–11. ISSN: 23752548. DOI: 10.1126/sciadv.aau0476.

[111] A. Fang et al. "Highly mechanosensitive ion channels from graphene-embedded crown ethers". In: *Nature Materials* 18.1 (2019), pp. 76–81. ISSN: 14764660. DOI: 10.1038/s41563-018-0220-4. URL: http://dx.doi.org/10.1038/s41563-018-0220-4.

[112] Song Wang, Sheng Dai, and De-en Jiang. " Entropic selectivity in air separation via a bilayer nanoporous graphene membrane ". In: *Physical Chemistry Chemical Physics* 21.29 (2019), pp. 16310–16315. ISSN: 1463-9076. DOI: 10.1039/c9cp02670c.

[113] V. Hung Nguyen et al. "Graphene nanomesh-based devices exhibiting a strong negative differential conductance effect". In: *Nanotechnology* 23.28 (2012). ISSN: 09574484. DOI: 10.1088/0957-4484/23/28/289502.

[114] Jing Li and Christophe Delerue. "Intrinsic transport properties of nanoporous graphene highly suitable for complementary field-effect transistors". In: *2D Materials* 6.3 (2019). ISSN: 20531583. DOI: 10.1088/2053-1583/ab1c25.

[115] Jacob D. Teeter et al. "Dense monolayer films of atomically precise graphene nanoribbons on metallic substrates enabled by direct contact transfer of molecular precursors". In: *Nanoscale* 9.47 (2017), pp. 18835–18844. ISSN: 20403372. DOI: 10.1039/c7nr06027k.

[116] Mikhail Shekhirev, Percy Zahl, and Alexander Sinitskii. "Phenyl functionalization of atomically precise graphene nanoribbons for engineering inter-ribbon interactions and graphene nanopores". In: *ACS Nano* 12.8 (2018), pp. 8662–8669. ISSN: 1936086X. DOI: 10.1021/acsnano.8b04489.

[117] Dong Han et al. "On-Surface Synthesis of Armchair-Edged Graphene Nanoribbons with Zigzag Topology". In: *Journal of Physical Chemistry C* 124.9 (2020), pp. 5248–5256. ISSN: 19327455. DOI: 10.1021/acs.jpcc.0c00018.

[118] César Moreno et al. "Bottom-up synthesis of multifunctional nanoporous graphene". In: *Science* 360.6385 (2018), pp. 199–203. ISSN: 0036-8075. DOI: 10.1126/science.aar2009. URL: http://www.sciencemag.org/lookup/doi/10.1126/science.aar2009.

[119] César Moreno et al. "Critical Role of Phenyl Substitution and Catalytic Substrate in the Surface-Assisted Polymerization of Dibromobianthracene Derivatives". In: *Chemistry of Materials* 31.2 (2019), pp. 331–341. ISSN: 15205002. DOI: 10.1021/acs.chemmater.8b03094.

[120] Cordelia Sealy. "Holey graphene from the bottom up". In: *Nano Today* 21 (2018), pp. 7–8. ISSN: 17480132. DOI: 10.1016/j.nantod.2018.06.003.

[121] Christiana Varnava. "Precise pores give graphene a bandgap". In: *Nature Electronics* 1.5 (2018), p. 264. ISSN: 25201131. DOI: 10.1038/s41928-018-0081-5. URL: http://dx.doi.org/10.1038/s41928-018-0081-5.

[122] Alexander Sinitskii. "A recipe for nanoporous graphene". In: *Science* 360.6385 (2018), pp. 154–155. DOI: 10.1126/science.aat2634NANOMATERIALS.

[123] Bohayra Mortazavi et al. "Nanoporous graphene: A 2D semiconductor with anisotropic mechanical, optical and thermal conduction properties". In: *Carbon* 147 (2019), pp. 377–384. ISSN: 00086223. DOI: 10.1016/j.carbon.2019.03.018. URL: https://doi.org/10.1016/j.carbon.2019.03.018.

[124] Farrokh Yousefi, Farhad Khoeini, and Ali Rajabpour. "Thermal conductivity and thermal rectification of nanoporous graphene: A molecular dynamics simulation". In: *International Journal of Heat and Mass Transfer* 146 (2020), p. 118884. ISSN: 00179310. DOI: 10.1016/j.ijheatmasstransfer.2019.118884. arXiv: 1906.04696. URL: https://doi.org/10.1016/j.ijheatmasstransfer.2019.118884.

[125] Gaetano Calogero et al. "Quantum interference engineering of nanoporous graphene for carbon nanocircuitry". In: *Journal of the American Chemical Society* (2019). ISSN: 0002-7863. DOI: 10.1021/jacs.9b04649.

[126] Gaetano Calogero et al. "Electron Transport in Nanoporous Graphene: Probing the Talbot Effect". In: *Nano Letters* 19.1 (2019), pp. 576–581. ISSN: 15306992. DOI: 10.1021/acs.nanolett.8b04616.

[127] Chun Shen, Hu Qiu, and Wanlin Guo. "Ultrahigh hydrogen and nitrogen selectivity achieved by the nanoporous graphene with a precise nanopore". In: *Carbon* 182 (2021), pp. 628–633. ISSN: 00086223. DOI: 10.1016/j.carbon.2021.06.011. URL: https://doi.org/10.1016/j.carbon.2021.06.011.

[128] Liliang Tian et al. "Density Functional Theory and Molecular Dynamics Simulations of Nanoporous Graphene Membranes for Hydrogen Separation". In: *ACS Applied Nano Materials* (2021). ISSN: 25740970. DOI: 10.1021/acsanm.1c01919.

[129] Tanveer Hussain et al. "Functionalized Two-Dimensional Nanoporous Graphene as Efficient Global Anode Materials for Li-, Na-, K-, Mg-, and Ca-Ion Batteries". In: *Journal of Physical Chemistry C* 124.18 (2020), pp. 9734–9745. ISSN: 19327455. DOI: 10.1021/acs.jpcc.0c01216.

[130] Rémy Pawlak et al. "Bottom-up Synthesis of Nitrogen-Doped Porous Graphene Nanoribbons". In: *Journal of the American Chemical Society* 142.29 (2020), pp. 12568–12573. ISSN: 15205126. DOI: 10.1021/jacs.0c03946.

[131] Suqin Cheng et al. "Stepwise On-Surface Synthesis of Porous Carbon Nanoribbons with Notched Zigzag Edges". In: *Journal of Physical Chemistry C* (2019). ISSN: 19327455. DOI: 10.1021/acs.jpcc.9b10059.

[132] Peter H Jacobse et al. "Bottom-up Assembly of Nanoporous Graphene with Emergent Electronic States Bottom-up Assembly of Nanoporous Graphene with Emergent Electronic States". In: *Journal of the American Chemical Society* (2020), pp. 1–9. DOI: 10.1021/jacs.0c05235.

[133] Marco Bieri et al. "Porous graphenes: Two-dimensional polymer synthesis with atomic precision". In: *Chemical Communications* 45 (2009), pp. 6919–6921. ISSN: 13597345. DOI: 10.1039/b915190g.

[134] Dingguan Wang et al. "Atomic-Level Electronic Properties of Carbon Nitride Monolayers". In: *ACS Nano* (2020), pp. 1–38. DOI: 10.1021/acsnano.0c06535.

[135] Rémy Pawlak et al. "On-Surface Synthesis of Nitrogen-Doped Kagome Graphene". In: *Angewandte Chemie International Edition* (2021), pp. 1–6. ISSN: 1433-7851. DOI: 10.1002/anie.202016469.

[136] Johanna Eichhorn et al. "On-surface ullmann coupling: The influence of kinetic reaction parameters on the morphology and quality of covalent networks". In: *ACS Nano* 8.8 (2014), pp. 7880–7889. ISSN: 1936086X. DOI: 10.1021/nn501567p.

[137] Min Chen et al. "Combined photoemission and scanning tunneling microscopy study of the surface-assisted ullmann coupling reaction". In: *Journal of Physical Chemistry C* 118.13 (2014), pp. 6820–6830. ISSN: 19327447. DOI: 10.1021/jp4121468.

[138] Guoqiang Shi et al. "Graphene-like Covalent Organic Framework with Wide Bandgap Synthesized On Surface via Stepwise Reactions". In: *Angewandte Chemie International Edition* (2020), pp. 16092–16096. ISSN: 1433-7851. DOI: 10.1002/anie.202006176.

[139] Ke Ji Shi et al. "Ullmann Reaction of Aryl Chlorides on Various Surfaces and the Application in Stepwise Growth of 2D Covalent Organic Frameworks". In: *Organic Letters* 18.6 (2016), pp. 1282–1285. ISSN: 15237052. DOI: 10.1021/acs.orglett.6b00172.

[140] Leonhard Grill and Stefan Hecht. "Covalent on-surface polymerization". In: *Nature Chemistry* 12.February (2020), pp. 115–130. ISSN: 1755-4349. DOI: 10.1038/s41557-019-0392-9. URL: http://dx.doi.org/10.1038/s41557-019-0392-9.

[141] Giang D. Nguyen et al. "Atomically precise graphene nanoribbon heterojunctions from a single molecular precursor". In: *Nature Nanotechnology* 12.11 (2017), pp. 1077–1082. ISSN: 17483395. DOI: 10.1038/nnano.2017.155.

[142] Eduard Carbonell-Sanromà et al. "Quantum Dots Embedded in Graphene Nanoribbons by Chemical Substitution". In: *Nano letters* 17.1 (2017), pp. 50–56. ISSN: 15306992. DOI: 10.1021/acs.nanolett.6b03148.

[143] P. H. Jacobse et al. "Electronic components embedded in a single graphene nanoribbon". In: *Nature Communications* 8.1 (2017), pp. 1–7. ISSN: 20411723. DOI: 10.1038/s41467-017-00195-2. URL: http://dx.doi.org/10.1038/s41467-017-00195-2.

[144] Tomas Marangoni et al. "Heterostructures through Divergent Edge Reconstruction in Nitrogen-Doped Segmented Graphene Nanoribbons". In: *Chemistry - A European Journal* 22.37 (2016), pp. 13037–13040. ISSN: 15213765. DOI: 10.1002/chem.201603497.

[145] Daniel J. Rizzo et al. "Length-Dependent Evolution of Type II Heterojunctions in Bottom-Up-Synthesized Graphene Nanoribbons". In: *Nano Letters* 19.5 (2019), pp. 3221–3228. ISSN: 15306992. DOI: 10.1021/acs.nanolett.9b00758.

[146] Prashant P. Shinde et al. "Graphene nanoribbons with mixed cove-cape-zigzag edge structure". In: *Carbon* 175 (2021), pp. 50–59. ISSN: 00086223. DOI: 10.1016/j.carbon.2020.12.069.

[147] Austin Evans et al. "Two-Dimensional Polymers and Polymerizations". In: *Chemical Reviews* (2021). DOI: 10.1021/acs.chemrev.0c01184.

[148] Nikolas A.A. Zwaneveld et al. "Organized formation of 2D extended covalent organic frameworks at surfaces". In: *Journal of the American Chemical Society* 130.21 (2008), pp. 6678–6679. ISSN: 00027863. DOI: 10.1021/ja800906f.

[149] R. Raval. "Chiral expression from molecular assemblies at metal surfaces: Insights from surface science techniques". In: *Chemical Society Reviews* 38.3 (2009), pp. 707–721. ISSN: 14604744. DOI: 10.1039/b800411k.

[150] Kuniaki Konishi et al. "Circularly polarized light emission from semiconductor planar chiral nanostructures". In: *Physical Review Letters* 106.5 (2011), pp. 1–4. ISSN: 00319007. DOI: 10.1103/PhysRevLett.106.057402.

[151] Jonathan M. Bonello, Federico J. Williams, and Richard M. Lambert. "Aspects of enantioselective heterogeneous catalysis: Structure and reactivity of (S)-(-)-1-(1-naphthyl)ethylamine on Pt{111}". In: *Journal of the American Chemical Society* 125.9 (2003), pp. 2723–2729. ISSN: 00027863. DOI: 10.1021/ja028436x.

[152] T. Mallat, E. Orglmeister, and A. Baiker. "Asymmetric catalysis at chiral metal surfaces". In: *Chemical Reviews* 107.11 (2007), pp. 4863–4890. ISSN: 00092665. DOI: 10.1021/cr0683663.

[153] Roman Fasel, Manfred Parschau, and Karl Heinz Ernst. "Chirality Transfer from Single Molecules into Self-Assembled Monolayers". In: *Angewandte Chemie - International Edition* 42.42 (2003), pp. 5178–5181. ISSN: 14337851. DOI: 10.1002/anie.200352232.

[154] Roman Fasel, Manfred Parschau, and Karl Heinz Ernst. "Amplification of chirality in two-dimensional enantiomorphous lattices". In: *Nature* 439.7075 (2006), pp. 449–452. ISSN: 14764687. DOI: 10.1038/nature04419.

[155] A. Mugarza et al. "Orbital specific chirality and homochiral self-assembly of achiral molecules induced by charge transfer and spontaneous symmetry breaking". In: *Physical Review Letters* 105.11 (2010), pp. 30–33. ISSN: 10797114. DOI: 10.1103/PhysRevLett.105.115702.

[156] Ying Xu et al. "Chirality of molecular nanostructures on surfaces via molecular assembly and reaction: manifestation and control". In: *Surface Science Reports* (2021). ISSN: 1043-6618. DOI: 10.1016/j.surfrep.2021.100531. URL: https://doi.org/10.1016/j.phrs.2020.104743.

[157] Oleksandr Stetsovych et al. "From helical to planar chirality by on-surface chemistry". In: *Nature Chemistry* 9.3 (2017), pp. 213–218. ISSN: 17554349. DOI: 10.1038/nchem.2662.

[158] Hiroshi Sakaguchi et al. "Homochiral polymerization-driven selective growth of graphene nanoribbons". In: *Nature Chemistry* 9.1 (2017), pp. 57–63. ISSN: 17554349. DOI: 10.1038/nchem.2614.

[159] Nestor Merino-Díez et al. "Transferring axial molecular chirality through a sequence of on-surface reactions". In: *Chemical Science* 11.21 (2020), pp. 5441–5446. DOI: 10.1039/d0sc01653e.

[160] Jie Yu Yue et al. "Simultaneous construction of two linkages for the on-surface synthesis of imine-boroxine hybrid covalent organic frameworks". In: *Chemical Science* 8.3 (2017), pp. 2169–2174. ISSN: 20416539. DOI: 10.1039/c6sc03590f.

[161] Anaïs Mairena et al. "Diastereoselective Ullmann Coupling to Bishelicenes by Surface Topochemistry". In: *Journal of the American Chemical Society* 140.45 (2018), pp. 15186–15189. ISSN: 15205126. DOI: 10.1021/jacs.8b10059.

[162] Christian Wäckerlin et al. "Surface-assisted diastereoselective Ullmann coupling of bishelicenes". In: *Chemical Communications* 52.86 (2016), pp. 12694–12697. ISSN: 1364548X. DOI: 10.1039/c6cc05849c.

[163] Qian Shen, Hong Ying Gao, and Harald Fuchs. "Frontiers of on-surface synthesis: From principles to applications". In: *Nano Today* 13 (2017), pp. 77–96. ISSN: 1878044X. DOI: 10.1016/j.nantod.2017.02.007. URL: http://dx.doi.org/10.1016/j.nantod.2017.02.007.

[164] C. Julian Chen. *Introduction to Scanning Tuneling Microscopy*. Second Ed. New York: Oxford University Press, 1993, pp. 1–473. ISBN: 9780199211500. DOI: 10.1093/acprof:oso/9780199211500.001.0001. URL: https://oxford.universitypressscholarship.com/view/10.1093/acprof:oso/9780199211500.001.0001/acprof-9780199211500.

[165] Bert Voigtländer. *Scanning probe microscopy (SPM)*. Springer US, 2015, pp. 1–377. ISBN: 9780128141830. DOI: 10.1016/B978-0-12-814182-3.00005-5.

[166] J. Tersoff and D. R. Hamann. "Theory and Application for the Scanning Tunneling Microscope". In: *The Anatomical Record* 50.25 (1983), pp. 1998–2001. ISSN: 10970185. DOI: 10.1002/ar.1092160117.

[167] J. Tersoff and D. R. Hamann. "Theory of the scanning tunneling microscope". In: *Physical Review B* 31.2 (1985), pp. 805–813. ISSN: 01631829. DOI: 10.1103/PhysRevB.31.805.

[168] C Julian Chen. "Tunneling matrix elements in three-dimensional space: The derivative rule and the sum rule". In: *Physical Review B* 42.14 (1990).

[169] Richard E. Prange. "Tunneling from a many-particle point of view". In: *Physical Review* 131.3 (1963), pp. 1083–1086. ISSN: 0031899X. DOI: 10.1103/PhysRev.131.1083.

[170] Hajo Söde et al. "Electronic band dispersion of graphene nanoribbons via Fourier-transformed scanning tunneling spectroscopy". In: *Physical Review B - Condensed Matter and Materials Physics* 91.4 (2015), pp. 1–6. ISSN: 1550235X. DOI: 10.1103/PhysRevB.91.045429. arXiv: 1412.1954.

[171] Jascha Repp et al. "Molecules on insulating films: Scanning-tunneling microscopy imaging of individual molecular orbitals". In: *Physical Review Letters* 94.2 (2005), pp. 1–4. ISSN: 00319007. DOI: 10.1103/PhysRevLett.94.026803.

[172] Leo Gross et al. "High-resolution molecular orbital imaging using a p-wave STM tip". In: *Physical Review Letters* 107.8 (2011), pp. 1–4. ISSN: 00319007. DOI: 10.1103/PhysRevLett.107.086101.

[173] Leo Gross et al. "The chemical structure of a molecule resolved by atomic force microscopy". In: *Science* 325.August (2009), pp. 1110–4. ISSN: 1095-9203. URL: http://www.ncbi.nlm.nih.gov/pubmed/19713523.

[174] Hapala Prokop and Pavel Jelinek. "Mechanism of high-resolution STM/AFM imaging with functionalized tips". In: *Physical Review B* 90 (2014), p. 9. ISSN: 17582067. DOI: 10.1103/PhysRevB.90.085421. arXiv: 1406.3562.

[175] Chi Lun Chiang et al. "Real-space imaging of molecular structure and chemical bonding by single-molecule inelastic tunneling probe". In: *Science* 344.6186 (2014), pp. 885–888. ISSN: 10959203. DOI: 10.1126/science.1253405.

[176] Prokop Hapala et al. "Origin of high-resolution IETS-STM images of organic molecules with functionalized tips". In: *Physical Review Letters* 113.22 (2014), pp. 1–5. ISSN: 10797114. DOI: 10.1103/PhysRevLett.113.226101. arXiv: 1409.3405.

[177] Pavel Jelinek. "High resolution SPM imaging of organic molecules with functionalized tips". In: *Journal of Physics Condensed Matter* 29.34 (2017). ISSN: 1361648X. DOI: 10.1088/1361-648X/aa76c7.

[178] K. Besocke. "An easily operable scanning tunneling microscope". In: *Surface Science* 181.1-2 (1987), pp. 145–153. ISSN: 00396028. DOI: 10.1016/0039-6028(87)90151-8.

[179] Cesar Moreno et al. "On-surface synthesis of superlattice arrays of ultra-long graphene nanoribbons". In: *Chemical Communications* 54.68 (2018), pp. 9402–9405. ISSN: 1364548X. DOI: 10.1039/c8cc04830d.

[180] H. Hertz. *Schriften vermischten Inhalts / von Heinrich Hertz ; herausgegeben von Ph. Lenard* . Ed. by Leipzig Ambrosius Barth. 1889. URL: https://books.google.es/books/about/Schriften{_}vermischten{_}Inhalts{_}herausgege.html?id=2bdOAQAAMAAJ{\&}redir{_}esc=y.

[181] George H. Major et al. "Assessment of the frequency and nature of erroneous x-ray photoelectron spectroscopy analyses in the scientific literature". In: *Journal of Vacuum Science & Technology A* 38.6 (2020), p. 061204. ISSN: 0734-2101. DOI: 10.1116/6.0000685.

[182] Martin Schmid, Hans Peter Steinrück, and J. Michael Gottfried. "A new asymmetric Pseudo-Voigt function for more efficient fitting of XPS lines". In: *Surface and Interface Analysis* 46.8 (2014), pp. 505–511. ISSN: 10969918. DOI: 10.1002/sia.5521.

[183] J. H. Scofield. "Hartree-Slater subshell photoionization cross-sections at 1254 and 1487 eV". In: *Journal of Electron Spectroscopy and Related Phenomena* 8.2 (1976), pp. 129–137. ISSN: 03682048. DOI: 10.1016/0368-2048(76)80015-1.

[184] M.P. Seah and W.A. Dench. "Quantitative Electron Spectroscopy of Surfaces :" in: *Surface And Interface Analysis* 1.1 (1979), pp. 2–11.

[185] M Soler et al. "The SIESTA method for ab initio order-N materials simulation". In: *Journal of Physics: Condensed Matter* 14 (2002), pp. 2745–2779. DOI: 10.1088/0953-8984/14/11/302.

[186] Emilio Artacho et al. "The SIESTA method; Developments and applicability". In: *Journal of Physics Condensed Matter* 20.6 (2008). ISSN: 1361648X. DOI: 10.1088/0953-8984/20/6/064208.

[187] Alberto García et al. "Siesta: Recent developments and applications". In: *The Journal of chemical physics* 152.20 (2020), p. 204108. ISSN: 10897690. DOI: 10.1063/5.0005077. arXiv: 2006.01270.

[188] Nick Papior. *sisl: v0.11.0*. 2021. DOI: 10.5281/zenodo.597181. URL: https://doi.org/10.5281/zenodo.597181.

[189] Koichi Momma and Fujio Izumi. "VESTA: A three-dimensional visualization system for electronic and structural analysis". In: *Journal of Applied Crystallography* 41.3 (2008), pp. 653–658. ISSN: 00218898. DOI: 10.1107/S0021889808012016.

[190] Ganhua Lu et al. "Semiconducting graphene: converting graphene from semimetal to semiconductor". In: *Nanoscale* 5.4 (2013), pp. 1353–1368. ISSN: 2050-7526. DOI: 10.1039/C2NR32453A. arXiv: arXiv:1310.8002v1. URL: http://dx.doi.org/10.1039/C2NR32453A.

[191] Shuaijun Wang et al. "Engineered Graphitic Carbon Nitride-Based Photocatalysts for Visible-Light-Driven Water Splitting: A Review". In: *Energy and Fuels* 35.8 (2021), pp. 6504–6526. ISSN: 15205029. DOI: 10.1021/acs.energyfuels.1c00503.

[192] Yaru Bian et al. "Nitrogen-rich holey graphene for efficient oxygen reduction reaction". In: *Carbon* 162 (2020), pp. 66–73. ISSN: 00086223. DOI: 10.1016/j.carbon.2020.01.110. URL: https://doi.org/10.1016/j.carbon.2020.01.110.

[193] Jiqian Yang et al. "S-Doped N-Rich Carbon Nanosheets with Expanded Interlayer Distance as Anode Materials for Sodium-Ion Batteries". In: *Advanced Materials* 29.6 (2017), pp. 1–5. ISSN: 15214095. DOI: 10.1002/adma.201604108.

[194] Ryan R. Cloke et al. "Site-Specific Substitutional Boron Doping of Semiconducting Armchair Graphene Nanoribbons". In: *Journal of the American Chemical Society* 137.28 (2015), pp. 8872–8875. ISSN: 15205126. DOI: 10.1021/jacs.5b02523.

[195] Yi Zhang et al. "Direct visualization of atomically precise nitrogen-doped graphene nanoribbons". In: *Applied Physics Letters* 105.2 (2014). ISSN: 00036951. DOI: 10.1063/1.4884359.

[196] Eduard Carbonell-Sanromà et al. "Doping of Graphene Nanoribbons via Functional Group Edge Modification". In: *ACS Nano* 11.7 (2017), pp. 7355–7361. ISSN: 1936086X. DOI: 10.1021/acsnano.7b03522. arXiv: 1705.07045.

[197] Peter Spijker et al. "Atomically controlled substitutional boron-doping of graphene nanoribbons". In: *Nature Communications* 6.1 (2015), pp. 1–6. DOI: 10.1038/ncomms9098. URL: http://dx.doi.org/10.1038/ncomms9098.

[198] Shigeki Kawai et al. "Multiple heteroatom substitution to graphene nanoribbon". In: *Science Advances* 4.4 (2018), pp. 1–8. ISSN: 23752548. DOI: 10.1126/sciadv.aar7181.

[199] Andrea Basagni et al. "Tunable Band Alignment with Unperturbed Carrier Mobility of On-Surface Synthesized Organic Semiconducting Wires". In: *ACS Nano* 10.2 (2016), pp. 2644–2651. ISSN: 1936086X. DOI: 10.1021/acsnano.5b07683.

[200] Giang D. Nguyen et al. "Bottom-Up Synthesis of N = 13 Sulfur-Doped Graphene Nanoribbons". In: *Journal of Physical Chemistry C* 120.5 (2016), pp. 2684–2687. ISSN: 19327455. DOI: 10.1021/acs.jpcc.5b09986.

[201] Yubin Fu et al. "On-Surface Synthesis of NBN-Doped Zigzag-Edged Graphene Nanoribbons". In: *Angewandte Chemie - International Edition* 59.23 (2020), pp. 8873–8879. ISSN: 15213773. DOI: 10.1002/anie.202000488.

[202] Xiao Ye Wang et al. "Bottom-Up Synthesis of Heteroatom-Doped Chiral Graphene Nanoribbons". In: *Journal of the American Chemical Society* 140.29 (2018), pp. 9104–9107. ISSN: 15205126. DOI: 10.1021/jacs.8b06210.

[203] Zhijing Feng et al. "Bottom-up synthesis of nitrogen-containing graphene nanoribbons from the tetrabenzopentacene molecular motif". In: *Carbon* 170 (2020), pp. 677–684. ISSN: 00086223. DOI: 10.1016/j.carbon.2020.07.018. URL: https://doi.org/10.1016/j.carbon.2020.07.018.

[204] Yolanda L. Li et al. "Fjord-Edge Graphene Nanoribbons with Site-Specific Nitrogen Substitution". In: *Journal of the American Chemical Society* 142.42 (2020), pp. 18093–18102. ISSN: 15205126. DOI: 10.1021/jacs.0c07657.

[205] Timothy H. Vo et al. "Nitrogen-Doping Induced Self-Assembly of Graphene Nanoribbon-Based Two-Dimensional and Three-Dimensional Metamaterials". In: *Nano Letters* 15.9 (2015), pp. 5770–5777. ISSN: 15306992. DOI: 10.1021/acs.nanolett.5b01723.

[206] Timothy H. Vo et al. "Bottom-up solution synthesis of narrow nitrogen-doped graphene nanoribbons". In: *Chemical Communications* 50.32 (2014), pp. 4172–4174. ISSN: 1364548X. DOI: 10.1039/c4cc00885e.

[207] Rebecca A. Durr et al. "Orbitally Matched Edge-Doping in Graphene Nanoribbons". In: *Journal of the American Chemical Society* 140.2 (2018), pp. 807–813. ISSN: 15205126. DOI: 10.1021/jacs.7b11886.

[208] Yan Fang Zhang et al. "Sulfur-doped graphene nanoribbons with a sequence of distinct band gaps". In: *Nano Research* 10.10 (2017), pp. 3377–3384. ISSN: 19980000. DOI: 10.1007/s12274-017-1550-2.

[209] Jingcheng Li et al. "Band Depopulation of Graphene Nanoribbons Induced by Chemical Gating with Amino Groups". In: *ACS Nano* 14.2 (2020), pp. 1895–1901. ISSN: 1936086X. DOI: 10.1021/acsnano.9b08162.

[210] Mirco Panighel et al. "Stabilizing Edge-Fluorination in Graphene Nanoribbons". In: *ACS Nano* (2020), pp. 1–27. DOI: 10.1021/acsnano.0c01837.

[211] Niklas Friedrich et al. "Magnetism of Topological Boundary States Induced by Boron Substitution in Graphene Nanoribbons". In: *Physical Review Letters* 125.14 (2020), pp. 1–6. ISSN: 10797114. DOI: 10.1103/PhysRevLett.125.146801. arXiv: 2004.10280.

[212] F. Cervantes-Sodi et al. "Edge-functionalized and substitutionally doped graphene nanoribbons: Electronic and spin properties". In: *Physical Review B - Condensed Matter and Materials Physics* 77.16 (2008), pp. 1–13. ISSN: 10980121. DOI: 10.1103/PhysRevB.77.165427. arXiv: 0711.2340.

[213] Muhammad Ali et al. "High gas-sensing selectivity of bilaterally edge-doped graphene nano-ribbons towards detecting NO2, O2 and SO3 gas molecules: Ab-initio investigation". In: *Applied Surface Science* 514.February (2020), p. 145866. ISSN: 01694332. DOI: 10.1016/j.apsusc.2020.145866. URL: https://doi.org/10.1016/j.apsusc.2020.145866.

[214] Pavel V Barkov and Olga E Glukhova. "Carboxylated Graphene Nanoribbons for Highly-Selective Ammonia Gas Sensors : Ab Initio Study". In: *Chemosensors* 9.84 (2021), pp. 1–13.

[215] Qitang Fan et al. "Biphenylene network: A nonbenzenoid carbon allotrope". In: *Science* 372.6544 (2021), pp. 852–856. ISSN: 10959203. DOI: 10.1126/science.abg4509.

[216] Grzegorz Gabka et al. “Ligand exchange in quaternary alloyed nanocrystals - a spectroscopic study”. In: *Physical Chemistry Chemical Physics* 16.42 (2014), pp. 23082–23088. ISSN: 14639076. DOI: 10.1039/c4cp03850a.

[217] Ruriko Hatada et al. “Preparation of aniline-based nitrogen-containing diamond-like carbon films with low electrical resistivity”. In: *Coatings* 10.1 (2020). ISSN: 20796412. DOI: 10.3390/coatings10010054.

[218] Arunabh Batra et al. “Probing the mechanism for graphene nanoribbon formation on gold surfaces through X-ray spectroscopy”. In: *Chemical Science* 5.11 (2014), pp. 4419–4423. ISSN: 20416539. DOI: 10.1039/c4sc01584c.

[219] Marco Di Giovannantonio et al. “On-Surface Growth Dynamics of Graphene Nanoribbons: The Role of Halogen Functionalization”. In: *ACS Nano* 12.1 (2018), pp. 74–81. ISSN: 1936086X. DOI: 10.1021/acsnano.7b07077.

[220] Bay V. Tran et al. “Surface-confined [2 + 2] cycloaddition towards one-dimensional polymers featuring cyclobutadiene units”. In: *Nanoscale* 9.46 (2017), pp. 18305–18310. ISSN: 20403372. DOI: 10.1039/c7nr06187k.

[221] Rafal Zuzak et al. “On-Surface Synthesis of Chlorinated Narrow Graphene Nanoribbon Organometallic Hybrids”. In: *Journal of Physical Chemistry Letters* (2020), pp. 10290–10297. ISSN: 19487185. DOI: 10.1021/acs.jpclett.0c03134.

[222] Weiwei Gao et al. “Chlorine adsorption on Au(111): Chlorine overlayer or surface chloride?” In: *Journal of the American Chemical Society* 130.11 (2008), pp. 3560–3565. ISSN: 00027863. DOI: 10.1021/ja077989a.

[223] Haiming Zhang et al. “Surface supported gold-organic hybrids: On-surface synthesis and surface directed orientation”. In: *Small* 10.7 (2014), pp. 1361–1368. ISSN: 16136829. DOI: 10.1002/smll.201303011.

[224] Meizhuang Liu et al. “Graphene-like nanoribbons periodically embedded with four- and eight-membered rings”. In: *Nature Communications* 8 (2017), pp. 1–7. ISSN: 20411723. DOI: 10.1038/ncomms14924.

[225] Chen Hui Shu et al. “Diverse supramolecular structures self-assembled by a simple aryl chloride on Ag(111) and Cu(111)”. In: *Chemical Communications* 54.97 (2018), pp. 13670–13673. ISSN: 1364548X. DOI: 10.1039/c8cc08673g.

[226] M. R. Ajayakumar et al. "Neutral Organic Radical Formation by Chemisorption on Metal Surfaces". In: *Journal of Physical Chemistry Letters* 11.10 (2020), pp. 3897–3904. ISSN: 19487185. DOI: 10.1021/acs.jpclett.0c00269.

[227] W. Chen et al. "Scanning tunneling microscopy observation of an electronic superlattice at the surface of clean gold". In: *Physical Review Letters* 80.7 (1998), pp. 1469–1472. ISSN: 10797114. DOI: 10.1103/PhysRevLett.80.1469.

[228] S. M. Hollen et al. "Modification of electronic surface states by graphene islands on Cu(111)". In: *Physical Review B - Condensed Matter and Materials Physics* 91.19 (2015), pp. 30–35. ISSN: 1550235X. DOI: 10.1103/PhysRevB.91.195425.

[229] Julia Tesch et al. "Structural and electronic properties of graphene nanoflakes on Au(111) and Ag(111)". In: *Scientific Reports* 6.March (2016), pp. 1–9. ISSN: 20452322. DOI: 10.1038/srep23439.

[230] Néstor Merino-Díez et al. "Width-Dependent Band Gap in Armchair Graphene Nanoribbons Reveals Fermi Level Pinning on Au(111)". In: *ACS Nano* 11.11 (2017), pp. 11661–11668. ISSN: 1936086X. DOI: 10.1021/acsnano.7b06765.

[231] A. Mugarza et al. "Electronic and magnetic properties of molecule-metal interfaces: Transition-metal phthalocyanines adsorbed on Ag(100)". In: *Physical Review B - Condensed Matter and Materials Physics* 85.15 (2012), pp. 1–13. ISSN: 10980121. DOI: 10.1103/PhysRevB.85.155437. arXiv: 1203.2747.

[232] Héctor González-Herrero et al. "Graphene Tunable Transparency to Tunneling Electrons: A Direct Tool to Measure the Local Coupling". In: *ACS Nano* 10.5 (2016), pp. 5131–5144. ISSN: 1936086X. DOI: 10.1021/acsnano.6b00322.

[233] Min Feng, Jin Zhao, and Hrvoje Petek. "Atomlike, hollow-core-bound molecular orbitals of C60". In: *Science* 320.5874 (2008), pp. 359–362. ISSN: 00368075. DOI: 10.1126/science.1155866.

[234] Hossein Taghinejad, Ali A. Eftekhar, and Ali Adibi. "Lateral and vertical heterostructures in two-dimensional transition-metal dichalcogenides [Invited]". In: *Optical Materials Express* 9.4 (2019), p. 1590. ISSN: 2159-3930. DOI: 10.1364/ome.9.001590.

[235] Gayatri Swain, Sabiha Sultana, and Kulamani Parida. "A review on vertical and lateral heterostructures of semiconducting 2D-MoS2with other 2D materials: A feasible perspective for energy conversion". In: *Nanoscale* 13.22 (2021), pp. 9908–9944. ISSN: 20403372. DOI: 10.1039/d1nr00931a.

[236] Zhe Li et al. "Chemically modified STM tips for atomic-resolution imaging of ultrathin NaCl films". In: *Nano Research* 8.7 (2015), pp. 2223–2230. ISSN: 19980000. DOI: 10.1007/s12274-015-0733-y.

[237] Saien Xie et al. "Coherent, atomically thin transition-metal dichalcogenide superlattices with engineered strain". In: *Science* 359.6380 (2018), pp. 1131–1136. ISSN: 10959203. DOI: 10.1126/science.aao5360.

[238] Prasana K. Sahoo et al. "One-pot growth of two-dimensional lateral heterostructures via sequential edge-epitaxy". In: *Nature* 553.7686 (2018), pp. 63–67. ISSN: 14764687. DOI: 10.1038/nature25155.

[239] Masoud Mahjouri-Samani et al. "Patterned arrays of lateral heterojunctions within monolayer two-dimensional semiconductors". In: *Nature Communications* 6 (2015), pp. 1–6. ISSN: 20411723. DOI: 10.1038/ncomms8749.

[240] Jianwei Wang et al. "Recent Advances in 2D Lateral Heterostructures". In: *Nano-Micro Letters* 11.1 (2019), pp. 1–31. ISSN: 21505551. DOI: 10.1007/s40820-019-0276-y. URL: https://doi.org/10.1007/s40820-019-0276-y.

[241] Xuelei Su et al. "Edge State Engineering of Graphene Nanoribbons". In: *Nano Letters* 18.9 (2018), pp. 5744–5751. ISSN: 15306992. DOI: 10.1021/acs.nanolett.8b02356.

[242] Jingcheng Li et al. "Electrically Addressing the Spin of a Magnetic Porphyrin through Covalently Connected Graphene Electrodes". In: *Nano Letters* 19.5 (2019), pp. 3288–3294. ISSN: 15306992. DOI: 10.1021/acs.nanolett.9b00883.

[243] Luis M. Mateo et al. "On-Surface Synthesis and Characterization of Triply Fused Porphyrin–Graphene Nanoribbon Hybrids". In: *Angewandte Chemie - International Edition* 59.3 (2020), pp. 1334–1339. ISSN: 15213773. DOI: 10.1002/anie.201913024.

[244] J. Tersoff. "Theory of semiconductor heterojunctions: The role of quantum dipoles". In: *Physical Review B* 30.8 (1984), pp. 4874–4877. ISSN: 01631829. DOI: 10.1103/PhysRevB.30.4874.

[245] Junfeng Zhang et al. "Band alignment of two-dimensional lateral heterostructures". In: *2D Materials* 4.1 (2017). ISSN: 20531583. DOI: 10.1088/2053-1583/aa50cc.

[246] Liangbo Liang and Vincent Meunier. "Atomically precise graphene nanoribbon heterojunctions for excitonic solar cells". In: *Journal of Physical Chemistry C* 119.1 (2015), pp. 775–783. ISSN: 19327455. DOI: 10.1021/jp510035e.

[247] Matthew Wright and Ashraf Uddin. "Organic-inorganic hybrid solar cells: A comparative review". In: *Solar Energy Materials and Solar Cells* 107 (2012), pp. 87–111. ISSN: 09270248. DOI: 10.1016/j.solmat.2012.07.006. URL: http://dx.doi.org/10.1016/j.solmat.2012.07.006.

[248] Linjie Zhi and Klaus Mullen. "A bottom-up approach from molecular nanographenes to unconventional carbon materials". In: *Journal of Materials Chemistry* 18.13 (2008), pp. 1472–1484. ISSN: 09599428. DOI: 10.1039/b717585j.

[249] Renwen Yu, Joel D. Cox, and F. Javier García De Abajo. "Nonlinear Plasmonic Sensing with Nanographene". In: *Physical Review Letters* 117.12 (2016), pp. 1–6. ISSN: 10797114. DOI: 10.1103/PhysRevLett.117.123904.

[250] Paolo Fantuzzi et al. "Color Sensitive Response of Graphene/Graphene Quantum Dot Phototransistors". In: *Journal of Physical Chemistry C* 123.43 (2019), pp. 26490–26497. ISSN: 19327455. DOI: 10.1021/acs.jpcc.9b05013.

[251] Marcin Stępień et al. "Heterocyclic Nanographenes and Other Polycyclic Heteroaromatic Compounds: Synthetic Routes, Properties, and Applications". In: *Chemical Reviews* 117.4 (2017), pp. 3479–3716. ISSN: 15206890. DOI: 10.1021/acs.chemrev.6b00076.

[252] Xiao Ye Wang et al. "Exploration of pyrazine-embedded antiaromatic polycyclic hydrocarbons generated by solution and on-surface azomethine ylide homocoupling". In: *Nature Communications* 8.1 (2017), pp. 4–10. ISSN: 20411723. DOI: 10.1038/s41467-017-01934-1. URL: http://dx.doi.org/10.1038/s41467-017-01934-1.

[253] Xiao Ye Wang et al. "Heteroatom-Doped Nanographenes with Structural Precision". In: *Accounts of Chemical Research* 52.9 (2019), pp. 2491–2505. ISSN: 15204898. DOI: 10.1021/acs.accounts.9b00322.

[254] Xiao Ye Wang et al. "Heteroatom-Doped Perihexacene from a Double Helicene Precursor: On-Surface Synthesis and Properties". In: *Journal of the American Chemical Society* 139.13 (2017), pp. 4671–4674. ISSN: 15205126. DOI: 10.1021/jacs.7b02258.

[255] Huan Yang et al. "NBN-doped nanographene embedded with five-And seven-membered rings on Au(111) surface". In: *Chinese Physics B* 30.5 (2021). ISSN: 20583834. DOI: 10.1088/1674-1056/abeede.

[256] Axel Belser et al. "Visualization of the Borazine Core of B3N3-Doped Nanographene by STM". In: *ACS Applied Materials and Interfaces* 12.16 (2020), pp. 19218–19225. ISSN: 19448252. DOI: 10.1021/acsami.0c02324.

[257] Kalyan Biswas et al. "On-Surface Synthesis of a Dicationic Diaza-hexabenzocoronene Derivative on the Au(111) Surface". In: *Angewandte Chemie* 133.48 (2021), pp. 25755–25760. ISSN: 0044-8249. DOI: 10.1002/ange.202111863.

[258] Brijesh Kumar Mishra and N. Sathyamurthy. "π-π Interaction in pyridine". In: *Journal of Physical Chemistry A* 109.1 (2005), pp. 6–8. ISSN: 10895639. DOI: 10.1021/jp045218c.

[259] Elie Geagea et al. "On-Surface Synthesis of Ligands to Elaborate Coordination Polymers on an Au (111) Surface". In: *Nanomaterials* 111 (2021).

[260] Jonas Björk, Felix Hanke, and Sven Stafström. "Mechanisms of halogen-based covalent self-assembly on metal surfaces". In: *Journal of the American Chemical Society* 135.15 (2013), pp. 5768–5775. ISSN: 00027863. DOI: 10.1021/ja400304b.

[261] Jonas Björk, Sven Stafström, and Felix Hanke. "Zipping up: Cooperativity drives the synthesis of graphene nanoribbons". In: *Journal of the American Chemical Society* 133.38 (2011), pp. 14884–14887. ISSN: 00027863. DOI: 10.1021/ja205857a.

[262] Yasuhiro Yamada et al. "Unveiling bonding states and roles of edges in nitrogen-doped graphene nanoribbon by X-ray photoelectron spectroscopy". In: *Carbon* 185 (2021), pp. 342–367. ISSN: 00086223. DOI: 10.1016/j.carbon.2021.08.085. URL: https://doi.org/10.1016/j.carbon.2021.08.085.

[263] M. R. Ajayakumar et al. "Toward Full Zigzag-Edged Nanographenes: Peri-Tetracene and Its Corresponding Circumanthracene". In: *Journal of the American Chemical Society* 140.20 (2018), pp. 6240–6244. ISSN: 15205126. DOI: 10.1021/jacs.8b03711.

[264] Jan Philip Joost, Antti Pekka Jauho, and Michael Bonitz. "Correlated Topological States in Graphene Nanoribbon Heterostructures". In: *Nano Letters* 19.12 (2019), pp. 9045–9050. ISSN: 15306992. DOI: 10.1021/acs.nanolett.9b04075. arXiv: 1910.01152.

[265] Jingcheng Li et al. "Topological phase transition in chiral graphene nanoribbons: from edge bands to end states". In: *Nature Communications* (2021), pp. 1–8. DOI: 10.1038/s41467-021-25688-z. URL: http://arxiv.org/abs/2103.15937.

[266] Leopold Talirz et al. "On-Surface Synthesis and Characterization of 9-Atom Wide Armchair Graphene Nanoribbons". In: *ACS Nano* 11.2 (2017), pp. 1380–1388. ISSN: 1936086X. DOI: 10.1021/acsnano.6b06405.

[267] Yen Chia Chen et al. "Tuning the band gap of graphene nanoribbons synthesized from molecular precursors". In: *ACS Nano* 7.7 (2013), pp. 6123–6128. ISSN: 19360851. DOI: 10.1021/nn401948e.

[268] James Lawrence et al. "Probing the Magnetism of Topological End States in 5-Armchair Graphene Nanoribbons". In: *ACS Nano* (2020). ISSN: 1936086X. DOI: 10.1021/acsnano.9b10191.

[269] Thomas Dienel et al. "Resolving Atomic Connectivity in Graphene Nanostructure Junctions". In: *Nano Letters* 15.8 (2015), pp. 5185–5190. ISSN: 15306992. DOI: 10.1021/acs.nanolett.5b01403.

[270] Leopold Talirz et al. "Termini of bottom-up fabricated graphene nanoribbons". In: *Journal of the American Chemical Society* 135.6 (2013), pp. 2060–2063. ISSN: 00027863. DOI: 10.1021/ja311099k.

[271] Matthias Koch et al. "Voltage-dependent conductance of a single graphene nanoribbon". In: *Nature Nanotechnology* 7.11 (2012), pp. 713–717. ISSN: 17483395. DOI: 10.1038/nnano.2012.169.

[272] J. Zak. "Berrys phase for energy bands in solids". In: *Physical Review Letters* 62.23 (1989), pp. 2747–2750. ISSN: 00319007. DOI: 10.1103/PhysRevLett.62.2747.

[273] W. P. Su, J. R. Schrieffer, and A. J. Heeger. "Solitons in polyacetylene". In: *Physical Review Letters* 42.25 (1979), pp. 1698–1701. ISSN: 00319007. DOI: 10.1103/PhysRevLett.42.1698.

[274] Jianmin Huang et al. "Topology Selectivity in On-Surface Dehydrogenative Coupling Reaction: Dendritic Structure versus Porous Graphene Nanoribbon". In: *ACS Nano* 15.3 (2021), pp. 4617–4626. DOI: 10.1021/acsnano.0c08920. URL: https://dx.doi.org/10.1021/acsnano.0c08920.

[275] Andrea Basagni et al. "Molecules-oligomers-nanowires-graphene nanoribbons: A bottom-up stepwise on-surface covalent synthesis preserving long-range order". In: *Journal of the American Chemical Society* 137.5 (2015), pp. 1802–1808. ISSN: 15205126. DOI: 10.1021/ja510292b.

[276] Zongping Chen et al. "Lateral Fusion of Chemical Vapor Deposited N = 5 Armchair Graphene Nanoribbons". In: *Journal of the American Chemical Society* 139.28 (2017), pp. 9483–9486. ISSN: 15205126. DOI: 10.1021/jacs.7b05055.

[277] Doreen Beyer et al. "Graphene Nanoribbons Derived from Zigzag Edge-Encased Poly(para-2,9-dibenzo[bc, kl]coronenylene) Polymer Chains". In: *Journal of the American Chemical Society* (2019), pp. 8–11. ISSN: 15205126. DOI: 10.1021/jacs.8b10407.

[278] Kewei Sun et al. "On-Surface Synthesis of 8- and 10-Armchair Graphene Nanoribbons". In: *Small* 15.15 (2019), pp. 3–9. ISSN: 16136829. DOI: 10.1002/smll.201804526.

[279] Cunde Wang and Weiming Wu. "A simple method to determine the R or S configuration of molecules with an axis of chirality". In: *Journal of Chemical Education* 88.3 (2011), pp. 299–301. ISSN: 00219584. DOI: 10.1021/ed1003383.

[280] Zhifu Liang et al. "Atomically dispersed Fe in a C2N Based Catalyst as a Sulfur Host for Efficient Lithium–Sulfur Batteries". In: *Advanced Energy Materials* 11.5 (2021). ISSN: 16146840. DOI: 10.1002/aenm.202003507.

[281] Tomonobu Nakayama et al. "Development and application of multiple-probe scanning probe microscopes". In: *Advanced Materials* 24.13 (2012), pp. 1675–1692. ISSN: 09359648. DOI: 10.1002/adma.201200257.

[282] O. Kubo et al. "Epitaxially grown WOx nanorod probes for sub-100 nm multiple-scanning-probe measurement". In: *Applied Physics Letters* 88.25 (2006). ISSN: 00036951. DOI: 10.1063/1.2213954.

[283] Lian Sun et al. "Strain effect on electronic structures of graphene nanoribbons: A first-principles study". In: *Journal of Chemical Physics* 129.7 (2008), pp. 1–7. ISSN: 00219606. DOI: 10.1063/1.2958285.

[284] Yang Lu and Jing Guo. "Band gap of strained graphene nanoribbons". In: *Nano Research* 3.3 (2010), pp. 189–199. ISSN: 19980124. DOI: 10.1007/s12274-010-1022-4.

[285] E. Flores et al. "Inducing a topological transition in graphene nanoribbons superlattices by external strain". In: *ArXiv* (2021). arXiv: 2109.10278. URL: http://arxiv.org/abs/2109.10278.

[286] Alexey Lipatov et al. "Electrical and Elastic Properties of Individual Single-Layer Nb4C3Tx MXene Flakes". In: *Advanced Electronic Materials* 6.4 (2020), pp. 1–10. ISSN: 2199160X. DOI: 10.1002/aelm.201901382.

[287] Feng Miao, Shi Jun Liang, and Bin Cheng. "Straintronics with van der Waals materials". In: *npj Quantum Materials* 6.1 (2021), pp. 2–5. ISSN: 23974648. DOI: 10.1038/s41535-021-00360-3. URL: http://dx.doi.org/10.1038/s41535-021-00360-3.

[288] Hao Li et al. "Strongly Anisotropic Strain-Tunability of Excitons in Exfoliated ZrSe3". In: *Advanced Materials* (2021). ISSN: 15214095. DOI: 10.1002/adma.202103571.